WEST BENGAL UNIVERSITY OF TECHNOLOGY

Magnetic, transport and electronic properties of inter-metallic perovskite compounds

By

Abhishek Pandey

S. N. Bose National Centre for Basic Sciences
Block-JD, Sector-III, Salt Lake
Kolkata-700098

A thesis submitted in partial fulfillment for the degree of Doctor of Philosophy

August 2009

"Many of life's failures are people who did not realize how close they were to success when they gave up."

Thomas Edison

Preface

Oxygen-based perovskite compounds have attracted significant attention during last couple of decades due to the observation many exciting properties of basic scientific interest as well as of technological importance in such compounds. On the other hand, there are indeed very limited investigations, so far, on metallic-perovskite compounds (compounds where oxygen is replaced by some metal atoms). This thesis deals with the experimental studies of a few metallic perovskite compounds. We have investigated structural, thermal expansion, magnetic, transport, valence and electronic properties of metallic perovskites $RT_3B_xC_{1-x}$ and the parent binary compound RT_3, where R and T represent rare-earth and transition metal atoms, respectively.

The thesis is primarily divided in to seven chapters. First chapter provides a general introduction to the main theme of the thesis, where we have tried to include the most of the essential background information required to understand the work described in the thesis. In this chapter, we have briefly introduced the structural information on perovskite materials and discussed the basic underlying features of oxide-perovskite and metallic perovskite compounds. In the following sections of chapter 1, a brief discussion on basic magnetic properties of rare-earth ions, phenomenon of negative thermal expansion, underlying mechanisms of negative temperature coefficient of resistivity in metallic compounds, and valence fluctuation in some of the rare-earth elements has been presented.

In second chapter, a brief description of the various experimental tools and techniques, that are used in the course of the experimental work related to the thesis, is presented.

We have presented the results and interpretations of experimental investigations performed on stoichiometric $GdPd_3B_xC_{1-x}$ and off-stoichiometric $GdPd_3B_x$ compositions in the third chapter. We have also tried to make a comparative study of various physical properties of stoichiometric and off-stoichiometric compositions of this series of compounds.

Fourth chapter is based on the study of valence fluctuation in Ce and Eu based metallic perovskites and related cubic phases. We have investigated the interdependence of the valency of Ce and Eu ions. We have also tried to study the effect of the lattice parameter enhancement and change of chemical environment around the rare-earth ions on their valence behavior.

Study of structural, magnetic and transport properties of binary composition YPd_3 is presented in the fifth chapter.

In sixth chapter, an investigation on the magnetic and transport behavior of cubic $TbPd_3$ and boron incorporated $TbPd_3B$ is presented.

The last chapter summarizes the main findings and conclusions of the works reported in the thesis. The scope of future works is also outlined in this chapter.

References to the relevant published works related to the content of the thesis are provided at appropriate places. The full reference list appears at the end of the main content of the thesis. A few figures from published works have been included in the introduction section. The proper references of the same are provided in the figure caption itself.

Separate lists for figures, tables, abbreviations, physical constants and symbols are included before the beginning of the main content of the thesis. Hyperlinks have been provided for references, sections, tables, figures and equations. The whole list of contents is hyperlinked to the texts it refers to. URL's are provided for most of the references included in the bibliography.

Abhishek Pandey

List of publications

1. Intermediate valency of Eu in a cubic intermetallic compound $Ce_{0.5}Eu_{0.5}Pd_3$
Abhishek Pandey, Chandan Mazumdar, R. Ranganathan, V. Raghavendra Reddy and Ajay Gupta
Appl. Phys. Lett. **94**, 182503 (2009).

2. Negative pressure driven valence instability of Eu in cubic $Eu_{0.4}La_{0.6}Pd_3$
Abhishek Pandey, Chandan Mazumdar and R. Ranganathan
J. Phys.: Condens. Matter **21**, 216002 (2009).

3. Observation of giant magnetoresistance and reversal of its sign upon boron filling in cubic $TbPd_3$
Abhishek Pandey, Chandan Mazumdar and R. Ranganathan
Appl. Phys. Lett. **94**, 172509 (2009).

4. Magnetism in ordered metallic perovskite compound $GdPd_3B_xC_{1-x}$
Abhishek Pandey, Chandan Mazumdar, R. Ranganathan and S. Dattagupta
J. Magn. Magn. Mater. **321**, 2311 (2009).

5. Negative temperature coefficient of resistance in a crystalline compound
Abhishek Pandey, Chandan Mazumdar, R. Ranganathan, Molly De Raychaudhury, T. Saha-Dasgupta, Saurabh Tripathi, Dhananjai Pandey and S. Dattagupta
Europhys. Lett. **84**, 47007 (2008).

6. Magnetic behavior of binary intermetallic compound YPd_3
Abhishek Pandey, Chandan Mazumdar and R. Ranganathan
J. Alloys Compd. **476**, 14 (2009).

7. Transverse vibrations driven negative thermal expansion in a metallic compound $GdPd_3B_{0.25}C_{0.75}$
Abhishek Pandey, Chandan Mazumdar, R. Ranganathan, S. Tripathi, D. Pandey and S. Dattagupta
Appl. Phys. Lett. **92**, 261913 (2008).

8. Intermediate valence behavior in $Ce_{0.5}Eu_{0.5}Pd_3B_x$
Abhishek Pandey, Chandan Mazumdar, R. Ranganathan, S. Dattagupta, V. R. Reddy and A. Gupta
AIP Conf. Proc. **1003**, 216 (2008).

*__9.__ Silica encapsulated Ni nanoparticles: Variation of optical and magnetic properties with particle size
Saumen Das, Subhendu K. Panda, Prithiwish Nandi, Subhadra Chaudhuri, **Abhishek Pandey** and R. Ranganathan
J. Nanosci. Nanotechnol. **7**, 4447 (2007).

10. Magnetism and transport in off-stoichiometric metallic perovskite compounds $GdPd_3B_x$ (x = 0.25, 0.50 and 0.75)
Abhishek Pandey, Chandan Mazumdar and R. Ranganathan
Communicated.

Acknowledgements

There are, indeed, several people who have contributed significantly in my professional as well as personal development and, in particular, to carry out this thesis work. I sincerely acknowledge and thank all of them.

First of all, I would like to thank Prof. R. Ranganathan, my thesis supervisor, for his guidance and help during the course of the thesis work. It was a wonderful experience for me to work with him. He gave me all the freedom a Ph.D student can think of. His support was always there with me whenever I faced some problem, not only professional but personal as well. He is the person who has taught me how to keep myself organized in my day-to-day life.

I sincerely thank Prof. S. Dattagupta, my thesis co-supervisor and teacher. I can safely say that he is the person who has motivated me most for pursuing research. He has always been there with me as an excellent teacher and a very motivating supervisor. He used to take his time off from his very busy schedules to play cricket with us, to lunch with us and to discuss all our academic and nonacademic problems. His positive thinking and attitude has taught me a lot.

Mere words can not be enough to thank Prof. Chandan Mazumdar, my Chandan da. He has been my wise mentor. He is the person who has influenced me most. He is the person with whom I could discuss any issue without any hesitation. Chandan da is the one who has taught me how to think, how to proceed and how to be calm and composed in difficulties. His impatient scoldings and cheerful appreciations will always be there with me.

I would like to thank my teachers, Prof. B. Dutta-Roy, Prof. J. K. Bhattacharjee, Prof. A. Mookerjee, Prof. H. S. Mani, Prof. T. K. Das and Prof. S. Sen for their excellent teaching and guidance.

I thank Dr. T. Saha-Dasgupta for her help and a very fruitful collaboration. Working with her was very enlightening for me. I also thank my other collaborators, Dr. M. De Raychaudhury, Prof. D. Pandey, Dr. V. R. Reddy and Prof. A. Gupta. I sincerely thank my friend Saurabh for his help and a very cheerful company. I also thank Deepti, my friend working in Prof. Gupta's lab, for her help. I thank Prof. I. Das for his various help and for allowing me to use his lab facilities. I also thank Prof. A. Poddar for his help during my stay in Saha Institute of Nuclear Physics (SINP), Kolkata. I must acknowledge the help, support and encouragements provided by my seniors, Dr. Gayathri Banerjee and Anulekha during my initial days in SINP.

I would like to name some of my friends who have made my stay in Kolkata wonderfully memorable. First of all I would like to mention the name of Mrinal and Debu, my two batch mates. I have learned a great deal from them. In short I can only say that I never felt alone or out of home in their presence. They are the people with whom I could share every grief and joy. My other batch mates, Shashank, Navin, Venkata, Manas, Swati and Sunandan, have also given me their pleasant company.

Time spend with Shailesh and Niraj was simply wonderful and it's not easy to write down those memories in words. Their presence in my life, both on and off the cricket field, is very significant and it's really going to be very tough for me to pass my days without seeing their faces.

I had an excellent time with my friends in S. N. Bose National Centre for Basic Sciences (SNBNCBS) and members of our beloved cricket team and I must mention the name of Chinmay, Hemant, Irfan, Sudip, Abhinav, Amartya, Kapil, Rajiv, Vikas, Prashant, Sujoy, Bibhas and Arya in this regard.

The word "thank" is certainly not enough for expressing my feelings for Dr. Uday Kumar who has always provided me a very homely environment and played the role of my elder brother and a very dependable friend.

I am grateful to Mr. S. K. Shukla and Lata bhabhi for providing all the support and homely environment.

I feel lucky to have a friend like Santosh. He is the person with whom I share almost everything, be it professional or personal in nature. Santosh and his wife Sanchita have always behaved like family members with me and they are an integral part of my memories related to Kolkata.

This acknowledgement is incomplete without mentioning the name of some of my beloved seniors, Manirul da, Abhishek da, Ain-ul Huda and Monodeep da, who have provided me every possible support. I will always cherish the memories of the days spend with them.

It is my pleasure to thank Anis da, Deep, Kuntal da, Tapas, Saumik da, Bhola, Rupak, Shantanu, Sajib da, Papri di and my other friends from SINP.

I would like to sincerely acknowledge the help of the security, canteen, library and workshop staff members of SINP. I would like especially mention the name of Mr. D. Debnath and Mr. J. Basu for their help.

I sincerely acknowledge all the members of Experimental Condensed Matter Physics Division of SINP for their help and support. I gratefully acknowledge Tapan da, Arun da and Anis da for their countless help.

I am grateful to the administration of SNBNCBS for providing me excellent teaching facilities during my M. Sc. course work and also for providing me Junior Research Fellowship and subsequent Senior Research Fellowship of the center. I thank all the staff members of SNBNCBS.

I am very grateful to the administration, research scholars and faculty members of SINP for their excellent support. I never felt like an outsider in SINP and was provided all the facilities a regular research scholar of SINP in general gets.

I would like to name some of my closest friends who have always provided me their full support and have been a constant source of inspiration and motivation. Among them, I would like to mention the name of Dharmbir, Praveen, Amit, Alok, Rakesh, Megha, Amitash and Vikas.

It is needless to say that this thesis would not have been possible without the support of my family members. Support and encouragements provided by my late father, Shri B. N. Pandey stands on the top of every other thing. My brothers Mr. Anil K. Pandey, Mr. Arvind K. Pandey and Mr. Anurag Pandey and my sisters Mrs. Sandya Tripathi and Mrs. Arti Mishra have always supported me in all the possible ways. The support of my brother-in-laws Mr. M. M. Shukla, Mr. R. K. Tripathi and Mr. M. Mishra was always there with me. My sister-in-laws, Mrs. Sushma Pandey, Mrs. Manorama Pandey and Mrs. Shalini Pandey have always guided and supported me. I would also like to mention the name of my special friend Nidhi, whose support and encouragements were always there with me in my difficult times.

There must be countless others whom I have failed to mention here, who have extended their support towards me. I offer my sincere thank to all of them.

Abhishek Pandey

Contents

List of Figures

List of Tables

Abbreviations

AFM	**A**ntif**e**rro**m**agnetic
BMC	**B**aym-**M**eisel-**C**ote
CMR	**C**olossal **M**agneto**r**esistance
CW	**C**urie-**W**eise
DFT	**D**ensity **F**unctional **T**heory
FC	**F**ield-**C**ooled
FM	**F**erro**m**agnetic
GMR	**G**iant **M**agneto**r**esistance
ICF	**I**nter**c**onfigurational **F**luctuation
ICP-AES	**I**nductively **C**oupled **P**lasma-**A**tomic **E**mission **S**pectroscopy
IS	**I**somer **S**hift
LDA	**L**ocal **D**ensity **A**pproximation
LMTO	**L**inear **M**uffin-**T**in **O**rbital
MR	**M**agneto**r**esistance
NN	**N**earest **N**eighbor
NTCR	**N**egative **T**emperature **C**oefficient of **R**esistivity
NTE	**N**egative **T**hermal **E**xpansion
RE	**R**are **E**arth
RKKY	**R**uderman-**K**ittel-**K**asuya-**Y**osida
RRR	**R**esidual **R**esistivity **R**atio
SQUID	**S**uperconducting **Qu**antum **I**nterference **D**evice
TCR	**T**emperature **C**oefficient of **R**esistivity
VF	**V**alence **F**luctuating
XRD	**X**-**r**ay **D**iffraction
ZFC	**Z**ero **F**ield-**C**ooled

Physical Constants

Electron rest mass	m_e	=	9.109534×10^{-31} kg
Boltzmann constant	k_B	=	1.380662×10^{-23} JK^{-1}
Avagadro number	N_A	=	6.022045×10^{23} mole^{-1}
Bohr magneton	$\mu_B = e\hbar/2m_e$	=	9.274078×10^{-24} Am^2
Planck constant	$\hbar = h/2\pi$	=	1.054589×10^{-34} Js

Symbols

a	Cubic lattice parameter
ρ	Resistivity
α	Thermal expansion coefficient
	and also used for Temperature coefficient of resistivity
x	Stoichiometry
θ_D	Debye temperature
m_{eff}	Electron effective mass
ν	Scattering rate
	and also used for valency of rare-earth ions
M	Magnetization
χ	Susceptibility
T_N	Néel temperature
θ_p	Paramagnetic Curie temperature
E_{ex}	Energy difference between two valence states $4f^n$ and $4f^{n-1}$
T_{sf}	Intrinsic fluctuation temperature
μ_n	Effective paramagnetic moment of $4f^n$ state
P_n	Fractional population of $4f^n$ state
J_n	Angular momentum of $4f^n$ state

Dedicated to my late parents...

Chapter 1

General introduction

1.1 Introduction

Crystal structure and the underlying symmetries plays an important role in determining most of the physical properties of the majority of solids. The contrasting characteristics of two forms of carbon, diamond and graphite, having different type of atomic arrangements can be taken as an evidence to this fact. As the underlying crystal-structure directly governs the electronic structure, sometimes manipulations in structural parameters and symmetries may lead to substantial modifications in physical properties. Study of the variation of various physical properties (such as magnetic, transport, valence, thermal-expansion properties *etc.*) generated by structural modifications as well as change in the chemical environment within the unit cell is the main focus area of this thesis.

Most of the compounds investigated in the this thesis crystallize in a *perovskite* or related simple cubic structures. The perovskite and its distorted variants are one of the most attractive systems to work with as they exhibit many exciting properties and phenomenon, both from theoretical as well as application point of view. While on one hand these compounds exhibit intriguing physical phenomenon of scientific interest, on the other hand they open up possibilities for application oriented research. The simple structure of these compounds makes theoretical modeling easy as well as experimental manipulations possible. There have been extensive studies on oxygen-based perovskite materials and many exotic properties, *e.g.* colossal magnetoresistance (CMR), magnetocaloric effect, ferroelectricity, multiferroic properties *etc.* have been discovered [1]. Comparatively very less attention has been paid on oxygen-free or metallic perovskite systems. In this thesis, we have studied various physical properties of rare earths and transition metals based metallic perovskites and related compounds.

This chapter is divided in to seven sections including the present introduction section. In section 1.2 a brief description of perovskite compounds, both oxygen-based and oxygen-free, is presented. While some of the important features of oxygen-based perovskite compounds have been summarized briefly, relatively more attention is paid on oxygen-free metallic perovskite compounds that constitute the main focus area of this work. Magnetic behaviour of rare-earth (RE) elements is discussed in section 1.3. Brief reviews on some of the topics that are directly related to the content of the thesis, *e.g.* phenomenon of Negative Thermal Expansion (NTE) (section 1.4), Negative Temperature Coefficient of Resistivity (NTCR) (section 1.5), valence fluctuation exhibited by RE ions (section 1.6) *etc.*, are also presented. Finally, a brief conclusion is presented in section 1.7

1.2 Materials with perovskite structure

The general chemical formula of the compounds that crystallize in the perovskite structure is ABX_3 [2]. A representative picture of the arrangements of atoms in an undistorted cubic perovskite compound is shown in Fig. 1.1. The undistorted cubic perovskites crystallize with $Pm\bar{3}m$ space group symmetry (space group number: 221). In most of the cases, the size (ionic and/or covalent radii) of the constituent elements, 'A', 'B' and 'X', are substantially different. In general, size of the atoms that occupy the cube corner site ('A' in the present case) is relatively larger than that of the atoms situated at the body centre site ('B' in the present case). In a cubic perovskite compound, as the one shown in Fig. 1.1, the atom occupying the body centre site is 6-fold (octahedrally) coordinated and the atom situated at cube corners is 12-fold coordinated with the atoms situated at face-centre positions (X-atoms) [2].

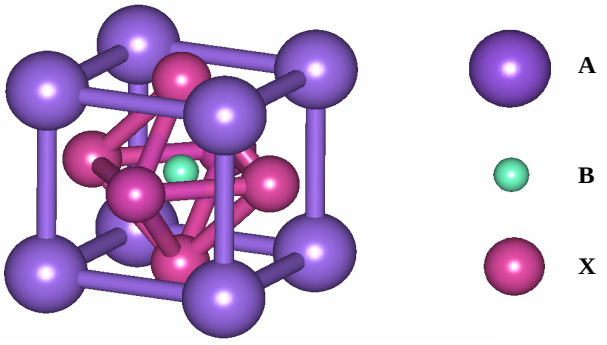

FIGURE 1.1: Arrangement of atoms in a typical undistorted cubic perovskite structure with general formula ABX_3. Atoms represented by 'A', 'B' and 'X' occupy the cube corner (0, 0, 0), body centre ($\frac{1}{2}$, $\frac{1}{2}$, $\frac{1}{2}$) and face centre ($\frac{1}{2}$, $\frac{1}{2}$, 0) positions respectively.

Although the ideal perovskite compounds crystallize in the above mentioned cubic structure [Fig. 1.1], many of them are prone to crystal distortions and thus lead to "*pseudocubic*" structures [2, 3]. As a consequence of such distortions, the symmetry of the crystals gets reduced. In addition, crystal distortions also results in lower coordination numbers of the constituents elements compare to that in the cubic structure. Most common crystal distortions from cubic structure are of orthorhombic, rhombohedral and tetragonal in nature [2]. Other known deviations from the ideal cubic structures, that are not so common, are with monoclinic and triclinic symmetry [2]. For example, the naturally occurring compounds $CaTiO_3$ was originally thought to be cubic, but its true symmetry was latter found to be orthorhombic [4]. The distorted structures that exist at room temperature, in general get transformed to the cubic structure at high temperatures [2].

A brief discussion on oxygen-based and metallic perovskite compounds is presented in the following section.

1.2.1 Oxygen-based perovskite compounds

Oxygen-based perovskite compounds are one of the most thoroughly investigated materials. Ample amount of theoretical and experimental studies have been performed on these systems. The general chemical formula of oxygen-based perovskite compounds is ABO_3. Where 'A' and 'B' are in general metal ions that act as cations, while oxygen atoms acts as anion. In most of the cases the size of the A cation is larger than B [2]. It is interesting to note that around 90% of the natural metallic elements of the periodic table are known to be stable in a perovskite-type oxide structures [2]. In addition, one can also synthesize multicomponent perovskites by partial substitution of cations A and B by A′ and B′, respectively, resulting in substituted compounds with formula $A_{1-x}A'_xB_{1-y}B'_yO_3$. This compositional and substitutional flexibility leads to a broad diversity of intriguing physical and chemical properties exhibited by this family of compounds. Some of the properties exhibited by oxide perovskites are also pregnent with the possibilities of technological applications. A few such propeties exhibited by the oxygen-based perovskite compounds, that are of current interests, are summarized below.

(i) Colossal magnetoresistance:

A very large change (a few orders of magnitude) in the resistivity upon application of external magnetic field is termed as *colossal magnetoresistance* [Fig. 1.2]. Many manganese-based perovskite oxides (manganites) are known to exhibit this phenomenon in the form of polycrystalline powders, thin films, nano-composites and single crystals

[1, 5–7]. In general CMR effect is observed in the vicinity of magnetic transitions. For example, $LaMnO_3$ and $CaMnO_3$ exhibit antiferromagnetic (AFM) ground state resulting from the superexchange interaction between the spins. On the other hand, the composition $La_{1-x}Ca_xMnO_3$ exhibit ferromagnetic (FM) ground state in certain doping range ($\sim 0.2 \leq x \leq 0.4$). In this compounds, ferromagnetic to paramagnetic transitions is accompanied by a sharp drop of resistivity leading to CMR effect [8]. Such large changes in the resistance invite the possibilities of using these materials for various technological applications.

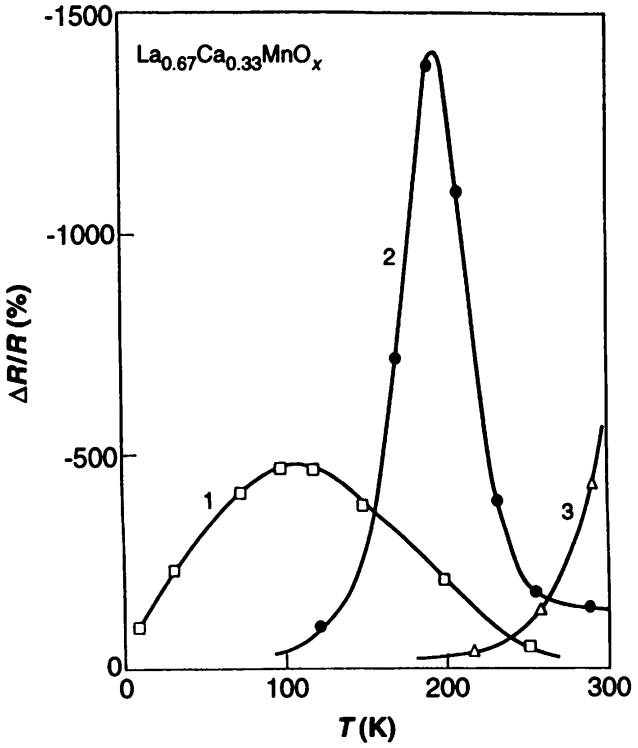

FIGURE 1.2: The variation of colossal magnetoresistance with temperature observed in thin oxide films of perovskite like $La_{0.67}Ca_{0.33}MnO_x$. The curve 1 shows results for as deposited film, the curved 2 is for the sample annealed at 700 ^{0}C in oxygen atmosphere for half an hour and the curve 3 is for the sample annealed at 900 ^{0}C in oxygen atmosphere for 3 hours. The figure is reproduced from *Jin et al. Science* **264**, *413 (1994).*

(ii) Charge ordering:

A real space ordering of different valence states of an element in a compound is know as *charge ordering*. Some compositions of manganites are known to exhibit charge ordering of Mn^{+3} and Mn^{+4} below certain temperatures [1, 9]. As shown in Fig. 1.3, in general charge-ordered states is associated with insulating and antiferromagnetic phase of the material [1]. In most of the cases lattice distortions play a crucial role in charge ordering

[1]. The charge-ordered states can be destabilized upon application of external magnetic field which sometimes results in large magnetoresistance and magnetocaloric effects.

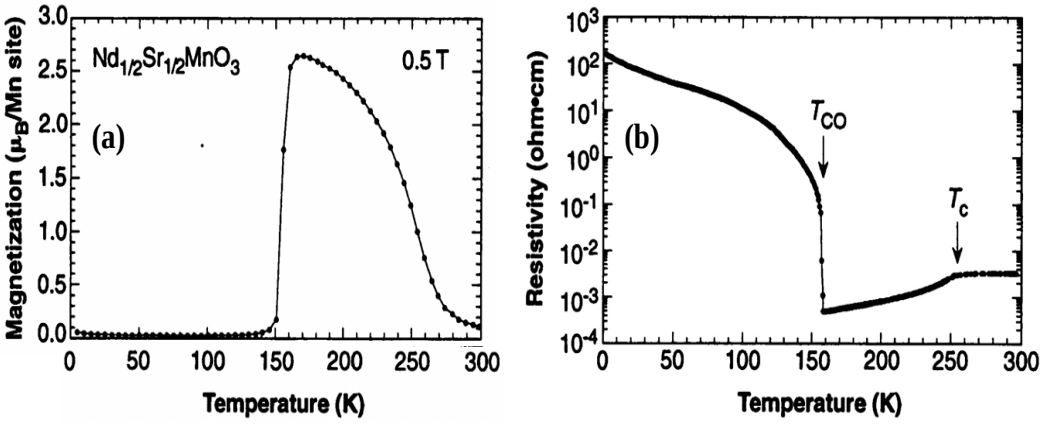

FIGURE 1.3: Temperature dependence of magnetization and resistivity for $Nd_{0.5}Sr_{0.5}MnO_3$in (a) and (b) respectively. The T_c and T_{CO} represent the Curie temperature and the critical temperature for the charge-ordering transition, respectively. In the vicinity of charge ordering transition the resistivity jumps by several order of magnitude. Simultaneously, the ferromagnetic state disappeared and antiferromagnetic state gets stabilized. The figure is reproduced from *Kuwahara et al. Science* **270**, *961 (1995).*

(iii) Diverse magnetic and electrical properties:

Oxygen based perovskites compounds exhibit vast diversity in their electrical and magnetic behaviour. On one hand these compounds are known to exhibit metallic, semiconducting as well as temperature dependent nature of electrical conduction mechanism, on the other hand they show various kind of magnetic ordering as well. It is well established that electronic conduction and magnetic properties in most of the oxide perovskites (especially manganites) are highly correlated. In general, the interactions that govern the electrical conduction in these compounds also influence the magnetic behaviour and vice-versa. The crystal-field effect, John-Teller distortion, electron-phonon interaction, superexchange and double exchange mechanisms *etc.* are some of the phenomena that influence the electrical and magnetic behaviour of oxide perovskite compounds.

(iv) Magnetocaloric effect:

The *magnetocaloric effect* is a magneto-thermodynamic phenomenon in which a reversible change in the temperature of a material can be achieved by exposing the material to a changing magnetic field. Magnetic refrigeration based on magnetocaloric effect is a promising alternative to conventional gas cycle refrigeration [10]. There have been

extensive studies on the observation of magnetocaloric effect in oxide perovskites, especially manganites that show large change of entropy (ΔS) and adiabatic change of temperature (ΔT) around magnetic transition temperatures [11].

(v) Ferroelectricity:

The materials that exhibit spontaneous electric polarization below certain temperature (Curie temperature) are called *ferroelectric* [3]. Such materials are characterized by displacement of ions from their centrosymmetric positions. Ferroelectric materials can be used in various device applications *e.g.* piezoelectric devices, capacitors with tunable capacitance, ferroelectric random access memory devices *etc.* Many oxygen-based perovskites, *e.g.* $BaTiO_3$, $PbTiO_3$ *etc.*, are known for their rich ferroelectric behaviour and have been attracting significant attention of researchers [12, 13].

(vi) Multiferroic materials:

By definition *multiferroic* materials are those that posses at least two '*ferroic*' properties: ferromagnetism, ferroelectricity and ferroelasticity [14, 15]. Recently ferrotoroidic order is also been considered as one of the possible 'ferroic' properties. The multiferroic materials can produce unprecedented cross coupling effects such as high tunability of magnetically induced electric polarization and dielectric constant by applied magnetic fields [14, 15]. This has raised hopes for there practical application as multifunctional devices such as high quality magnetic sensors, transformers and gyrators, microwave devices *etc.* [16]. Oxygen-based perovskite materials have been identified as one of the most promising candidates for multiferroic functional materials. Study of such oxide perovskites is a topic of current interest [14–16].

1.2.2 Metallic and other non oxide perovskite compounds

In contrast to the oxygen-based perovskite compounds (ABO_3), metallic and other non-oxide perovskite compounds do not contain oxygen. Oxygen is in general replaced by some transition metal atoms (T) in the case of metallic perovskites and by some other light elements (X) in the case of other non-oxide perovskites respectively. Hence the general chemical formula of metallic and other other non-oxide perovskites can be written as AXT_3 and ABX_3 respectively. Similar to oxygen-based perovskite compounds (section - 1.2.1), ideal metallic perovskite compounds also crystallize in a simple cubic structure with $Pm\bar{3}m$ space group symmetry (space group number: 221). The metallic perovskites (AXT_3) are slightly different from the oxide perovskites (ABO_3) in context to the arrangement of atoms in the cubic unit cell. For example, in $LaMnO_3$ the transition

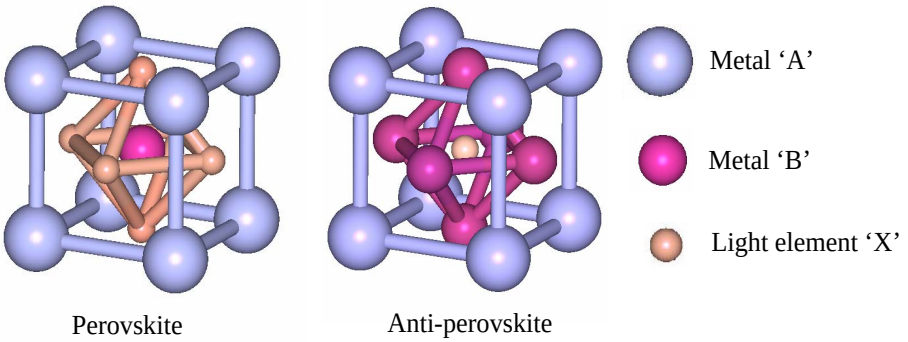

FIGURE 1.4: The atomic arrangements in perovskite and anti-perovskite structures. In general the metal 'A' is a RE ion, metal 'B' is a transition metal and the atom. It is clear from the picture that in anti-perovskite structure the position of transition metal and light element is interchanged.

metal Mn is placed at the body centre position $(\frac{1}{2}, \frac{1}{2}, \frac{1}{2})$ while the light element (O) is placed at the face-centre position $(\frac{1}{2}, \frac{1}{2}, 0)$ of the unit cell. In contrast, in the case of metallic perovskite AXT_3, the transition metal T occupies face-centre lattice site while the light element X occupies the body centre site [Fig. 1.4]. Hence in some cases metallic perovskites are also referred as *anti-perovskite* or *inverse-perovskite* compounds [Fig. 1.4].

Although relatively less attention has been paid on metallic perovskite compounds compared to the oxide perovskites, significant work in being carried out at present on such compounds. [17–63]. These compounds have been reported to exhibit many interesting and application oriented properties such as superconductivity, high-density magnetic recording capacity, NTE *etc.* A brief summary of some of the known families of metallic and other non-oxide perovskite compounds is presented below.

1.2.2.1 $RT_3B_xC_{1-x}$ (R: Sc, Y and rare-earth ions; T: transition metal)

Compounds with chemical formula $RT_3B_xC_{1-x}$ (R: rare-earth, T: transition metal) are one of the most well-studied metallic perovskite compounds [17–25, 64–68]. In general these compounds exhibit metallic character and crystallize in a cubic perovskite structure with $Pm\bar{3}m$ space group symmetry [Fig. 1.5]. Parent binary RT_3 compounds also crystallize in the cubic $AuCu_3$ structure with $Pm\bar{3}m$ space group symmetry, however the body centre position $(\frac{1}{2}, \frac{1}{2}, \frac{1}{2})$ remains vacant [Fig. 1.5]. The RE ions exhibit +3 valency in most of the RT_3 and $RT_3B_xC_{1-x}$ compounds [1].

In general, the introduction of light elements, *e.g.* B, C, Si *etc.*, at the vacant body centre site of the parent binary compounds RT_3 generates negative chemical pressure

[1] The properties of rare earth ions will be discussed in detail in section 1.3.

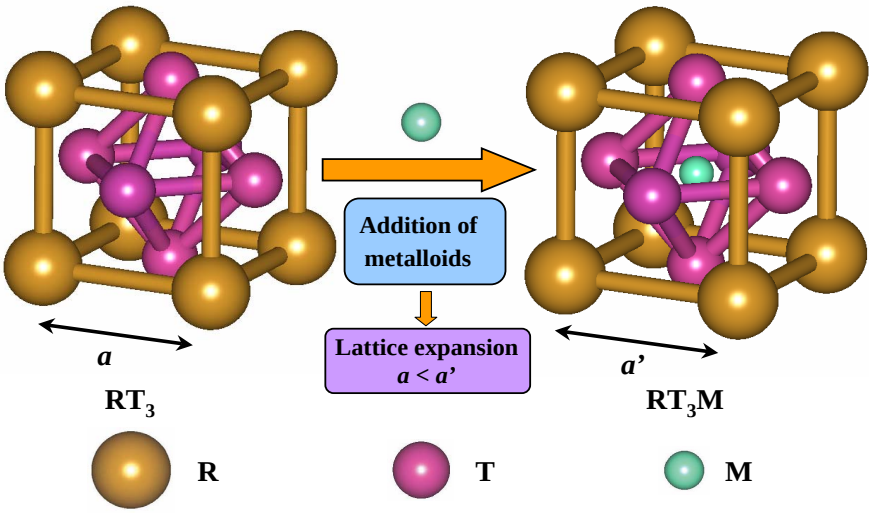

FIGURE 1.5: The atomic arrangements in undistorted cubic unit cell of a metallic perovskite compound with chemical formula RT_3M (right) and the parent compound RT_3 (left) having vacant body centre cite. The insertion of light element (X) in the vacant body centre site of parent compounds in general leads to lattice expansion resulting in hither lattice parameter a' of RT_3X compare to a of RT_3.

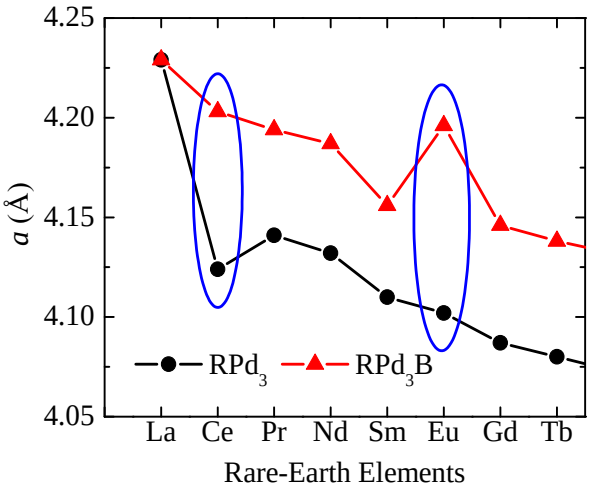

FIGURE 1.6: Variation of lattice parameter (a) with RE elements that occupy the cube corner positions in RPd_3 and RPd_3B. Anomalous high increment in the value of a observed in the case of $CePd_3B$ and $EuPd_3B$ are indicated. The data has been taken from *Dhar et al. Mat. Res. Bull.* **16**, *1557 (1981).*

and results in a lattice expansion [Fig. 1.5 & 1.6]. Hence the lattice parameter of boron (and/or carbon) incorporated metallic perovskite $RT_3B_xC_{1-x}$ is higher than the parent binary RT_3 compounds [Fig. 1.6]. In a few cases the observed lattice expansion exhibits anomalously high value. For example, the observed lattice expansion upon boron incorporation is anomalously high in the case of $CePd_3B$ and $EuPd_3B$ [Fig. 1.6]. Such anomalous increment in the lattice parameter values upon boron incorporation has

been mainly attributed to the valence change of RE ions from mixed valent ($+3 < \nu < +4$) to normal +3 in the case of $CePd_3 \rightarrow CePd_3B$ and from normal +3 to mixed valent ($+2 < \nu < +3$) in the case of $EuPd_3 \rightarrow EuPd_3B$ [64–66, 69]. In addition to the lattice expansion, in most of the cases the incorporation of light elements also significantly modifies the electronic structure near the Fermi level. Formation of stable crystalline phases, both in RT_3 and $RT_3B_xC_{1-x}$ compositions, helps to perform a comparative study with respect to the effect of negative chemical pressure, change in electronic structure near Fermi level *etc.* induced by boron (and/or carbon) incorporation.

Most of the earlier studies on $RT_3B_xC_{1-x}$ compounds are concentrated on structural [17, 70–72], valence [64–69] and elastic [17–22] properties. There are, however, very less studies on magnetic, thermal expansion, electrical and magnetotransport properties of these compounds. This thesis is based on the investigations of structural, magnetic, electrical, magnetotransport and thermal expansion properties of RPd_3 and $RPd_3B_xC_{1-x}$ compounds. The experimental data and their analysis along with the relevant introductions related to the main theme of the investigation will be discussed in the respective chapters.

1.2.2.2 $MCNi_3$ (M: Mg, Cd, In, Ga and Al)

After the discovery of superconductivity in Ni rich cubic metallic perovskite compound $MgCNi_3$ [Fig. 1.7], significant research is being carried out on this and other related materials $MCNi_3$ (M = Cd, In, Ga, Al) [30–45]. Although the superconductivity occurs at quite low temperature (~ 8 K) in $MgCNi_3$, the material has attracted remarkable attention due to its puzzling behaviour. In fact, the partially filled Ni-*d* orbitals of $MgCNi_3$ are expected to establish ferromagnetic ground state rather than the superconductivity. Hence the observation of superconductivity in $MgCNi_3$ is quite unconventional and produces the possibility to investigate the intriguing competition between ferromagnetism and superconductivity in the same compound. It has been found that this compound can be driven to ferromagnetism by partial ($\sim 12\%$) replacement of Mg by a monovalent metal such as Li and Na [31].

1.2.2.3 Sc_3MX (M: Al, Ga, In and Tl; X: B and N)

Discovery of unusual superconductivity in Ni rich $MgCNi_3$ has stimulated intense search of new metallic perovskite materials that could be the probable candidates for exhibiting superconductivity and other related phenomena. Recently Sc based Sc_3MX (M= Al, Ga, In, Tl & X= B and N) are being investigated in this regard and attempts have been made to understand the electronic, electrical, magnetic and elastic properties of these

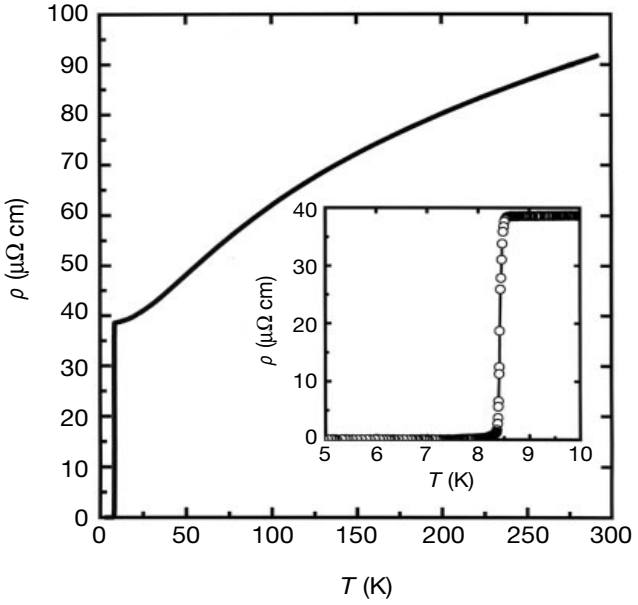

FIGURE 1.7: Temperature dependence of the resistivity of $MgCNi_3$. Inset exhibits the temperatures region near the superconducting transition. The figure is reproduced from *He et al. Nature* **411**, *54 (2001).*

compounds [26–29]. It may be mentioned here that at present YRh_3B is the only known metallic perovskite compound besides $MgCNi_3$ which is reported to exhibit superconductivity (T_c = 0.8 K) [73]. Theoretical electronic structure calculation have shown some possibility of appearance of superconductivity in some of the Sc_3MX compositions [27]. In addition, these calculation suggest the presence of weak ferromagnetism in some of the binary Sc_3M compositions [27]. It has been found through theoretical calculations that introduction of boron at the face centre position destroys the magnetic ground state and likely to stabilize in to superconducting phase [27]. However, more detailed theoretical as well as experimental evidences are required to establish such concepts.

1.2.2.4 MFe_3N (M: Co, Ni, Ru, Rh, Pd, Os, Ir and Pt)

Cubic binary compounds Fe_4N and its derivatives MFe_3N (M= Co, Ni, Ru, Rh, Pd, Os, Ir, Pt) that crystallize in metallic perovskite structure have been extensively studied due to their possible application as a high-density recording material [46–53]. The γ'-Fe_4N exhibits a large saturation magnetization of $\sim$ 200 emu/g, which is close to that α-Fe (218 emu/g), and have low coercive field of 460 Am^{-1} [46, 47]. It was realized latter that the magnetic properties of γ'-Fe_4N can be modified by replacing the Fe atoms on Wyckoff position 1*a* and/or 3*c*. The newly introduced atoms can be used to control the crystal growth and yielding magnetic particles with a pronounced anisotropic shape as well as a high coercive field, which makes the materials suitable for high-density storage

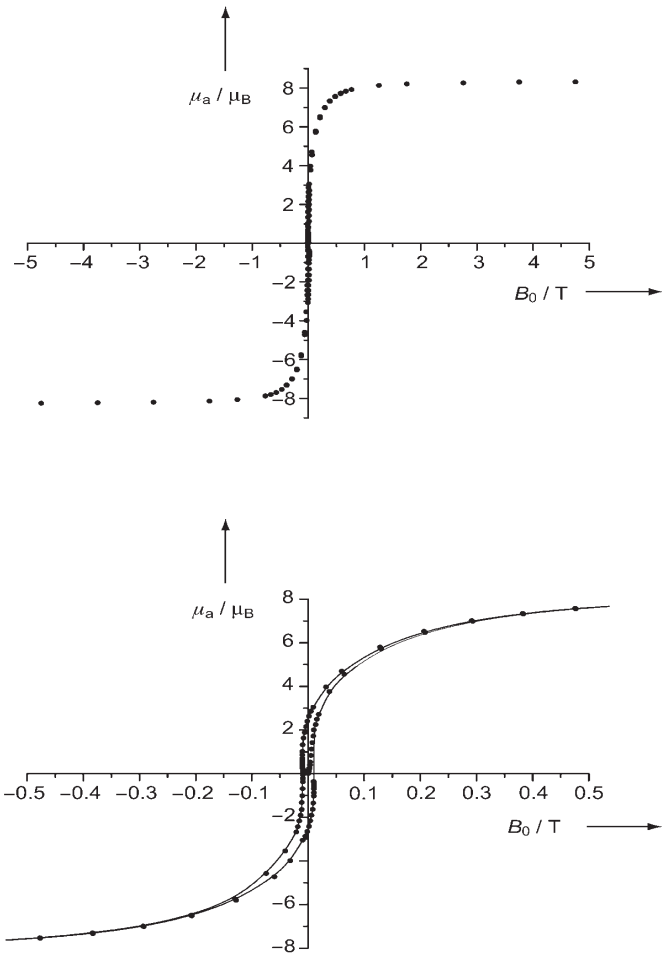

FIGURE 1.8: Magnetic hysteresis of $RhFe_3N$ taken at $T = 5$ K (top) and the same in an expanded scale showing remanent magnetization and coercive field (bottom). In the bottom figure, the solid lines are only guide to eye. The figure is reproduced from *Houben et al. Angew. Chem. Int. Ed.* **44**, *7212 (2005).*

devices [47]. Figure 1.8 exhibits the hysteresis loop for $RhFe_3N$. The coercive field of $RhFe_3N$ is found to be nearly one order of magnitude larger than that of γ'-Fe_4N [47]. In addition to their promising magnetic properties, these materials are chemically more inert compared to their constituting materials. These features make them one of most promising candidates for data storage based research.

1.2.2.5 Mn_3MX (M: Al, Cu, Zn, Ga, In and Sn; X: C and N)

Mn based manganese nitrides Mn_3MX (M = Al, Cu, Zn, Ga, In, Sn & X= C and N) are one of the most thoroughly investigated metallic perovskite compounds [54–62]. These compounds have been reported to exhibit giant NTE behaviour [Fig. 1.9] [54, 55]. The materials that exhibit NTE are technologically very important as they

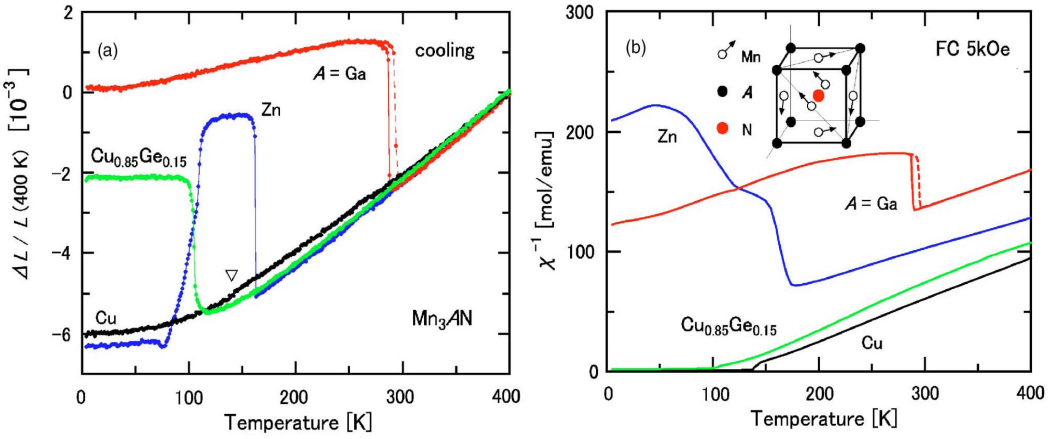

FIGURE 1.9: Temperature dependence of (a) thermal expansion and (b) inverse molar susceptibility of Mn_3AN. Solid lines represent data taken during cooling and dashed lines exhibit the data taken during heating. Inset in (b) exhibits the antiferromagnetic Γ^{5g} spin structure of Mn_3ZnN and Mn_3GaN. The figure has been taken from *Takenaka et al., Appl. Phys. Lett.* **87**, *261902 (2005).*

can provide a fine control on thermal expansion by compensating or controlling the positive thermal expansion of normal metals. In these materials, the NTE occurs as result of volume expansion associated with magnetic ordering. Such phenomena is in general called *magnetovolume* effect. Efforts are being made to broaden the width of the magnetovolume transition in these materials by substitution at cube corner lattice site [54–56].

1.2.2.6 Few other relatively less studied metallic perovskite compounds

Synthesis and structural studies along with some initial magnetic and electrical measurements on a few other metallic perovskite phases, *e.g.* Mg_3MN (M = As, Sb), Ca_3MN (M = P, As, Sb, Bi, Ge, Sn and Pb), R_3InZ (R = Y and La, Z=B, C, N and O) *etc.*, are reported in literature [63, 74, 75]. Unlike the earlier discussed metallic perovskite compounds these phases are not reported to exhibit any intriguing and(or) application oriented properties and thus have received relatively less attention.

1.2.2.7 Other non-oxide, non-metallic perovskite compounds

Significant attention has been paid on a few other non-oxide perovskite compounds other than metallic perovskites. These are the materials where some non metallic elements other than oxygen, *e.g.* F, H *etc.*, occupy the face centre position (occupied by oxygen in ABO_3) in the cubic unit cell. Fluorides perovskites *viz.* ABF_3 (A: Na, Mg, K and

Ca; B: Mn, Cu and Rb) are the most investigated members of this family [76–84]. One of the such fluoride perovskite material $KCuF_3$ is being investigated thoroughly as it presumably present one of the best realizations of one dimensional (1D) antiferromagnetic Heisenberg chain [76–78]. $KCuF_3$ is an insulator and crystallizes in a pseudocubic structure at room temperature with distorted CuF_6 octahedra. Cooperative John-Teller effect, orbital ordering and low dimensional magnetism exhibited by this compound are the topic of current interest [76–78]. Another related fluoride perovskite material $RbMnF_3$ is believed to be the closest realization of isotropic 3-dimensional (3D) Heisenberg antiferromagnet [85–92]. In contrast to $KCuF_3$, $RbMnF_3$ crystallizes in simple cubic structure without any noticeable distortion [89–91]. In this materials manganese Mn^{+2} ions have large spin moment of $S = 5/2$ that arises from a half-filled $3d$-shell. The magnetic moments are arranged on a simple cubic lattice and are antiferromagnetically coupled by a Heisenberg nearest neighbor interaction that originates from superexchange mediated by fluorine F^- ions [90].

Similar to the fluoride perovskites, some hydride perovskite compounds, *viz.* MTH_3 (T = Pd, Mg & M = Na, K, Rb, Ca, Sr, Eu, Yb) and $BeLiH_3$ are also investigated [93–95]. These materials have attracted some attention due to their high gravimetric hydrogen densities, which may be useful for mobile hydrogen storage application. However, such applications often require many other characteristics besides high hydrogen density such as appropriate thermodynamics and kinetics of hydrogen uptake and release *etc.* Such thorough investigations on these materials are not reported so far.

1.2.3 Some underlying differences between oxide and metallic perovskite compounds

Although the metallic perovskites are structurally related to the oxide perovskites, there are indeed several underlying differences between both the families of compounds. As mentioned earlier, while the oxide perovskites are extensively investigated and many of the underlying features are well established, in contrast the metallic perovskites are relatively less explored. Lack of thorough investigations and established facts makes it difficult to compare in detail the physical properties of metallic perovskites with that of their oxygen-based counterparts. However, some of the major differences can be drafted as follows;

(i) As discussed earlier in the section 1.2.2, the position of transition metal and light element are interchanged in metallic perovskites when compared with oxide perovskites. Even though the crystal structure remains unchanged (considering the structure to be ideal cubic) electronic structure, that depends sensitively to the atomic arrangements in

the unit cell, gets immensely modified. This in general results in significant differences in the physical properties of metallic perovskites compared to oxide perovskites.

(ii) In comparison to oxide perovskites, metallic perovskite are in general less prone to crystal distortions from ideal cubic structure at normal pressure and room temperature. Many families of metallic perovskites *e.g.* RT_3X, $MgCNi_3$, MFe_3N, Mn_3MC *etc.* are known to exist in the ideal cubic perovskite structure. Predominantly metallic character of bonding in the case of metallic perovskites compared to ionic or covalent bonding in the case of oxide perovskites could be one of the possible underlying reason for the more stable cubic structure in the former compared to the latter. In addition, the Jahn-Teller effect which is often considered to be responsible for structural distortion in oxide materials are rarely observed in metallic systems.

(iii) In contrast to oxide perovskites, the phenomenon like superexchange and double exchange interactions are in general not reported in the case of metallic perovskites. The different atomic arrangement (*i.e.* interchanged positions of light element X and transition metal T) and absence of ligands like oxygen and fluorine that facilitate such phenomena in oxide and other non-oxide perovskites are the possible reasons why one does not observed superexchange or double exchange interactions in metallic perovskites.

(iv) The metallic perovskite compounds in general exhibit usual metallic character in electrical transport measurements. This is due to the presence of sufficient density of states at Fermi level contributed mainly by transition metal occupying the face centre lattice site. In contrast, oxide perovskites exhibit very rich electrical transport behaviour that ranges from metallic to semiconducting as well insulating in some cases.

(vi) The oxide perovskites in general exhibit highly correlated magnetic and electrical properties that lead to intriguing phenomena such as CMR, multiferroic behaviour *etc.* Although, metallic perovskite also exhibit some correlation between structural, magnetic and electrical properties, the observation of CMR, multiferroic behaviour *etc.*, to our knowledge, are not reported so far.

In the present section, we have presented a brief survey of perovskite materials (both oxide and non oxide perovskites). We have discussed their crystal structure and various other physical properties. We have also tried to compare some of the features of oxide and non-oxide perovskite compounds. In the next section, we will discuss about the magnetic behaviour of RE ions that occupy the cube corner position of the cubic unit cell of RPd_3 and $RPd_3B_xC_{1-x}$ compounds.

1.3 Magnetic behaviour of rare-earth elements

It is fairly safe to say that two series of elements play most important role in the field of magnetism, both for fundamental understanding as well as in technological applications: one hand, we have iron group elements characterized by a progressive filling of $3d$-shells, and on the other hand, the RE elements characterized by progressive filling of $4f$-shells. Here we focus on magnetic behaviour of RE elements.

1.3.1 Properties of trivalent rare earth ions

Magnetism in RE elements (R) arises from their deep lying unfilled $4f$-shell that does not overlap with f electrons of adjacent ions. Due to the localized behaviour of the $4f$-shell, magnetic behaviour of rare-earths can be reasonably described by the respective free trivalent ion properties. In most of the alloys and compounds (except in the case of valence fluctuating materials described latter in this chapter), the RE ions are in trivalent state (R^{+3}). This happens because the loosely bound $5d^1 6s^2$ electrons are removed from the RE ion to contribute in bonding. The magnetic moment of the free R^{+3} ions are satisfactorily described by their total angular momentum $\boldsymbol{J}$ ($\boldsymbol{L} + \boldsymbol{S}$, $\boldsymbol{L}$: orbital angular momentum and $\boldsymbol{S}$: spin angular momentum) under *Russel-Saunder's coupling* scheme with ground state angular momentum governed by *Hund's rule* [96]. The magnetic moments and other relevant parameters are summarized in table 1.1.

Paramagnetic susceptibility of RE ions can be, in general, described by the the relation;

$$\chi(T) = \frac{Ng^2 J(J+1)\mu_B^2}{3k_B(T-\theta_p)} = \frac{C}{T-\theta_p} \tag{1.1}$$

Where χ is susceptibility, N is total number of ions, J is total angular momentum quantum number, μ_B is the Bohr magneton, k_B is the Boltzmann constant, θ_p is paramagnetic Curie temperature and C is the Curie constant. Some times an additional temperature independent Van-vleck susceptibility term (χ_0) is added on the right hand side of the equation 1.1 to describe the paramagnetic susceptibility of RE ions. Compared to the susceptibility of magnetic RE ions, the Van-vleck susceptibility is usually negligible.

In the case of materials having Eu and Sm ions, the next higher excited state of multiplet levels of J lies at an energy comparable to $k_B T$. Therefore, in these two cases, the susceptibility gets modified considerably compared to Curie-Weiss (CW) law and can be written as [97],

Rare-Earth ion	$4f^n$	$^{2S+1}L_J$	S	L	J	g	μ_{eff} (μ_B)	gJ	G_J	G_S	δ(K)
La^{+3}, Ce^{+4}	$4f^0$	$^1S_0$	0	0	0	-	0	0	0	0	-
Ce^{+3}	$4f^1$	$^2F_{5/2}$	1/2	3	5/2	6/7	2.54	2.14	0.011	0.048	3168
Pr^{+3}	$4f^2$	$^3H_4$	1	5	4	4/5	3.58	3.20	0.051	0.127	3096
Nd^{+3}	$4f^3$	$^4I_{9/2}$	3/2	6	9/2	8/11	3.62	3.28	0.116	0.238	2736
Pm^{+3}	$4f^4$	$^5I_4$	2	6	4	3/5	2.68	2.40	0.217	0.381	2304
Sm^{+3}	$4f^5$	$^6H_{5/2}$	5/2	5	5/2	2/7	0.84	0.72	0.283	0.555	1440
Eu^{+3}, Sm^{+2}	$4f^6$	$^7F_0$	3	3	0	0	0	7	0	0.762	504
Gd^{+3}, Eu^{+2}	$4f^7$	$^8S_{7/2}$	7/2	0	7/2	2	7.94	7	1	1	-
Tb^{+3}	$4f^8$	$^7F_6$	3	3	6	3/2	9.72	9	0.667	0.762	2880
Dy^{+3}	$4f^9$	$^6H_{15/2}$	5/2	5	15/2	4/3	10.63	10	0.450	0.555	4752
Ho^{+3}	$4f^{10}$	$^5I_8$	2	6	8	5/4	10.60	10	0.386	0.381	7488
Er^{+3}	$4f^{11}$	$^4I_{15/2}$	3/2	6	15/2	6/5	9.59	9	0.162	0.238	9360
Tm^{+3}	$4f^{12}$	$^3H_6$	1	5	6	7/6	7.57	7	0.074	0.127	11952
Yb^{+3}, Tm^{+2}	$4f^{13}$	$^2F_{7/2}$	1/2	3	7/2	8/7	4.54	4	0.020	0.048	14832
Lu^{+3}, Yb^{+2}	$4f^{14}$	$^1S_0$	0	0	0	-	0	0	0	0	-

TABLE 1.1: The table summarizes the ground state properties of free R^{+3} ions. The physical quantities listed in the table are: the number of electrons in $4f$ level ($4f^n$), ground state configuration ($^{2S+1}L_J$), spin (S), orbital (L) & total (J) angular momentums, Lande g factor (g), effective paramagnetic moment (μ_{eff}), de Gennes scaling factors for J and S (G_J and G_S respectively) and separation between ground level and first excited level (δ). The data presented in the table have been taken from *C. Mazumdar, Superconducting, valence fluctuating and magnetic properties of some rare-earth intermetallic compounds, Ph.D thesis submitted to Indian Institute of Technology, Bombay (1995).*

$$\chi = N\frac{\sum_{J=|L-S|}^{J=|L+S|}\{[g_J^2\mu_B^2 J(J+1)/3k_BT] + \alpha_J\}(2J+1)e^{-E_j^0/k_BT}}{\sum_{J=|L-S|}^{J=|L+S|}(2J+1)e^{-E_j^0/k_BT}} + \chi_0 \tag{1.2}$$

where the α_J is the term that arises from the joint contribution of the high frequency elements of the paramagnetic moments (particularly, when the multiplet intervals are small compared to k_BT) and the diamagnetic contribution. This term originates from the 'non-permanent' behaviour of the resulting magnetic moment which can have different relative alignment of L and S ($J = |L-S|$ to $|L+S|$). E_J^0 is the zero-th order energy of J-th level.

1.3.2 Ruderman-Kittel-Kasuya-Yosida interaction

Magnetic order in RE intermetallic compounds is in general determined by Ruderman-Kittel-Kasuya-Yosida (RKKY) type interaction. The RKKY interaction was originally proposed by Ruderman and Kittel [98] to describe the interaction between nuclear magnetic moments, and later on extended by Kasuya [99], Yosida [100] and de Gennes [101] to consider the coupling between highly localized $4f$-electrons. The spatial extent of $4f$-electrons is very limited and far less than the inter atomic distances, and correspondingly there can be no direct interaction between the $4f$-electrons of different atoms [102]. The magnetic moments associated with localized $4f$-electrons interact with each other though indirect RKKY interaction mediated via conduction electrons. This interaction can be expressed in terms of the $4f$ spins $\mathbf{S_i}$ localized at lattice site $\mathbf{R_i}$ and the spins of the conduction electrons $\sigma(\mathbf{r})$ as;

$$E = -\sum_{\mathbf{R_i},\mathbf{r}} J(\mathbf{R_i} - \mathbf{r})\mathbf{S_i}\sigma(\mathbf{r}) \tag{1.3}$$

This interaction is highly localized and correspondingly we can write it in the form, $\mathbf{J}(\mathbf{R_i} - \mathbf{r}) = \delta(\mathbf{R_i} - \mathbf{r})$. The equation 1.3 infers that the conduction electrons interact with RE ions at site $\mathbf{R_i}$ through a field created by the spins of RE ions. This local field polarizes the conduction electrons and this polarization propagates through the lattice, creating at any other site $\mathbf{R_j}$ a magnetization of the conduction electrons. This indeed amounts to an indirect interaction between the spins (or magnetic moments) associates with two different lattice sites $\mathbf{R_i}$ and $\mathbf{R_j}$. It can be shown that this indirect exchange interaction between two RE sites varies as [102];

$$J_{ex} \sim f(\mathbf{2k_F R_{ij}}) = [\mathbf{2k_F R_{ij}}\cos(\mathbf{2k_F R_{ij}}) - \sin(\mathbf{2k_F R_{ij}})]/(\mathbf{2k_F R_{ij}})^4 \tag{1.4}$$

Where $\mathbf{k_F}$ is the Fermi wave vector that determine the wavelength of the oscillation and $\mathbf{R_{ij}}$ is the distance between two RE ions situated at $\mathbf{R_i}$ and $\mathbf{R_j}$. This exchange interaction oscillates between positive and negative values as a function of $\mathbf{R_{ij}}$ [Fig. 1.10]. These interactions are of the same order of magnitude in nearly all the rare-earths. However, the ordering temperatures that they lead to can vary substantially (19 K for Nd and 289 K for Gd). This disparity is due to the variation in the magnitude of magnetic moments of different RE ions [102].

An estimate of the magnetic ordering temperature T_{mag} can be obtained from RKKY type of interaction through the paramagnetic Curie temperature, θ_p, which is proportional to T_{mag}. The θ_p can be obtained from a combination of molecular field model

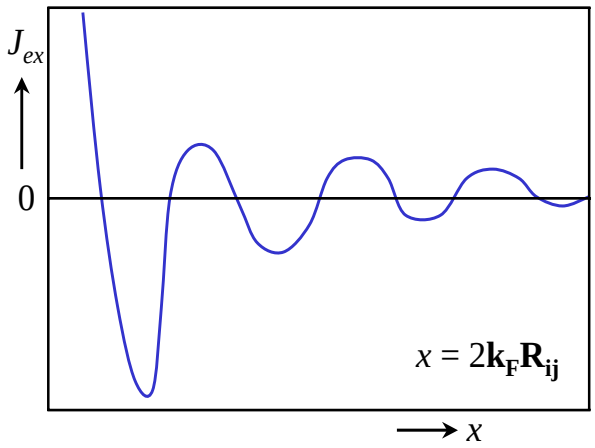

FIGURE 1.10: Schematic representation of the oscillation in strength of the interaction between two magnetic moments of RE ions.

[101, 103] with the expression of the second order perturbation energy associated with the $s-f$ exchange interaction as [100];

$$\theta_p = -\left[\frac{3\pi n^2 J_{ex}(0)^2}{k_B E_F}\right] S(S+1) \sum_i f(\mathbf{2k_F R_i}) \tag{1.5}$$

Where $J_{ex}(\mathbf{q}) \equiv J_{ex}(\mathbf{k'} - \mathbf{k})$ is the exchange integral, $\mathbf{k}$ and $\mathbf{k'}$ are the wave vectors of the conduction electrons before and after the scattering with localized spin respectively, $J_{ex}(0) \equiv J_{ex}(\mathbf{q})$ is a constant and the function $f(\mathbf{2k_F R_i})$ is described in the equation 1.4.

1.3.3 de Gennes scaling

In the case of rare-earths, J being the good quantum number instead of S, the term $S(S+1)$ in equation 1.5 has to be replaced by $(g-1)^2 J(J+1)$. Since $\boldsymbol{k_F}$ is proportional to reciprocal lattice vector, the product $\boldsymbol{k_F R_i}$ is more or less unchanged (strictly obeyed by cubic structure, but approximately for the structure with lesser symmetry) even though there is a decrease of lattice parameter across a RE series of compounds and will therefore leave $\sum f(\mathbf{2k_F R_i})$ also scarcely changed in the whole RE series. Therefore, θ_p should be proportional to $(g-1)^2 J(J+1)$ which is the well known *de Gennes scaling* of magnetic ordering temperatures of isotropic compounds in the RE series.

de Gennes scaling predicts that among the RE series of compounds isotopic Gd-based compounds should have the maximum ordering temperature as, $L = 0$ and $J = S = 7/2$ for Gd^{3+} ion. This also suggests that the ordering temperatures of other members of the series should be scaled accordingly with respect to that of the Gd-based compound.

Sometimes, however, it has been observed that de Gennes scaling is not obeyed. A possible reason for such a behaviour has been given by Kaplan and Lyons [104]. They have shown that the extension of the concept of exchange interaction from $S_i.S_j$ to $J_i.J_j$ being not strictly valid, can lead to a modified exchange interaction between the $4f$-moments. It has been shown [105] that when one uses the bilinear scalar exchange interaction appropriate to indirect exchange via conduction electron, the actual paramagnetic Curie temperature can be expressed as;

$$\begin{aligned}\theta_p &= (3k_B)^{-1}J(J+1)[(g-1)^2Q_{0101} + (2-g)Q_{1010} + C_n^2Q_{2121} \\ &\quad + 2(g-1)(2-g)Q_{1001} + 2(g-1)C_nQ_{0121} + 2(2-g)C_nQ_{1021}] \qquad (1.6)\end{aligned}$$

Where $Q_{p_1k_1p_2q_2}$ is the generalization of the term $J_{ex}(0)\sum_i^2 f(\mathbf{2k_F R_i})$ [105]. They originate from the pair interaction described by orbital and spin tensor operators of ranks p and k. The last three terms are present only if there is an appreciable spin-orbit splitting in the conduction electron states which carry the indirect exchange interaction [106]. It is to be noted here that even the θ_p derived by above considerations may differ from the actually observed values (obtained by extrapolating the inverse susceptibility above the transition temperature to zero) due to crystal field effects. The proper θ_p can only be derived from a measurement made on a single crystal, from where the C_n's can be determined.

1.3.4 Crystalline electric field

In an intermetallic compound, the constituent elements contribute their valence electrons to the conduction band and thus may be considered to be a system having a lattice of positive charges immersed in a sea of conduction electrons. In a RE system, the $4f$-electrons of the RE experience the electric field produced by the screened charge of the surrounding ions. This electric field, which is known as crystalline electric field, when acts on the $4f$ electronic state, completely or partially remove the $(2J+1)$ fold degeneracy of the ground J-multiplet levels. Because of this, below a certain temperature (less than the total splitting of the ground state) the sublevels would have a population distribution as per Boltzmann distribution function which would result in a deviation of physical properties from that of free ion behaviour. In the cases of rare-earths, normally the crystalline electric field splitting is small compared to the spin orbit interaction. Hence, one can consider the CEF as a small perturbation and J can still be considered as a good quantum number. The CEF Hamiltonian can be expressed as,

$$H_c = -e \sum_i V(r_i) \tag{1.7}$$

where $V(r_i)$ is the electrostatic potential, experienced by a single electron, due to other electrons surrounding it and the summation extends to all $4f$ electrons at distance r_i forming part of the RE ion under consideration.

The CEF depends on the site symmetry and charge of the surrounding ions. Though the assumption of point charges in the calculations is not very realistic, in the case of $4f$-systems one can get a qualitative features of the system. In the case of magnetic property, the CEF effect can reduce the RE magnetic moment. It should be cautioned that such reduced moments can often be mistaken for effects of valence fluctuation. In the case of RE ions having even number of electrons, the CEF splitting can lead to a singlet ground state with zero magnetic moment. A direct information on the level scheme on the CEF ground state can be determined by inelastic neutron scattering measurements.

In the present section, we have discussed some aspects of magnetic behaviour or RE ions that are relevant to the discussions present in the subsequent chapters. In the next section, we discuss the phenomena of NTE that constitute a important part of this thesis.

1.4 Phenomenon of thermal expansion

In general, volume of solids changes in response to a change in temperature. Most of the solids, especially metals, expand upon heating as the average distance between their constituting atoms increases with increase in thermal energy. This usual behaviour is known as *positive thermal expansion*. However, there are indeed some materials that shrink with increase in temperature and lead to what is known as *negative thermal expansion*. In the case of solid materials, in respective of the nature of thermal expansion, the linear thermal expansion coefficient (α) can be defined as,

$$\alpha = \left(\frac{1}{l}\right)\left[\frac{dl}{dT}\right] \tag{1.8}$$

where l is the length of the solid. We discuss below the mechanisms that lead to positive and negative thermal expansion in materials.

1.4.1 Mechanism of positive thermal expansion of materials

In most of the solid, the pair potential or sum of the forces (both attractive and repulsive) between two neighboring atoms has *anharmonic* dependence on inter atomic distance [Fig. 1.11]. This is indeed the anharmonic nature of the forces that lead to the positive thermal expansion in most of the solid materials with increase of temperature. In the absence of any thermal vibration, the preferred state of atoms is at bottom of the potential well, with a mean inter atomic distance of r_0 [Fig. 1.11]. As shown in the Fig.1.11, in the anharmonic potential well, the mean inter atomic distance increases with increase in temperature. Although this picture is primitive, this indeed reveals the most important mechanism for positive thermal expansion and successfully indicates that atomic vibrations give rise to thermal expansion only because of the anharmonicity of the potential. It may be mentioned here that a *harmonic* potential well will always keep the mean inter atomic distance fix and would not produce any thermal expansion or contraction with increase or decrease in temperature [Fig. 1.11].

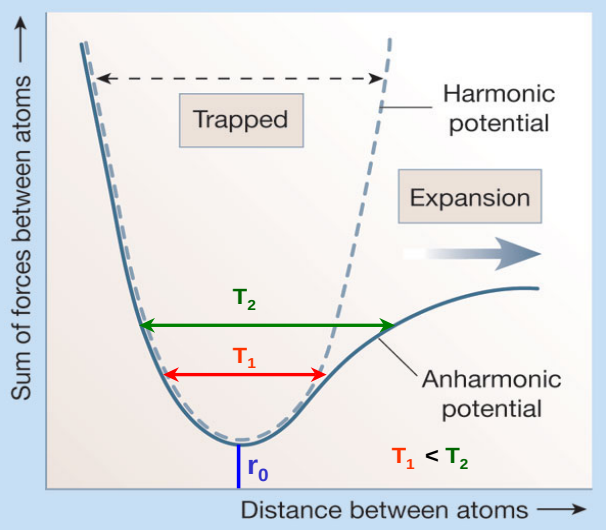

FIGURE 1.11: The typical representation of anharmonic pair potential (or in other words, sum of the forces between two atoms) as a function of inter atomic distance. The figure shows that the inter atomic distance increases with increase in temperature. The figure is reproduced from *A. Sleight, Nature (London)* **425**, *674 (2003)*. A partial modification has been introduced in the figure by indicating two different inter atomic distances at two different temperatures and the mean inter atomic distance r_0.

1.4.2 Negative thermal expansion of materials and underlying mechanisms

As discussed above (section 1.4), some materials shrink when they are heated and lead to NTE. Probably the most familiar material that exhibits NTE in a certain temperature range is water, which exhibits an increase in its density between 0 and 4 ^{0}C. Such NTE of water is indeed very crucial for the preservation of aquatic life during very cold weather. There are also examples of anisotropic structures that exhibit positive thermal expansion in some direction(s) and NTE in other direction(s) [107–109]. The overall thermal evolution of the volume in such materials depends upon the resultant of the two effects.

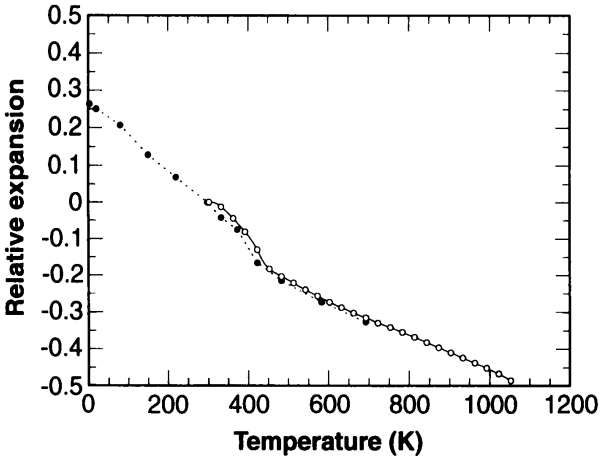

FIGURE 1.12: Percentage relative expansion as a function of temperature for ZrW_2O_8. Open circles are dilatometer data and solid circles are neutron diffraction data. The figure has been reproduced from *Marry et al. Science* **272**, *90 (1996).*

Interest in negative and nearly zero thermal expansion materials started with the discovery of *Invar alloys* [110] in 1896 and the attention was renewed after the discovery of NTE over a wide temperature range of $\sim$ 1000 K in ZrW_2O_8 [Fig. 1.12] [111]. The materials that exhibit negative or nearly zero thermal expansion are receiving remarkable attention due to their possible industrial applications [54, 55, 107, 110–120]. Such materials are used in many precision instruments where the devise efficiency delicately depends upon the physical dimensions of its components.

In contrast to the usual positive thermal expansion behaviour, the phenomenon of NTE in solids can not be explained using any single unique mechanisms and has different origins in different materials. In a very broad sense, based on the underlying physical origins, the phenomenon of NTE in solids can be divided in following three different categories;

1.4.2.1 Magnetic instability driven negative thermal expansion

There are many materials that exhibit anomaly in thermal expansion behaviour close to their magnetic ordering temperature [Fig. 1.9] [54–58, 110]. The phenomena, where thermal expansion anomaly occurs as a result of associated magnetic phase transition, is known as *magnetovolume effect* [54] or *magnetostriction* [110]. Such magnetic effects driven anomaly in crystal dimensions occurs when the energy associated with the ordering of magnetic moments is compatible with the crystallization energy. Alterations in crystal dimensions results in a compromise where total energy is minimum. In many such cases, one observes a large volume change accompanying the onset of spontaneous magnetization (in the case of ferromagnetic phase) or the onset of sublattice magnetization (in the case of antiferromagnetic phase) [54–58, 110]. When such spontaneous magnetostriction is large enough to cancel the normal positive thermal expansion (section 1.4) caused by lattice vibrations, we observe a very small or even NTE [Fig. 1.13].

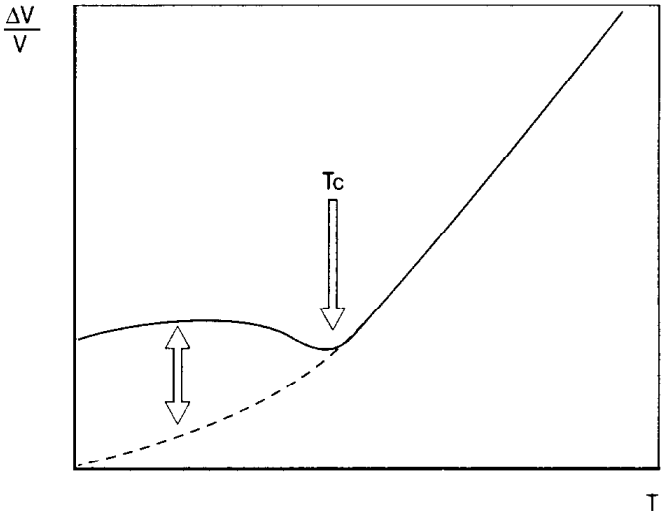

FIGURE 1.13: Schematic representation of invar-type anomaly in thermal expansion. Dashed curve indicates the normal thermal expansion behaviour of the hypothetical paramagnetic state. The difference between the two curves (solid and dashed lines) corresponds to the spontaneous volume magnetostriction. T_c is Curie (or Néel) temperature. The figure is reproduced from *M. Shiga, Curr. Opin. Solid State Mater. Sci* **1**, *340 (1996).*

The most famous materials that exhibit such magnetic effects induced anomaly in thermal expansion are *invar alloys*. Invar alloys are binary compound of Fe and Ni with composition $Fe_{65}Ni_{35}$ [110]. This alloy was invented in 1896 by Swiss scientist Charles Edouard Guillaume, who received the *Nobel Prize* in Physics in 1920 for his pioneering discovery. Mn based metallic perovskite compounds Mn_3MX (section 1.2.2.5) also exhibit such magnetization driven anomaly in thermal expansion [Fig. 1.9]. However, unlike the invar alloys where the transition is of second order and occurs over a wide

temperature range, the same is a sharp first order in nature in Mn_3MX [55]. Such a sharp first order transition leads to sudden change in the lattice volume over a very limited temperature range [Fig. 1.9]. This in fact is a drawback as far as industrial applications are concerned. The efforts to widen the temperature width of transition in Mn3MX are underway [54–58].

1.4.2.2 Vibrational mechanisms driven negative thermal expansion

Vibrational mechanisms are one of the most common phenomena that produce NTE in variety of materials. This phenomena is in general observed in the case of framework materials and the compounds that have low density open structures rather than the close-packed ones [112]. The most common vibrational mechanisms that lead to NTE can be broadly divided in two categories: the vibration of bridging atom and rigid unit modes. These are briefly discussed below.

(A) Vibrational of bridging atom in two-fold coordination:

This mechanism can be understood by a primitive picture shown in the Fig. 1.14. The figure depicts the two metal atoms (M) that are connected with a bridging atom (say, oxygen for example) such that the M-O-M bond angle is nearly 180^0. As shown in the figure 1.14(b), if due to thermal excitations the bridging oxygen atom vibrates transverse to the M-O-M bond direction then the effective distance between the two metal atoms would essentially decrease. However, there are certain conditions that must be met for this mechanism of thermal contraction to be effective. (i) The coordination of oxygen should be *only two*. This is indeed a very essential criterion as any additional atom bound to the oxygen atoms, even if only weakly, will suppress the vibration of oxygen atom perpendicular to M-O-M linkage [121]. (ii) The M-O bond must be strong. The strong M-O bond would have two important consequences: First, the thermal expansion of M-O bond will be small and second, the thermal vibration of oxygen will be very small in the direction of M atoms [121].

In addition to such decrease in the effective distances between the atoms induced by the above mentioned transverse vibrations, there would indeed be an increase of the same induced by positive thermal expansion driven by the anharmonic nature of forces (section 1.4). The overall thermal expansion behaviour of the material, whether it is positive or negative, would be governed by the mechanism that dominants over the temperature range of interest. The transverse vibrations that induced NTE do not induce any bond stretching, *i.e.* increase of M-O bond length and so have low energy (or frequency). Such low frequency excitations are in general achieved at relatively

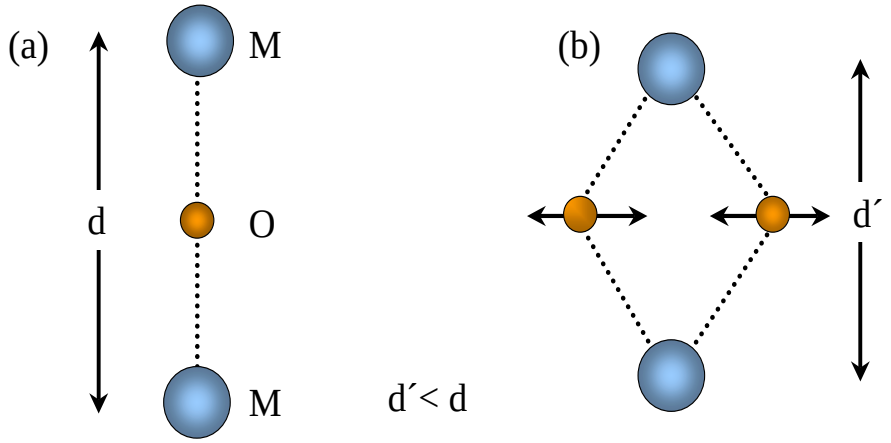

FIGURE 1.14: The picture depicts the apparent decrease in the average inter atomic distance of two metal atoms (M) due to the transverse thermal vibrations of bridging oxygen atom.

low temperatures. In contrast, the mechanisms that lead to positive thermal expansion involve bond stretching that cost more energy and hence are excited at relatively high temperatures [112]. Thus, the vibrational phenomena that leads to volume contraction is more effective at low temperature while at high temperatures the mechanisms that produces positive thermal expansion dominates. The NTE observed in CO_2, SiO_2, rubber *etc.* can be explained using the above discussed transverse vibration mechanism [121].

(B) Rigid unit modes:

There are many materials (mainly oxygen based) that are built up with rigid polyhedra (SiO_4, WO_4. ZrO_6 *etc.*) linked at their corners by shared oxygen atoms [111, 112]. Such rigid polyhedra consist of highly covalent M-O bonds with almost unaffected bond lengths. In such materials, large amplitude transverse vibrations of the oxygen atoms can occur only through coupled vibration of the tetrahedra and octahedra forming the framework structure [Fig. 1.15]. Such coupled vibrations are termed as *rigid unit modes* [112]. The rigid unit modes do not involve any change in intra-unit bond distance and angles, and so have relatively large amplitude and low frequencies. One such example in two dimension is shown in figure 1.15(a), where rigid MO_4 squares are connected to their neighbors by share oxygen atoms. Figure 1.15(b) exhibits a possible rigid unit modes in which neighboring square lattice of MO_4 librate in opposite directions. As shown in the figure, such modes lead to a reduction of the effective lattice parameter from a_0 to $a_0 \cos\theta$, where θ is average deformation angle.

The above described rigid unit modes are responsible for the NTE in well known compound ZrW_2O_8 [111, 112] (also see section 1.4). This cubic compound exhibits a large

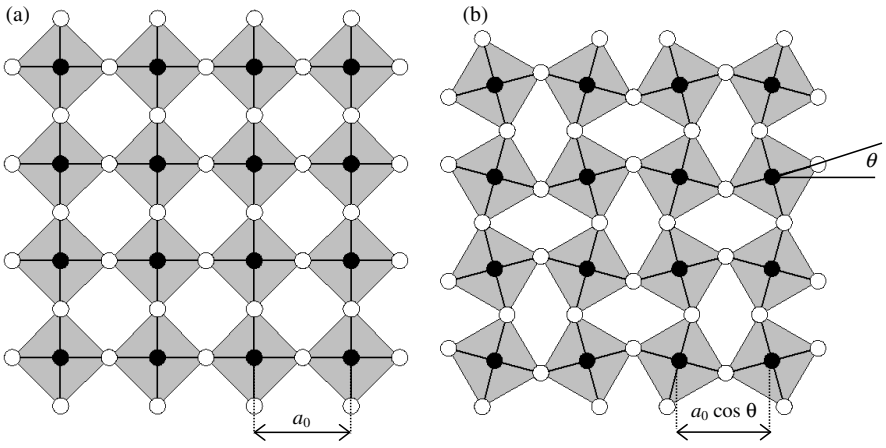

FIGURE 1.15: (a) A perfect square lattice of rigid MO_4 units with M-O-M bond angle of π. Filled circles and open circles represent M and O atoms respectively. (b) Rigid Unit Modes driven rotational displacements in the MO_4 units. The figure also demonstrates the static lattice with a bent M-O-M bond angle $\pi - 2\theta$. The figure is reproduced from *Barerra et al. J. Phys. Condens. Matter* **17**, *R217 (2005).*

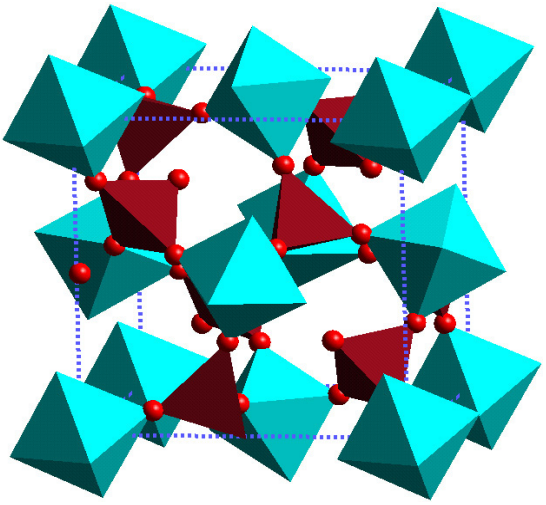

FIGURE 1.16: The room temperature structure of ZrW_2O_8. The ZrO_6 octahedra (cyan in colour) and WO_4 tetrahedra (maroon in colour) are shown in the figure. The small spheres represent bridging oxygen atoms. The figure is reproduced from *Barerra et al. J. Phys. Condens. Matter* **17**, *R217 (2005).*

NTE over wide temperature range of 0.3 to 1050 K [Fig. 1.12] [111]. As the cubic symmetry of the compound persists over the entire stability range, the observed NTE can termed as *isotropic* in nature [111]. The schematic representation of the crystal structure of ZrW_2O_8 is shown in Fig. 1.16. In this structure each ZrO_6 unit shares its corners with six different WO_4, while each WO_4 unit shares only three of its corners with ZrO_6 units. The remaining one oxygen in each WO_4 unit remains singly coordinated. The existence of singly coordinated oxygen enhances the flexibility of the framework structure that can

readily accommodate the changes in M-O-M bond angles due to transverse vibrations [111]. The theoretical and experimental investigations have established that the low energy phonon modes corresponding to these coupled rotations are indeed responsible for the observed NTE in this material [111, 112].

1.4.2.3 Valence instability driven negative thermal expansion

Valence instability driven NTE is observed in several compounds containing unstable valence RE ions [112, 118, 119, 122]. Many RE elements, *e.g.* Ce, Eu, Sm, Yb *etc.* are known to exhibit *valence fluctuation* between two different valence states in many of their compounds [2]. This phenomenon occurs due to the hybridization caused by the proximity of $4f$ level to the Fermi level in such elements. In general, transition between the two different $4f$ states also results in the changes of ionic radii [$r(4f^n)$>$r(4f^{n-1})$]. Temperature assisted change in the relative population of the valence configurations thus lead to significant change in the volume and also sometimes results in NTE in many materials [119, 122]. For example, one of the such unstable valence compound $Sm_{2.75}C_{60}$ exhibits NTE between 4.2 to 32 K with $\alpha = -130$ ppmK^{-1} [Fig. 1.17] [119]. Which is an order of magnitude larger than the same observed in the case of well-known ZrW_2O_8 ($\alpha = -9.4$ ppmK^{-1}).

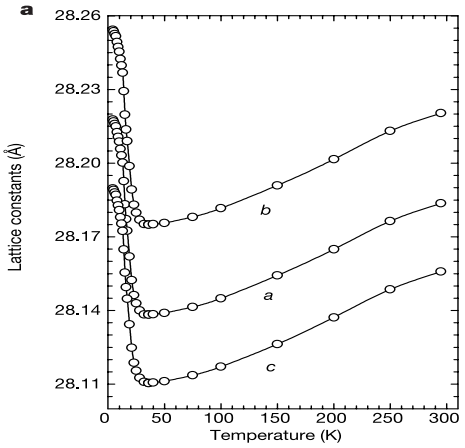

FIGURE 1.17: The temperature dependence of the lattice parameter of $Sm_{2.75}C_{60}$. The figure has been reproduced from *Arvanitidis et al. Nature (London)* **425**, *599 (2003).*

The mechanisms described above are successfully used in explaining the NTE behaviour observed in many materials. There is indeed significant current interest in materials that exhibit such unusual behaviour and more quantitative descriptions are expected to come in the future. In the next section, we discuss about the occurrence of NTCR in metallic compounds and alloys.

[2] The phenomenon of valence fluctuation is discussed in detail in the section 1.6.

1.5 Negative Temperature Coefficient of Resistivity in metals

In general, temperature dependence of resistivity (ρ) of normal metals and metallic compounds are expressed using Bloch-Grüneisen expression given by the equation (1.9).

$$\rho(T) = \rho_0 + C\left(\frac{T}{\theta_D}\right)^5 \int_0^{\theta_D/T} \frac{x^5 dx}{(1-e^{-x})(e^x-1)} \tag{1.9}$$

Where ρ_0 is the residual resistivity, θ_D is the *Debye* temperature and C is a numerical constant. The second term of the of the equation (1.9) represents the resistivity due to *electron-phonon scattering* (ρ_{ph}). As the total number of phonons (scatterers) on the surface of allowed wave vectors for scattering of a given electron is directly proportional to temperature, the ρ_{ph} increases linearly with temperature for $T \gg \theta_D$ [123]. This phenomenon results in a positive temperature coefficient of resistivity (TCR) (α), defined as;

$$\alpha(T) = \frac{1}{\rho(T)}\left[\frac{d\rho(T)}{dT}\right] \tag{1.10}$$

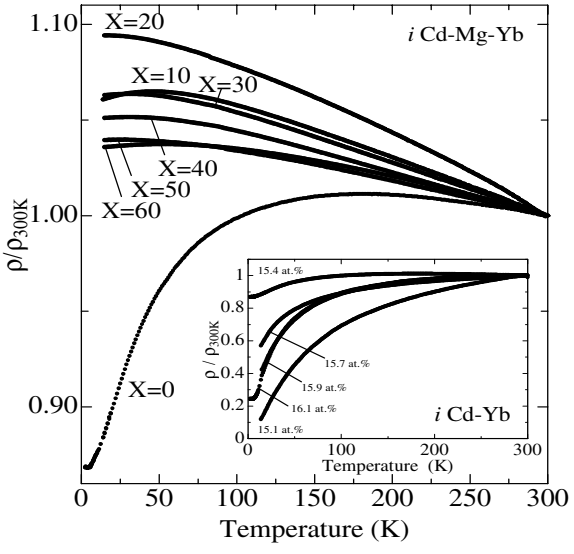

FIGURE 1.18: The temperature dependence of resistivity ratio (ρ/ρ_{300K}) of i $Cd_{84.6-x}Mg_xYb_{15.4}$ in a wide composition range with $x = 0, 10, 20, 30, 40, 50$ and 60. The inset exhibits the same of binary i Cd-Yb with Yb concentration ranging from 15.1 to 16.1 atomic %. The figure is reproduced from *R. Tamura et al. Phys. Rev. Lett.* **90**, *226401 (2003).*

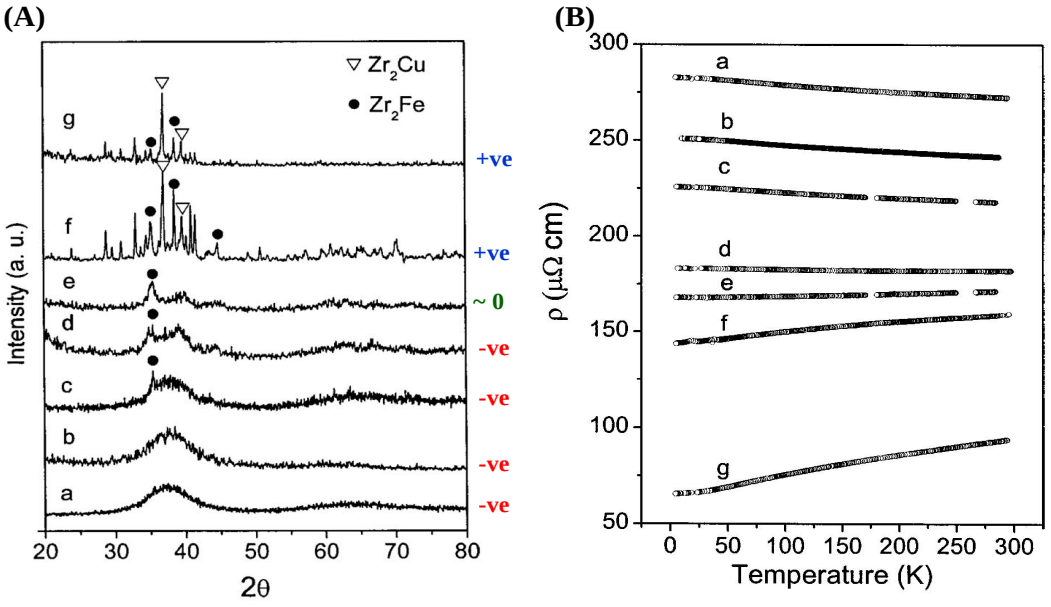

FIGURE 1.19: (A) XRD patterns and (B) temperature dependence of the electrical resistivity of $Zr_48Nb_8Cu_12Fe_8Be_24$ at various annealing temperatures; (a) as prepared, (b) annealed at 573 K for 2 h, (c) 663 K for 2 h, (d) 693 K for 2 h, (e) 733 K for 2 h, (f) 813 K for 2h, and (g) 873 K for 4 h. The figure is reproduced from *H. Y. Bai et al. J. Appl. Phys.* **95**, *1269 (2004).*

Nearly all the crystalline metals and intermetallic compounds are characterized by a positive value of α near room temperature. There are, however, examples of metallic compounds and alloys that exhibit NTCR [Fig 1.18]. The materials that exhibit such behaviour are in general structurally [124] and chemically [125] disordered materials, liquid metals [126] and quasi crystals [127]. It has been found that the sign of α is very sensitive to the degree of crystallinity and changes substantially with heat treatments and other processes that modify the structural order in the material [124]. One such example is shown in the figure 1.19, where magnitude of the room temperature resistivity decreases and α changes sign from negative to positive upon annealing [124].

There exists a well known *Mooij criterion* that correlates the sign of the TCR with the value of resistivity for conductors and suggests that the TCR calculated at room temperature changes sign and becomes negative when the resistivity crosses the critical value, $\rho_c \sim 150$ $\mu\Omega-$cm [128]. Later Tsuei collected more than 500 data over various samples and modified the Mooij criterion with a modified value of ρ_c that can vary from 30 to 400 [Fig. 1.20] $\mu\Omega-$cm [129].

As discussed above, the nature of atomic structure of a material plays a crucial role in determining its electrical transport properties and the underlying mechanisms. In the following section, we discuss and compare the atomic structure of liquid metals,

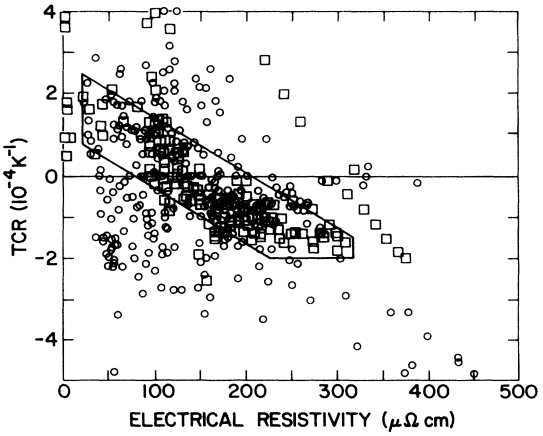

FIGURE 1.20: TCR vs resistivity for various crystalline disordered metallic conductors (open squires) and amorphous metals (open circles) at room temperature. The solid lines are used to outline the region where the original Mooij data points were distributed. The figure is reproduced from *Tsuei et al. Phys. Rev. Lett.* **57**, *1943 (1986).*

amorphous solids and crystalline materials, and in subsequent section we discuss the mechanisms that govern the electrical transport in these materials.

1.5.1 Atomic structure of liquid metals, amorphous solids and crystalline materials

The atomic structure of a material can broadly be classified in terms of its pair distribution function $g(r)$, which can be defined as;

$$n(r) = \rho_0 g(r) 4\pi r^2 dr \tag{1.11}$$

where $n(r)$ is the number of atoms found in the volume element $4\pi r^2 dr$ at the radius r from an atom present at $r = 0$ and ρ_0 is average number density of atoms given by the ratio of N atoms over the volume of V. It is clear from the equation 1.11 that the volume of spherical shell, $4\pi r^2 dr$, as well as number of atoms contained therein, $n(r)$, both increase with increasing r. Thus, if we divide the both side of the equation 1.11 by the cell volume $4\pi r^2 dr$, we will essentially end up with an average number density ρ_0, which leads to the relation;

$$\lim_{r \to \infty} g(r) = 1 \tag{1.12}$$

Figure 1.21 illustrates the atom distribution and corresponding $g(r)$ for gas, liquid metals, amorphous solid and crystalline materials [130]. The atomic arrangement in a crystalline material can be uniquely determined within a well defined unit cell [Fig. 1.21]. Such materials possess various translational and rotational symmetries. On the other hand, such unit cell can not be defined in the case of liquid and amorphous metals because of the disordered distribution of atoms [Fig. 1.21].

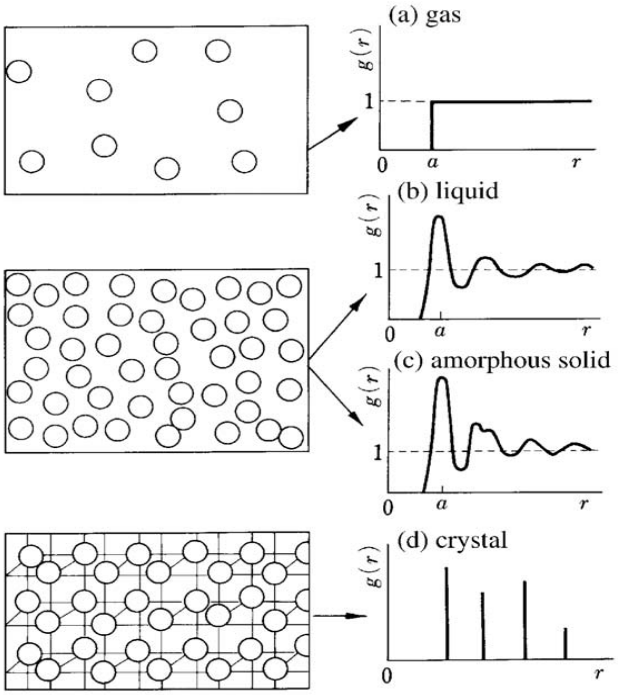

FIGURE 1.21: Distribution of atoms with radius $a/2$ (left column) and the corresponding pair distribution function $g(r)$ (right column) in (a) gas, (b) liquid, (c) amorphous solid, and (d) crystalline materials. The figure (b) and (c) are drawn on a plane projected from the three-dimensional space so that the atoms are positioned as if they are overlapped. The figure is reproduced from *U. Mizutani, Introduction to the electron theory of metals, Cambridge University Press, Chapter 15 (2001).*

If we take one of the atoms as the origin and plot the $g(r)$, the results will be entirely different for gas, liquid metals, amorphous solids and crystalline materials [Fig. 1.21]. In the case of crystalline materials, the distribution of atoms is described by a series of delta functions. This happens because a definite number of atoms are found at a definite distance. In contrast, the density of atoms in a gas is so low that their distribution is independent of the distance r except for the region below the diameter of the atom, a, where two neighboring atoms can no be geometrically overlapped. On the other hand, liquid metals and amorphous solids exhibit some correlation in atomic distribution. The distribution is zero for $r \leq a$ because of geometrical restrictions mentioned above. Additionally, there is a prominent peak at the nearest neighbor distance, both in liquid metals

and amorphous solids, indicating that the probability of finding atoms at this distance is high. Further peaks occurring at second, third *etc.* neighbor distance appear with decreasing intensities and eventually converge to an average density. Such oscillating behaviour is a characteristic feature of liquid metals and amorphous solids.

As described above, the atomic arrangement inside the liquid metals and amorphous solids is entirely different to that of crystalline materials. Such random distribution of atoms causes the *Bloch theorem* to fail in liquid metals and amorphous solids and also leads to relatively high resistivity values in these material phases compared to crystalline metallic compounds. The mechanisms that govern the electrical transports in liquid metals and amorphous solids will be briefly discussed in the next section. In addition to liquid metals and amorphous solids, there is one more family of metallic materials, *quasicrystals*, that exhibit characteristics entirely different to that of crystalline metals. Quasicrystals exhibit five-fold symmetry that is incompatible with the translational symmetries [130]. Such incompatible symmetries lead to break down of Bloch theorem in the case of quasicrystals as well. Hence, these compounds can also be grouped together with liquid metals and amorphous solids in to the category of *non-periodic systems*, in spite of the possession of a high degree of ordering evidenced by sharp Bragg reflections [127, 130].

1.5.2 Mechanisms of electron transport in non-periodic systems

The mechanisms of electron transport in non-periodic liquid metals and amorphous solids are substantially different from those in periodic crystalline materials. Significant understanding has been developed regarding the nature of electrical transport in such non-periodic metallic systems. There are various proposed mechanisms and models, *viz. Ziman model, Structural Kondo model, Incipient localization, Baym-Meisel-Cote theory, Narrow band gap semiconductors etc.*, that successfully explain the NTCR observed in many highly disordered materials. Some of them are are briefly discussed below.

1.5.2.1 Ziman model

The resistivity behaviour of liquid metals at sufficiently high temperatures was successfully explained by Ziman [130, 131]. The expression derived by him is given in the equation 1.13;

$$\rho = \left(\frac{3\pi\Omega_0}{4e^2\hbar v_F^2 k_F^4}\right) \int_0^{2k_F} |U_p(K)|^2 a(K) K^3 dK \tag{1.13}$$

Where, Ω_0 is volume per atom, v_F is Fermi velocity, k_F is Fermi wave vector, $|U_p(K)|$ is atomic form factor and $a(K)$ is called interference function or static structure factor. The formula considers the interaction of conduction electrons with *static* distribution of ions in liquid metals. This is indeed equivalent to elastic scattering of the conduction electrons with ions [130].

There are three basic assumptions in the Ziman expression: (i) The linearized *Boltzmann* transport equation is assumed, which implies that the mean free path of the conduction electrons must be longer than average inter atomic distance. (ii) The *Born approximation* is assumed to calculate the transition probability, which is justified by the pseudopotential approach that holds only for systems in group-V but fails to systems in group-IV. (iii) Elastic scattering is considered as the dominant scattering mechanism. This limits the applicability of the Ziman formula only to liquid metals, because elastic scattering dominates either at very low temperature of at temperatures well above the *Debye temperature*. As the equation 1.13 contains the weight factor K^3, the contribution of $a(K)$ and $|U(K)|^2$ becomes substantial only in the K region near to upper limit of $2k_F$.

The elastic scattering of conduction electrons always takes place on the *Fermi surface*. The magnitude of the scattering vector (K) is related to the scattering angle (θ) and Fermi wave vector (k_F) through the following relation;

$$\sin\frac{\theta}{2} = \frac{K}{2k_F} \tag{1.14}$$

As the allowed range for θ is $0 \leq \theta \leq \pi$, hence the possible K values are $0 \leq K \leq 2k_F$. This indicates that scattering vector is limited by the diameter of the Fermi sphere. The figure 1.22 illustrates the K dependence of both $a(K)$ and $|U(K)|^2$ for a typical liquid metal. In general, the K dependence of $|U(K)|^2$ is fairly small and almost flat in the region of our interest ($1.0 \leq e/a \leq 4.0$, where e/a is the number of valence electrons per atom) [Fig. 1.22]. Thus the contribution of $a(K)$ is more important. The $a(K)$ is characterized by the first main peak centered at wave number K_p, the inverse of which roughly corresponds to average inter atomic distance of the liquid metal (section 1.5.1).

Using the resistivity expression given in equation 1.13 and the variation of $a(K)$ shown in the Fig. 1.22, one can make a comparative estimate of the resistivity values of liquid metals with various e/a values. For monovalent metals with $e/a = 1$ like Na, the $2k_F$ value is relatively small and the condition $2k_F < K_p$ holds. As shown in the Fig. 1.22, the relatively small $a(K)$ (~ 1) values yield fairly small resistivity values. The main peak of $a(K)$ gets broadened with increase in temperature due to increase in free volume and structural disorder. However, as in the case of monovalent metals we

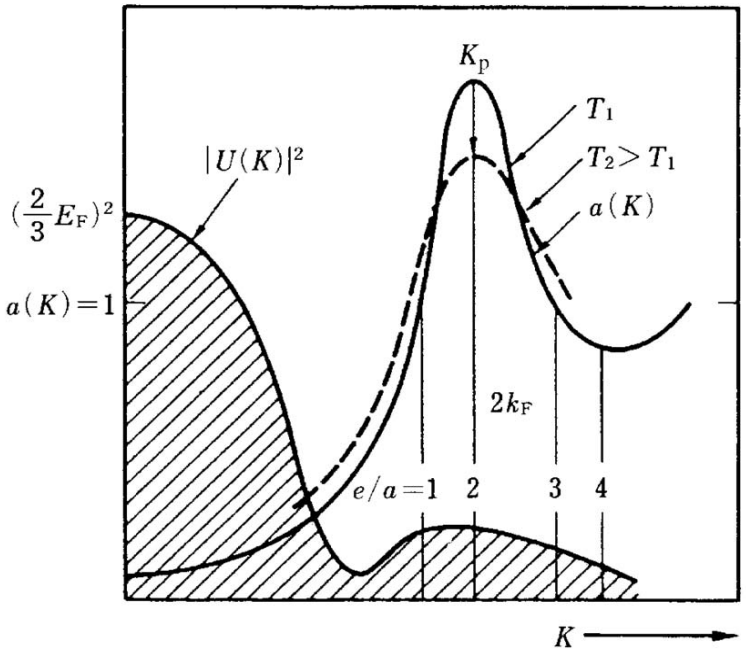

FIGURE 1.22: The wave number dependence of the integrands $a(K)$ and $|U(K)|^2$ appearing in the Ziman expression given in equation 1.13. The position of $2K_F$ corresponding to various e/a (number of valence electrons per atom) values are shown by the vertical lines. The figure is reproduced from *U. Mizutani, Introduction to the electron theory of metals, Cambridge University Press, Chapter 15 (2001).*

have $a(K)_{T=T_2} > a(K)_{T=T_1}$ $(T_2 > T_1)$, hence the resistivity values monitor increase in with increase in temperature leading to a positive TCR. The situation is nearly same for polyvalent metals $(e/a = 3.0 - 4.0)$ that also produce small resistivity value and a positive TCR. In contrast, in divalent metals with $e/a = 2.0$ like Zn and Cd, the condition $2k_F \sim K_p$ holds. As the upper limit of $2k_F$ coincides with the main peak of $a(K)$ [Fig. 1.22], the resistivity values are relatively higher. In addition, the decrease in the height of main peak of $a(K)$ with increasing temperature reduces the resistivity values and results in a NTCR in divalent metals.

1.5.2.2 Baym-Meisel-Cote theory

The Ziman theory, discussed in the last section, works well for liquid metals but it fails to describe the resistivity behaviour of amorphous alloys. Among the three underlying assumptions of Ziman theory (section 1.5.2.1), the linearized Boltzmann transport equation and Born approximation are equally applicable for amorphous alloys. However, the assumption of the elastic scattering fails in the case of amorphous alloys [130]. This happens because the electron transport properties of the amorphous alloys are discussed at temperatures well below their Debye temperature (θ_D) or even below 300 K in most

of the cases. In contrast to the liquid metals, the ions in amorphous alloys can no longer be treated as independent particles at such low temperatures. Thus, the concepts of collective excitations of phonons and inelastic electron-phonon scattering are essential to describe the electron-transport properties of amorphous alloys of group-V. The resistivity behaviour of amorphous alloys can be well described by using *Baym-Meisel-Cote theory* [132–135]. In this theory, the temperature dependence of resistivity can be approximates as;

$$\rho(T) = [\rho_0 + \Delta\rho(T)]exp[-2W(T)] \tag{1.15}$$

Where, ρ_0 is the residual resistivity, $\Delta\rho(T)$ is the term arising from the inelastic electro-phonon scattering and $exp[-2W(T)]$ represent the *Debye-Waller factor*. In first approximation, $\Delta\rho(T)$ exhibits $+T^2$ temperature dependence at low temperatures ($\sim<$ 20 K) and $+T$ at higher temperatures. The Debye-Waller factor exhibits $(1-\alpha T^2)$ dependence at low temperatures and $(1-\beta T)$ at high temperatures ($\sim>$ 50 K) [130].

If ρ_0 value is small ($\sim 50-60\mu\Omega$-cm), the term $\Delta\rho(T)$ dominates and $+T$ dependence of resistivity is observed at high temperatures leading to a positive TCR. On the other hand, when the ρ_0 values are relatively higher ($\sim> 60\mu\Omega$-cm), then the Debye-Waller factor begins to play a more important role. In such cases the resistivity exhibits $(1-\alpha T^2)$ dependence at low temperature and $(1-\beta T)$ dependence at high temperatures leading to NTCR. This means that the sign of TCR in amorphous solids is determined by the interplay between $\rho_0 exp[-2W(T)]$ and $\Delta\rho(T)exp[-2W(T)]$ instead of $2k_F/K_p$ in liquid metals (section 1.5.2.1).

1.5.2.3 Localization theory

The compounds and alloys possessing high residual resistivity often exhibit localization effects. The high residual resistivity arises from the elastic scattering of conduction electrons from the random distribution of ions at absolute zero temperature. We have discussed in the previous section (equation 1.15) that although the inelastic electron-phonon scattering plays an important role in determining the temperature dependence of electrical resistivity in amorphous alloys, its contribution becomes less important as the value of residual resistivity increases.

If we consider a conduction electron with energy E_0 in a periodic potential then the Bloch wave derived from the tight-binding approximation will form a narrow band of width W [Fig. 1.23(a)]. If we introduce some disorder in the potential by incorporating some external impurities, the periodicity of the lattice will get destroyed. Figure 1.23(b)

illustrates the distribution of such potential that vary irregularly in the range $-V_0/2 < V < V_0/2$. Anderson [136] showed that electrons in such non-periodic lattices can not form the Block wave and get localized if the ratio V_0/W exceeds a critical value [130, 136]. At finite temperatures, such localized electrons are able to exchange their energy with phonons and hop from one lattice site to another. This phenomenon is termed as *hopping conduction*.

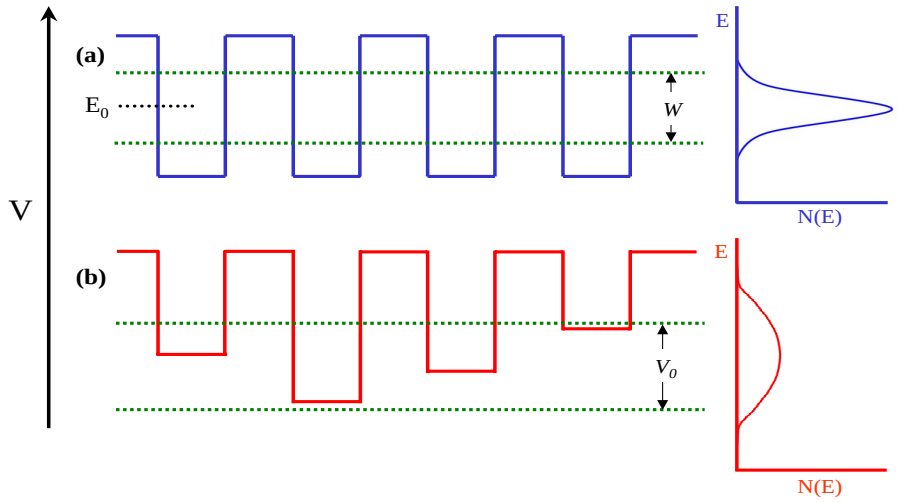

FIGURE 1.23: Variations of potential in (a) periodic and (b) non-periodic lattices. In the case of periodic potential, electrons with energy E_0 form the Bloch state with band width W. On the other hand, in the case of non-periodic potential with V_0 degree of disorder, electrons get localized if V_0/W exceeds some critical value.

It can be shown that the multiple elastic scattering accompanying the momentum transfer of $2k_F$ become more frequent in systems possessing high residual resistivity. This results in enhanced probability of having electron at the same position where it was before the scattering took place [130]. This scattering is also often called as *quantum interference effect* or $2k_F$ *scattering*. The elastic scattering dominates at low temperatures, while at finite temperatures electrons begin to get scattered inelastically with phonons. Which results in a gradual loss of phase coherence during successive scatterings leading to delocalization of electrons. The delocalization of electrons with increasing temperature results in NTCR of disordered material under consideration.

It was later pointed out by Altshuler and Aronove [137] that electron-electron Coulomb interaction gets enhanced when electrons tend to localize. The enhanced electron-electron interaction coupled with weak localization leads to $\sqrt{T}$-dependence of electrical conductivity at low temperatures (say below 20 K) that can be expressed as;

$$\sigma(T) = \sigma_0(1 + \alpha\sqrt{T}) \tag{1.16}$$

At relatively high temperatures (say above 30 K), the conductivity follows $\sigma \propto T$.

1.5.2.4 Narrow band gap semiconductors

The temperature variation of the resistivity of a typical semiconductor can be be described as;

$$\frac{1}{\rho(T)} = \sigma_0 exp\left[\frac{-E_g}{2k_B T}\right] \tag{1.17}$$

Where E_g is the band gap, which is of the order of one eV is most of the common semiconductors. Thermal excitation of electrons across such energy gaps is not possible at temperatures comparable to room temperature. However, if the band gap is reduced to the size of a few meV then electrons can be thermally activated at temperatures comparable to room temperature and conduction will occur [138]. Such small band gap semiconductors are in general referred as *narrow band semiconductors* [139]. The activated temperature dependence of the resistivity, given by equation 1.17, leads to NTCR in these compounds [139]. In general, the resistivity of the narrow band semiconductors is of the order of a few m$\Omega-$cm, which higher than metals and lower than usual semiconductors.

In the present section, we have tried to discuss most of the mechanisms that lead to NTCR in metallic compounds and alloys. In the next section, we discuss an entirely different topic of valence fluctuation in RE elements.

1.6 Valence fluctuation in some of the rare-earth elements

As discussed in section 1.3, in general, RE ions are in trivalent state (R^{+3}) state in most of the RE intermetallic compounds and physical properties of these materials are determined by the number of localized f-electrons. However, there are a class of RE and actinide materials that exhibit a non-localized and correlated behaviour of f electrons. This leads to various interesting phenomenon, such as valence fluctuation, Kondo lattice, heavy fermion behaviour *etc.*, that have been extensively studied [140–147]. Here, in this section, we will mainly focus on the phenomenon of valence fluctuation.

In the phenomenon of valence fluctuation, valency of the RE ion, instead of being stable and integral (usually +3), fluctuates between two configurations, $4f^n$ and $4f^{n-1}$. This happens when the two configurations are energetically very closely spaced or the levels are broad enough to mix or overlap. In the fast fluctuation limit, which usually is the

case, with fluctuation frequency of about 10^{-13} sec, the average valence and many of the physical properties are a thermal population weighted average of the two valence states.

It may be mentioned here that for the phenomenon of valence fluctuation, various terms, such as, *intermediate valence, mixed valence, interconfiguration fluctuation*, *etc.* are in general interchangeably used. However, there are indeed some distinction in the terminologies. The term mixed-valence (which is most often used in the literature for valence fluctuation) normally implies the static mixed-valence state *i.e.*, different valence states of RE ions at two inequivalent crystallographic sites of a lattice. This is some times also termed as heterogeneous mixed valence. Whereas, valence fluctuation is a continuous dynamic change of the valence at one crystallographic site and is sometimes termed as homogeneous mixed valence. The term intermediate valence could apply to a situation where the average valence is non integral and unaffected by external parameters such as temperature.

Some of the properties in which the phenomenon of valence fluctuation is reflected are: lattice parameters, resistivity, magnetization, X-ray L_{III}-edge absorption, ^{151}Eu-Mössbauer measurement (for Eu-based systems only) *etc.* Valence fluctuation phenomenon has been found in the f-elements such as Ce, Sm, Eu, Tm, Yb and U. While many Ce-based valence fluctuating systems are known, relatively fewer are known in Eu and Yb and only rarely in Sm, Tm and U.

Amongst the valence fluctuation systems, Eu-based materials provide ideal systems to investigate the phenomenon as ^{151}Eu-Mössbauer spectroscopy is a powerful tool to determine the valence state of Eu in its compounds. For a trivalent Eu-ion, the ^{151}Eu-Mössbauer resonance occurs with an isomer shift (with respect to EuF_3) in the range -1 mm/sec to +4 mm/sec while for a divalent Eu-ion, the isomer shift turns out to be in the range -8 mm/sec to -14 mm/sec. This difference in isomer shift for the two valence states is quite large compared to the width of the resonance ($\approx$2.5 mm/sec) which allows one to determine the valence of Eu in a given material unambiguously. If Eu ion is in valence fluctuation state, usually, the fluctuation time ($\approx 10^{-13}$ sec) being smaller than the probe time ($\approx 10^{-9}$ sec), Mössbauer resonance shows a single line with an isomer shift intermediate (population weighted average of the isomer shift of the two individual valence states) to that of Eu^{2+} and Eu^{3+} ions. Further, the value of isomer shift of a valence fluctuation system would be temperature dependent, as the relative population of the two valence states depends on temperature. In general, the fluctuation frequency remains faster than the probe time even at lowest temperature, and thus the resonance line remains a single line down to lowest temperatures. Apart from these, any presence of impurity is not likely to interfere with the signal, as the Mössbauer line of impurity is likely to have a different isomer shift and can be recognized and taken care of in the

analysis. Thus, Mössbauer spectroscopy gives a distinct advantage in identifying and analyzing Eu-based valence fluctuation materials.

1.6.1 Interconfigurational fluctuation model

Interconfigurational fluctuation (ICF) model is a phenomenological model to describe the magnetic susceptibility of valence fluctuating systems. It was firs proposed by Hirst [148–151] and latter implemented successfully by Sales and Wohlleben [152].

According to Hirst, a f-electron system has a discrete spectrum of many electron levels characterized by a different integral occupation number n. The total energy of the system depends on n and consists of the repulsive Coulomb interaction energy U_{ff} between two localized f-electron (taken as a pair) and the binding energy V of the f electron with the nucleus. The energy E_n of a f^n ionic configuration is then given by;

$$E_n = U_{ff}\frac{n(n-1)}{2} + nV \tag{1.18}$$

The above expression can be rewritten as;

$$E_n = \frac{1}{2}U_{ff}(n - n_{min})^2 + \text{constant} \tag{1.19}$$

where;

$$n_{min} = -\frac{V}{U_{ff}} + \frac{1}{2} \tag{1.20}$$

Thus, from equation 1.19, we see that E_n is a parabolic function of n and n_{min} is the minimum of the parabola [Fig. 1.24]. If the state with occupation number n is the ground state and that with $n-1$ is the higher state, then the excitation energy, E_{ex}, which would take the system from configuration n to configuration $n-1$ would be $E_{ex} = E_{n-1} - E_n$. It can be easily seen that the value of E_{ex} varies between zero (when the value of n_{min} is half integral) to $U_{ff}/2$ (when the value of n_{min} is integral). If E_{ex} is comparable to the thermal energy then one would observes an interconfiguration fluctuation between two valence states of the RE ions.

In addition to the above consideration, one must note that the f-levels can be broadened by the hybridization due to the conduction electrons. The width, Δ, of the broadening can be obtained using the Friedel-Anderson theory [153, 154] as;

$$\Delta = \pi\rho(E)\langle|V_{cf}|\rangle \tag{1.21}$$

Where $|V_{cf}|$ is the matrix element of Coulomb (mixing) interaction due to the conduction electron wave function and the f-electron wave function, $\rho(E)$ is the density of states of the conduction electrons. It must also be noted that this broadening is associated with each configuration energy state and can also be treated as an intrinsic fluctuation temperature, $T_{sf} \simeq \Delta/k_B$, and the fluctuation frequency is given by $\omega \simeq k_B T_{sf}/\hbar$, where k_B is the *Boltzmann constant*. We may recall that the fluctuation frequency is $\approx 10^{-13}$ sec. If $\Delta << E_{ex}$ and $E_{ex} >> k_B T$ then the valence state of the f-element would be a stable integral one. If $\Delta \geq E_{ex}$, then the fluctuation between the two configurations, f^n and f^{n-1}, would be temperature independent and would persist even at $T \to 0$.

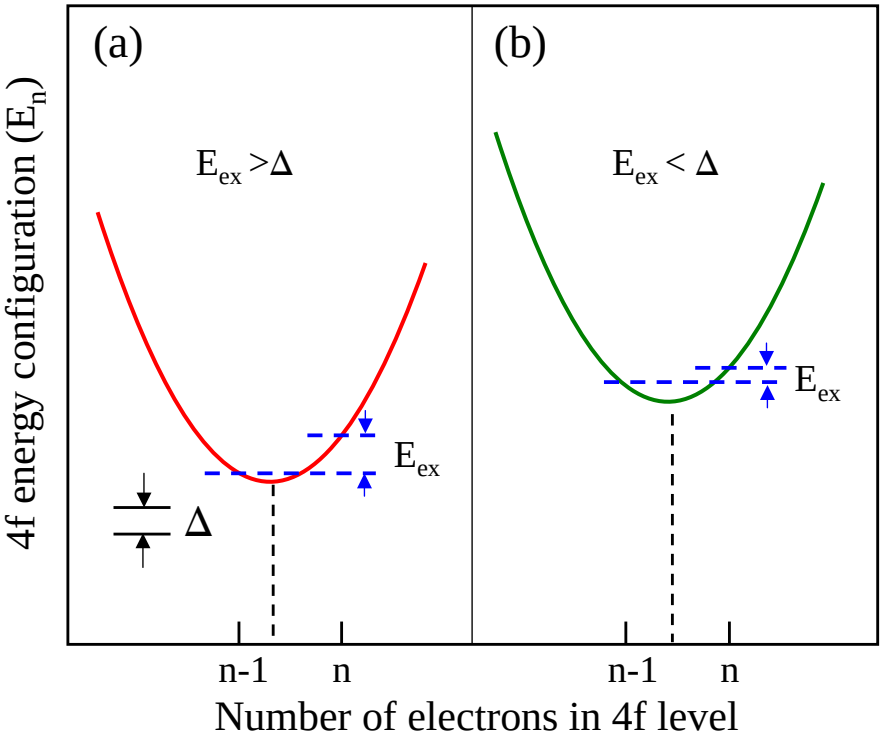

FIGURE 1.24: Energy levels in the ICF model as a function of occupation number n of the $4f$-shell. The stable $4f$-configuration is illustrated in (a), while the situation in intermediate valence regime is shown in (b).

Sales and Wohlleben [152] applied the above ICF model to explain the thermal susceptibility of a valence fluctuating material. In this model, any physical property, such as magnetic susceptibility is assumed to be the population weighted average of the property of the individual configuration state of the two levels with the distinct energies E_n and E_{n-1} [106]. The population at each of these two levels is given by the usual exponential

Boltzmann relation controlled by E_{ex}. Sales and Wohlleben proposed [152] that the broadening of levels due to hybridization, as discussed above, can be taken into account by replacing the thermodynamic temperature T by an effective temperature T^* where $T^* = T + T_{sf}$. This also takes care of finite and nearly temperature independent value of susceptibility at $T \rightarrow 0$. However, later it had been pointed that this form of T^* violets Nernst's law which requires the first-derivative at T=0 to be zero [155]. This problem was overcome by Franz *et al.* [156] by defining T^* as $\sqrt{T^2 + T_{sf}^2}$. Under these conditions, at high temperatures where $T >> T_{sf}$, the quantum mechanical fluctuations would be dominated by thermal fluctuations, while at low temperatures, $T << T_{sf}$, the quantum mechanical fluctuations would dominate [106].

Using the above mentioned conditions and assumptions the magnetic susceptibility of a valence-fluctuating compounds can be expresses as;

$$\chi(T) = \left(\frac{N}{k_B}\right)\left[\frac{\mu_n^2 P_n(T) + \mu_{n-1}^2 P_{n-1}(T)}{\sqrt{T^2 + T_{sf}^2}}\right] \tag{1.22}$$

Where $P_n(T)$ and $P_{n-1}(T)$ are the fractional occupation of ground state (E_n) and first excited state (E_{n-1}) configurations, respectively (with the condition, $P_n + P_{n-1} = 1$). The μ_n, μ_{n-1} are the effective paramagnetic moments of the states E_n and E_{n-1}, respectively

The temperature dependence of $P_n(T)$ can be described as;

$$P_n(T) = \frac{(2J_n + 1)}{(2J_n + 1) + (2J_{n-1} + 1)exp(-E_{ex}/\sqrt{T^2 + T_{sf}^2})} \tag{1.23}$$

Where, Jn and J_{n-1} are the total angular momentums of the ground and excited states respectively. As discussed above, T_{sf} is the intrinsic fluctuation temperature. At high temperatures where $T >> T_{sf}$, the equation 1.22 predicts a CW behaviour of susceptibility but with an effective magnetic moment which is the population weighted average of the moments of the individual states.

Figure 1.25 exhibits the temperature variation of the magnetic susceptibility of $Ce_2Ni_3Si_5$ [157], where Ce ions are in temperature dependent intermediate valence state. The $\chi(T)$ has been interpreted using ICF model and an additional CW term originating from stable impurities of Ce^{+3} ions. As can be seen from the figure the resultant fit is quite satisfactory in the entire temperature range of measurement. This demonstrates the appropriateness of the ICF model in describing the temperature dependence of magnetic susceptibility of a material containing valence fluctuating ions.

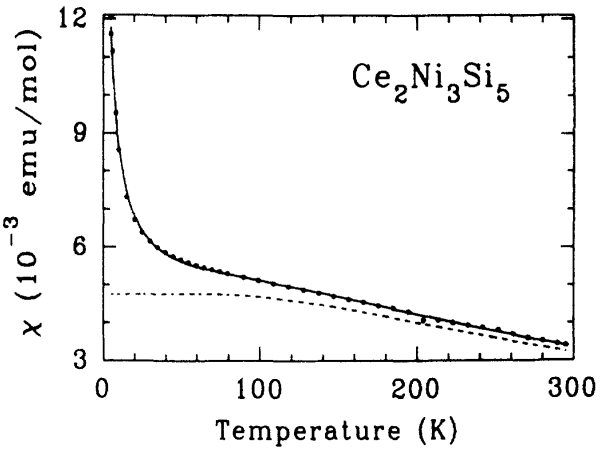

FIGURE 1.25: Temperature variation of the magnetic susceptibility of $Ce_2Ni_3Si_5$. The solid line is a fit to the experimental data using ICF model. The dashed line is the susceptibility obtained from the fit after subtracting a impurity component coming from stable Ce^{+3} ions. The figure is reproduced from *Mazumdar et al. Phys. Rev. B* **46**, *9009 (1992).*

1.7 Conclusions

In the present chapter, we have tried to provide a brief background survey of the topics that directly relate to the main contents of the thesis discussed in the subsequent chapters. As mentioned in section 1.1, the thesis is based on the experimental investigations performed on a set of RE and transition metals based metallic perovskite compounds. In the present chapter, first of all we have briefly discussed in section 1.2 the main features of perovskite structure and the oxygen-based perovskite compounds. We have then introduced most of the known families of metallic perovskite compounds and briefly discussed their important characteristics. We have also tried to compare some of the main features of oxide and metallic perovskite compounds. As the only magnetic elements present in the materials investigated in this thesis are the rare earth ions, we have discussed the magnetic behaviour of rare earth ions in section 1.3. Observation of NTE and NTCR in ordered crystalline metallic perovskite compounds is one of the main focus area of the thesis. The mechanisms that lead to NTE and NTCR are elaborated in section 1.4 and 1.5, respectively. The phenomenon of valence fluctuations observed in the case of some of the RE elements is discussed in section 1.6.

Chapter 2

Experimental techniques and their basic principles

2.1 Introduction

In this chapter, a brief description has been presented about the sample preparation techniques used in this work as well as various experimental tools used for their characterization. The underlying theoretical concepts related to some of the experimental techniques are also briefly discussed. All the compounds studied here have been prepared using an argon arc-melting furnace (Centorr Associates Inc.) followed by vacuum annealing. X-ray diffraction measurements have been performed using in house X-ray diffractometers (Rigaku-D/max-2500/PC, Rigaku-Miniflex and Phillips-PW). Magnetic measurements have been performed by a super conducting quantum interference device magnetometer (MPMS-7, Quantum design-Inc., USA). Transport (electrical resistivity and magnetoresistance) measurements have been performed in a liquid-He cryostat (Oxford Instruments, UK) consisting a superconducting magnet (Oxford Instruments, UK). Temperature dependent Eu-Mössbauer measurements were performed is a close-cycle refrigerator based setup using SmF_3 source.

2.2 Preparation of intermetallic compounds

The compounds investigated in this thesis have been prepared by melting the stoichiometric amount of high purity ($> 99.9\%$) constituent elements in an argon arc-melting furnace (Centorr Associates Inc.). In most of the cases we were succeeded in preparing a regular cylindrical rod-shaped samples [Fig. 2.1] using an indigenous home-made die.

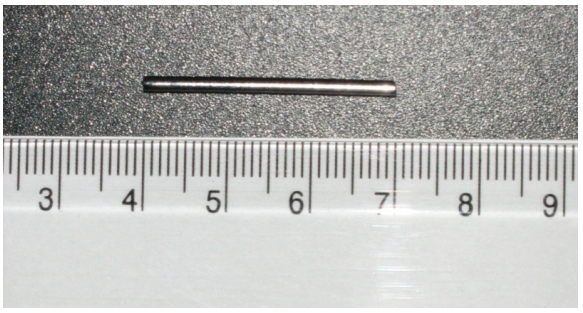

FIGURE 2.1: The rod of a metallic sample prepared in arc furnace using the die described in section 2.2.2. The approximate length of the rod is 30 mm.

The cylindrical rod shape of the sample is very useful for magnetization and resistivity measurements as it minimizes the effect of demagnetization factor in magnetization data as well as reduces the errors in resistivity values due to more accurate measurement of shape parameters. The detailed description of sample preparation procedures related to specific samples will be presented in the respective chapters. Basic features of argon arc-furnace and the design of indigenous die to prepare circular rod-shaped samples are discussed below.

2.2.1 Argon arc-furnace attached with vacuum set-up

Figure 2.2 shows a representative block diagram of the arc-melting furnace setup used in the sample preparation process. Main brass body of the furnace, DC-power supply (not shown in the figure), copper hearth and resistance box (not shown in the figure) attached with electrodes are cooled using a chilled water circulation system (not shown in figure). Constituent elements are placed on the copper hearth (part 13, Fig. 2.2) and inserted in the quartz chamber (part 5, Fig. 2.2). The quartz chamber is first evacuated with the help of a vacuum pump (attached to part 7, Fig. 2.2) and then purged several times by filling argon gas purified by a guttering furnace (attached with part 19, Fig. 2.2), and subsequent flushing using the same vacuum pump. This procedure was repeated several times. After the purging is over, vacuum pump is disconnected using vacuum locks (parts 6 and 8, Fig. 2.2) and a steady flow of argon is maintained through the quartz chamber. Argon outlet pipeline (part 20, Fig. 2.2) is connected to the top of the brass structure (part 3, Fig. 2.2) and attached with a one-way gas valve (Part 15, Fig. 2.2). One-way gas valve prevents any gaseous impurity from the atmosphere entering in the melting chamber. The argon gas comes out from the quartz chamber and passes through two cylindrical glass chambers (part 16, Fig. 2.2) and finally detected in the oil kept in second glass chamber (part 17, Fig. 2.2). With the help of this arrangement one can visually see the outflow of the argon through the speed of bubble formation and regulate it. The melting can be started once a steady flow of argon is achieved. In most of

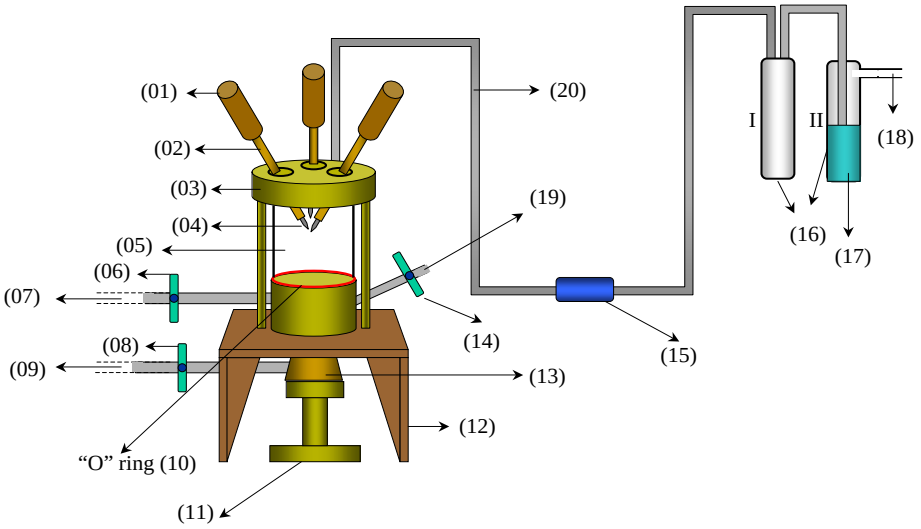

(01) Wooden handle	(06) Vacuum lock	(11) Support to hearth	(16) Glass chambers
(02) Copper electrode	(07) To vacuum pump	(12) Wooden stand	(17) Oil or water
(03) Brass structure	(08) Vacuum lock	(13) Copper hearth	(18) Gas outlet
(04) Tungsten tips	(09) To vacuum pump	(14) Gas lock	(19) Argon inlet
(05) Quartz chamber	(10) "O" ring	(15) One way valve	(20) Metal pipeline

FIGURE 2.2: Schematic diagram of argon arc-furnace used in the preparation of the compounds investigated in this work. The individual important parts of the setup have been indicated below the figure.

the cases, the melting was performed using electrode current values ranging 50 to 200 Amperes. At first the constituent elements are melted using a normal copper hearth. The resultant irregular button shaped compound is then used for casting the rod-shaped samples.

2.2.2 Design of the die for preparation of circular rod-shaped samples

A representative picture depicting design of the home-made die used for rod-shaped sample preparation is shown in Fig 2.3(a) [158]. Cross-sectional view of the same is presented in Fig. 2.3(b). The body of the die can be divided in to three separable parts; top, middle and bottom, marked as T, M and B respectively in Fig. 2.3(b). As cast button of the material synthesized using the arc-furnace described in section 2.2.1, is placed on the sample stage and then the die is placed inside the quartz chamber. Most of the bottom part of the die and the vacuum pump connector remain out of the quartz chamber. After the die is properly placed, a vacuum line is connected to the die through part 9 [Fig. 2.2]. Now there are two connections with the vacuum pump − one directly connected to the quartz chamber and another to the die. Once the die is mounted and the vacuum lines are connected, purging is performed in the similar fashion as discussed in the previous section. After purging quite a few times, the vacuum pump is kept

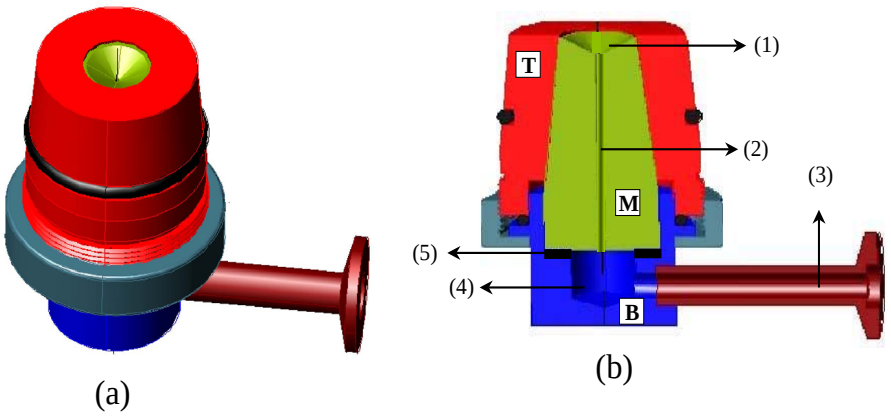

FIGURE 2.3: A representative picture of the copper die used for preparation of circular rod-shaped metallic samples. (a) Full view (b) Cross-sectional view.

running but disconnected with the quartz chamber and the die using the vacuum locks (parts 6 and 8 in Fig. 2.2). Now the argon flow is maintained and the setup is left for approximately half an hour so that a good vacuum gradient is build-up just out side the vacuum connector of the die. As mentioned in the previous section, chilled water circulation is used for cooling down the various component of melting furnace and metallic die.

Now the setup is ready to cast rod-shaped sample. The button is melted using a bit high electrode current. In a few cases, the molten sample flows immediately in to the cylindrical hole and gets solidify in the form of a shiny cylindrical rod. However, in many cases the surface tension of the molten phase (the tendency to remain in the spherical shape) is sufficiently high to counter the effect of gravity. In such cases we need to use the vacuum gradient present just out side the vacuum lock (part 8 in Fig. 2.2) to suck the sample inside the cylindrical hole. This id done by quickly opening the vacuum lock. Excess amount of the sample flows in to the available hollow space in the bottom part of the die [Fig. 2.3(b)]. As an example, a picture of the rod-shaped sample casted using this arrangement is shown in Fig. 2.1. The cylindrical samples of various diameters can be casted using the separate middle parts of the die having different diameters of the cylindrical hole. The rod shown in figure 2.1 is of 1.9 mm diameter and approximately 30 mm in length.

2.3 Structural characterization

Structural characterization of the compounds was performed by non destructive powder X-ray diffraction (XRD) technique. A typical wave length of X-rays is of the order of a few Angstroms. This makes it suitable for probing the crystals of the compounds comprised of atoms of nearly the same dimensions. In the course of this work, the basic room temperature XRD measurements to check the phase formation were performed in Phillips-PW and Rigaku-Miniflex X-ray diffractometer. More specific and temperature dependent measurements were performed in Rigaku-D/max-2500/PC high resolution powder X-ray diffractometer, which based on a rotating anode X-ray source in the temperature range 12-300 K. This diffractometer operates in the Bragg- Brentanno geometry. It is fitted with a curved crystal monochromator in the diffraction beam which enables the detection of even very weak reflections. A He close-cycle refrigerator based attachment supplied by Rigaku was used for varying the sample temperature. Most of the temperature dependent measurements were carried out at 8 kW generator power, which was found adequate for resolving some very low intensity peaks appearing at low angles in the compounds investigated in this work. Different scan speeds were used according to the need of the specific measurements. The step interval was kept fixed at 0.02 degrees in most of the measurements. FullPROF package [159] was used for powder pattern simulations and powder XRD data refinement by Le-Baile and Rietveld refinement techniques. The Bragg's diffraction relation, which is the basic principle for the operation of X-ray diffractometers, is described below.

2.3.1 Bragg's Law

Bragg's law is one of the most fundamental principles of X-ray crystallography and widely used in XRD and neutron diffractions studies. This law is named after *Sir William Lawrence Bragg* and his father *Sir William Henry Bragg*, who were awarded *Nobel prize* in 1915 for their pioneering work.

According to Bragg's law, the condition for constructive interference between the x-ray beams diffracted from crystal planes [Fig. 2.4] is,

$$n\lambda = 2dsin\theta \tag{2.1}$$

where n is the integer defining the order of diffraction, λ is the wave length of X-rays or neutrons, d is the spacing between the crystal planes of the crystalline lattice of the material and θ is the angle between the incident ray and the scattering planes. d is the

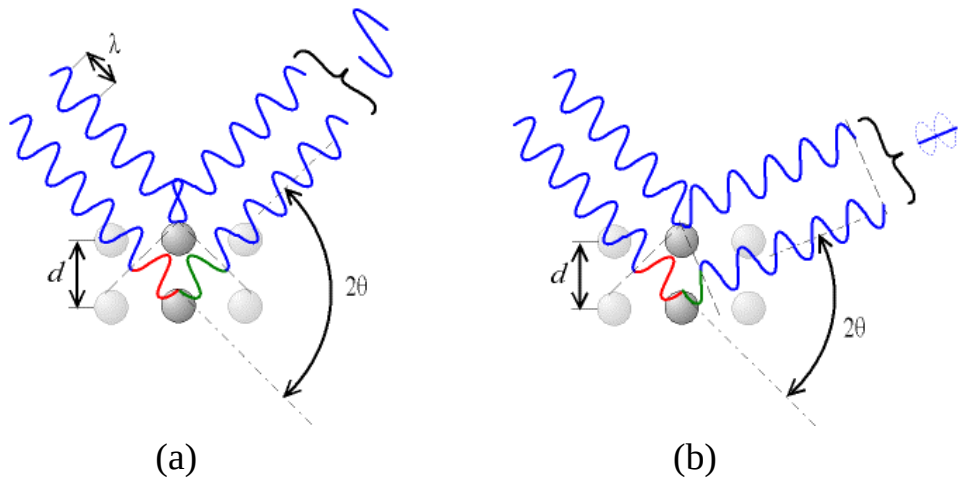

FIGURE 2.4: A cartoon depicting the conditions of (a) constructive and (b) destructive interference of X-rays in a crystalline material. The picture is reproduced from English wikipedia.

intrinsic property of the crystalline material under investigation whereas λ and θ are tunable parameters.

2.3.2 Diffraction methods and powder X-ray diffraction technique

Phenomenon of X-ray or neutron diffraction occurs only when the condition of Bragg law, given in equation (2.1), is satisfied. It is not very straight forward to satisfy the stringent condition of Bragg's law for any given single crystal. For example, for any monochromatic radiation and for a known crystal plan and spacing, it is extremely difficult task to perfectly set the crystal orientation to get any diffracted beam. One way to satisfy this condition is the continuous variation of λ or θ over a wide range of values. A beam of white radiation (a continuous spectrum from X-ray source) is used for varying the λ. Variation in θ is achieved by rotating the single crystal or using powder specimen [160].

There are basically three different experimental methods for studying the diffraction phenomenon. **(i) Laue method:** λ is variable and θ is fixed, **(ii) Rotating-crystal method:** λ is fixed and variation of θ through rotation of the single crystal, and **(iii) Powder method:** λ is fixed and θ is variable due to random orientation of the tiny crystals.

In this study, we have used versatile powder diffraction technique to analyse the crystal structure of our polycrystalline compounds. Indeed, the powder technique is the only available diffraction method for structural investigations of polycrystalline materials.

Other methods, e.g. Laue and Rotating-crystal method, can only be used in the case of single crystals. In the powder diffraction technique, polycrystalline compound under investigation is reduced to very fine tiny particles, may be of the size of few microns. Each such fine particle is made-up of several tiny single crystals randomly oriented in all possible directions. Thus the assembly of these fine particles produce the effect of a single crystal having gone through all the possible rotations along all the possible axes. Due to such a random distribution of crystals, for any particular lattice plane there will be a number of tiny single crystals oriented in such a fashion that Bragg's diffraction condition would satisfy for specific values of 2θ. Hence, every lattice plane would produce diffraction phenomenon.

2.4 Transport measurement

We have carried out temperature and applied magnetic field dependent electrical resistivity and magnetoresistance measurements on rod shaped samples [Fig. 2.1] using four probe technique. The details are described below.

2.4.1 Electrical resistivity

Electrical resistivity (ρ) measurements were performed using a conventional four-probe method [Fig. 2.5]. In this method, current is supplied through two outer leads while the voltage is measured across two inner leads. This method is of particular importance for ρ measurement of low-resistance materials, e.g. metals and metallic compounds etc., as it eliminates the contribution from contact resistance which may be sometimes even higher than the actual resistance of the specimen. The ρ of any material is defined as,

$$\rho = R\frac{A}{L} \tag{2.2}$$

where A and L are the cross-sectional area and the distance between two voltage leads respectively. R is the electrical resistance defined as, $R = (V^+ - V^-)/I$.

The measurements were performed in a commercial cryostat purchased from Oxford Instruments. In this cryostat system, by pumping the He the temperature of the sample space can be lowered down to ~ 1.5 K. The data were taken using a home-made indigenous sample insert [Fig. 2.6(a)], where total 22 samples can be mounted at time and data can be collected for 8 samples simultaneously [161]. A calibrated Cernox sensor is used for the measurement of sample space temperature. The electrical connections between

the sample insert and various electronic devices. e.g. nano voltmeter (Keithley-2182), current source meter (Keithley-2400), temperature controller (Lakeshore-DRC93CA), Switching system (Keithley-7002) and scanner cards (Keithley-7056 and Keithley-7168) etc. have been shown in Fig. 2.6(b). To eliminate the effect of thermo-emf generated due to temperature gradient across the sample (if any), the voltage across the connecting voltage leads were also measured by reversing the direction of the current.

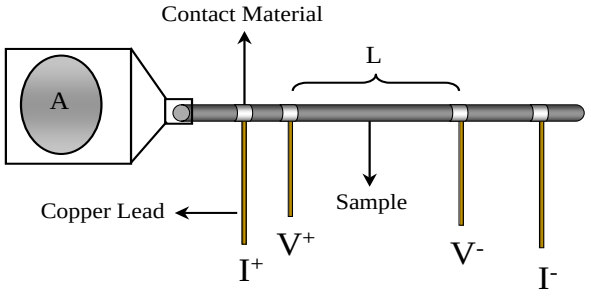

FIGURE 2.5: Leads contact scheme in the four-probe method. The length between two voltage leads has been marked as 'L' while the cross-sectional area has been indicated as 'A'.

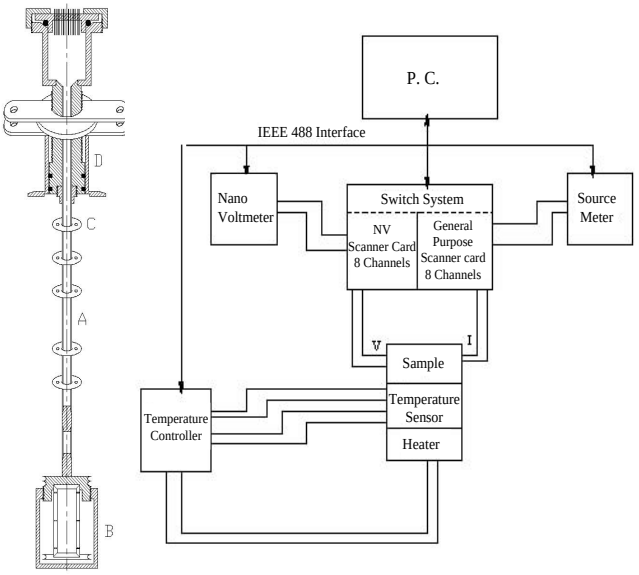

FIGURE 2.6: (a) Schematic diagram of the sample insert used for resistivity and magnetoresistance measurements. (b) A block diagram of the circuitry of the measurement setup. Electrical connections to only one sample has been shown in the figure.

2.4.2 Magnetoresistance

Measurements of magnetoresistance, which is the measure of change in resistivity upon application of an external magnetic field, were also performed by conventional four-probe

method [Fig. 2.5] as discussed in the previous section. Depending upon the requirement of particular measurements, the DC-magnetic field generated by the superconducting magnet was varied in the range of 0-7.5 T. The direction of the external field, which is always parallel to the axis of the cylindrical cryostat, was varied in both positive (upward) and negative (downward) directions.

2.5 Magnetic measurement

Temperature and field dependent DC and AC magnetic measurements were performed for the magnetic characterization of the compounds. These measurements were carried out using a Superconducting QUantum Interference Device (SQUID) magnetometer (MPMS-7, Quantum design-Inc., USA). Most of the measurements were performed in the temperature range 2-300 K.

2.5.1 DC-magnetic measurements

SQUID-magnetometer is the most sensitive (sensitivity $\sim 10^{-15}$ T) device for magnetic measurements and can be easily operated up to the field of ~ 7 T. Liquid-He was used for achieving low temperatures during the measurement. Two block-diagrams of the SQUID-magnetometer, first depicting the main components of the setup and second showing the basic circuitry, have been shown in figures 2.7 and 2.8 respectively. The magnetometer contains various superconducting components, e.g. SQUID, superconducting magnetic shield surrounding the SQUID, superconducting magnet and a superconducting detection coil [Fig. 2.7 and 2.8]. A brief description of the superconducting components, that together constitute the most important part of the magnetometer operation, is presented below.

(i) SQUID: The sensitivity of the magnetometer depends entirely upon SQUID, which is a very small device connected in detection circuit. SQUID contains a few Josephson junctions in a closed superconducting loop [162, 163]. The Josephson effect exhibited by Josephson junctions [162] is the phenomenon of tunneling across two weakly coupled superconductors, separated by a very thin insulating barrier. This effect is named after British scientist *Brian David Josephson*, who received the *Nobel prize* in 1973 for this pioneering discovery. In a Josephson junction, the phase of electron wave function in one superconductor maintains a fixed relationship with the phase of the same in another superconductor. This linking up of phase is called *phase coherence* or phenomenon of *quantum interference* [164]. The magnitude and phase of oscillating Josephson current

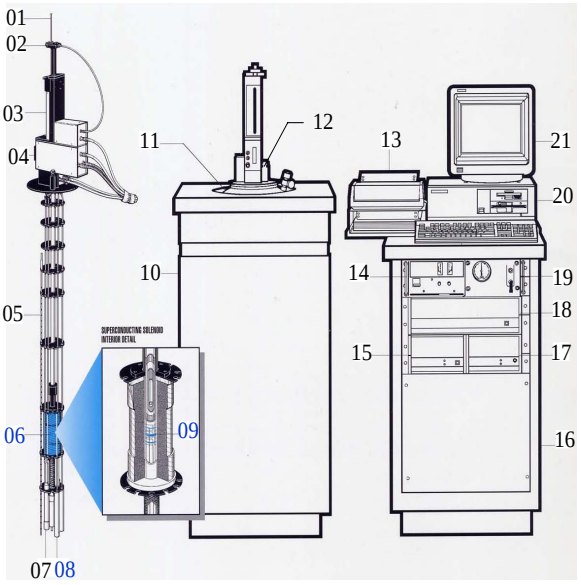

(01) Sample Rod
(02) Sample Rotator
(03) Sample Transport
(04) Probe Assembly
(05) He Level Sensor
(06) Superconducting Solenoid
(07) Flow Impedance
(08) SQUID Capsule with Magnetic Shield
(09) Superconducting Pick-up Coil
(10) Dewar Isolation Cabinet
(11) Dewar
(12) Liquid-He Inlet
(13) Printer
(14) Magnetic Power Supply
(15) Temperature Controller
(16) Console Cabinet
(17) Power Distribution Unit
(18) MPMS Controller
(19) Gas/Magnet Control Unit
(20) Computer
(21) Monitor

FIGURE 2.7: Schematic diagram of various components of Quantum design SQUID-magnetometer. Superconducting components of the setup are shown in blue. The figure has been taken from the operation manual of MPMS-7, Quantum design-Inc., USA.

flowing across the Josephson junctions depends delicately upon the change of flux of external magnetic field crossing the superconducting ring. The flux of external field is quantized in terms of *quantum magnetic flux*, $\Phi_a = h/2e \sim 2 \times 10^{-15}$ T-m^2, which sets the accuracy limit of the device. It may be mentioned as an example of the accuracy of the instrument, that the strength of the magnetic flux associated with *brain waves* is of the order of 10^{-14} T and hence can it be detected using SQUID magnetometer.

(ii) Superconducting Magnetic Shield: As the SQUID present in the detection circuit is extremely sensitive to the small fluctuations in the magnetic field, it requires a very efficient shielding from the magnetic fields present around its components. A superconducting shield is employed to provide the requisite shield around the SQUID and its coupling transformers. The operation of SQUID does not necessarily require that the field around its component be extremely small, however it does require that the field inside the shield be extremely stable. Hence one of the main functions of the superconducting magnetic shield is to trap and stabilize the ambient fields present in the laboratory besides providing shielding from large magnetic field generated by the superconducting magnet. The requirement of shield can be appreciated when one considers the magnetic flux produced by a small sample could be even less than a Φ_a, while the magnetic field produced by earth is of the order of a million Φ_a.

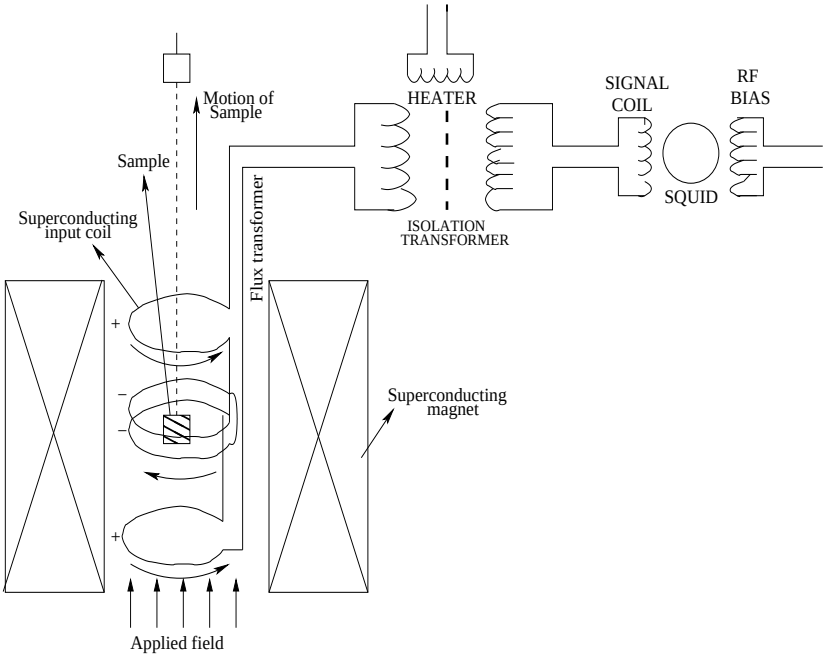

FIGURE 2.8: Block diagram of basic circuitry of the SQUID magnetometer. The figure is based on the scheme given in the operation manual of MPMS-7, Quantum design-Inc., USA.

(iii) Superconducting Detection Coil: Detection coil is a set of three coils made by a single superconducting wire in the form of second order gradiometer placed at the centre of the superconducting magnet outside the sample chamber [Fig. 2.8]. In this configuration, the upper coil is a single turn wound clockwise, the centre coils is made by two turns wound in counterclockwise direction while the bottom coils is again single turn wound in the clockwise direction. This configuration of the detection coil helps to reduce the noise and background drift in the detection circuit generated due to fluctuations and relaxation of the field of superconducting magnet. If the magnetic field is relaxing uniformly then the flux change in clockwise wound top and bottom coils gets exactly canceled with the flux change of counterclockwise wound centre coils.

(iv) Superconducting Magnet: The superconducting magnet is made of superconducting wires wound in solenoidal configuration in a completely closed loop. This configuration enables it to operate in a *persistent mode* without using any external power supply. A persistent current switch, which is basically a heater, is used to turn a portion of the superconducting loop in to a normal state during changing the current flowing across the solenoid. Once the superconducting loop is open by switching the heater on, a power supply is used to charge the magnet at a desired current level. After the charging is over, the persistent current switch is put off. Liquid-He is used for cooling the superconducting wires of the solenoid below their critical temperature.

Measurement Procedure:

The sample under investigation is usually wrapped in a teflon tape and placed in a non-magnetic straw. The straw is then attached to the sample rod and inserted in the sample space. The sample space is purged several times during the sample insertion process. Optimum position of the sample is set by scanning the output signal as function of position of the sample. Once the proper sample position is obtained, the setup is ready for the measurement. The setting up and control of the required magnetic fields, temperatures, time intervals and field-frequencies (in the case of AC measurements) are all performed with the help of a software package provided with the instrument. During the measurements, the sample moves up and down through the detection coils in steps with the help of a stepper motor. Change in the sample position modifies the flux associated with the detection coils and manifests in a change of current flowing in the detection circuit. During the measurement, the sample is stopped at number of positions over the specified length and at each step several reading of the SQUID voltage are collected and then averaged. The voltage as a function of sample position output signal is analysed with the help of fit routines and exact magnetic moment of the sample is determined in terms of emu.

2.5.2 AC-magnetic measurements

AC-magnetic measurement, where an external AC-magnetic field is applied and AC-magnetic response of a sample is measured, is an important tool for characterization of magnetic materials. In contrast to DC-measurements, time dependent induced moments obtained in AC-measurements provide information about magnetization dynamics in the material. AC-susceptibility is defined as slope of the magnetization curve, (dM/dH), and can be expressed in terms of a complex quantity,

$$\chi_{ac} = \chi^{'} + i\chi^{''} \tag{2.3}$$

where, real or in-phase component $(\chi^{'})$ is similar to DC-susceptibility and exhibit magnetic response of the material, while imaginary or out-of-phase component $(\chi^{''})$ shows the dissipative loss in the system. AC-susceptibility measurements were carried in SQUID-magnetometer (described in the previous section). The most of the measurements were performed in frequency range 1 Hz-1 kHz while keeping the magnitude (rms value) of the applied AC-field at 1 Oe.

2.6 Mössbauer Spectroscopy

Nobel Prize winning Mössbauer effect was discovered by *Rudolf Mössbauer* in 1958 [165]. Classically, the Mössbauer effect may be stated as the recoilless emission and recoilless resonance nuclear absorption of a gamma ray. Under normal circumstances, it is not possible to achieve nuclear resonance absorption of gamma ray between an identical pair of emitting nucleus (in excited state) and absorbing nucleus. This is because when gamma ray is emitted from a free nucleus, in order to conserve the momentum taken away by the gamma photon, the nucleus recoils with the an equal and opposite momentum. The energy, E_r, used up in this process of recoil is taken from the emitted gamma photon. Thus the emitted gamma photon would have an energy E_e, which is less compared to excited state energy E_γ ($E_e = E_\gamma - E_r$). A similar consideration is applicable in the process of absorption and therefore, the incoming gamma photon should have an energy $E_\gamma + E_r$, if the resonance absorption has to take place. Thus, there is an over all deficit of $2E_r$ in the gamma energy with respect to energy required to achieve resonance. If this deficit ($2E_r$) is larger than the nuclear excited state level width (which is the case for a free nucleus/atom) then, resonance absorption cannot take place.

In the phenomenon of Mössbauer effect, both the emitter and the absorber nuclei are not free but embedded in a solid. In such a case, the whole recoiled momentum is distributed in entire solid. It may be mentioned that even a sample of very small dimension contains about 10^{20} atoms. Hence the recoil energy, which would be distributed among all such atoms, would be less by the same factor and becomes almost negligible compared to the excited state line width. Under such condition, resonance absorption can readily take place. Quantum mechanically, recoil would mean excitation of phonons. A recoilless emission and absorption is therefore a process with zero phonon excitation. It can be shown that there is a non-zero probability for zero phonon excitation process. This probability is called the 'f-factor' or Lamb-Mössbauer factor and can be expressed by,

$$f = \exp\left[\frac{-6E_R}{k_B\Theta_D}\left\{\frac{1}{4} + \left(\frac{T}{\Theta_D}\right)^2 \int_0^{\Theta_D/T} \frac{xdx}{e^x - 1}\right\}\right] \tag{2.4}$$

where Θ_D is the Debye temperature of the material and E_R is the recoil kinetic energy of the lattice. At any given temperature, the f-factor and hence the resonance absorption will be significant if the temperature is less compared to the Debye temperature of the solid in which the nucleus is embedded. Thus, one would get a better Mössbauer absorption at room temperature if the Debye temperature of the host lattice is large. The line shape of the resonance is the overlap integral of emission line shape and absorption

cross section. For a thin absorber, assuming that line width of source and absorber are same, it is given by the Lorentzian relation,

$$I(E) = \frac{\Gamma}{2\pi} \frac{1}{(E - E_0)^2 + (\Gamma/2)^2} \tag{2.5}$$

where E_0 is the resonance energy and Γ is twice the full width at half maximum of the γ-ray energy distribution.

The resonance absorption process described above assumes that the emitting and absorbing nuclei are under identical environments. Under normal circumstances, the energy levels shift/split due to hyperfine interactions (interaction of nucleus with electrons of the ion) and the extent of shift and splitting would be different in source and absorber. If this difference is greater than the line width of the resonance, again one would not achieve the resonance. However, this shift in resonance energy would usually be of the order of a few line widths and the resonance condition can be brought back by means of *Döppler shift* produced by moving either the source or the absorber with a velocity, v, relative to each other. The velocity required to produce a shift of energy ΔE is $E_\gamma(v/c)$ where c is the velocity of light. This feature of varying the energy in a controlled manner with a resolution of about 10^{-8} eV makes Mössbauer effect as a research tool and provides a means of studying the hyperfine interactions in solids.

Due to considerations of energy of γ-ray [1], life time of parent nucleus producing the Mössbauer nucleus in excited state, line width of Mössbauer γ-ray [2], abundance of Mössbauer isotope *etc.,* Mössbauer spectroscopy can be performed only in certain favorable isotopes of certain elements. ^{57}Fe, ^{119}Sn and ^{151}Eu are amongst them and are convenient to study.

2.6.1 Hyperfine interactions

The hyperfine interactions occurring between the nucleus and the electrons of the atom have been reasonably understood [166]. The three most common and dominant terms of the interactions and the modification of the nuclear energy level under these interactions are given below.

(i) Electric monopole interaction:

Electric monopole interaction arises due to interaction of nuclear charge with the *s*-electron density at the nucleus [3]. It also arises because of the non-zero and different

[1] For $E_\gamma >\sim$100 keV, f-factor would be very small at room temperature

[2] Narrow line widths make experiments difficult and large widths makes resonance insensitive

[3] It can be shown that only *s*-electrons have non zero density at the nucleus

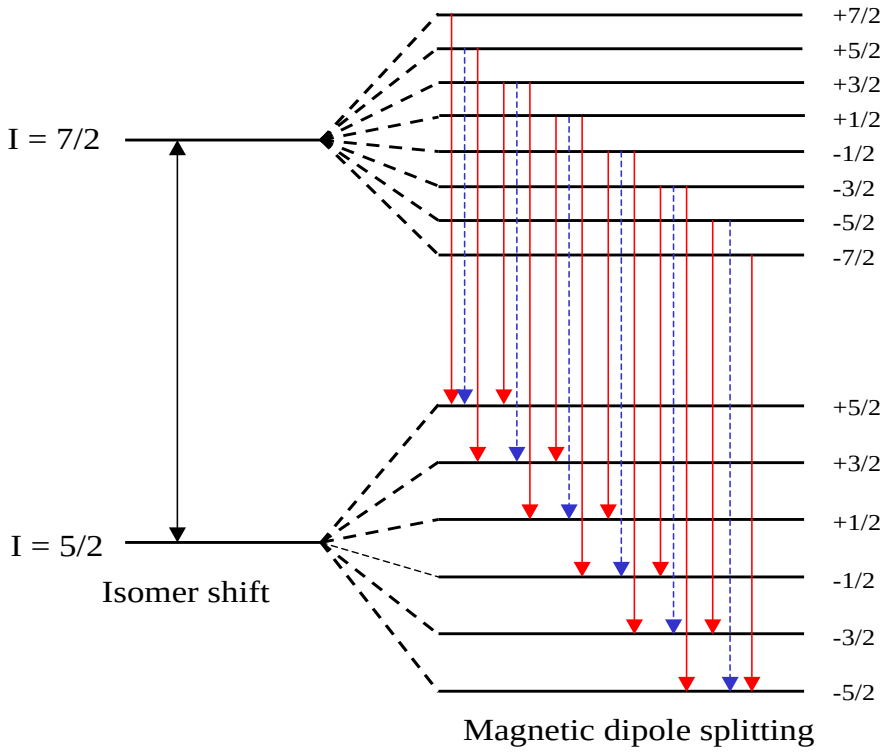

FIGURE 2.9: Schematic representation of the nuclear level scheme and allowed transitions in ^{151}Eu-Mössbauer spectrum. The possible transitions represented by solid lines are for $\Delta m = \pm 1$ and the same represented by dashed lines are for $\Delta m = 0$.

spatial extent of the nucleus in the ground state and in the excited state. This interaction causes a shift in both ground state as well as excited state levels. The shift would be different in source and absorber if they have different chemical environments. The net shift in resonance position is given by,

$$\delta = \frac{2}{3}\pi Z e^2 \{|\psi_A(0)^2|^2 - |\psi_A(0)^2|^2\}\{\langle R_e^2\rangle - \{\langle R_g^2\rangle\} \tag{2.6}$$

where $\langle R_e^2\rangle$ and $\langle R_g^2\rangle$ are the root mean square radii of excited and ground states, $\psi_S(0)$ and $\psi_A(0)$ are the non-relativistic Schrödinger wave functions of the s electrons at absorber and source nuclei, respectively. Since this energy difference or the shift in resonance originates from the s-electrons, which depends on the chemical state or valence state, this shift is termed as *chemical shift* or *isomer shift* (IS). The energy level scheme corresponding to this interaction is shown in Fig. 2.9. Thus, in the Mössbauer spectrum of materials with different chemical state, *e.g.*, the spectrum of Eu_2O_3 obtained using a ^{151}Eu source in EuF_3 host, a single resonance line at a position away from zero velocity would be observed. The isomer shift is one of the most useful parameter for investigating the phenomenon of valence fluctuations in Eu- based materials.

(ii) The magnetic dipole interaction:

Under a magnetic field, the nuclear energy levels, both the ground state and excited state get split due to magnetic dipole interactions. The interaction energy is given by the relation,

$$E_M = -\mu H m_I / I = -g\mu_N H m_I \tag{2.7}$$

where μ is the magnetic dipole moment of nucleus, H is the magnetic field at the nucleus, g is the nuclear Lande-factor, μ_N is the nuclear Bohr magneton, I is the nuclear spin quantum number, and m_I is the magnetic quantum number (with values from $-I$ to $+I$). The schematic representation of energy level scheme under magnetic hyperfine field for the case of ^{151}Eu is shown in Fig. 2.9. The transitions follow the selection rule, $\Delta m = 0, \pm 1$. In the case of ^{151}Eu, which is of our interest, there are 18 allowed transitions. However, because of overlapping of different lines, normally, one observes 8 lines in a magnetically split Eu-Mössbauer pattern. Internal field generated at the Eu nucleus of a magnetically ordered system is mainly from the local moment on Eu ion and usually one gets a well resolved magnetically hyperfine split spectrum. The extent of line splitting represents the strength of the magnetic hyperfine field at the Mössbauer nucleus.

(iii) The electric quadrupole interaction:

It can be shown that electric dipole term does not exist in the expression for hyperfine interaction. The next order electric term is the quadrupole interaction which is an interaction between the quadrupolar moment of the nucleus (ground state and/or excited state) and an electric field gradient (EFG) present at the nucleus. The interaction term is given by the relation,

$$E_Q = \frac{e^2 qQ}{4I(2I-1)}\left[3m_I^2 - I(I+1)\right]\left(1+\frac{\eta^2}{3}\right)^{\frac{1}{2}} \tag{2.8}$$

where Q is the nuclear quadrupole moment, and η is the asymmetry parameter of the EFG tensor, given by

$$\eta = \frac{V_{xx} - V_{yy}}{V_{zz}} \tag{2.9}$$

where V is the electrostatic potential. Customarily, the principal axis of the system is defined in such a way that $V_{zz} = eQ$ is the maximum value of field gradient. In

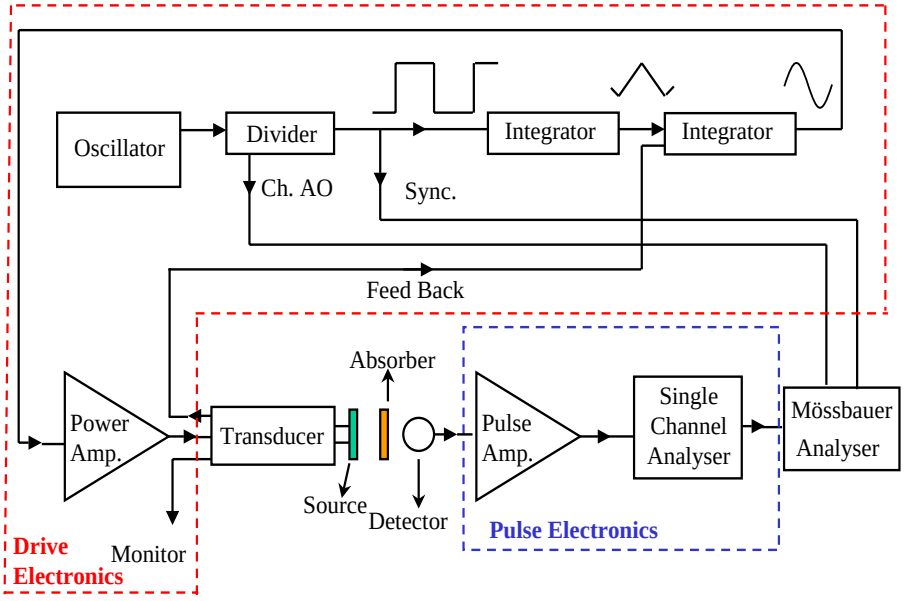

FIGURE 2.10: Block diagram of the circuitry of a typical Mössbauer setup.

most of the cases of ^{151}Eu, due to the weak quadrupolar interaction of Eu nuclei in comparison to the line width, the effect of quadrupolar interaction is observed only as an asymmetry in the line. Often, quadrupolar interaction is a perturbation compared to magnetic interaction. In such a case, the interaction energy is an algebraic addition of the energies due to the two interactions. If the two interactions are comparable, then the Hamiltonian will have to be appropriately solved. Numerical solutions for standard cases are available in literature [167].

2.6.2 Experimental setup for recording Mössbauer spectrum

The schematic diagram of the Mössbauer spectrometer is shown in Fig. 2.10. A close-cycle He-cryostat was used for cooling the system during measurements. ^{151}Eu in EuF_3 matrix as $^{151}SmF_3$ has been used as source material. The Mössbauer source is mounted on the shaft of the Mössbauer drive, also known as transducer [Fig. 2.10].

For recording the Mössbauer spectrum of any specimen (or absorber), at first the material is pulverized in the form of very fine powder and then spread uniformly on an aluminum foil or a thin metal-free adhesive tape. The specimen is mounted in between the source and the detector. The thickness of the absorber (expressed in mg/cm^2) should have an optimum value. Though increasing thickness increases Mössbauer absorption, it also reduces the intensity of transmitted gamma rays thereby reducing the signal. The optimum thickness of the specimen can be calculated from the known *characteristic absorption thickness* of the individual elements present in the absorber. The gamma

rays from the source after passing through the absorber are detected by the detector (usually a gas proportional counter or a thin NaI(Tl) scintillation detector). The source is moved at different precisely controlled velocities by the drive and a 'spectrum' of the counts are obtained a function of velocity. The resonance position and the line shape gives the required information on the hyperfine interactions taking place in the solid (section 2.6).

One of the most important constituent parts of the spectrometer is the Mössbauer drive, which is an electromagnetic system, effectively, formed out of a pair of mechanically coupled (along the axis) loud-speakers but without their diaphragms. One of them (the driving coil) is for achieving the motion and the other (the pick up coil) is for monitoring the motion and stabilizing the motion through feedback electronics. The drive is operated in constant acceleration mode in which the velocity varies linearly with time. It can be easily shown that the voltage wave form that one must feed to the drive coil to achieve a linear velocity is a parabola. Hence, sometimes this type of drive is also called a parabolic drive. In this system, the velocity is scanned through a cycle, $\mathrm{V}_{max} \rightarrow 0 \rightarrow -V_{max} \rightarrow 0 \rightarrow V_{max}$. The Mössbauer data is recorded in an electronic data collection system, known as multi scaler analyzer.

The electronics for the Mössbauer spectrometer consists of three major parts, the drive electronics, the nuclear electronics and the data acquisition system. In order to maintain synchronism of the drive with respect to data collection, the parabolic wave form ($\sim$10 Hz) to drive the transducer is derived from the clock pulses (from a crystal controlled oscillator, for stability in time) of the multichannel analyzer of the data acquisition part. The frequency of drive is chosen to match with the mechanical response of the transducer and the response of the data acquisition system.

Once the transducer is set into motion, a voltage would be induced across the pick-up coil which would be proportional to the velocity of the drive at any instant of time. This signal, which is a triangular wave form, is fed back to the circuit for comparison with the triangular wave form which in turn would produce the driving parabola. Appropriate feed back circuitry takes care of the stability of the velocity wave form, i.e., a precise linear variation of velocity with time. A precision and stability of about 1% is usually required to avoid broadening of Mössbauer line. The nuclear electronics [Fig. 2.10] consists of a high voltage ($\sim$600 V) unit to accelerate the photo-electrons in the photomultiplier of the scintillation detector, a pulse amplifier to amplify the pulses arising from detected gamma rays, a single channel analyzer to select only the pulses arising from the Mössbauer gamma rays (21.6 keV for ^{151}Eu), and a scaler to count the pulses.

The data acquisition part, which is also called the multi scaler analyzer, is a circuit block whose functions are as follows. The time period of the Mössbauer drive is divided into a number (usually 512) of smaller time intervals (called channels) so that at each time interval, the change in velocity of the transducer could be considered negligible for practical purposes (say, about 0.1 of the line width of the resonance). The counts originating during each of these intervals are counted in separate 'counters' (also called scalers) of the data acquisition system. The system effectively averages a Mössbauer spectrum over a certain duration of time. The above data accumulation process is carried out till the required statistical accuracy of the spectrum is attained. The statistical accuracy is proportional to $\sqrt{N}$ where N is the number of counts in any given channel.

It may be mentioned that the Mössbauer resonance line widths are of the order of fraction of mm/sec and any vibration of this magnitude will be superposed on the velocity of the transducer and/or the absorber and this will result in line distortion/broadening and the data will be unreliable to that extent. To avoid the effects of such unwanted vibrations, the transducer is kept on a vibration free table. The final data that one gets is the accumulated counts as a function of channel number. The channel number represents velocity. The calibration of channel number in terms of velocity (or energy) is obtained from the Mössbauer spectrum of a known sample. Usually ^{57}Fe resonance of Fe metal is used for this purpose where one gets the standard six line spectrum due to magnetic hyperfine splitting of the energy states of ^{57}Fe nuclei. The separation of the first and last line is known to be 10.6245 mm/sec [168].

Chapter 3

Studies on Gd and Pd based metallic perovskite compounds

3.1 Introduction

As remarked earlier in chapter 1 (section 1.2.2), the $RT_3B_xC_{1-x}$ (R: rare-earth, T: transition metal) compounds are one of the most investigated metallic perovskite compounds. In this chapter, we will discuss the various physical properties of Gd and Pd based metallic perovskite compounds with chemical formula $GdPd_3B_xC_{1-x}$ ($x = 0.25, 0.50, 0.75$ and 1.00) along with the parent binary compound $GdPd_3$. We have attempted to study the structural, magnetic, transport and thermal expansion properties of these compounds. In addition to the experimental investigations, the electronic structure calculations have also been carried out to elucidate some of our observations. The $GdPd_3B_xC_{1-x}$ compounds exhibit novel behavior of negative thermal expansion (NTE) [169], Negative Temperature Coefficient of Resistance (NTCR) [170] and correlated structural, magnetic and transport properties [169–171].

The chapter is primarily divided in eight sections (including the introduction). We have briefly summarized the sample preparation technique and the experimental methods used for various physical properties measurements in section 3.2. In section 3.3, we have discussed the structural characterization of the compounds. The analysis of the temperature dependent powder X-ray diffraction data presented in this section constitutes the basis of the underlying crystal structure of the compounds studied in this thesis.

Some of the contents of this chapter are published in the following articles;
1. Abhishek Pandey *et al. Appl. Phys. Lett.* **92**, 261913 (2008).
2. Abhishek Pandey *et al. Europhys. Lett.* **84**, 47007 (2008).
3. Abhishek Pandey *et al. J. Magn. Magn. Mater.* **321** 2311 (2009).
4. Abhishek Pandey *et al.* (Communicated).

Since the compounds discussed in the other chapters (chapter 4 and 5) also crystallize in the same structure, this analysis is indeed relevant to them as well. We have investigated the thermal expansion behavior of $GdPd_3B_xC_{1-x}$ (x = 0.25, 0.50, 0.75 and 1.00) in section 3.4. The electrical transport properties and results of electronic structure calculations have been reported in section 3.5. In section 3.6, the magnetic and magneto-transport properties of $GdPd_3$ and $GdPd_3B_xC_{1-x}$ have been discussed. In section 3.7, the study of off-stoichiometric metallic perovskite compounds $GdPd_3B_x$ ($x = 0.25, 0.50$ and 0.75) is presented and the results are compared with that obtained in the case of stoichiometric compositions $GdPd_3B_xC_{1-x}$. Finally, a short conclusion of the work is presented in section 3.8.

3.2 Experimental details

The polycrystalline sample of $GdPd_3$, $GdPd_3B_xC_{1-x}$ and $GdPd_3B_x$ were prepared by arc-melting technique described in chapter 2.The highly pure (>99.9%) constituent elements were used for sample preparation. The constituent elements were cleaned thoroughly to minimize any external impurity. At first, surface of yttrium was removed by a fine cleaning bit using DREMEL kit (DREMEL, The Netherlands) to minimize the surface impurities. Before use, the bit was cleaned in an ultrasonic bath. After removing the suface of yttrium, both Y and Pd were cleaned in ultrasonic bath.

The sample chamber was first vacuumed and then a steady flow of argon coming from guttering furnace was maintained for several minutes before the start of melting process. We first thoroughly melted a titanium ball to insure that the argon coming from guttering furnace does not contain any oxygen. The shining surface of melted titanium ball insured for oxygen free argon. The sample was then melted quite a few times after flipping each time to insure proper homogeneity and then casted in the form of a rod of 1.9 mm diameter. The sample was then wrapped in a molybdenum foil and sealed in a quartz tube and then annealed for 240 hours at 1000 ^{0}C to increase the homogeneity.

Structural characterization was performed by powder XRD technique using CuKα radiation on a Rigaku-D/max-2500/PC high resolution powder diffractometer having a rotating anode X-ray source. This diffractometer is fitted with a curved crystal monochromator in the diffraction beam, that enables the detection of even very weak reflections. The powder XRD measurements were carried out in the temperature range 12-300 K. He-close cycle refrigerator based attachment supplied by Rigaku was used for varying the sample temperature. The DC zero field cooled (ZFC) magnetization (M) measurements were carried out in the temperature range 2-300 K at H = 1 kOe applied magnetic field. Isothermal magnetization (hysteresis) measurements were carried out at T = 2 K

by varying the applied field from -7 to +7 T in all quadrants. The AC-susceptibility (χ_{ac}) data were taken in the temperature range 2-30 K and the ac-field amplitude was maintained at 1 Oe. The measurements were performed at four different field frequencies, ν = 1, 10, 100 and 1000 Hz. Resistivity measurements at H = 0 and 7 T were carried out by four-probe method in the temperature range 2-300 K. Magnetoresistance (R_H) measurements were also performed by the conventional four-probe method at four different temperatures, T = 1.6, 4.2, 10 and 40 K by varying the applied dc-magnetic field in the range 0-7 T.

3.3 Structural characterization

As mentioned earlier in chapter 1 (section 1.2.2), $GdPd_3B_xC_{1-x}$ compounds crystallize in a cubic perovskite structure with $Pm\bar{3}m$ space group symmetry [Fig 3.1]. The parent binary compound $GdPd_3$ also crystallizes with the same space group symmetry but the body centre position remains vacant. We have carried out powder X-ray diffraction measurements, both at room as well as at low temperatures, to characterize the samples. The results are discussed in the following section.

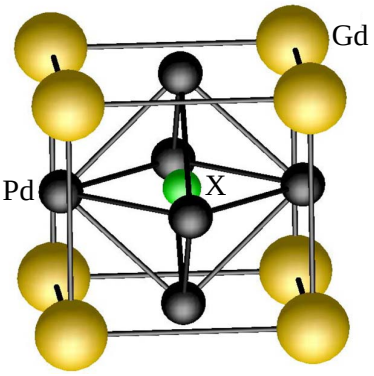

FIGURE 3.1: Schematic representation of the crystal structure of $GdPd_3B_xC_{1-x}$. In the cubic unit cell of the compound, Gd atoms occupy the cube corner positions (0, 0, 0). The face-centre sites (1/2, 1/2, 0) are occupied by Pd atoms and the B and (or) C atoms occupy the body-centre position (1/2, 1/2, 1/2). The atom at the body-centre site (marked by 'X') denotes the position of B and (or) C.

3.3.1 Room temperature powder X-ray diffraction measurements

Figure 3.2 exhibits the room temperature powder X-ray diffraction patterns for $GdPd_3$ and $GdPd_3B_xC_{1-x}$ ($x = 0.25, 0.50, 0.75$ and 1.00) along with Rietveld fits and difference profiles. Although the Rietveld fits appears to be satisfactory, they are not sufficient to rule out any antisite disorder.

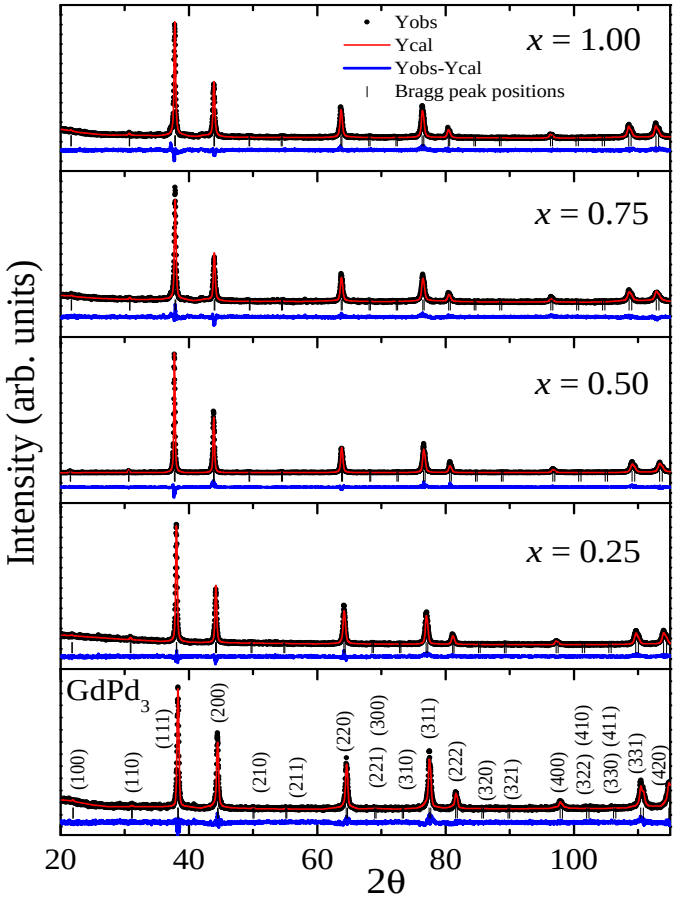

FIGURE 3.2: Room temperature powder XRD patterns of $GdPd_3$ and $GdPd_3B_xC_{1-x}$ ($x = 0.25, 0.50, 0.75$ and 1.00). The experimental data are shown along with the Rietveld fits, difference profile and Bragg positions.

To further probe the quality of our polycrystalline compounds and the presence of any antisite disorder, we performed very slow scan powder XRD measurements with 33% extra power (8 kW) and four times slower scan rates (0.5 degree/min.). These results are shown in figure 3.3 that exhibits the XRD profiles for two extreme compositions; $GdPd_3$ and $GdPd_3B$ along with one intermediate composition $GdPd_3B_{0.50}C_{0.50}$. All the peaks in this figure could be indexed with respect to the cubic unit cell. In principle, $GdPd_3$ may be ordered or disordered with primitive or face centered cubic lattices (fcc), respectively. In the uniformly disordered $GdPd_3$, the space lattice would be fcc for which the permitted reflections are those whose Miller indices correspond to either three odd or three even integers only, but not to odd-even mixed integers. For the ordered $GdPd_3$, the space lattice becomes primitive for which even mixed (*i.e.* both odd and even) integer indices are permitted. In order to verify if $GdPd_3$ is ordered or disordered, we depict in the inset to Fig. 3.3(a), zoomed profile for 2θ range 20 to 32 degrees. The presence of 100 and the 110 cubic peaks in the insets clearly rules out a completely disordered fcc lattice.

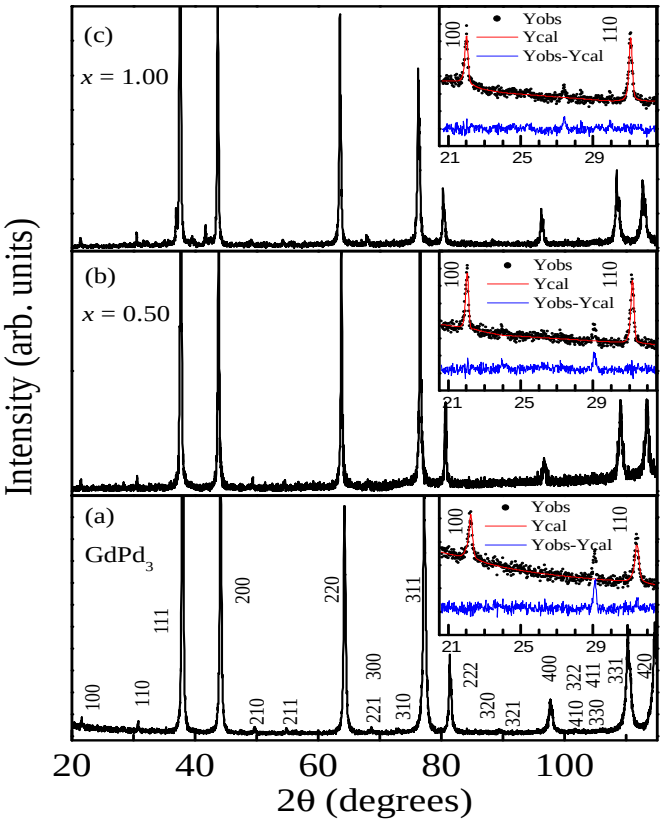

FIGURE 3.3: Powder XRD patterns at room temperature of (a) $GdPd_3$, and $GdPd_3B_xC_{1-x}$ with (b) $x = 0.50$ and (c) $x = 1.00$. The insets in each layer depict low angle primitive cubic peaks ,(100) and (110), on a magnified scale along with Rietveld fits and difference profile.

The simulated powder pattern using $Pm\bar{3}m$ space group for the fully ordered $GdPd_3$ matches very well with the observed one, as can be seen from Fig. 3.4, which depicts the observed and calculated profiles for the 100 and 110 reflections. The results suggest the formation of an ordered $GdPd_3$ compound free from disorder and are in agreement with the reported data for this family of compounds [64]. For the other extreme composition, *i.e.* $GdPd_3B$, the situation is a little complex. In contrast to $GdPd_3$, the space lattice of $GdPd_3B$ shall always be primitive even if Gd and Pd are fully disordered. This is because of the B atom sitting at the body center position of the cubic unit cell. It is evident from figure 3.4(b) that the presence of B modifies the relative intensities of 100 and 110 reflections in the sense that 110 is now stronger in intensity than 100, whereas it was just opposite for the pure $GdPd_3$.

In the case of $GdPd_3B$, intensities of the characteristic primitive cubic reflections (*e.g.* 100 and 110) would be modified drastically by inclusion of even a partial Gd/Pd disorder. We illustrate this in Fig. 3.5, which depicts the simulated powder patterns for $GdPd_3B$ considering the fully ordered (*i.e.* with no cross site substitution) and partially

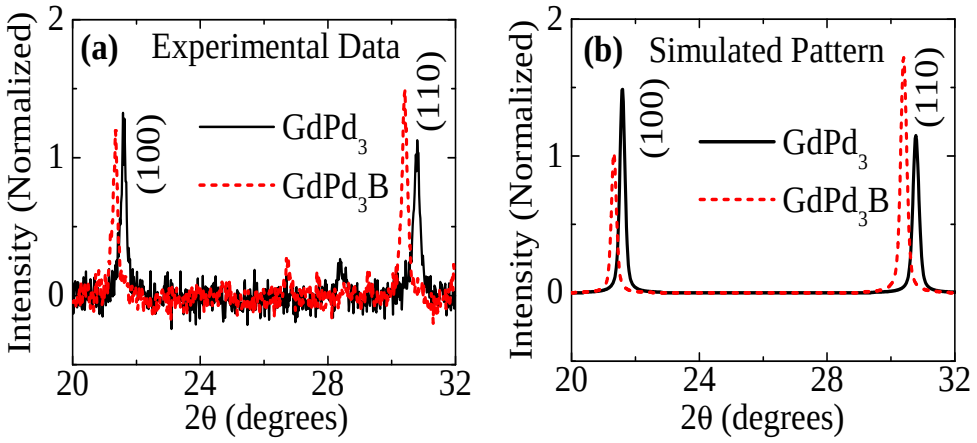

FIGURE 3.4: (a) Experimentally observed (normalized with respect to 111 Bragg peak) powder XRD patterns of $GdPd_3$ and $GdPd_3B$, depicting (100) and (110) Bragg peaks. A polynomial fit has been used to subtract the background. (b) Simulated pattern of the same compounds.

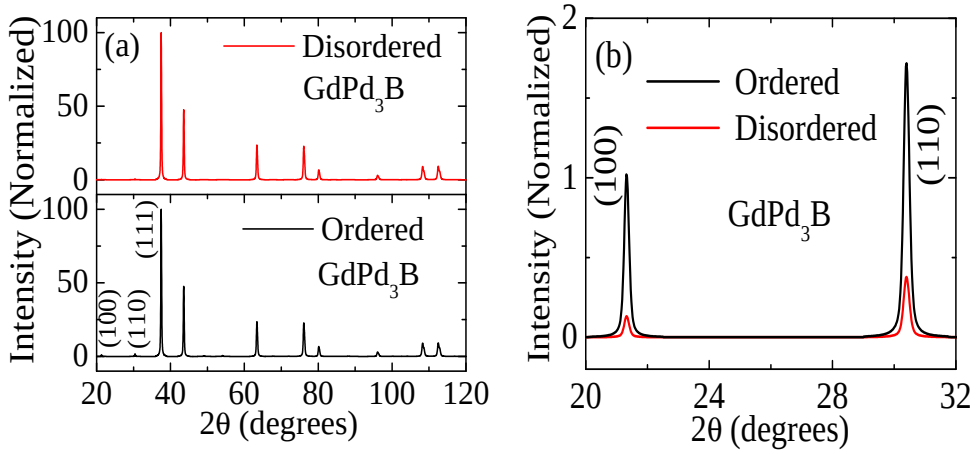

FIGURE 3.5: (a) Simulated XRD patterns of $GdPd_3B$. Bottom row exhibits the pattern with an ordered arrangement. Top row exhibits the pattern of a partial disordered arrangement (where 1/6th of Pd atoms have exchanged their positions with Gd atoms). (b) The same simulated pattern on an enlarged scale to depicting 100 and 110 Bragg peaks.

disordered arrangements of Gd and Pd atoms at the cube corner and face-centered positions, keeping always boron at the body-centered position. In the absence of ordered arrangement of Gd and Pd, the intensities of the two peaks are reduced drastically (from about 1 and 1.5% to about 0.12 and 0.4% , respectively, when one-sixthof Pd atoms have exchanged their positions with Gd atoms). Figure 3.4 compares the observed and simulated profiles for the fully ordered $GdPd_3B$ compound. The agreement between the two profiles is very good in terms of the relative intensities of the 100 and 110 peaks. The presence of Gd/Pd disorder would have reduced the intensities of 100 and 110 reflections well below 0.5%, as can be inferred from Fig. 3.5. We may thus infer that $GdPd_3B$ is

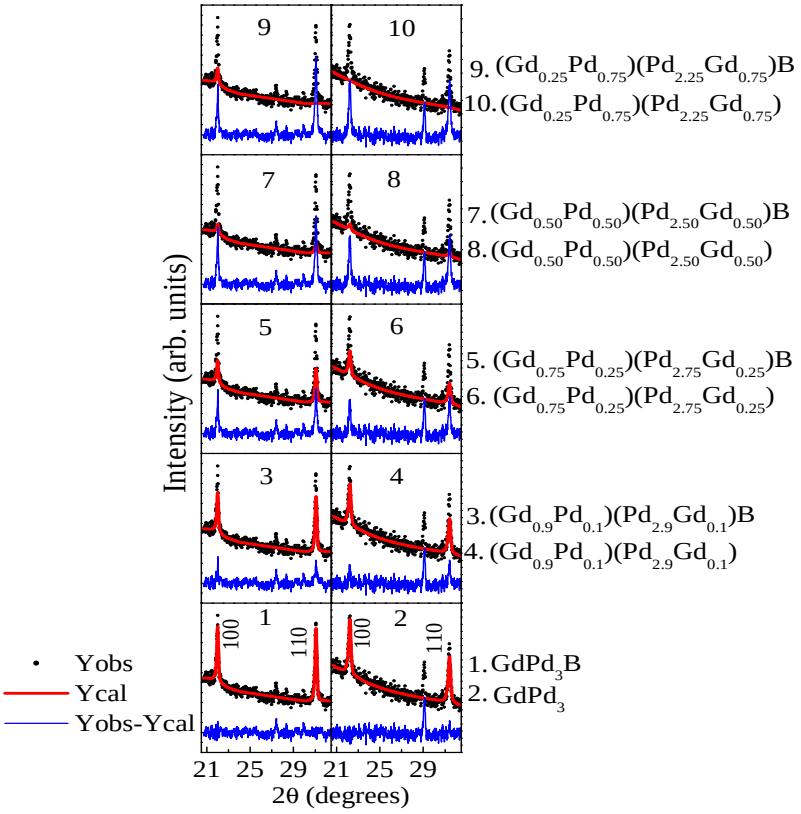

FIGURE 3.6: Observed, calculated and difference profiles of ordered and different disordered arrangements in $GdPd_3$ and $GdPd_3B$.

also ordered. Further, for the intermediate compositions ($GdPd_3B_xC_{1-x}$) also, the 100 and 110 reflections are not only present but their intensities are of the order of 1 and 1.5%, respectively (see Fig. 3.3 for $x = 0.50$), as expected for the ordered arrangement of Gd and Pd atoms.

For a more quantitative confirmation of the ordered arrangement of atoms, we carried out full pattern Rietveld refinements for the ordered (*i.e.* Gd at (0, 0, 0) and Pd at $(\frac{1}{2},\frac{1}{2},0)$, $(\frac{1}{2},0,\frac{1}{2})$ and $(0,\frac{1}{2},\frac{1}{2})$) and partially disordered (*i.e.* $Gd_{1-x}Pd_x$ at (0, 0, 0) and $Pd_{3-x}Gd_x$ at $(\frac{1}{2},\frac{1}{2},0)$, $(\frac{1}{2},0,\frac{1}{2})$ and $(0,\frac{1}{2},\frac{1}{2})$ with $x = 0.10, 0.25, 0.50, 0.75$) arrangements. Figure 3.6 depicts the fits between the observed and the calculated profiles along with the difference profiles, for the (100) and (110) Bragg peaks of two extreme compositions, $GdPd_3$ and $GdPd_3B$. As can be seen from this figure, the fully ordered structure gives the best fits for both the compounds. It is also evident that exchange of even 10% Gd sites with Pd deteriorates the fits considerably, the effect being more pronounced for $GdPd_3B$. With further increase in disorder, the fits worsen drastically. We can therefore conclude that $GdPd_3$, $GdPd_3B$ and $GdPd_3B_xC_{1-x}$ are ordered phases.

We have also performed the total energy and force calculations [172–175] to check the most stable configuration of atoms in the lattice. These calculations suggests that the

minimum energy configuration is achieved only when B/C are in body centered position and Gd/Pd antisite disorder is absent. Movement of B to any other sites, *e.g.* $(\frac{1}{2}, 0, 0)$, is energetically not favorable. In short, we did not find any detectable disorder and antisite movements in these compounds. We can thus conclude that within the limit of the resolution of our XRD measurements ($> 0.2\%$) the $GdPd_3$ and $GdPd_3B$ compounds form well-ordered structures. However, more detailed microscopic characterizations will be helpful to further establish the above-mentioned ordered structure of the compounds.

3.3.2 Low temperature powder X-ray diffraction measurements

We have also carried out low temperature powder X-ray diffraction measurements to investigate the evolution of crystal structure with temperature. The low temperature powder XRD data and calculated Rietveld profiles for $GdPd_3B_xC_{1-x}$ are shown in figures 3.7, 3.8, 3.9 and 3.10, respectively for $x = 0.25$, 0.50, 0.75 and 1.00. In the case of $GdPd_3B_{0.25}C_{0.75}$ [Fig. 3.7], $GdPd_3B_{0.50}C_{0.50}$ [Fig. 3.8] and $GdPd_3B$ [Fig. 3.10] the crystal structure and the underlying symmetries remain conserved down to $T = 12$ K. In contrast, in the case of $GdPd_3B_{0.75}C_{0.25}$, although the structure remains simple cubic with $Pm\bar{3}m$ space group symmetry for $T \geq 50$ K, we observe a redistribution of a few peak intensities below 50 K [Fig. 3.9]. As a result of the redistribution of the peak intensities, we could not obtained any satisfactory Rietveld fit of XRD data using $Pm\bar{3}m$ space group symmetry for temperatures below 50 K. This redistribution of peak intensities can be considered as a signature for the modification of structural symmetries due to some change in the average atomic positions of various constituting elements. The possible underlying reasons for the observed structural modification obtained in the case of $GdPd_3B_{0.75}C_{0.25}$ and there implications will be discussed in the following sections.

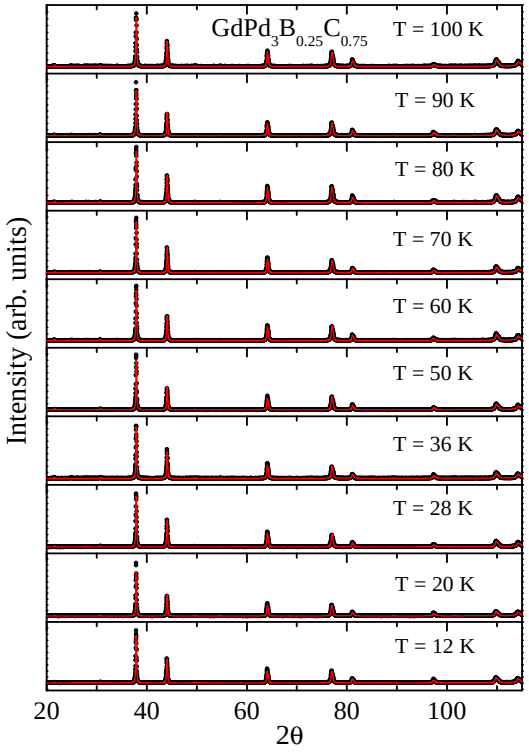

FIGURE 3.7: Observed and calculated powder XRD profiles of $GdPd_3B_{0.25}C_{0.75}$ taken at various temperatures between 12 and 100 K.

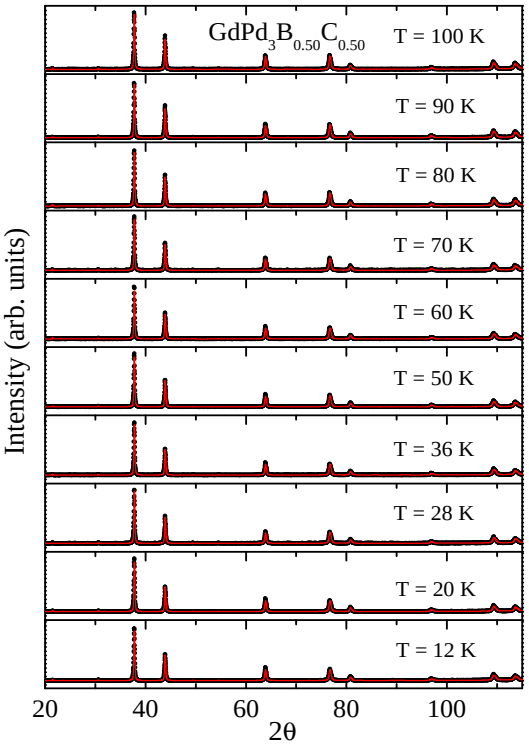

FIGURE 3.8: Observed and calculated powder XRD profiles of $GdPd_3B_{0.50}C_{0.50}$ taken at various temperatures between 12 and 100 K.

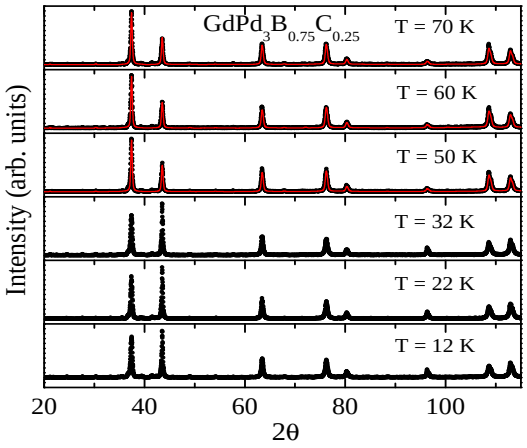

FIGURE 3.9: The powder XRD profile of $GdPd_3B_{0.75}C_{0.25}$ taken at six different temperatures. The calculated profiles are shown for T = 50, 60 and 70 K. The powder XRD profiles below 50 K exhibit redistribution of a few peak intensities.

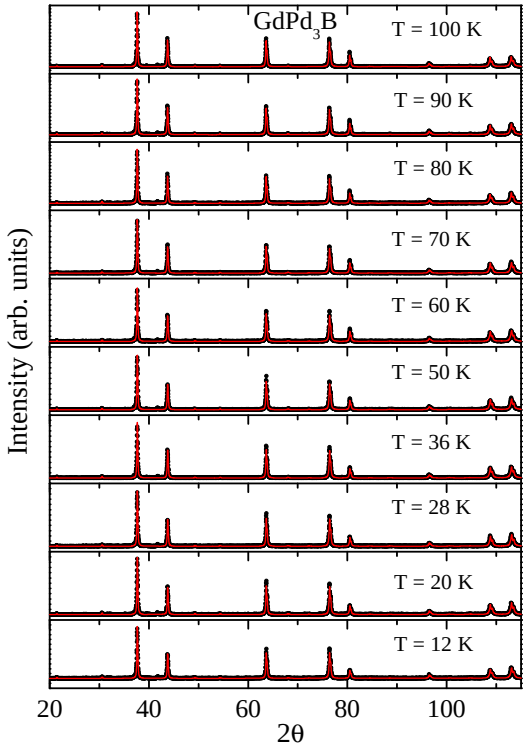

FIGURE 3.10: Observed and calculated powder XRD profiles of $GdPd_3B$ taken at various temperatures between 12 and 100 K.

3.4 Thermal expansion behavior of $GdPd_3B_xC_{1-x}$ ($x = 0.25$, 0.50, 0.75 and 1.00)

As mentioned earlier in chapter 1 (section 1.4), negative and zero thermal expansion materials [109] have attracted enough attention after the discovery of invar alloys [110] in 1896 because of their promising technological applications. The interest in such materials is regenerated recently after the observation of NTE in ZrW_2O_8 over a large temperature range of 0.3 to 1050 K [111]. These materials are widely used for many industrial and technological applications, where one needs a controlled thermal expansion properties, *e.g.*, in many precision instruments, laboratory devices, shadow masks, antimagnetic watches etc. The materials with such anomalous properties even find their application in medical industry *e.g.*, as a filling material for dental cavity. However, most of the usage demand materials that do not creep as well as metallic and nonmagnetic and in nature. The materials exhibiting NTE are mainly non-metals and oxygen based materials [112] but there are also a few metallic compounds which show NTE, *e.g.*, above discussed invar alloys [110]. The basic mechanism that leads to NTE in metals is either valence instability [119] of lattice ions or magnetic [110] in nature.

In our study, we have investigated the thermal expansion behavior of metallic perovskite compounds $GdPd_3B_xC_{1-x}$ ($x = 0.25$, 0.50, 0.75 and 1.00). We have observed isotropic NTE in $GdPd_3B_{0.25}C_{0.75}$ for temperatures below ~ 50 K. In our analysis, we have proposed an alternative mechanism for the observed isotropic NTE in $GdPd_3B_{0.25}C_{0.75}$ and show that transverse vibrations at low temperatures, arising from site anisotropy, can induce lattice contraction thereby resulting in an isotropic NTE in this metallic compound. Structurally related compound $GdPd_3B_{0.50}C_{0.50}$ exhibits approximately zero thermal expansion at low temperatures. Another structurally related compound $GdPd_3B_{0.75}C_{0.25}$ exhibit structural transition at low temperature [Fig. 3.9] (section 3.3.2) and hence its thermal expansion behavior can not be compared with other three compounds with $x = 0.25, 0.50$ and 1.00. The $GdPd_3B$ exhibits normal positive thermal expansion in the entire temperature range of measurement. We have also demonstrated the pronounced effect of lattice contraction on electrical conduction behavior, which could be observed due to the metallic nature of the compounds.

In our analysis, we find that to understand the nature of the underlying mechanism that lead to NTE in $GdPd_3B_{0.25}C_{0.75}$ and normal positive thermal expansion in $GdPd_3B_{0.50}C_{0.50}$ (and also in $GdPd_3B$) the comparative study of the atomic arrangements in both the compounds is necessary. We discuss the proposed atomic arrangements in $GdPd_3B_{0.25}C_{0.75}$ and $GdPd_3B_{0.50}C_{0.50}$ in the next section.

3.4.1 Atomic arrangement in $GdPd_3B_{0.25}C_{0.75}$ and $GdPd_3B_{0.50}C_{0.50}$

As already discussed in detail in the section 3.3, the Rietveld refinements of XRD data using *FullPROF* package[159], indicates that both, $GdPd_3B_{0.25}C_{0.75}$ and $GdPd_3B_{0.50}C_{0.50}$, crystallize in a cubic perovskite structures [Fig. 3.1] with $Pm\bar{3}m$ space group symmetry, possessing room temperature lattice parameters $a = 4.109$ and 4.121 Å respectively. Boron is larger in size than carbon, thus higher B stoichiometry naturally causes a larger value of lattice parameter. The Gd atoms have 12 Pd as nearest neighbors (NN) and 8 B(and/or C) as second nearest neighbors (2NN). In contrast, Pd atoms have just 2 B(and/or C) atoms as NN, and 4 Gd and 8 Pd as 2NN. Thus the Pd atoms are arranged in the crystal lattice with the low coordination number of 2 and hence they are relatively loosely packed. The total energy and structural optimization calculations [172–175] support the atomic arrangements presented in Fig. 3.11. It may be noted that in order to minimize the strain and maintain the symmetry, in the lowest energy configuration, two B atoms sit on the extreme diagonal positions in an arrangement of eight corner-sharing octahedra of $GdPd_3B_{0.25}C_{0.75}$ [Fig. 3.11(b)]. On the other hand, in $GdPd_3B_{0.50}C_{0.50}$, four B and four C atoms are uniformly distributed as shown in Fig. 3.11(c).

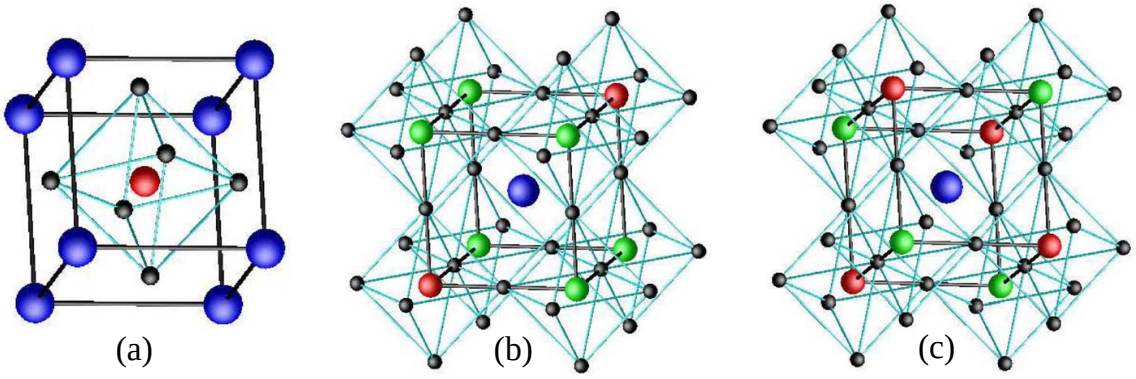

FIGURE 3.11: (a) Schematic representation of crystal structure. Gd atoms (blue spheres) occupy the cube corner positions $(0, 0, 0)$. The face center positions $(\frac{1}{2}, \frac{1}{2}, 0)$ are occupied by Pd atoms (black spheres) and the body center position $(\frac{1}{2}, \frac{1}{2}, \frac{1}{2})$ is occupied by either B (red spheres) or C (green spheres). Eight corner sharing octahedra surrounding central Gd atom in (b) $GdPd_3B_{0.25}C_{0.75}$ and in (c) $GdPd_3B_{0.50}C_{0.50}$.

3.4.2 Negative thermal expansion in $GdPd_3B_{0.25}C_{0.75}$

Figure 3.12 shows the temperature dependence of lattice parameter (a) of $GdPd_3B_{0.25}C_{0.75}$, which exhibits a minimum around 50 K. The increase in a with decrease of temperature below 50 K is anomalous and indicative of NTE. On the other hand, the lattice parameter of $GdPd_3B_{0.50}C_{0.50}$ does not display such an anomaly and decreases with

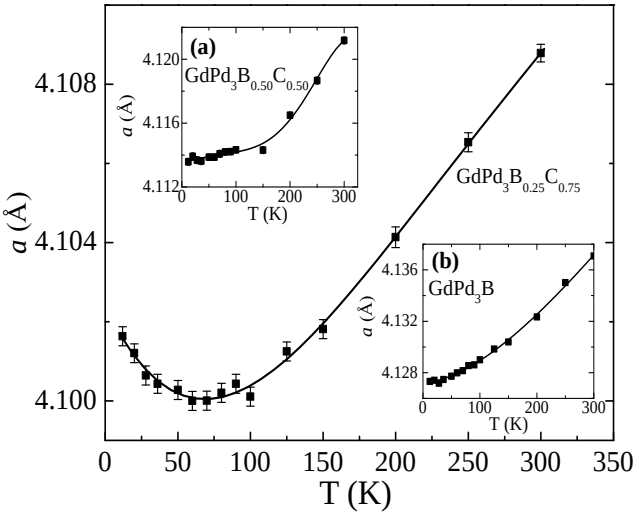

FIGURE 3.12: Lattice parameter(a) of $GdPd_3B_{0.25}C_{0.75}$ as a function of temperature. The solid line is guide to eye. Error bars have been doubled for better visibility. The inset (a) and (b) show the same for $GdPd_3B_{0.50}C_{0.50}$ and $GdPd_3B$, respectively. The solid lines in the insets are guide to eye. The error bars in the insets equal the size of the symbols.

decreasing temperatures and levels off at low temperatures [inset (a), Fig. 3.12]. Similarly, temperature variation of the lattice parameter of $GdPd_3B$ exhibits normal positive thermal expansion behavior [inset (b), Fig. 3.12]. As discussed in section 3.3.2 and also mentioned earlier in section 3.4, $GdPd_3B_{0.75}C_{0.25}$ exhibits structural transition below 50 K [Fig. 3.9], hence its thermal expansion behavior can not be compared with other three compositions mentioned above. As evident from low temperature powder XRD data and their analysis presented in section 3.3.2, $GdPd_3B_{0.25}C_{0.75}$, $GdPd_3B_{0.50}C_{0.50}$ and $GdPd_3B$ maintain the structure and symmetry throughout the temperature range of XRD measurements. The preservation of symmetry implies that the observed NTE in $GdPd_3B_{0.25}C_{0.75}$ as well as the positive thermal expansion in $GdPd_3B_{0.50}C_{0.50}$ and $GdPd_3B$ are isotropic in nature. Thus it precludes the development of micro-cracks during thermal processing, as anisotropic thermal expansions may lead to development of such cracks. This makes such materials useful for technological applications.

The observed NTE also casts its signature in electrical transport properties. In the case of $GdPd_3B_{0.25}C_{0.75}$, resistivity decreases linearly with the decrease of temperature undergoes an abrupt change of slope around 50 K, below which the resistivity decreases at much faster rate with temperature [Fig. 3.13]. We attribute this abrupt change in slope of resistivity to the anomaly in thermal expansion of the material, observed in the same temperature range. In contrast $GdPd_3B_{0.50}C_{0.50}$ which does not show any anomaly in thermal expansion behavior also does not display any anomalous resistivity behavior [Fig. 3.13].

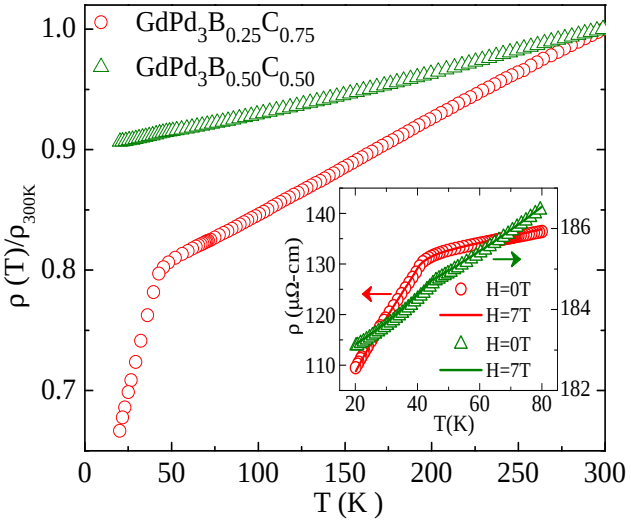

FIGURE 3.13: Resistivity ratio, $\rho(T)/\rho_{(300K)}$, for $GdPd_3B_{0.25}C_{0.75}$ and $GdPd_3B_{0.50}C_{0.50}$ as a function of temperature. Inset shows $\rho(T)$ in a restricted temperature range for magnetic fields, $H = 0$ T and $H = 7$ T.

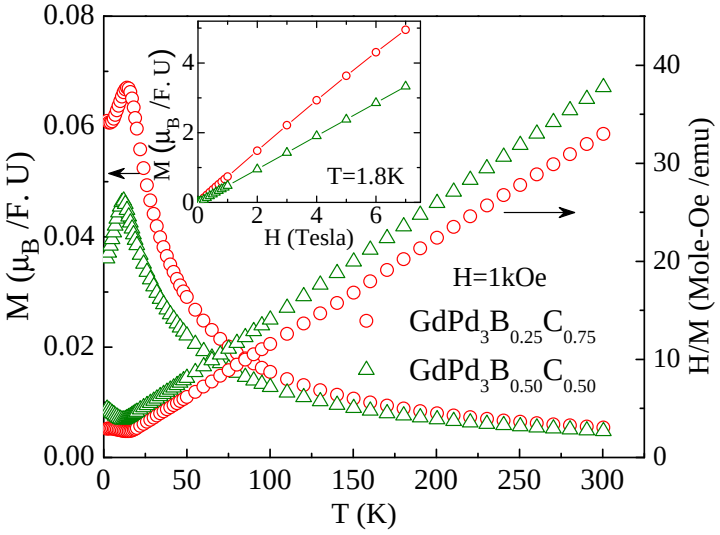

FIGURE 3.14: Variation of DC-magnetization (left axis) and inverse molar susceptibility (right axis) with temperature for $GdPd_3B_{0.25}C_{0.75}$ and $GdPd_3B_{0.50}C_{0.50}$. Inset shows isothermal magnetization as a function of applied field.

To check any possible magnetic origin of observed NTE and anomaly in electrical resistivity, we carried out DC-magnetization measurements. The data exhibits antiferromagnetic (AFM) transition in both $GdPd_3B_{0.25}C_{0.75}$ and $GdPd_3B_{0.50}C_{0.50}$ with corresponding *Nèel* temperature of 15 K and 12 K, respectively [Fig. 3.14]. The inverse susceptibility (χ^{-1}) is linear in T in paramagnetic region (Curie-Weiss Law) [Fig. 3.14]. The effective paramagnetic moments (μ_{eff}) calculated from the inverse susceptibility data are 8.59 and 8.19 μ_B for $GdPd_3B_{0.25}C_{0.75}$ and $GdPd_3B_{0.50}C_{0.50}$, respectively. Slightly higher value of μ_{eff} obtained here can be attributed to partial polarization of conduction

electrons upon carbon doping (section 3.6). No unusual behavior in magnetization has been noticed around 50 K, below which $GdPd_3B_{0.25}C_{0.75}$ exhibits NTE. The absence of any magnetic anomaly around 50 K implies that the magnetism related effects do not in any way bear a relation to the observed NTE in $GdPd_3B_{0.25}C_{0.75}$. The detailed magnetic measurements of this series of compounds will be discussed in section 3.6. Similar conclusion can be derived from the resistivity measurements in the presence of 7 T magnetic field, which retraces the values obtained for zero magnetic field for $T > T_N$, in both the materials [inset, Fig. 3.13]. We can also rule out the influence of valence fluctuation due to hybridization caused by the proximity of 4f level to the Fermi level, which are known to yield NTE in some cases [118, 119], because for Gd ions the 4f levels lie much deeper and hence they do not exhibit valence fluctuation effects. In addition, the closed packed structure of compounds studied here precludes the occurrence of rigid unit modes(RUM), which lead to NTE in the flexible framework structure of ZrW_2O_8 [111].

To discuss the possible origin of observed NTE, we consider the atomic arrangement in cubic unit cells presented in Fig 3.11. It may be noted here that in oxides materials exhibiting NTE, the vibration of bridging oxygen atom manifests in NTE only when it has a coordination number of 2 [111]. Since the coordination number of Pd atoms is 2 in these compounds, the transverse vibration driven mechanism seems suitable for underlying NTE phenomenon in this compound. The atomic arrangement in the eight corner sharing octahedral of $GdPd_3B_{0.25}C_{0.75}$ indicates anisotropy in site occupancy at body center of the cubic unit cell. Due to the bigger size of B, the B-Pd bond length is bigger than the C-Pd bond length. The bond lengths have been calculated through structural optimization procedure [172–175]. In the case of $GdPd_3B_{0.50}C_{0.50}$, at $T = 300$ K, the B-Pd and C-Pd bond lengths are 2.069 and 2.049 Å, respectively. However, in the case of $GdPd_3B_{0.25}C_{0.75}$, B-Pd and C-Pd bond lengths are 2.064 and 2.052 Å, respectively, at $T = 300$ K. The increase in C-Pd bond length, which is in majority in $GdPd_3B_{0.25}C_{0.75}$, implies the presence of a stretch along this bond direction. Because of this additional stretch in the C-Pd-C arrangement, the vibration of the Pd atoms, which are relatively loosely packed (having coordination number 2), along this bond direction in expected to be more prominent in $GdPd_3B_{0.25}C_{0.75}$. This vibrational motion of Pd atoms is perpendicular (transverse) to the face of the unit cell [Fig. 3.11(a)] and causes the Gd atoms to move closer to each other. Accordingly the effective lattice parameter of the unit cell is reduced, which indeed has been observed for $GdPd_3B_{0.25}C_{0.75}$ below 50 K. Our electronic structure calculations show that, partially filled B$-p$ (and/or C$-p$) states appear close to Fermi level and strongly hybridize with Pd$-d$ states and form directional B$-p$ (and/or C$-p$) bonds [1]. In addition, the hybridization between C$-p$

[1]Discussed in detail in section 3.5.1

and Pd−d is more prominent as the C−p level lies much closer to Pd−d level than B−p to Pd−d. This leads to more directional C-Pd bond compare to B-Pd bond. This could be a stimulating force behind the above discussed transverse vibrations. On the other hand, in the case of $GdPd_3B_{0.50}C_{0.50}$, where we have equal distribution of B and C atoms, the bond arrangements around Pd atoms are of B-Pd-C type. The kind of transverse modes discussed above will also be present for a B-Pd-C arrangement but will not be so effective because of the asymmetry in the bond arrangement on the both sides of Pd atoms. As a result, the NTE observed in $GdPd_3B_{0.25}C_{0.75}$ is absent in $GdPd_3B_{0.50}C_{0.50}$, where the lattice parameter almost saturates below 50 K [inset (b), Fig. 3.12].

In order to arrive at a quantitative estimate of NTE, we estimate the thermal expansion coefficient (α) which is defined as $\alpha = (1/a)[da/dT]$. Thermal expansion coefficient for $GdPd_3B_{0.25}C_{0.75}$ turns out to be negative below 50 K and has a value equal to -15.1 p.p.m K^{-1} at $T = 12$ K. This may be compared to the value of $\alpha = -9.39$ ppm K^{-1} for ZrW_2O_8[115] and much larger value of -130 ppm K^{-1} for the valence fluctuating $Sm_{2.75}C_{60}$ [119]. In the case of $GdPd_3B_{0.25}C_{0.75}$, α vanishes in the temperature range 60-70 K where the high-energy longitudinal phonon modes (responsible for normal thermal expansion) neutralize the effect of the low energy transverse modes (responsible for NTE). Above 70 K, α becomes positive and reaches a value, $\alpha(300K) = +11.3$ ppm K^{-1}. The temperature $T = 50$ K, below which α is negative, defines an energy scale for the low energy phonon modes responsible for NTE in $GdPd_3B_{0.25}C_{0.75}$: $E = h\omega = kT \sim 5meV$.

In general, the oxygen-based compounds that exhibit NTE, *e.g.*, ZrW_2O_8 etc., are semiconductors or insulators [176]. In such systems, the electrical conduction mechanism is an activated one and thus relatively unaffected by the phonon modes that lead to NTE. In contrast, the compounds discussed here are metallic and hence the electrical transport properties are dominated by electron-phonon scattering. Thus the phonon modes that lead to the NTE, would have a pronounced effect on the electrical properties of the compound. Our thermal expansion and resistivity data clearly exhibit such correlation. Close correlation between thermal expansion and resistivity behaviors suggests that the gradual freezing of the above discussed low energy transverse modes below 50 K is responsible for the sharp fall of the resistivity below this temperature in $GdPd_3B_{0.25}C_{0.75}$.

3.5 Electrical transport properties of $GdPd_3$ and $GdPd_3B_xC_{1-x}$ ($x = 0.25$, 0.50, 0.75 and 1.0)

As discussed in chapter 1 (section 1.5), the electrical transport in metals is in general characterized by a positive temperature coefficient of resistance (TCR), defined as α(T)

$= 1/\rho(T)[d\rho(T)/dT]$. However there are also examples of materials whose resistivity (ρ) decreases with increasing temperature [124, 125, 177]. Such materials with negative TCR (NTCR) are amorphous metals, highly disordered compounds (both structurally [124] and chemically [125]), liquid metals [126] and quasicrystals [127]. There exists a well known Mooij criterion that correlates the sign of TCR with the value of ρ for conductors and further suggests that the TCR changes sign and becomes negative when the value of ρ crosses the critical value, $\rho_c \sim 150$ $\mu\Omega-$cm [128]. Later Tsuei collected more than 500 data over various samples and modified the Mooij criterion with a value of ρ_c that can vary from 30 to 400 $\mu\Omega-$cm [129].

In our study, we find the unusual result of a NTCR in an ordered, non-Kondo crystalline intermetallic compound, $GdPd_3B$. Our data suggest that chemical disorder is not the causative factor for NTCR; on the contrary, we are able to tune the sign of the TCR of $GdPd_3B_xC_{1-x}$ in a controlled fashion from negative for $x \geq 0.75$ to positive for $x \leq 0.50$ by introducing disorder at the B site through partial substitution with C. We find this effect by analyzing the electrical transport and structural properties of the compounds $GdPd_3$ and $GdPd_3B_xC_{1-x}$ ($x = 0.25$, 0.50, 0.75 and 1.0). For comparison we have also investigated off-stoichiometric compounds $GdPd_3B_x$ ($x = 0.50$ and 0.75). Experimental studies are accompanied by electronic structure calculations for gaining more insight into the conduction mechanism.

3.5.1 Electrical transport and electronic structure

Figure 3.15 shows the temperature dependence of $\rho(T)/\rho_{300K}$ for $GdPd_3$ and $GdPd_3B_xC_{1-x}$. We notice that room temperature resistivity increases with increase in B content [inset, Fig 3.15]. The residual resistivity ratio (RRR) for the host compound, $GdPd_3$, can be approximately estimated to 0.7. The value of RRR for non-magnetic analogues of $GdPd_3$, *viz.* YPd_3 and $LuPd_3$, are 0.68 and 0.66, respectively. A similar magnitude of RRR in polycrystalline $GdPd_3$ and its diamagnetic analogues suggests a non-magnetic origin of observed high RRR in these compounds. It may be noted that for electron-phonon (e-ph) interaction in crystalline materials, RRR depends sensitively on Debye temperature. Focusing on the high temperature behavior, the important feature to notice is that the sign of the TCR varies from a positive for $GdPd_3$ to negative value for $GdPd_3B$. In other words, the sign of TCR varies from positive to negative value as the B content (x) is increased in the $GdPd_3B_xC_{1-x}$ series. On partial replacement of B with C, the TCR can be tuned from negative value for $x = 0.75$ to a positive value for $x = 0.25$. The other feature to notice is a transition in ρ(T) around $T^* \approx 45$ K in $GdPd_3B_xC_{1-x}$ series; below T* the TCR has positive sign for all values of x. The crossover at T^* is relatively less sharp for the stoichiometrically symmetric compounds

with $x = 0.50$ and 1.00 but quite sharp for $x = 0.25$ and 0.75. The variation of α_{300K} with x is linear as α changes sign from positive to negative [inset, Fig. 3.15].

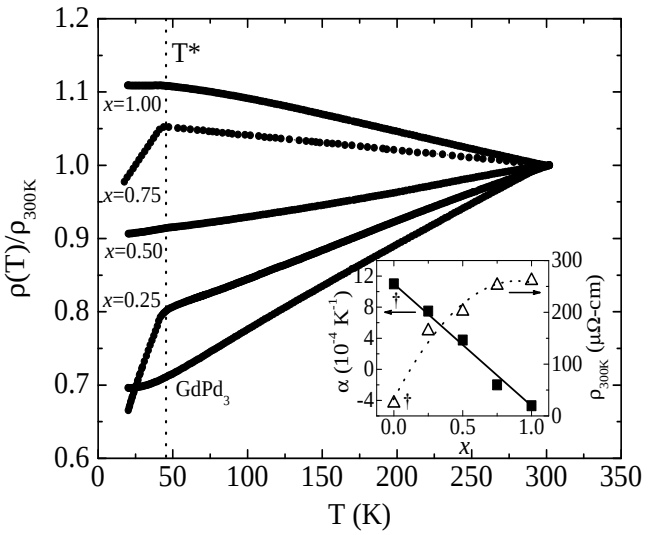

FIGURE 3.15: Resistivity ratio, $\rho(T)/\rho_{300K}$, of $GdPd_3$ and $GdPd_3B_xC_{1-x}$ as a function of temperature. The temperature (T^*) where the slope of resistivity changed has been marked by a dotted vertical line. Inset shows the variation of ρ_{300K} and α_{300K} as a function of B stoichiometry. †The $x = 0.0$ datum represents the value for $GdPd_3$.

Magnetic measurements exhibit that all the five compounds investigated are paramagnetic in the discussed temperature range (20-300 K). However, compounds undergo AFM like ordering at further low temperatures with $T_N = 6$ K for host compound $GdPd_3$, consistent with reported value [178]. Among these compounds, highest observed T_N is 15 K for $x = 0.25$. Details of magnetic properties shall be discussed in section 3.6.

We have carried out electronic structure calculations within the local density approximation(LDA) within density functional theory (DFT) in the linear muffin-tin orbital (LMTO) basis [179]. The calculations for mixed compounds, $GdPd_3B_xC_{1-x}$, were made with supercells of dimension $2 \times 2 \times 2$ containing 8 formula units. Although the attempts to prepare single phase $GdPd_3C$ were not successful, its electronic structure calculations were found to be useful for a systematic comparison. Although the band structure calculations have been carried out for all the five compounds presented in figure 3.15, the results are shown for only $GdPd_3$, $GdPd_3B$ and also for $GdPd_3C$ [Fig. 3.16]. The calculations were carried out considering the room temperature crystal structure data. These suggest that all the compounds are metallic. This conclusion has been checked in the presence of magnetism of Gd-4f states and correlation effects beyond LDA in Gd and Pd via LDA+U calculations. We have also verified our results from energetically more accurate, full potential augmented plane wave (LAPW) calculations [180]. The effect of spin-orbit coupling in the presented electronic structure calculation has been checked and found to be not important for the paramagnetic phases under consideration.

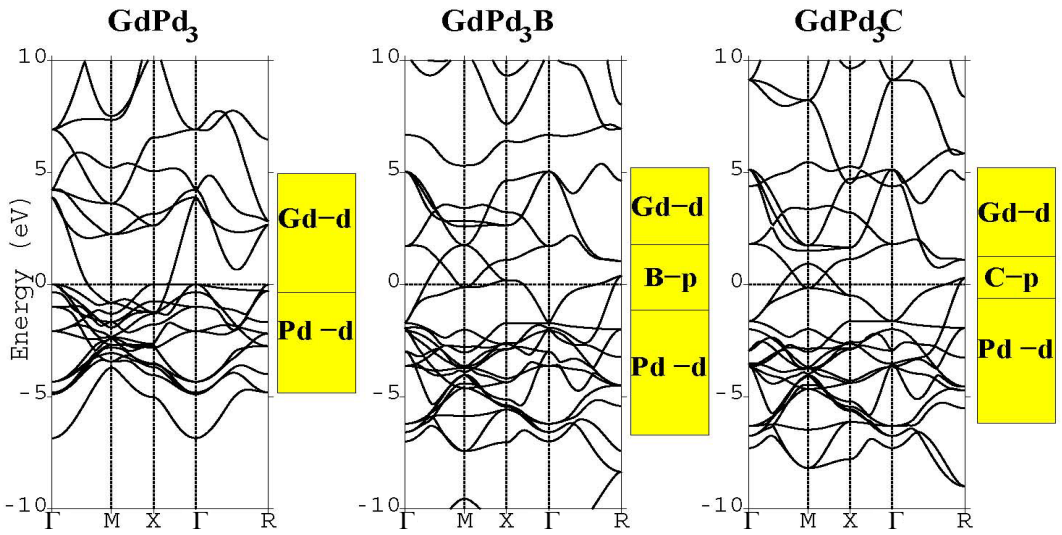

FIGURE 3.16: Non-spin polarized LDA band structure of $GdPd_3$, $GdPd_3B$ and $GdPd_3C$, plotted along the high symmetry directions of the cubic BZ, Γ=(0,0,0)-M=(π,π,0)-X=(π,0,0)-R=(π,π,π). The zero of energy is fixed at Fermi level. The bars indicate the dominant band characters.

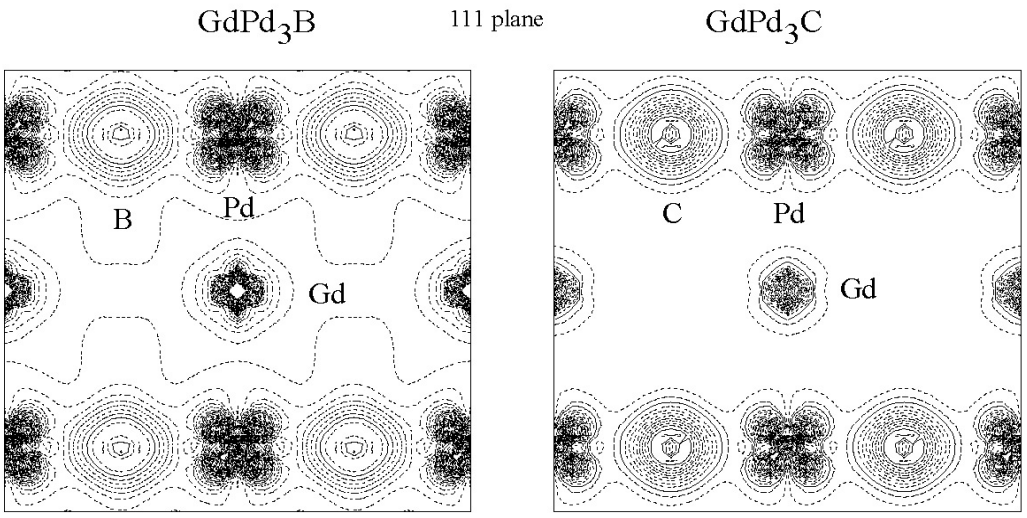

FIGURE 3.17: Charge density plots in (111) plane for $GdPd_3B$ and $GdPd_3C$ contributed by bands in ±1 eV around the Fermi energy.

The basic electronic structure of $GdPd_3$ consists of nearly full Pd−d and nearly empty Gd−d bands. With introduction of B, B−p states which are partially filled appear close to the Fermi level and strongly hybridize with Pd−d. The hybridization between Gd−d and B−p is small due to large inter atomic separation of the second nearest neighbors. Replacing B by C results in three primary effects: (i) The hybridization between C−p and Pd−d is enhanced since C−p level is much closer to Pd−d level than B−p is to Pd−d. (ii) The C−Pd bond becomes more directional, as can be seen from the charge density plot given in Fig. 3.17. (iii) C has one more electron than B, which acts as a

band filling effect, moving the Fermi level up in energy. For both $GdPd_3$ and $GdPd_3C$, highly dispersive bands cross the Fermi level, therefore it is expected that the Fermi velocity and the mobility of the carriers will be high and hence the effective mass (m_{eff}) will be low. On the other hand for $GdPd_3B$ the Fermi level lands in a region of flat bands with low velocity. The mobility of the carriers is therefore expected to be low with high m_{eff}. One would therefore predict the resistivity of $GdPd_3$ and $GdPd_3C$ to be lower than that of $GdPd_3B$ and the compounds with relatively higher carbon stoichiometry in $GdPd_3B_xC_{1-x}$ to be more conducting. Accordingly, we have calculated the conductivities of $GdPd_3B$ and $GdPd_3C$ using the density of states at Fermi level and Fermi velocity. The electrical conductivity of $GdPd_3C$ is found to be about 3 times to that of $GdPd_3B$. This trend is also found in experiments [inset, Fig. 3.15].

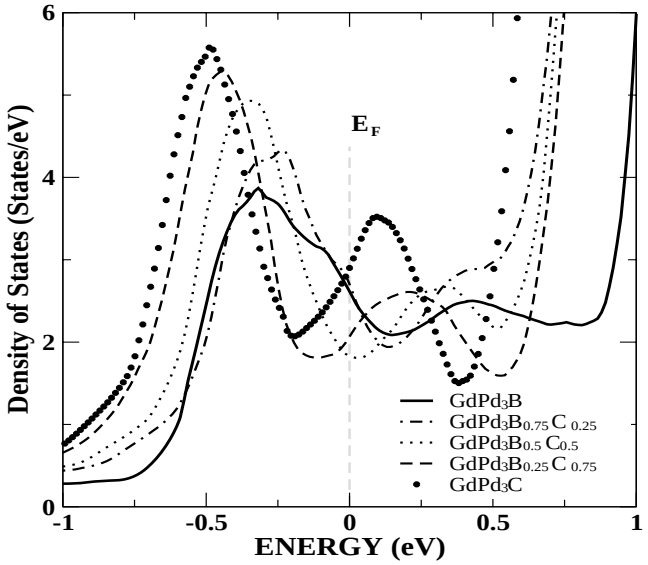

FIGURE 3.18: Density of states of one formula unit of $GdPd_3B_xC_{1-x}$. Line at zero denotes the position of the E_F.

The computed density of states presented in figure 3.18 show a hump-dip-hump kind of structure which arises due to hybridization between Pd$-d$ and B$-p$. We observe the systematic effect of band filling and simultaneous pronouncing of hump-dip-hump structure as one changes the B concentration from 1.0 to 0.0. Therefore, one would also expect a systematic, monotonic decrease in resistivity as the B concentration is reduced from 1.0 to 0.0, as is also observed in experiment.

Figure 3.19 shows that as long as x is ≥ 0.75, the NTCR persists in the stoichiometric compositions. However, NTCR can result even for $x < 0.75$ in the off-stoichiometric composition, *e.g.*, $GdPd_3B_{0.50}$ [Fig. 3.19]. The introduction of C in the off-stoichiometric compound $GdPd_3B_{0.50}$, thereby turning it to $GdPd_3B_{0.50}C_{0.50}$, causes drastic changes in that the sign of the TCR reverts from negative to positive. This suggests that disorder at B site is not the causative factor for observed NTCR. This conclusion is in conformity

with electronic structure calculations, which indicate that the introduction of C in the lattice makes the compound more conducting. We notice from the inset of figure 3.19 that $GdPd_3B_{0.50}$ and $GdPd_3B_{0.50}C_{0.50}$ which show large difference in the value and sign of TCR also concurrently show large difference in lattice parameter. The compounds $GdPd_3B_{0.75}$ and $GdPd_3B_{0.75}C_{0.25}$ that have nearly same lattice parameter also show similar resistivity behavior. This suggests that along with chemical stoichiometry the structural parameters also play an important role in determining the sign of TCR in these materials. The size of B is more than the size of octahedral void at the center of the cubic unit cell; thus its introduction causes a negative pressure or a tensile stress and results in the lattice expansion [64]. By substituting B with C, which is smaller in size than B, the lattice parameter decreases [inset, Fig. 3.19] and one can fine tune the magnitude of negative pressure generated by oversized B atom. We believe that this negative pressure is crucial to the NTCR behavior in our system.

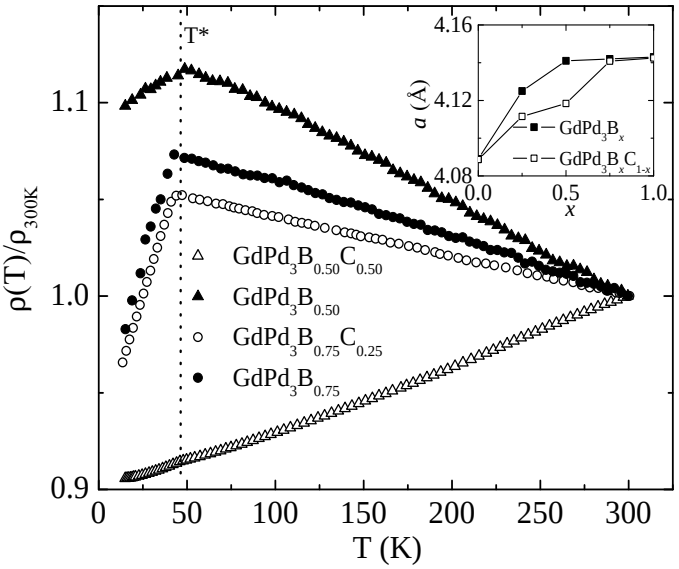

FIGURE 3.19: Resistivity ratio, $\rho(T)/\rho_{300K}$, for $GdPd_3B_x$ and $GdPd_3B_xC_{1-x}$ ($x = 0.50$ & 0.75) as a function of temperature. T* has been marked by a dotted vertical line. Inset shows lattice constant (a) as a function of B content (x).

3.5.2 Origin of NTCR behavior in high boron stoichiometry compositions

Focusing on the possible explanations for observed NTCR in high B stoichiometry compounds, we may rule out oft-quoted mechanisms *e.g.*, the Ziman model [131], incipient localization [181] etc., as all these refer to highly disordered systems and exhibit a non-linear $\rho(T)$ behavior, except the Ziman model which yields a linear T-dependence for

$T \geq \theta_D$ (θ_D: Debye temperature) [2]. But the Ziman model is relevant only for liquid metals where there is no structural correlation between atoms. In addition, the presence of sufficient density of states at Fermi level [Fig. 3.18] rules out the possibility of narrow band gap semiconductor like behavior [139]. Grain boundary effects can also be ruled out as they primarily cause a change in magnitude of resistivity by a constant factor in metallic systems [182]. Moreover, grain boundaries are present in all the compounds studied here, irrespective of negative or positive TCR. In addition, optical micrograph of the host compound, $GdPd_3$, suggests a good quality of the sample. We believe long duration of annealing has homogenized the ordered phase and the grain size in large enough so that the grain boundary volume fraction becomes negligible in comparison to the grain volume.

One might be tempted to use Baym-Meisel-Cote theory (BMC) [130, 133] to explain the observed NTCR, as it predicts occurrence of NTCR and a linear variation of $\rho(T)$. However, this theory is valid only for non-magnetic amorphous compounds exhibiting weak Pauli paramagnetism. In contrast, as mentioned earlier, the crystalline compounds studied here undergo AFM like ordering at low temperature and exhibit Curie-Weiss paramagnetic behavior at high temperature. Hence, the possibility of weak Pauli paramagnetism can be ruled out. Considering the above deviations, the application of BMC theory does not seems suitable here. For example, let us consider $GdPd_3B$, which shows largest NTCR. This compound exhibit magnetic ordering at low T ($T_N = 8$ K) and paramagnetic character at high T ($\mu_{eff} = 8.04\mu_B$ and $\theta_P = -20.2$ K) [3]. To use the BMC theory for $GdPd_3B$, we need to consider the presence of significant structural disorder (which is not distinctively discernible in XRD measurement discussed in section 3.3) and extend the validity of the theory to compounds having substantial paramagnetic moment. Thus, under the present experimental observations, this approach does not seems applicable.

The other possible scenario could be the interpretation of observed $\rho(T)$ within the *Drude framework* in which the temperature dependence arises from the product of ν (scattering rate) and m_{eff} which occur in the numerator of $\rho(T)$ in a product form ($\rho = \nu m_{eff}/ne^2$). Because ν is known to increase linearly with T for e-ph scattering in crystalline metals, this increase must be offset by a more accelerated decrease of m_{eff} with T. Such a scenario is indeed possible as size of the octahedral void would increase with T due to the linear thermal expansion of metal, resulting in reduction of strain and thereby causing a decrease in strain-modulated e-ph mass enhancement. The rate at which m_{eff} decreases with T is expected to increase with increasing B stoichiometry. The strong temperature dependence of m_{eff} on higher B stoichiometry is discernible

[2] The mechanisms that lead to NTCR are discussed in detail chapter 1 section 1.5
[3] For details, see the section 3.6

in the experiments. We do not, however, need exceptionally large change in m_{eff} to observe this effect. Indeed for $GdPd_3B_{0.75}C_{0.25}$, where the change is maximum, reduction of m_{eff} by a factor of ~ 1.78 can produce the observed results. This value is close to those reported for some alkali metals [183]. We must mention here that this decrease in strain modulated e-ph mass enhancement with the increase in temperature should not be confused with normal lattice expansion effects that leads to band narrowing and hence in turn results in increase in m_{eff}. Our electronic structure calculations suggest that the lattice expansion in the discussed temperature range does not produce any significant band narrowing.

3.5.3 Low temperature structural anomalies and their effect on electrical transport behavior

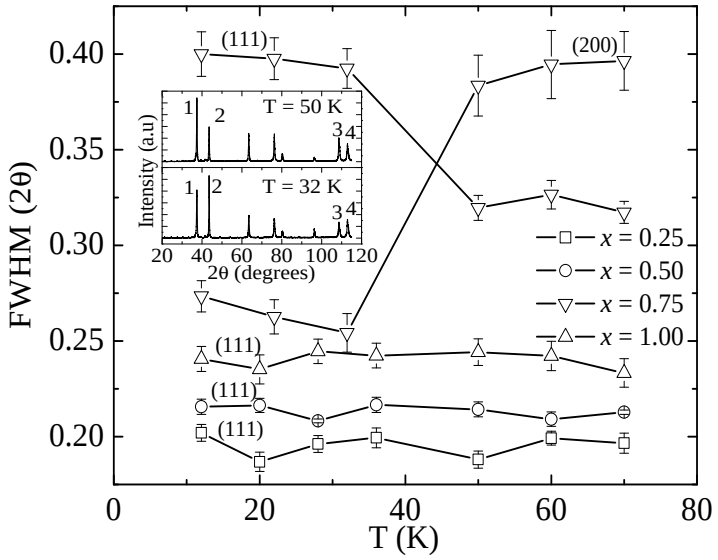

FIGURE 3.20: Peak width (FWHM) of (111) Bragg peak as a function of temperature. FWHM of (200) peak for $GdPd_3B_{0.75}C_{0.25}$ has also been presented. Lines are guide to eye. Inset shows XRD profile of $GdPd_3B_{0.75}C_{0.25}$ at two different temperatures.

Turning to the low temperature behavior and issues of existence of T^*, we now discuss the low temperature structural analysis, where we observe quite distinct behavior of the compounds with symmetric distribution of B and C ($x = 0.50$ and 1.00) and the compounds with asymmetric distribution ($x = 0.25$ and 0.75). The low temperature XRD pattern of $GdPd_3B_{0.75}C_{0.25}$ exhibits a redistribution of peak intensities of (111)/(200) and (331)/(420) Bragg peaks below T^* [inset, Fig. 3.20], associated with redistribution of peak width of (111) and (200) peaks [Fig. 3.20]. For example, below T^*, peak width of (111) peak exhibits a sudden increase though the peak intensity gets reduced, while the reverse is true for (200) peak. No such behavior is observed in the XRD pattern of other

compositions ($x = 0.25$, 0.50 and 1.00). The detailed analysis of the structural changes in $GdPd_3B_{0.75}C_{0.25}$ below T^* is not straight forward and beyond the scope of this thesis work. However, our observations suggest that the change from NTCR to positive TCR at T^* in this compound may be linked with a structural phase transition occurring in the same temperature region. This again infers that electrical transport in this series exquisitely depend upon the structural parameters. In contrast, in $GdPd_3B_{0.25}C_{0.75}$, which also has the asymmetric distribution of B and C, the sign of the coefficient of thermal expansion becomes negative below T^* *i.e.* the cubic lattice parameter decreases down to about T^* and then increases with further decrease in T below T^* leading to NTE.

In the case of $GdPd_3B$ and $GdPd_3B_{0.50}C_{0.50}$, where we have symmetric distributions of B and C, no NTE is observed and no remarkable change in $\rho(T)$ behavior below T^* is noted either [Fig. 3.15]. In the case of $GdPd_3B_{0.75}C_{0.25}$, where we have asymmetry with higher B stoichiometry, the effect seems stronger causing more significant changes in structural parameters [inset, Fig. 3.20], leading probably to a structural phase transition.

3.6 Magnetic properties of $GdPd_3$ and $GdPd_3B_xC_{1-x}$ ($x = 0.25$, 0.50, 0.75 and 1.00)

We have performed the detailed study of magnetic and magneto-transport properties of $GdPd_3B_xC_{1-x}$, and also the undoped parent compound $GdPd_3$. As discussed in the section 3.4 and 3.5, few members of $GdPd_3B_xC_{1-x}$ series exhibit novel properties of NTCR and NTE in an ordered crystalline state. Hence, in order to investigate any possible correlation with the observed NTCR and NTE, it is of fundamental interest to make detailed investigation of magnetic properties of this series. As discussed in section 3.3, in $GdPd_3B_xC_{1-x}$ compounds, B and C occupy the body centered site of the cubic unit cell (see Fig. 3.1). As boron is bigger than carbon, the lattice parameter can be tuned by varying the stoichiometric ratio of these two elements. This in turn causes an alteration of the distances between the localized $4f$-electrons carrying Gd^{+3} ions. The resultant change in the nature and strength of RKKY interaction can yield dominating ferromagnetic (FM) to AFM ordered states and sometimes even manifests canted magnetic structures. It may be mentioned that, the only magnetic ion in the compounds studied here is Gd^{+3}, which is a spherically symmetric **S** state ion and thus reduces the possibility of complexity due to additional interactions, *viz.* magnetocrystalline anisotropy, crystal-field effect etc.

3.6.1 DC and AC magnetic measurements

Figure 3.21 shows the temperature dependence of zero field cooled (ZFC) magnetization (M) of $GdPd_3$ and $GdPd_3B_xC_{1-x}$ measured in an applied DC-magnetic field of $H = 1$ kOe. The M(T) of three compounds, $GdPd_3$, $GdPd_3B_{0.25}C_{0.75}$ and $GdPd_3B_{0.50}C_{0.50}$ exhibits a peak at $T = 6$, 15 and 12 K, respectively [insets, Fig. 3.21], resembling AFM like ordering. In the case of other two compounds, $GdPd_3B_{0.75}C_{0.25}$ and $GdPd_3B$, the change in slope (dM/dT) exhibits a maxima at temperatures 7 and 8 K respectively, which have been taken as their respective Néel temperatures (Table 3.1). The variation of inverse susceptibility (χ^{-1}) with temperature is presented in Fig. 3.22. The values of lattice parameter (a) and the parameters derived from the magnetization and inverse susceptibility data *e.g.* Néel temperature (T_N), paramagnetic Curie temperature (θ_p) and the effective paramagnetic moment (μ_{eff}), have all been summarized in Table 3.1. It is interesting to note that except for $GdPd_3$, the value of θ_p is negative for all other compounds. The small and positive value of θ_p (3.5 K) observed for $GdPd_3$ is consistent with the reported value [178] and suggests that the nature of magnetic interactions in this compound are different from that in pure AFM systems for which a negative θ_p is expected.

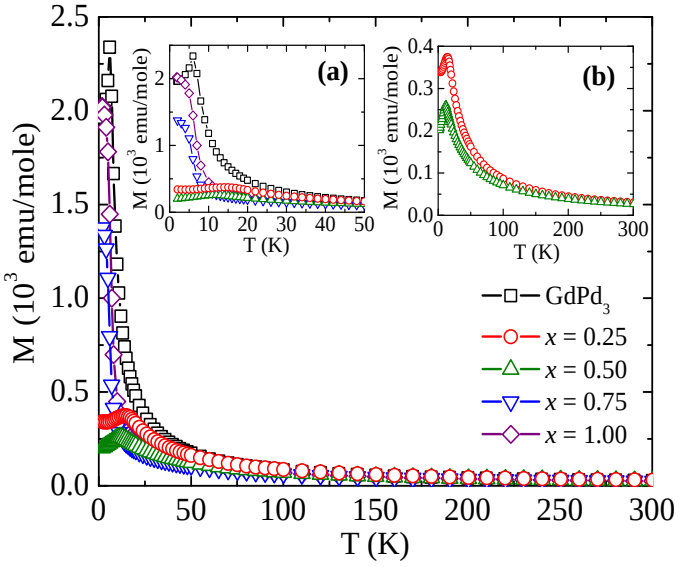

FIGURE 3.21: ZFC DC-magnetization of $GdPd_3$ and $GdPd_3B_xC_{1-x}$ as a function of temperature. Inset (a) shows the same in restricted temperature range close to magnetic ordering. Inset (b) exhibits the M(T) values for the two AFM compounds $GdPd_3B_{0.25}C_{0.75}$ and $GdPd_3B_{0.50}C_{0.50}$.

Results of hysteresis measurements performed at 2 K are presented in Fig. 3.23. The compounds studied here do not show any magnetic hysteresis, hence we have presented only one quadrant data for easy visualization. Isothermal magnetization varies linearly

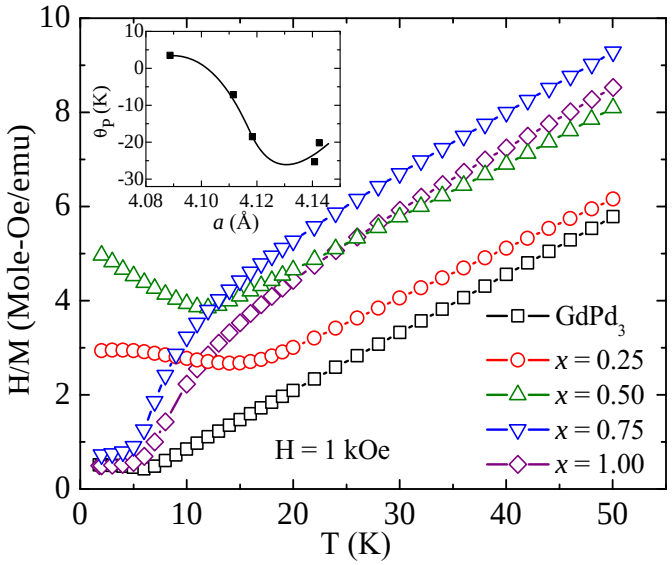

FIGURE 3.22: Inverse molar susceptibility of $GdPd_3$ and $GdPd_3B_xC_{1-x}$ as a function of temperature. Inset shows the variation of paramagnetic Curie temperature (θ_c) with lattice parameter (a). The line in inset is guide to eye.

Compounds	a**(Å)**	T_N**(K)**	θ_p**(K)**	$\mu_{\mathbf{eff}}(\mu_{\mathbf{B}})$	$\chi(T=0)/\chi(T=T_N)$
$GdPd_3$	4.089	6	3.5	8.03	0.82
$GdPd_3B_{0.25}C_{0.75}$	4.112	15	-7.2	8.60	0.92
$GdPd_3B_{0.50}C_{0.50}$	4.118	12	-18.5	8.19	0.73
$GdPd_3B_{0.75}C_{0.25}$	4.141	7	-25.3	7.99	2.72
$GdPd_3B$	4.143	8	-20.2	8.04	2.96

TABLE 3.1: The lattice parameter (a), Néel temperature (T_N), paramagnetic Curie temperature (θ_P), effective paramagnetic moment (μ_{eff}) and ratio of susceptibilities at $T = 0$ K (determined by extrapolation of the data) and $T = T_N$ for $GdPd_3$ and $GdPd_3B_xC_{1-x}$. T_N has been taken as the temperature where the change in the slope of susceptibility is maximum. Both DC and AC susceptibilities produce the same value of T_N.

with H at high fields ($H > 1$ T) for all the compounds, except $GdPd_3$ in which it saturates [Fig. 3.23]. We have also performed AC-susceptibility (χ_{ac}) measurements to further probe the nature of magnetic ordering and to obtain information about the relaxation and dissipation mechanisms. In the case of $GdPd_3$, $GdPd_3B_{0.75}C_{0.25}$ and $GdPd_3B$ both χ'(T) and χ''(T) exhibit peak at T_N [Fig. 3.24]. In contrast, in the case of $GdPd_3B_{0.25}C_{0.75}$ and $GdPd_3B_{0.50}C_{0.50}$, χ'(T) exhibits a peak at T_N but the value of χ''(T) vanishes in the whole temperature range of measurements [inset, Fig. 3.24]. The values of T_N derived from AC-susceptibility data are the same as those derived from DC-magnetization data (Table 3.1). The AC-susceptibility of data this series of

compounds do not show any frequency dependent shift in frequency range 1 Hz to 1 kHz.

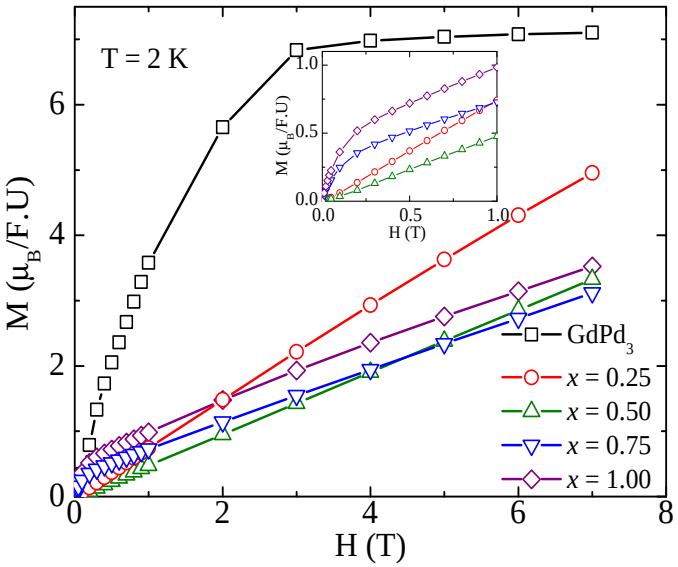

FIGURE 3.23: Isothermal magnetization of $GdPd_3$ and $GdPd_3B_xC_{1-x}$ as a function of applied DC-magnetic field. The inset shows the same in small field range for four compositions, $x = 0.25$, 0.50, 0.75 and 1.00. The lines in inset are fit, which are linear in H for $x = 0.25$ and 0.50, and proportional to $H^{\frac{1}{2}}$ for $x = 0.75$ and 1.00.

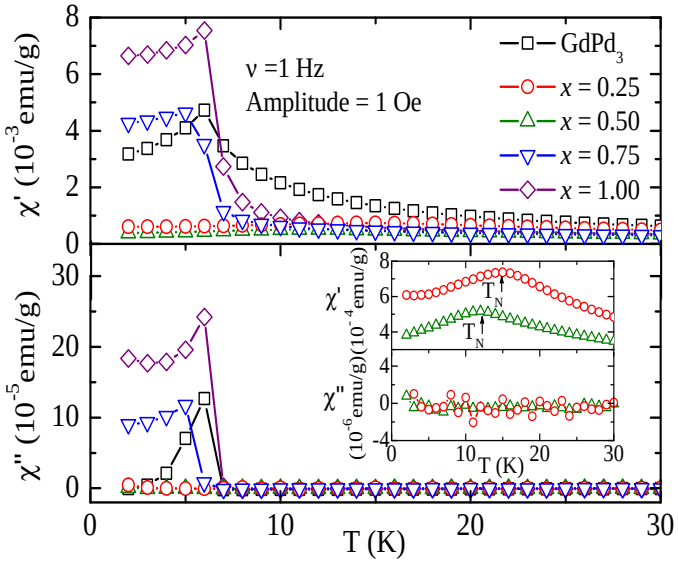

FIGURE 3.24: In-phase (χ') and out-of-phase (χ'') components of AC-susceptibility as a function of temperature for $GdPd_3$ and $GdPd_3B_xC_{1-x}$. Inset shows the same for $x = 0.25$ and 0.50 in an expanded scale.

Saturation of moments at high fields, occurrence of positive θ_p and non-zero value of χ'' below T_N clearly indicate that the dominating magnetic interaction in $GdPd_3$ is not purely of AFM in nature, as it was reported earlier [178]. Anomalous magnetic

properties suggest the presence of competing interactions in this compound. Since the value of θ_P is small and positive, the dominating interaction is expected to be of FM in nature. One possibility of the existence of such competing interaction could be the importance of second nearest neighbor interaction.

As mentioned earlier, when we introduce B and C in the lattice and thus increase the distances between the moment carrying Gd^{+3} ions (Table 3.1), we monitor remarkable changes in the magnetic properties of $GdPd_3B_{0.25}C_{0.75}$ and $GdPd_3B_{0.50}C_{0.50}$ in comparison to $GdPd_3$. For example, we observe (i) significant reduction in the amplitude of DC-magnetization maxima close to T_N [Fig. 3.21], (ii) absence of saturation in isothermal magnetization [Fig. 3.23], (iii) vanishing out-of-phase component of AC-susceptibility [Fig. 3.24] etc. In the case of $GdPd_3B_{0.25}C_{0.75}$ and $GdPd_3B_{0.50}C_{0.50}$, ZFC-magnetization data exhibit a peak, thus suggesting the existence of AFM ordering [inset (b), Fig. 3.21]. The negative θ_p (Table 3.1) and linear variation of M with H in entire field range of measurement [Fig. 3.23] further imply the presence of AFM ordering. In addition, the absence of absorption term (χ'') for $T \leq T_N$ in AC-susceptibility measurements confirms the AFM ordering in these two compounds. The observation of vanishing absorption component in the AC-susceptibility data is of particular importance as it establishes the presence of strong AFM coupling in $GdPd_3B_{0.25}C_{0.75}$ and $GdPd_3B_{0.50}C_{0.50}$ below T_N with no dissipation loss and hysteresis. We would also like to point out here that among these two compounds, the ratio of susceptibilities at $T = 0$ K and $T = T_N$ (Table 3.1) for $GdPd_3B_{0.50}C_{0.50}$ is closest to the theoretical value 2/3 expected for a strongly-coupled two-sublattice ideal antiferromagnet [184].

When we further increase the lattice parameter by substituting more B in to the lattice ($x = 0.75$ and 1.00), the amplitude of M(T) increases for $GdPd_3B_{0.75}C_{0.25}$ and $GdPd_3B$ below their respective magnetic ordering temperatures and becomes comparable to that of undoped $GdPd_3$ [Fig. 3.21]. Although the M(T) resembles more like that of a ferromagnet, the large and negative values of θ_p (-25.3 and -20.2 K for $x = 0.75$ and 1.00, respectively) suggest the dominance of AFM interaction. However, the possibility of ideal AFM ordering can also be ruled out by the appearance of a peak in $\chi''(T)$ data in the AC-susceptibility measurement [Fig. 3.24], which indicates the hysteresis (and/or dissipation) loss below T_N. In addition, the value of $\chi(T = 0)/\chi(T = T_N)$ is relatively high (>1) (Table 3.1) which also refutes the presence of AFM ordering. Further, in contrast to the linear $M-H$ behavior expected for AFM systems at moderate applied fields, M varies as $H^{\frac{1}{2}}$ at lower fields (up to $H = 1$ T) and then linearly for higher fields [inset, Fig. 3.23]. All these observations concurrently suggest that the magnetic interactions in high-boron stoichiometry compounds, $GdPd_3B_{0.75}C_{0.25}$ and $GdPd_3B$, can not be classified either as FM or as AFM in nature. The 'S' shape nature of M vs. H data taken at $T = 2$ K [Fig. 3.25] suggests the possibility of presence of a canted magnetic structure

[185, 186] in these two compounds. The suggestion of the canted structure also gets credence from the inverse susceptibility behavior that gets reduced as one approaches the respective transition temperature [Fig. 3.22]. Such behavior has been observed in other magnetic materials that posses a canted AFM structure [187].

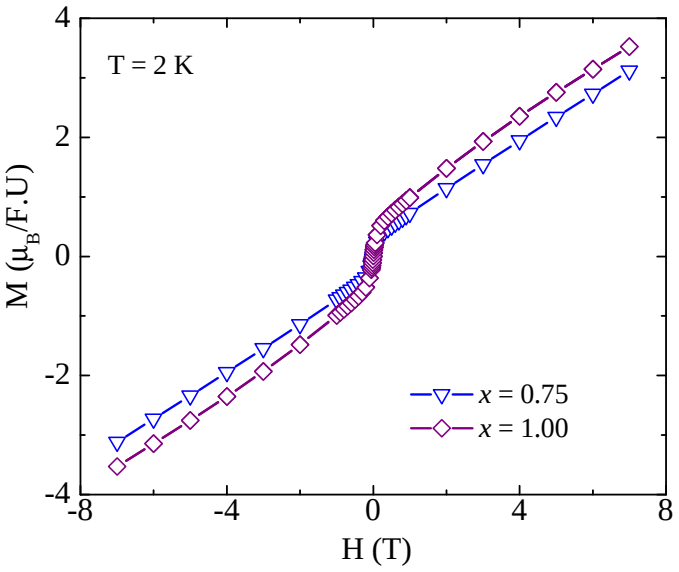

FIGURE 3.25: Magnetic hysteresis of $GdPd_3B_{0.75}C_{0.25}$ and $GdPd_3B$ measured at $T = 2$ K.

However, it must be pointed out that the proposed canted magnetic structure of $GdPd_3B_{0.75}C_{0.25}$ and $GdPd_3B$ is only a hypothesis based on magnetization measurements. To find out the exact magnetic structure of the compounds one needs to perform a detailed neutron diffraction studies. As ^{157}Gd (as well as natural boron) is highly neutron absorbing, studying neutron diffraction in these systems is extremely difficult task and remains out of the purview of this work.

In the compounds studied here, the values of μ_{eff} derived from the linear part of $\chi^{-1}(T)$ data ($T > 50$ K) are close to 7.94 μ_B expected for a free Gd^{3+} ions (Table 3.1), except for the high-carbon stoichiometry compounds ($x = 0.25$ and 0.50) that posses slightly higher values (Table 3.1). The outcome of our electronic structure calculations helps to resolve this discrepancy. As discussed in section 3.5.1 the electronic structure of the compounds under investigation reveals that the introduction of C, which has one more electron than B, acts as a band-filling effect and in that the Fermi level moves up in the energy. The relatively high values of μ_{eff} obtained for $x = 0.25$ and 0.50 suggest the partial polarization of conduction electrons in these two compounds induced by the presence of highly dispersive C$-p$ states. Further, the values of μ_{eff} derived from the experiments indicate that only the localized moments of Gd^{3+} ions are responsible for magnetism in $GdPd_3$ and $GdPd_3B_xC_{1-x}$ compounds. The electronic structure calculations also suggest that there is no induced moment on palladium and boron (and/or carbon) atoms. We have

also calculated Rhodes-Wohlfarth ratio [188], p_C/p_S, to investigate any possible contribution from itinerant magnetism due to Pd and the effect of hybridizations, if any. The p_C can be derived from μ_{eff} through the relation ${\mu^2}_{eff} = p_C(p_C + 1)$ and p_S is spontaneous moment per magnetic ion. The latter can be estimated from the Arrot plot for FM compounds below the transition temperature [188]. We have calculated this ratio for $GdPd_3$ as this is the only compound in present investigation with dominant FM interaction and exhibits saturation at higher fields. We find $p_C/p_S \sim 1.037$ which is close to the value 1, expected for a FM compound with localized moments. Thus the experimental values of μ_{eff}, electronic-structure calculations and the Rhodes-Wohlfarth ratio calculated for $GdPd_3$, concurrently establish that the magnetization in these compounds in entirely due to localized moments of rare-earth (RE) Gd^{+3} ions.

From the experimental data and their analysis discussed so far we have established that competing magnetic interactions exist in undoped $GdPd_3$. However, when we dope it with metalloids like B (and/or C) and in turn increase the distance between magnetic Gd^{+3} ions, compounds with $x = 0.25$ and 0.50 become AFM. Further increment of lattice parameter by introducing more B ($x = 0.75$ and 1.00) in to the lattice, the magnetic structure evolves toward a canted one. Absence of frequency dependent shift in AC-susceptibility data rules out the possibility of spin-glass like behavior and existence of uncorrelated short-range magnetic orders in the compounds. It may be worth mentioning here that we find $GdPd_3B_{0.25}C_{0.75}$ to be an interesting system exhibiting a combination of various properties, *viz.*, metallic behavior, NTE and antiferromagnetism with an isotropic cubic structure.

The value of θ_p directly correlates to the strength and nature of magnetic interactions present in a localized moment systems. In $GdPd_3B_xC_{1-x}$ compounds, the nature of variation of θ_p with lattice parameter [inset, Fig. 3.22] suggests the presence of RKKY oscillations, realization of which is not so common in bulk systems. In the case of multilayers, where one can tune the thickness (up to a few Angstroms) of non-magnetic spacer layer sandwiched between two magnetic layers, the observation of such oscillations is comparatively easy [189]. In contrast, in the case of bulk compounds one can tune only a very restricted spatial span. In the present study, we could only slightly vary the distance between magnetic ions (by insertion of appropriate amount of B and/or C), maintaining the isotropy and crystal symmetry. Due to such a restricted range of variation of lattice parameter, and hence the distance between magnetic RE ions, it is difficult to provide any quantitative estimate for the wavelength of the RKKY oscillation in the present case.

3.6.2 Magneto-transport measurements

3.6.2.1 Temperature dependence of resistivity

We have performed the magneto-transport measurements to further elucidate the nature of magnetic ordering present in the compounds. Depending upon the resistivity (ρ) behavior in the presence of external DC-magnetic field, the compounds studied here can be classified in two groups; (i) compounds exhibiting pure AFM ordering ($x = 0.25$ and 0.50) [Fig. 3.26(a)] and (ii) compounds possessing considerable FM or competing interactions ($GdPd_3$, $x = 0.75$ and 1.00) [Fig. 3.26(b)]. The variation of ρ as a function of T at two different externally applied DC-magnetic fields $H = 0$ and 7 T is presented in Fig. 3.26. As discussed in section 3.5, the ρ(T) behavior of $GdPd_3B_xC_{1-x}$ exhibits a change in slope around $T^* \sim 45$ K. One of the interesting aspect of the magneto-transport data is, the compounds that exhibit antiferromagnetism ($x = 0.25$ and 0.50) do not exhibit any appreciable magnetoresistance in the entire temperature range of measurement [Fig. 3.26(a)]. Other three compounds ($GdPd_3$ and $x = 0.75$, 1.00) that have significant presence of FM and (or) competing interactions, exhibit considerable negative magnetoresistance even in the paramagnetic range above their respective transition temperatures [Fig. 3.26(b)].

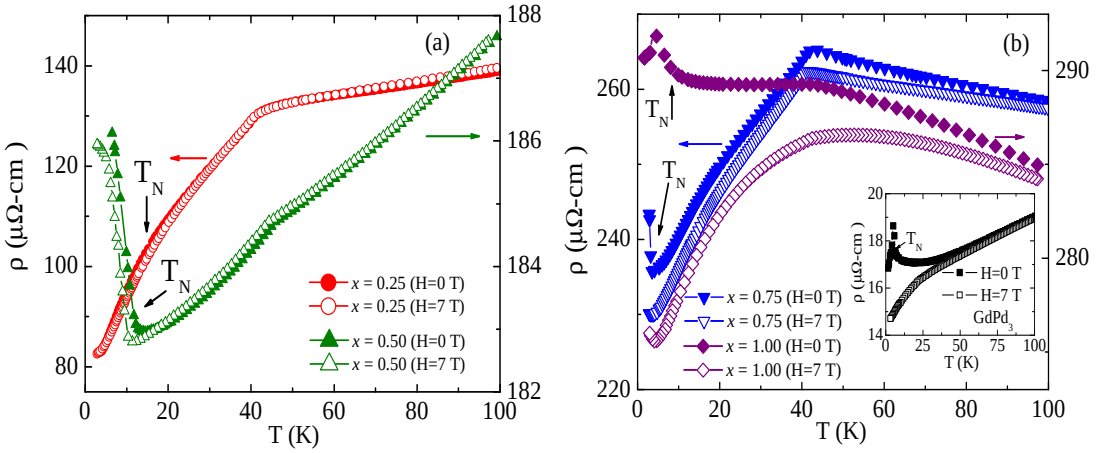

FIGURE 3.26: $\rho(H,T)$ as a function of temperature for $GdPd_3B_xC_{1-x}$ [(a) $x = 0.25$ & 0.50, and (b) $x = 0.75$ & 1.00]. Inset in (b) exhibits the $\rho(H,T)$ behavior for $GdPd_3$. Filled and open symbols represent measurements taken under $H = 0$ and 7 T respectively. The respective magnetic transition temperatures have been indicated by arrows.

The another aspect of ρ(T) behavior is the increase in ρ values below the respective magnetic ordering temperatures of the compounds. This increase has been monitored in all the compounds studied except $GdPd_3B_{0.25}C_{0.75}$ [Fig. 3.26]. Such an increase in ρ values below T_N has been mainly attributed to the opening of AFM super-zone gap [190, 191]. Super-zone gap appears due to presence of AFM magnetic-structure incommensurate

with the periodicity of crystal lattice. In that, the magnetic superlattice distorts the Fermi surface leading to the formation of an energy gap in the conduction band that affects the electrical transport and results in sharp increase of ρ below T_N. This effect reflects in the negative divergence of temperature derivative of ρ ($d\rho/dT$) below T_N [190, 191]. We have presented the variation of ($d\rho/dT$) with T in Fig. 3.27. It can be noticed from this figure that $H = 0$ data for all the compounds, except $GdPd_3B_{0.25}C_{0.75}$, exhibit a negative divergence below their corresponding magnetic ordering temperatures. However, in the case of $GdPd_3B_{0.25}C_{0.75}$ the value always remain positive. It suggests that in this compound the magnetic ordering, which was argued above as pure AFM, is also commensurate with the periodicity of the crystal lattice. On the other hand, the ρ(T) data for other four compounds suggest the opening of super-zone gap and in turn the existence of the incommensurate magnetic structures.

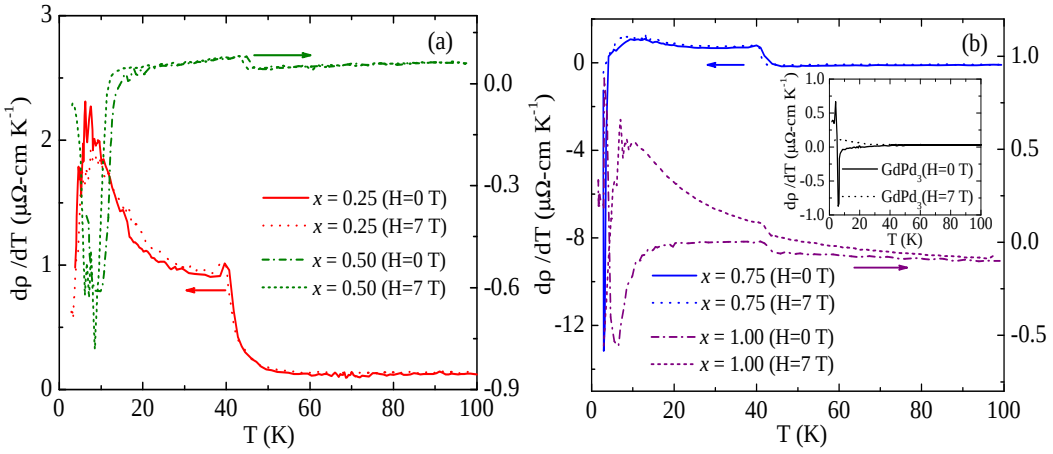

FIGURE 3.27: Temperature dependence of temperature derivative of resistivity for $GdPd_3B_xC_{1-x}$ [(a) $x = 0.25$ & 0.50, and (b) $x = 0.75$ & 1.00]. Inset in (b) exhibits the same for $GdPd_3$.

In most of the cases the effects of super-zone gap can be suppressed by the application of external magnetic fields [190, 191]. This collapse of super-zone gap in the presence of external magnetic field suppresses the ρ values below T_N and thus lead to negative magnetoresistance. This indeed is the case with three compounds, *viz.* $GdPd_3$, $x = 0.75$ and 1.00 [Fig. 3.26(b)]. However, the results are different for remaining two compounds, $GdPd_3B_{0.25}C_{0.75}$ and $GdPd_3B_{0.50}C_{0.50}$. As discussed above, AFM compound $GdPd_3B_{0.25}C_{0.75}$ does not show any signature of the presence of super-zone gap and hence its magnetic structure appears to be commensurate with the lattice periodicity. Application of moderate lab magnetic fields are not expected to alter the electrical properties, below T_N, of such systems. On the other hand, the situation is different for $GdPd_3B_{0.50}C_{0.50}$, which shows the signature of the presence of super-zone gap (the ρ increases below T_N), but the application of external magnetic field of 7 T does not effectively alter the ρ values below T_N. This suggests that in this compound, the moments

are strongly coupled in an AFM arrangement which is incommensurate with the lattice periodicity and the strength of coupling between magnetic moments is strong enough to refute the effect of externally applied magnetic field of 7 T. Thus it leads to negligible value of magnetoresistance below T_N.

3.6.2.2 Magnetic field dependence of resistivity

We have measured ρ as function of applied DC-magnetic field (magnetoresistance, R_H) at various temperatures (above and below the magnetic ordering temperatures of the compounds), *viz.* 4.2, 10 and 40 K [Fig. 3.28]. In addition, the MR of $GdPd_3$ has also been measured at a further lower temperature of 1.6 K [Fig. 3.28(a)] to investigate the oscillating behavior that has been observed at 4.2 K in this compound [Fig. 3.28(b)]. The results of data refinement and fitting parameters taken close to or above the ordering temperatures (T = 10 and 40 K), are reported in table 3.2. The value of MR for $GdPd_3$ is highest among the compounds studied here. In addition, MR for $GdPd_3$ exhibits oscillations between positive to negative values [Fig. 3.28 (a) and (b)], indicating the occurrence of spin-reorientation transitions on the application of external magnetic field. The MR data taken at T = 1.6 K exhibits the oscillatory behavior with more pronounced amplitude compare to that at T = 4.2 K. One would expect the appearance of such a phenomenon for a compound having competing magnetic interactions. In addition, the MR values for $GdPd_3$ tend to saturate above H = 2.5 T [Fig 3.28(a)], where the isothermal magnetization taken at 2 K [Fig. 3.23] also exhibits the tendency towards saturation, suggesting a common origin of both the observations.

The value of MR for $GdPd_3B_{0.25}C_{0.75}$ and $GdPd_3B_{0.50}C_{0.50}$ is very small at T = 4.2 K [Fig. 3.28(b)]. This is expected for a strongly coupled AFM systems below the ordering temperature, and has also been discussed in the previous section. For other two compounds (x = 0.75 and 1.00), the MR values are comparatively higher at this temperature [Fig. 3.28(b)]. At T = 10 K, the MR values for $GdPd_3B_{0.25}C_{0.75}$, $GdPd_3B_{0.50}C_{0.50}$ and $GdPd_3B_{0.75}C_{0.25}$ exhibit H^2 dependence in the whole range of applied field (Table 3.2). This behavior (H^2 dependence), which is a manifestation of the effect of external magnetic field on paramagnetic spin fluctuations, is expected in the paramagnetic temperature region [192, 193]. However, in the case of two extreme end-compositions (in the sense of lattice parameters values), $GdPd_3$ and $GdPd_3B$, the H^2 dependence persists only at low field and data at high fields deviate from this dependence [Fig. 3.28(c)]. This observation indicates that in these two compounds short-range magnetic correlations persists up to 10 K, which is slightly higher than their respective magnetic ordering temperatures. At T = 40 K, which is well above the magnetic ordering temperatures of all the compounds, the values of MR for AFM $GdPd_3B_{0.25}C_{0.75}$ and $GdPd_3B_{0.50}C_{0.50}$

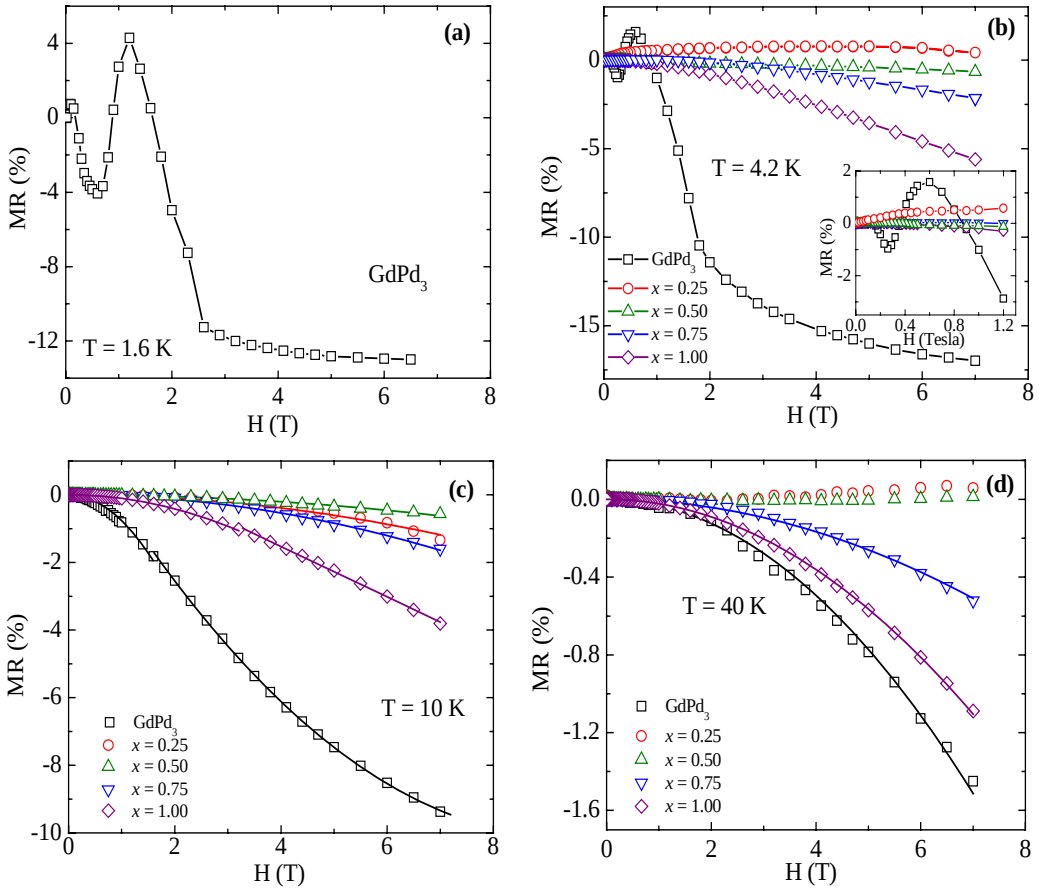

FIGURE 3.28: Magnetoresistance, $R_H = \frac{\rho(H)-\rho(H=0)}{\rho(H=0)}$(%), as function of applied DC magnetic field, at four different temperatures, (a) $T = 1.6$, (b) 4.2, (c) 10 and (d) 40 K. The lines in plot (a) and (b) are guide to eye, whereas the lines in plot (c) and (d) are fit to the data with fitting functions and parameters described in Table 3.2. Inset in plot (b) shows the same in restricted field range at $T = 4.2$ K.

become very small and could not be fitted to any desirable function (Table 3.2). However, MR exhibits H^2 dependence for other three compounds in the whole range of applied magnetic fields.

The field and temperature dependent electrical-transport behavior suggests that the electrical transport in this series of compounds critically correlates with the nature of magnetic ordering present in the compounds, particularly at low temperature.

Compounds	**Nature of Ordering**	**MR (T=10 K)**	**MR (T=40 K)**
$GdPd_3$	Competing interactions	aH^2 $(0 \leq H < 1.6$ T) $(a = -0.728)$ $aH^2 + bH + c$ $(1.6 \leq H \leq 7$ T), $(a = 0.142, b = -2.633, c = 2.150)$	aH^2 $(0 \leq H \leq 7$ T) $(a = -0.031)$
$GdPd_3B_{0.25}C_{0.75}$	AFM (Commensurate)	aH^2 $(0 \leq H \leq 7$ T) $(a = -0.024)$	$R_H < 0.07\%$ $(0 \leq H \leq 7$ T)
$GdPd_3B_{0.50}C_{0.50}$	AFM (incommensurate)	aH^2 $(0 \leq H \leq 7$ T) $(a = -0.013)$	$R_H < 0.02\%(0 \leq H \leq 7$ T)
$GdPd_3B_{0.75}C_{0.25}$	Canted structure	$aH^2(0 \leq H \leq 7$ T) $(a = -0.034)$	aH^2 $(0 \leq H \leq 7$ T) $(a = -0.010)$
$GdPd_3B$	Canted structure	aH^2 $(0 \leq H < 2.9$ T) $(a = -0.104)$ $bH + c$, $(2.9 \leq H \leq 7$ T) $(b = -0.747, c = 1.462)$	aH^2 $(0 \leq H \leq 7$ T) $(a = -0.023)$

TABLE 3.2: The type of ordering present in the compounds, nature of the fit and corresponding parameters for magnetoresistance, $R_H = \rho(H) - \rho(H = 0)/\rho(H = 0)$, at $T = 10$ and 40 K for $GdPd_3$ and $GdPd_3B_xC_{1-x}$ (x=0.25, 0.50, 0.75 and 1.00).

3.7 Study of off-stoichiometric metallic perovskite compounds $GdPd_3B_x$ (x = 0.25, 0.50 and 0.75)

As discussed in the previous section, the magnetic interactions present in Gd and Pd based metallic-perovskite compounds, $GdPd_3B_xC_{1-x}$, can be modified by changing the distance between the magnetic Gd^{+3} ions. The variation in the distance between the Gd^{+3} ions, that occupy the cube corner positions (0, 0, 0) of the cubic unit-cell of this compound, is achieved by introducing non-magnetic light metalloids (boron and carbon) at the body center lattice site of the unit-cell. Magnetic behavior of the parent binary compound, $GdPd_3$, suggests the presence of competing interactions in this compound *i.e.* the significant presence of both FM as well as AFM interactions. On the other hand, depending upon their lattice parameter (a) values, boron and (or) carbon doped compounds exhibit dominating AFM behavior or occurrence of canted magnetic structures.

It has been found that while the off-stoichiometric compositions with boron, $GdPd_3B_x$, crystallize with the same crystal-structure [Fig. 3.1] as that of $GdPd_3B_xC_{1-x}$, the same with carbon, $GdPd_3C_x$, do not form in a single phase. However, in contrast to the stoichiometric $GdPd_3B_xC_{1-x}$ where all the body-center sites are filled either with boron or with carbon, the off-stoichiometry of boron in $GdPd_3B_x$ leads to vacancies at the body-center sites of a fraction (1-x) of the unit cells. In addition, similar to $GdPd_3B_xC_{1-x}$, the lattice parameter of of $GdPd_3B_x$ can also be modified by varying

the boron-stoichiometry. As the electrical and magnetic properties of $GdPd_3B_xC_{1-x}$ exhibit a strong-dependence on the value of lattice parameter, it is worth to make a comparative study of the various macroscopic physical properties of $GdPd_3B_x$ *vis-à-vis* $GdPd_3B_xC_{1-x}$ compositions having nearly the same value of lattice parameter.

In this work, we present the magnetic, electrical and magneto-transport properties of the off-stoichiometric metallic-perovskite compounds $GdPd_3B_x$ ($x = 0.25, 0.50$ and 0.75). The present study of $GdPd_3B_x$ and comparison of the results with those of $GdPd_3B_xC_{1-x}$ helps us to investigate the role played by carbon in stabilizing the pure-AFM structure in some of the compositions of $GdPd_3B_xC_{1-x}$. It also helps in resolving the underlying reason for the observed high effective paramagnetic moment values (μ_{eff}) in high carbon-stoichiometric compositions of $GdPd_3B_xC_{1-x}$. Our results suggest that similar to $GdPd_3B_xC_{1-x}$, the magnetic behavior of $GdPd_3B_x$ depends sensitively on the $Gd^{+3} - Gd^{+3}$ distance and changes considerably with the increment in the value of lattice parameter induced by the boron doping.

3.7.1 Crystal structure of $GdPd_3B_x$

The powder XRD data analysis suggests that similar to stoichiometric $GdPd_3B_xC_{1-x}$ (section 3.3), all the $GdPd_3B_x$ compositions crystallize in a single phase cubic structure with $Pm\bar{3}m$ space-group symmetry [Fig. 3.29]. The values of lattice parameters of cubic unit-cells deduced from the XRD data refinement have been listed in Table 3.3. The XRD data analysis suggests that insertion of boron at the body center site leads to isotropic lattice expansion, in that the value of a increases with boron stoichiometry (x). However, this increment in a becomes negligible for $x \geq 0.50$ where the value tends to saturate (Table 3.3). This observation is different from that in the case of $GdPd_3B_xC_{1-x}$, where the a tends to saturate for $x \geq 0.75$ (Table 3.3). It may be mentioned that for any particular value of x (x=0.25, 0.50 and 0.75), the value of a for $GdPd_3B_x$ is greater than that of $GdPd_3B_xC_{1-x}$. For example, the value of a for $GdPd_3B_{0.50}$ is 4.141 Å, which is significantly greater than that of $GdPd_3B_{0.50}C_{0.50}$ for which a is 4.118 Å. It may also be mentioned here that the outcome of our electronic-structure calculations performed on $GdPd_3B_xC_{1-x}$ suggests that, C-Pd bonds are more directional compared to B-Pd bonds (section 3.5.1). It appears that insertion of carbon, which is smaller than boron and forms a more directional bond with Pd, leads to stabilize the cubic unit-cells with relatively small volume.

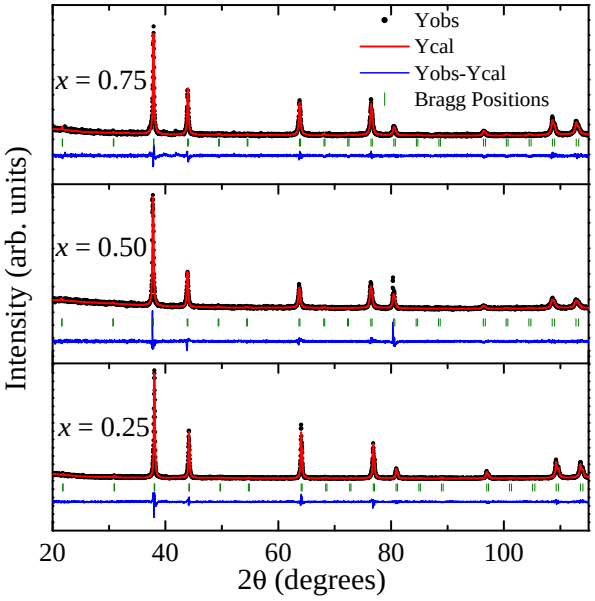

FIGURE 3.29: Powder-XRD patterns of $GdPd_3B_x$ ($x = 0.25, 0.50$ and 0.75) measured at room temperature. The picture exhibits experimental data points, calculated and difference profiles along with Bragg positions.

3.7.2 DC and AC magnetic measurements

Temperature variation of zero-field-cooled (ZFC) magnetization (M) of $GdPd_3B_x$ ($x = 0.25, 0.50$ and 0.75) is shown in Fig. 3.30. For comparison, the data for $GdPd_3$ ($x = 0.00$) and $GdPd_3B$ ($x = 1.00$) are also presented in the figure. The figure exhibits that the increase in lattice parameter by introducing a small amount of boron ($x = 0.25$) leads to a significant decrease in the M(T) values. The results exhibit that the M(T) of $GdPd_3B_{0.25}$, near the ordering temperature, is approximately an order of magnitude smaller than that of undoped $GdPd_3$. Further increase of lattice parameter generated by increasing the value of x, reverses this trend and in that the M(T) starts increasing with increase in the value of x for $x \geq 0.50$. A similar behavior was earlier observed in the case of stoichiometric compositions, $GdPd_3B_xC_{1-x}$, and was attributed to variation of the strength and nature of magnetic interactions with $Gd^{+3} - Gd^{+3}$ ions distance (section 3.6.1).

Temperature dependence of inverse-molar susceptibility (χ^{-1}) is shown in Fig. 3.31. The values of various parameters, *e.g.* Néel temperature (T_N), paramagnetic Curie temperature (θ_p) and the effective paramagnetic moment (μ_{eff}) etc., deduced from M(T) and χ^{-1}(T) data have been summarized in Table 3.3. For comparison, we have also included the values of all these parameters (section 3.6.1) for the stoichiometric compositions $GdPd_3B_xC_{1-x}$. The values of θ_p, for all the three off-stoichiometric compositions ($x = 0.25, 0.50$ and 0.75), are high in magnitude and negative in sign. This infers the

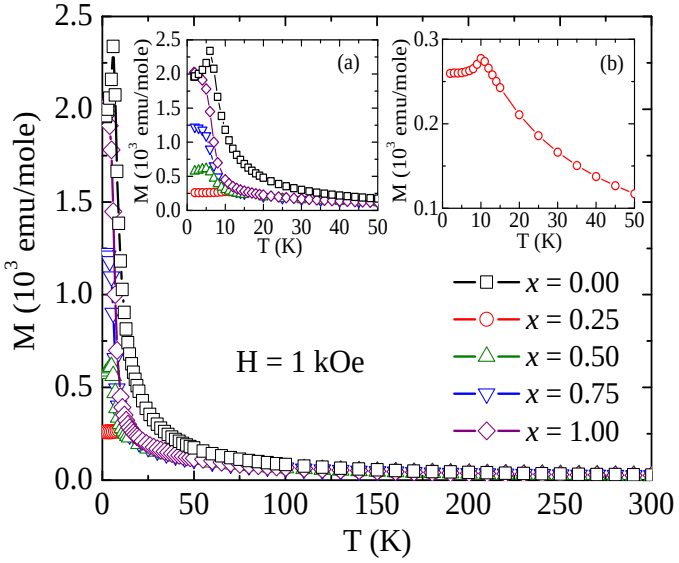

FIGURE 3.30: Temperature dependence of ZFC-magnetization of $GdPd_3B_x$ ($x = 0.00, 0.25, 0.50, 0.75$ and 1.00). The data for two extreme compositions, $x = 0.00$ and 1.00, have been already been discussed in section 3.6.1. Inset (a) exhibits the same in low temperature region. Inset (b) shows M(T) behavior of $x = 0.25$ composition. For this composition, M(T) is nearly one order of magnitude less compare to that of $GdPd_3$.

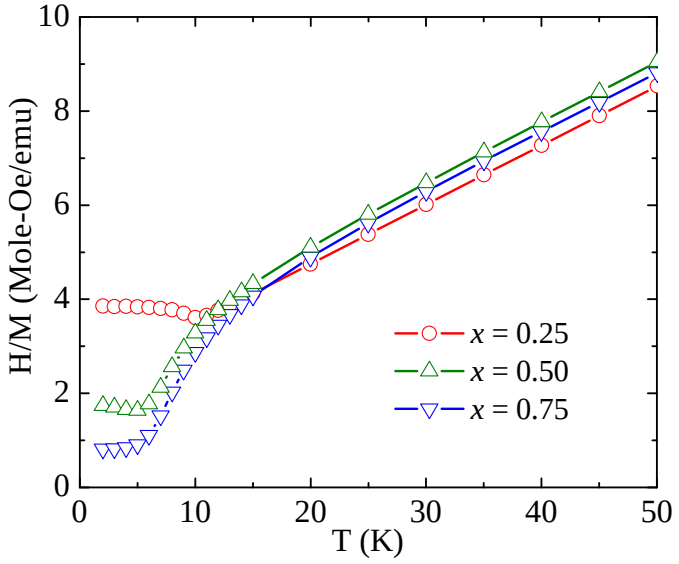

FIGURE 3.31: Temperature dependence of inverse-molar susceptibility of $GdPd_3B_x$ ($x = 0.25, 0.50$ and 0.75).

domination of AFM-interaction in these compound. In the case of $GdPd_3B_{0.25}$, the nature of the observed M(T) behavior, that exhibits a peak at 10 K, is close to that expected from an AFM system. On the other hand, the χ^{-1}(T) that gets reduced with the decrease in temperature and then tends to saturate at low temperatures, indicates that the magnetic structure for $GdPd_3B_{0.50}$ and $GdPd_3B_{0.75}$ compositions could be of canted

in nature [187]. A similar behavior was earlier observed in the case of stoichiometric compositions $GdPd_3B_{0.75}C_{0.25}$ and $GdPd_3B$ (section 3.6.1). As already mentioned in the case of $GdPd_3B_{0.75}C_{0.25}$ and $GdPd_3B$ in section section 3.6.1, the proposed canted structure for $x = 0.50$ and 0.75 compositions is only a hypothesis based on macroscopic magnetic measurements and the exact magnetic structure can only be deduced from neutron diffraction measurements.

The results of AC-susceptibility measurements on $GdPd_3B_x$ ($x = 0.25, 0.50$ and 0.75) are shown in Fig. 3.32. In the case of $GdPd_3B_{0.50}$ and $GdPd_3B_{0.75}$, both χ' and χ'' exhibit peak [Fig. 3.32]. These results also suggest that although the dominating interaction in the case of these two compounds is of AFM nature, the magnetic structure is not purely AFM type and be of canted in nature. In contrast, in the case of $GdPd_3B_{0.0.25}$, χ' exhibits a peak resembling AFM ordering, however χ'' is nearly zero in the entire temperature range of measurement [Fig. 3.32]. This behavior is very similar to what we observed in the case of $GdPd_3B_{0.25}C_{0.75}$ and $GdPd_3B_{0.50}C_{0.50}$ (section 3.6) and suggest that the magnetic ordering in $GdPd_3B_{0.0.25}$ is of AFM type.

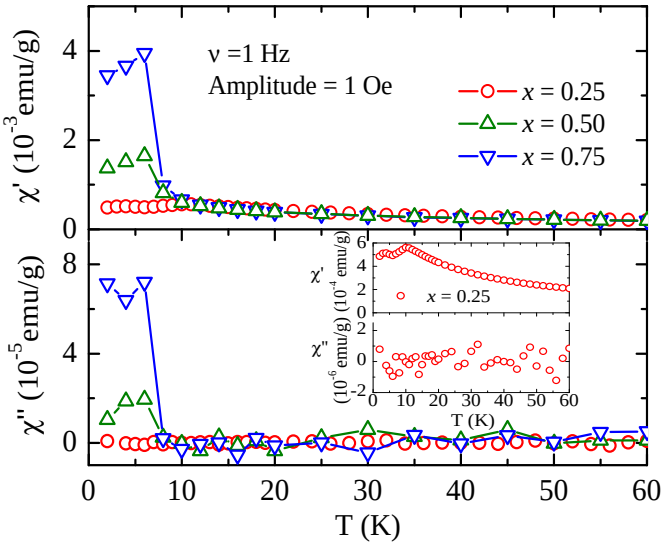

FIGURE 3.32: In-phase (χ') and out-of-phase (χ'') components of AC-susceptibility as a function of temperature for $GdPd_3B_x$ ($x = 0.25, 0.50$ and 0.75). Inset shows the same for $x = 0.25$ in an expanded scale.

We would like to emphasis that the compounds that possess nearly the same value of $Gd^{+3} - Gd^{+3}$ distance, irrespective of weather the composition is $GdPd_3B_x$ or $GdPd_3B_xC_{1-x}$, exhibit nearly the same magnetic behavior. For example, all the compositions with $a \sim 4.14$ Å ($GdPd_3B_{0.50}$, $GdPd_3B_{0.75}$, $GdPd_3B_{0.75}C_{0.25}$ and $GdPd_3B$) exhibit the possibility of the presence of canted magnetic structure and possess nearly the same values of various parameters (Table 3.3) that define the magnetic behavior of

Compounds	a**(Å)**	T_N**(K)**	θ_p**(K)**	$\mu_{eff}(\mu_B)$	$\chi(T=0)/\chi(T=T_N)$
$GdPd_3B_{0.25}$	4.125	10	-17.9	7.96	0.94
$GdPd_3B_{0.50}$	4.141	5	-20.5	7.94	0.89
$GdPd_3B_{0.75}$	4.142	8	-23.0	8.09	2.56
$GdPd_3$	4.089	6	3.5	8.03	0.82
$GdPd_3B_{0.25}C_{0.75}$	4.112	15	-7.2	8.60	0.92
$GdPd_3B_{0.50}C_{0.50}$	4.118	12	-18.5	8.19	0.73
$GdPd_3B_{0.75}C_{0.25}$	4.141	7	-25.3	7.99	2.72
$GdPd_3B$	4.143	8	-20.2	8.04	2.96

TABLE 3.3: The lattice parameter (a), Néel temperature (T_N), paramagnetic Curie temperature (θ_P), effective paramagnetic moment (μ_{eff}) and ratio of susceptibilities at $T = 0$ K (determined by extrapolation of the data) and $T = T_N$ for $GdPd_3B_x$ ($x = 0.25, 0.50$ and 0.75), $GdPd_3$ and $GdPd_3B_xC_{1-x}$ ($x = 0.25, 0.50, 0.75$ and 1.00).

a compound. This again strengthen the concept that the magnetic behavior of doped compounds (both $GdPd_3B_x$ and $GdPd_3B_xC_{1-x}$) depends delicately on the distance between Gd^{+3} ions. In addition, it must be pointed out that although the distance between Gd^{+3} ions plays a major role in defining the magnetic behavior of both $GdPd_3B_x$ and $GdPd_3B_xC_{1-x}$, the observation of anomalously high value of μ_{eff} and stabilization of a pure-AFM structure in the compounds having high carbon-stoichiometry, *viz.* $GdPd_3B_{0.25}C_{0.75}$ and $GdPd_3B_{0.50}C_{0.50}$ (section 3.6.1), suggests that presence of carbon also significantly affects the magnetic behavior of the compounds. Our claim made in the section section 3.6.1 in the case of $GdPd_3B_xC_{1-x}$ that the anomalously high value of μ_{eff} observed for high carbon-stoichiometry compounds, $GdPd_3B_{0.25}C_{0.75}$ and $GdPd_3B_{0.50}C_{0.50}$, is a manifestation of the partial polarization of the conduction electrons induced by the presence of carbon atoms, gets credence by comparing the μ_{eff} values of $GdPd_3B_{0.25}C_{0.75}$ and $GdPd_3B_{0.50}C_{0.50}$ with that of carbon deficient $GdPd_3B_{0.25}$ and $GdPd_3B_{0.50}$ (Table 3.3).

For example, the value of μ_{eff} for $GdPd_3B_{0.25}C_{0.75}$ is 8.60 μ_B, while the same for $GdPd_3B_{0.25}$ is 7.96 μ_B. This clearly indicates that presence of carbon influences the μ_{eff} and in that the value increases. On the other hand, the role played by carbon in stabilizing the AFM structure becomes more evident when we compare the magnetic behavior of off-stoichiometric compositions, *viz.* $GdPd_3B_{0.50}$, with the compositions containing carbon, *viz.* $GdPd_3B_{0.50}C_{0.50}$. While the magnetic behavior of $GdPd_3B_{0.50}$ suggests the presence of a canted-magnetic structure, the same for $GdPd_3B_{0.50}C_{0.50}$ exhibits a AFM type ordering. This observation indicates that the introduction of carbon helps in stabilizing a AFM behavior. However, we would like to point out that,

as the introduction of carbon also leads to reduction in the value of a (Table 3.3), it is difficult to resolve from the available informations whether the stabilization of AFM structure in the carbon-doped compounds is due to the modified electronic-structure or merely a manifestation of the change in $Gd^{+3} - Gd^{+3}$ distance.

The variation of isothermal magnetization of $GdPd_3B_x$ with applied DC-magnetic field is shown in Fig. 3.33. Depending upon the value of x, the three different compositions exhibit slightly different M(H) behavior. As expected from an AFM system, the isothermal magnetization of $GdPd_3B_{0.25}$ varies linearly with the applied DC-field in the range of $0 \leq H \leq 5$ T. However, at $H = 5$ T, the slope of M(H) curve exhibits a change and in that it increases. This behavior is indicative of some kind of field-induced effect occurring at 5 T. On the other hand other two compounds, $GdPd_3B_{0.50}$ and $GdPd_3B_{0.75}$ exhibit linear M(H) behavior at high fields ($H > 0.25$ T for $x = 0.50$ and $H > 1.00$ T for $x = 0.75$) and exhibit non-linear behavior at low fields. As discussed earlier in section 3.6.1, the observed low-field non-linear behavior of M(H) can be considered as an indication of the presence of proposed canted-magnetic structures in $GdPd_3B_{0.50}$ and $GdPd_3B_{0.75}$.

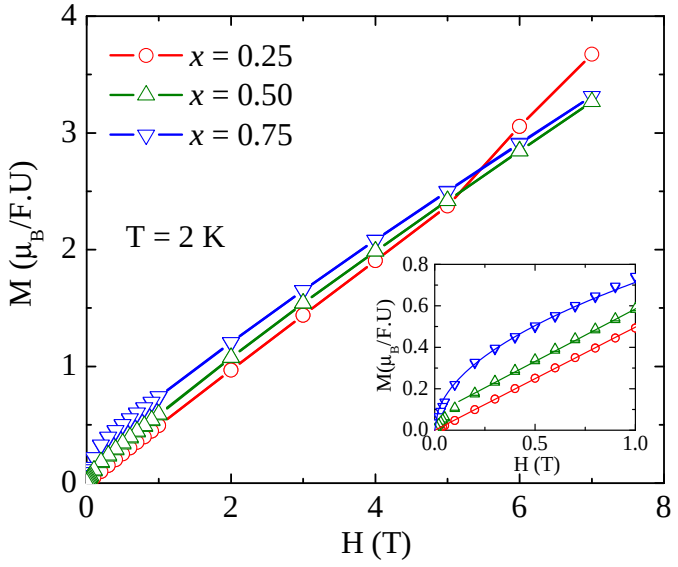

FIGURE 3.33: Variation of isothermal magnetization of $GdPd_3B_x$ ($x = 0.25, 0.50$ and 0.75) with applied DC-magnetic field. Inset exhibits the same in lower field region. The lines in the main plot are guide to eye while the same in the inset are fit, which are linear for $x = 0.25$ and 0.50 and proportional to $H^{1/2}$ for $x = 0.75$.

3.7.3 Electrical and magneto-transport measurements

Results of heating and cooling-cycle measurements of the zero-field $\rho(T)$ of $GdPd_3B_x$ ($x = 0.25$, 0.50 and 0.75) are shown in Fig. 3.34. For comparison, the ρ(T) of $GdPd_3B$ is

also included in the inset of Fig. 3.34(b). One important observation is the occurrence of a transition in TCR at $T^* \sim 45$ K. While no such transition in TCR was observed in the case of $GdPd_3$, it reflected its signature nearly at the same temperature (~ 45 K) in the case of all doped stoichiometric compositions $GdPd_3B_xC_{1-x}$ (section 3.5). The observed transition in TCR of $GdPd_3B_xC_{1-x}$ compositions, which was attributed to the structural anomalies occurring at the same temperature, is an inherent property of boron (and/or carbon) doped metallic perovskite compounds. In addition, while the transition is very sharp in the case of $GdPd_3B_{0.50}$ and $GdPd_3B_{0.75}$, it manifests only as a minor kink in ρ(T) of $GdPd_3B_{0.25}$ [Fig. 3.34]. In the case of $GdPd_3B_{0.25}$ and $GdPd_3B_{0.75}$, where there is an asymmetric distribution of boron and vacancies, the heating and cooling cycle data exhibit a clear hysteresis at 45 K [Fig. 3.34]. This suggests that the structural transition in these two compounds is of first order in nature. On the other hand, for $GdPd_3B_{0.50}$ (and also for $GdPd_3B$) that have symmetric distribution of boron and vacancies, the structural anomalies appear to be reversible in nature [Fig. 3.34].

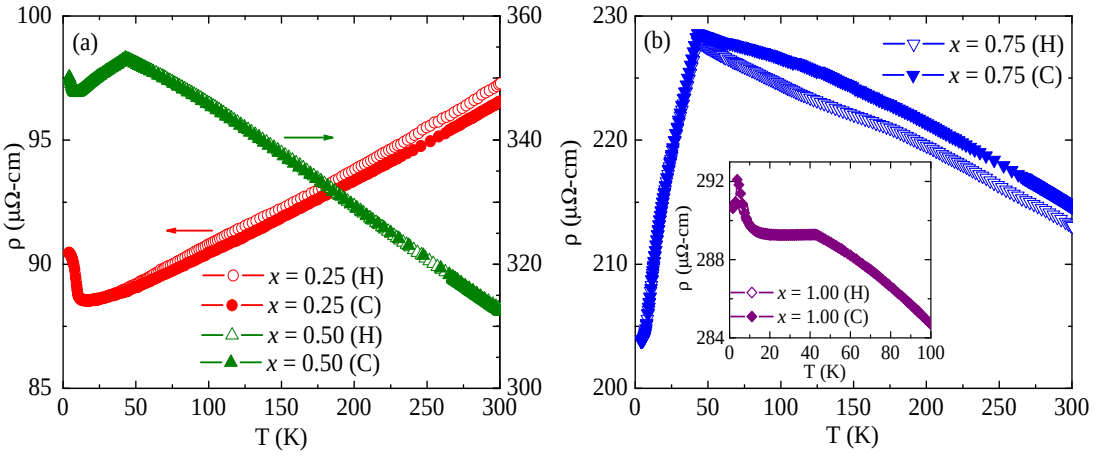

FIGURE 3.34: Resistivity (ρ) as function of temperature for $GdPd_3B_x$ [(a) $x = 0.25$ and 0.50, and (b) $x = 0.75$]. For comparison, the data of $x = 1.00$ have also been shown in (b). The figure exhibits the $\rho(T)$ data taken in both heating (denoted by 'H') and colling cycles (denoted by 'C') of measurements.

For $T > 45$ K the TCR of $GdPd_3B_{0.25}$ exhibits a positive value while the same is negative for $GdPd_3B_{0.50}$ and $GdPd_3B_{0.75}$. It was hypothesized earlier in the case of $GdPd_3B_xC_{1-x}$ that the negative pressure generated upon boron insertion in the cubic unit-cells leads to some local distortions and strain in the lattice, particularly at low temperatures (section 3.5). As the powder-XRD measurement only produces the average macroscopic picture, such local lattice distortions can not be detected by this technique [54]. This strain manifests in an increment of electron-effective mass, which relaxes with temperature due to thermal expansion and leads to a negative value of TCR in high boron-stoichiometry compounds. A similar explanation is also applicable for the observed negative TCR (for $T > 45$ K) in the case of $GdPd_3B_{0.50}$ and $GdPd_3B_{0.75}$.

In the low temperature region, ρ(T)exhibits an increase with decrease in temperature below the respective magnetic-ordering temperatures of $GdPd_3B_{0.25}$ and $GdPd_3B_{0.50}$ [Fig. 3.34(a)]. As mentioned in the section 3.6.2.1, this behavior can be attributed to the effect of opening of superzone gap in the conduction band due to the presence of a magnetic-lattice incommensurate with the periodicity of crystal-lattice. In general, application of external magnetic field suppresses the effect of superzone gap. However, in the case of $GdPd_3B_{0.25}$ and $GdPd_3B_{0.50}$, even the application of $H = 7$ T field does not make any significant difference in the sense that $\rho(T)$ still exhibits an increase below T_N [Fig. 3.35(a)]. This behavior suggests that the coupling between magnetic moments in the incommensurate AFM structure of $GdPd_3B_{0.25}$ and $GdPd_3B_{0.50}$ is strong enough to refute the effect of external applied field of 7 T. A similar behavior was earlier observed in the case of $GdPd_3B_{0.50}C_{0.50}$ (section 3.6.2.1). One the other hand, in the case of $GdPd_3B_{0.75}$, ρ(T) does not exhibit any increase below T_N [Fig. 3.34(b)], suggesting the absence of superzone gap effect in this composition. $GdPd_3B_{0.75}$ has been argued earlier to possess canted-magnetic structure and in general in the case of such canted-structured compounds one expects more prominent effect of superzone gap. Hence the absence of the signature of superzone gap effect in this compound is a bit puzzling. In fact, in the case of $GdPd_3B_{0.75}$, ρ(T) exhibits an increase below T_N in the presence of applied field of 7 T [Fig. 3.35(b)]. This behavior suggests that application of external magnetic field disturbs an otherwise commensurate magnetic structure. The exact underlying reason for this behavior is yet to be understood.

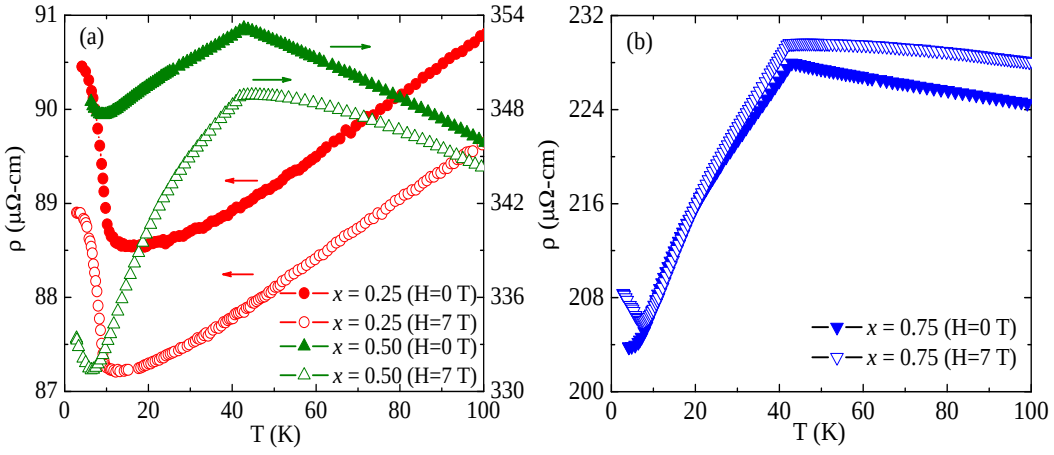

FIGURE 3.35: Temperature variation of resistivity ρ(H, T) of $GdPd_3B_x$ in the presence of external magnetic of $H = 0$ and 7 T [(a) $x = 0.25$ and 0.50, and (b) $x = 0.75$].

The variation of MR with the applied magnetic field for $GdPd_3B_x$ ($x = 0.25$, 0.50 and 0.75) is shown in Fig. 3.36. In the case of $GdPd_3B_{0.25}$, the MR values are relatively smaller ($\sim$ 1%) compare to other two compositions [inset, Fig. 3.36(a)] and become neglizible for $T > 20$ K. Small and negative value of observed MR for $GdPd_3B_{0.25}$ suggets that although the magnetic behavior indicates for the presence of dominating AFM

interaction, FM interactions also have contribution that manifest in the observed negative MR in this compound. The magnitude of MR of $GdPd_3B_{0.50}$, which is highest among all the three compositions studied here, decreases with the increase of temperature [Fig. 3.36(a)]. At $T = 10.0$ K, which is higher than the ordering temperature of this compound, MR exhibits H^2 dependence at low fields ($H < 3.5$ T) and then varies linearly at high fields. It may be mentioned that the suppression of paramagnetic spin-fluctuations in the presence of external magnetic field leads to a H^2 field-dependence of MR in paramagnetic temperature region [192, 193]. In the case of $GdPd_3B_{0.50}$, the deviation from H^2 dependence above 3.5 T suggests that field-induced short-range magnetic correlations persist up to 10 K in this compound. For $T = 20.0$ and 50. K, the MR exhibits a typical H^2 dependence in the whole range of applied magnetic field.

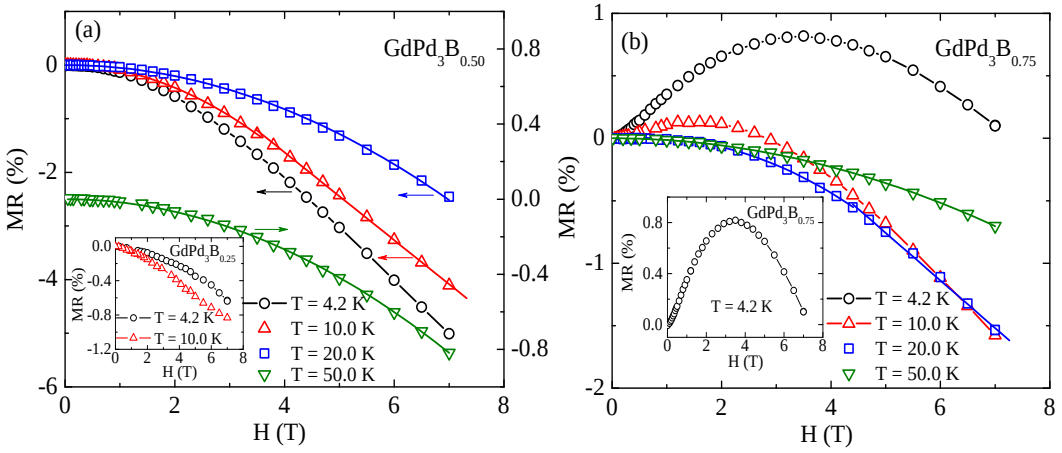

FIGURE 3.36: Field dependence of magnetoresistance, $R_H = \frac{\rho(H)-\rho(H=0)}{\rho(H=0)}(\%)$, of $GdPd_3B_x$ measured at $T = 4.2, 10.0, 20.0$ and 50.0 K [(a) $x = 0.50$, and (b) $x = 0.75$]. The inset in (a) exhibits the same for $x = 0.25$ measured at $T = 4.2$ and 10.0 K. Inset in (b) exhibits the magnetoresistance behavior of $x = 0.75$ composition at $T = 4.2$ K. This data is same as that shown in the main figure. In the case of $GdPd_3B_{0.50}$, the lines at $T = 10, 20$ and 50 K are the fit (see the text), while the same at $T = 4.2$ K is guide to eye. In the case of $GdPd_3B_{0.75}$, the lines at $T = 20$ and 50 K are fit (see the text), while the same at $T = 4.2$ and 10 K are guide to eye. The lines in both the insets are guide to eye.

Similar to the ρ(T), MR of $GdPd_3B_{0.75}$ also exhibits anomalous behavior. In contrast to $GdPd_3B_{0.25}$ and $GdPd_3B_{0.50}$, MR of $GdPd_3B_{0.75}$ exhibits a positive value in the entire field range of measurement when measured at 4.2 K. At this temperature, which is lower than the ordering temperature (T_N=8 K) of $GdPd_3B_{0.75}$, MR first increases with the increase of field, exhibits a cusp with a maximum at $H = 3.5$ T and then starts decreasing with the further increase of the field. The field dependence of MR is almost symmetrical around $H = 3.5$ T. A similar behavior was earlier observed in the case of $Dy_2Ni_3Si_5$ [194], where the observed maxima in the MR(H) was attributed to

the metamagnetic transition occurring at the same field in the isothermal magnetization measurement. However, in the case of $GdPd_3B_{0.75}$ we do not observed any evidence of such metamagnetic transition in isothermal magnetization measurement and M varies linearly with H for $H > 1$ T [Fig. 3.33]. In contrast to the sharp metamagnetic transition that occurs in the case of $Dy_2Ni_3Si_5$, we believe that the observed field dependence of MR is due to a gradual spin-reorientation transition occurring with the increase in applied field in this compound. It may be mentioned here that the evidence of such spin-reorientation transitions in MR(H) measurements was also monitored in the case of $GdPd_3$ for $H < 2$ T (section 3.6.2.2), where the observed oscillating behavior of MR(H) does not also correlate to any kind of field-induced metamagnetic transition in isothermal magnetization measurement. At $T = 10$ K, which is slightly higher than the ordering temperature of $GdPd_3B_{0.75}$, MR exhibits a positive value for $0 < H < 3$ T with a maxima at $H = 1.6$ T and then it turns negative with further increase of H [Fig. 3.36(b)]. For $T \geq 20$ K, the MR exhibits the typical H^2 dependence with negative values in entire field range [Fig. 3.36(b)]. It is worth mentioning here that ρ(T) of $GdPd_3B_{0.75}$ exhibits a strong hysteresis effect, both in terms of temperature as well as applied magnetic field. For example, in a measurement where we first heat the sample up to the desired temperature (say 50 K, which is higher than T_N of this compound) and then measure the field dependence of MR, we observe a typical H^2 dependence with negative values [Fig. 3.36(b)]. On the contrary, when we perform the measurement during the heating cycle keeping the applied field constant (0 or 7 T), at a particular temperature $T > T^*$ (say 50 K), the observed values of $\rho(H = 7$ T) are greater than the same of $\rho(H = 0$ T), thus leading to positive MR values [Fig. 3.35(b)]. These observations suggest that when we first apply the magnetic field of 7 T at lowest temperature of measurement and then heat the sample, some uncorrelated short-range-orders persist even for $T > T^*$ and contribute in the scattering process, thus leading to an increased value of the ρ.

3.8 Conclusion

In this chapter, we have investigated the structural, thermal expansion, magnetic and transport (electrical and magneto-transport) properties of Gd and Pd based metallic perovskite compounds $GdPd_3B_xC_{1-x}$ ($x = 0.25, 0.50, 0.75$ and 1.00) along with the parent binary compound $GdPd_3$. An attempt has been made to compare and correlate the various physical properties of stoichiometric compositions $GdPd_3B_xC_{1-x}$ with that of off-stoichiometric compositions $GdPd_3B_x$. In our study, we have observed novel phenomenon of NTE in one of the stoichiometric compositions $GdPd_3B_{0.25}C_{0.75}$. We have also observed NTCR in an ordered crystalline compound $GdPd_3B$.

Our data and their analysis presented section 3.4 show that low energy transverse vibrational modes, which play a crucial role in determining the sign of thermal expansion coefficient in oxides, may also be dominant in the case of doped metallic system. The gradual freezing of these transverse modes, responsible for isotropic NTE observed in metallic $GdPd_3B_{0.25}C_{0.75}$, below a critical temperature causes a significant reduction in the resistivity values at low temperatures. The synergy between isotropic NTE and electrical transport in metals appears to be a promising area of application oriented research.

In section 3.5, we have investigated the electrical transport behavior of $GdPd_3B_xC_{1-x}$ and $GdPd_3$. We have observed unusual NTCR in an ordered (within the resolution limit $> 0.2\%$) polycrystalline compound. Our data suggests that chemical disorder is not the causative factor and the possible origins of NTCR have been discussed. Electronic structure calculations confirm the metallic nature of the compounds throughout the concentration range. We have observed a contrasting electrical and structural properties of stoichiometrically symmetric ($x = 0.50$ and 1.00) and asymmetric ($x = 0.25$ and 0.75) $GdPd_3B_xC_{1-x}$ compounds in the low temperature region. $GdPd_3B_xC_{1-x}$ series of compounds show existence of a transition temperature with distinctly different low temperature behavior, which is more prominent in stoichiometrically asymmetric compounds.

Similar to the TCR, the magnetic interactions present in these compounds also delicately depend upon the cubic lattice parameter. The magnetic interaction in $GdPd_3$, which was earlier argued to be AFM, is found competing with dominating FM contribution. $GdPd_3B_{0.25}C_{0.75}$ and $GdPd_3B_{0.50}C_{0.50}$, that have slightly higher lattice parameter in comparison with $GdPd_3$ with the same crystal symmetry, exhibit AFM ordering. The temperature and magnetic field dependent electrical-transport measurements indicate that the AFM order present in $GdPd_3B_{0.25}C_{0.75}$ is commensurate with the periodicity of the crystal lattice. However, the same in $GdPd_3B_{0.50}C_{0.50}$ is incommensurate in nature. Further increase of inter atomic Gd-Gd distance, by increasing the B stoichiometry, leads to a canted arrangement of moments in $GdPd_3B_{0.75}C_{0.25}$ and $GdPd_3B$. The variation of experimentally derived θ_p in $GdPd_3B_xC_{1-x}$ resembles RKKY oscillations. Results of magneto-transport measurements are consistent with the nature of magnetic ordering present in the compounds. The value of MR for $GdPd_3$ is highest among the compounds studied here and exhibits oscillating behavior, which is suggestive of the occurrence of spin-reorientation transitions with the application of external magnetic field. The value of R_H for $GdPd_3B_{0.25}C_{0.75}$ and $GdPd_3B_{0.50}C_{0.50}$ was found to be very small as expected for a strongly coupled AFM system.

In section 3.7, we have investigated the structural, magnetic and transport properties of off-stoichiometric metallic perovskite compounds $GdPd_3B_x$ ($x = 0.25, 0.50$ and 0.75) and compared the results with that of stoichiometric compositions $GdPd_3B_xC_{1-x}$. The studies on $GdPd_3B_x$ compounds further confirm that the magnetic and transport properties of this series critically depend upon structure and especially the distance between magnetic Gd^{+3} ions. The results suggest that presence of carbon also affects the magnetic behavior of the carbon-doped compounds. Our studies on $GdPd_3B_xC_{1-x}$ and $GdPd_3B_x$ compounds suggest that all the boron (and/or carbon) doped compositions exhibit a transition temperature $T^* \sim 45$ K, where TCR monitors a sudden change in sign (and/or magnitude). It has been observed that all the compositions with asymmetric distribution of boron and vacancies (or carbon) exhibit first-order like structural anomaly while the same for the compositions with the symmetric distribution is reversible in nature.

Chapter 4

Observation of valence fluctuation in some of the intermetallic perovskite like compounds

4.1 Introduction

As discussed in chapter 1 (section 1.6), some of the rare-earth (RE) and actinide elements exhibit non-localized behavior of f-electrons, which some times leads to phenomenon of valence fluctuation. In the phenomenon of valence fluctuation, the valency of RE ions fluctuates between two configurations, $4f^n$ and $4f^{n-1}$. In many cases the average valency and many other valence dependent physical properties (*e.g.* magnetic susceptibility) are a thermal population weighted average of the two valence states.

In this chapter, we will mainly discuss the valence behavior of some of the Ce and(or) Eu based cubic metallic perovskite like compounds. We have investigated the valence, magnetic and electrical transport properties of $Ce_{0.5}Eu_{0.5}Pd_3B_x$ (x =0.0, 0.5 and 1.0) and $Eu_{0.4}La_{0.6}Pd_3$ by the means of ^{151}Eu-Mössbauer, magnetic susceptibility and electrical resistivity measurements. The chapter is divided into six sections (including introduction). The experimental details are briefly described in section 4.2. Section 4.3 is devoted to the study of valence behavior of Ce and Eu in $Ce_{0.5}Eu_{0.5}Pd_3$. In section 4.4, we discuss the effect of boron incorporation on the valence and magnetic properties of resultant $Ce_{0.5}Eu_{0.5}Pd_3B_x$ ($x = 0.5$ and 1.0). We investigate the valence behavior of Eu

Some of the contents of this chapter are published in the following articles;
1. Abhishek Pandey *et al. Appl. Phys. Lett.* **94**, 182503 (2009).
2. Abhishek Pandey *et al. AIP. Conf. Proc.* **1003**, 216 (2008).
3. Abhishek Pandey *et al. J. Phys.: Condens. Matter* **21** 216002 (2009).

ions present in cubic $Eu_{0.4}La_{0.6}Pd_3$ in section 4.5. The main conclusions are outlined in the final section 4.6.

4.2 Experimental details

The compounds investigated in this chapter were prepared by standard argon arc-melting technique described in chapter 2 (section 1.2). The as-cast samples were then wrapped in a molybdenum foil and sealed in separate quartz tube under vacuum and annealed for 240 hours at 1000 ^0C to homogenize the phase. Structural characterization was preformed by powder X-ray diffraction (XRD) technique using Cu K_α radiation in Rigaku-Miniflex diffractometer. Magnetic measurements were performed using superconducting quantum interference device (MPMS-7, Quantum design-Inc., USA) magnetometer in the temperature range of 2-300 K. ^{151}Eu-Mössbauer measurements were carried out using SmF_3 source at two different temperatures, 25 and 300 K. Electrical resistivity measurements were performed by conventional four-probe method in temperature range of 2-300 K in a home-build setup.

4.3 Study of the valence behavior of Ce and Eu ions in a cubic intermetallic compound $Ce_{0.5}Eu_{0.5}Pd_3$

It has been pointed out in chapter 1 and subsequently discussed in chapter 2 that metallic perovskite compounds have recently attracted lot of attention due to the observation of many intriguing and application oriented properties *e.g.* superconductivity [30], negative thermal expansion [55, 169, 195], negative temperature coefficient of resistance [170], interesting elastic properties [20, 22], high density magnetic-recording capacity [47, 49] etc.

As already discussed in section 1.2.2 of chapter 1 [1], the RE and Pd-based metallic-perovskite compounds $RPd_3B_xC_{1-x}$ (R: rare-earth ions) crystallize with $Pm\bar{3}m$ space-group symmetry [169]. Parent RPd_3 compounds also form a stable phase with the same crystal symmetry but having vacant body center position [169, 170]. One of the members of RPd_3 series, $CePd_3$ (a = 4.124 Å), exhibits a deviation from usual lanthanide contraction of lattice parameters [Fig. 4.1] due to the intermediate valence state ($+3 < \nu < +4$) of Ce-ions in this compound [64]. Resistivity of $CePd_3$ shows a dense-Kondo behavior near room temperature accompanied by coherence phenomenon

[1] Also discussed in section 3.3 of chapter 3

at low temperatures [196]. On the other hand, boron-doped $CePd_3B$ exhibits a stable +3 valency of Ce [64]. The situation is just opposite in the case of $EuPd_3$ ($a = 4.102$ Å) that exhibits a stable +3 valency of Eu and follows the trend of lanthanide contraction, while boron-doped $EuPd_3B$ shows deviation from lanthanide contraction behavior [Fig. 4.1] with a temperature independent mixed-valent state of Eu ($+2 < \nu < +3$) and also exhibits charge-ordering at low temperatures [65, 66].

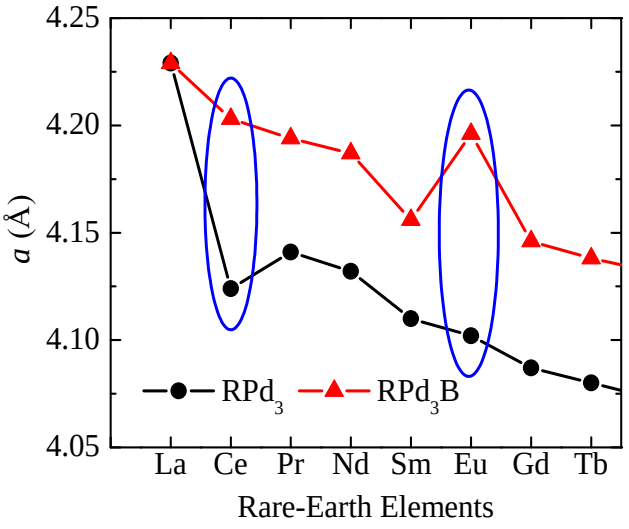

FIGURE 4.1: Variation of lattice parameter (a) with rare-earth elements that occupy the cube corner positions in RPd_3 and RPd_3B. Anomalous high increment in the value of a observed in the case of $CePd_3B$ and $EuPd_3B$ are indicated. The data has been taken from *Dhar et al. Mat. Res. Bull.* **16**, *1557 (1981).* This figure is also included in chapter 1 as Fig. 1.6.

It may be mentioned that, as the ionic radius of Eu^{+2} is greater than that of Eu^{+3} and the ionic radius of Ce^{+4} is less than that of Ce^{+3}, the deviation of the lattice parameter of $EuPd_3B$ from expected lanthanide contraction is opposite in sign to the deviation of the same observed in the case of $CePd_3$ [Fig. 4.1]. While the lattice parameter of the former exhibits a value anomalously higher than that expected from the lanthanide contraction trend, the lattice parameter of the latter shows an anomalously low value [66] [Fig. 4.1]. The chemical pressure-induced increment of the unit cell volume and(or) boron distribution around the RE ions have earlier been considered as the underlying reasons for the observed valence transition of Eu in $EuPd_3B$ [65, 68]. Additionally, in reference to $CePd_3B$ it has been suggested by Dhar *et al.* [64] that besides changing the chemical environment around RE ions, the introduction of boron also contributes electrons to the conduction band. This may in turn lead to variety of other phenomenon *e.g.* change in the interaction between f-electrons and the conduction states, modification of electron-phonon dynamics etc. In the present work, we investigate half substituted $Ce_{0.5}Eu_{0.5}Pd_3$ where Ce and Eu ions, both capable of exhibiting valence fluctuation, occupy the same

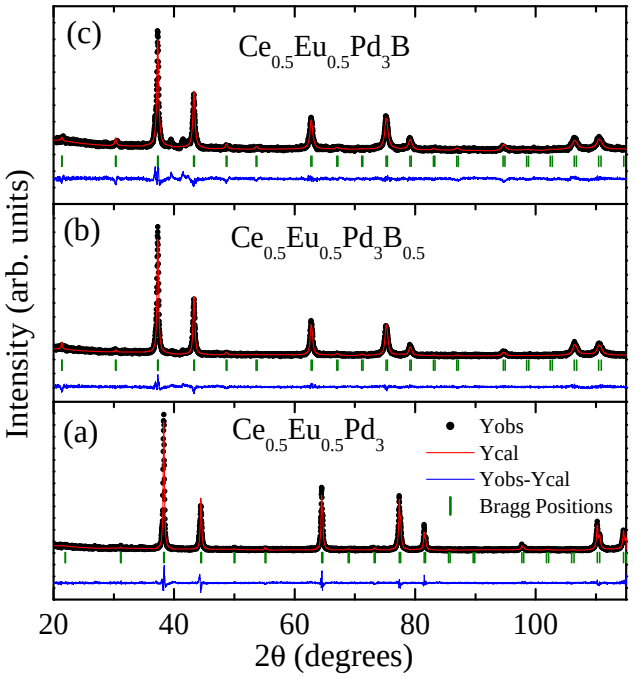

FIGURE 4.2: Room temperature powder XRD data, Rietveld fit, difference profile and Bragg peak position for $Ce_{0.5}Eu_{0.5}Pd_3B_x$ (x =, 0.0, 0.5 and 1.0).

lattice site (0, 0, 0) of the cubic unit cell. Though there is no boron and no lattice expansion has been observed in comparison with $EuPd_3$, our results suggest that Eu as well as Ce are in mixed-valent state in this compound [197].

Rietveld refinement of powder XRD data [Fig. 4.2]using FULLPROF package [159] confirms the formation of single phase $Ce_{0.5}Eu_{0.5}Pd_3$ with cubic lattice parameter, a = 4.101 Å. This value of a is almost same as that reported in literature for $EuPd_3$ [65, 66]. Results of Rietveld refinement also suggest that both Ce and Eu-ions occupy the cube corner lattice site 1a (0, 0, 0) of the cubic unit cubic cell. The refinement of powder XRD data of $Ce_{0.5}Eu_{0.5}Pd_3B_{0.50}$ also appears satisfactory [Fig. 4.2] and yields the cubic lattice parameter value of 4.20 Å. However, in the case of $Ce_{0.5}Eu_{0.5}Pd_3B$, although the refinement is satisfactory, there are indeed some small impurity peaks in the XRD profile close to $2\theta = 40^0$. Such impurity peaks suggests for the presence of small amount of additional phases in the material. The value of cubic lattice parameter obtained in the case of $Ce_{0.5}Eu_{0.5}Pd_3B$ is nearly same as that of $Ce_{0.5}Eu_{0.5}Pd_3B_{0.50}$, with a value of 4.20 Å.

4.3.1 Eu-Mössbauer studies on $Ce_{0.5}Eu_{0.5}Pd_3$

Eu-Mössbauer measurement has been carried out to investigate the valence state of Eu-ions present in $Ce_{0.5}Eu_{0.5}Pd_3$. The calibration of the channel numbers in terms

of velocity is obtained using the standard six-finger Mössbauer hyperfine pattern of Fe-metal [168]. The results exhibit nearly temperature-independent position (~ -5 mm/sec) of the isomer shift (IS) [Fig. 4.3]. As the usual positions of IS for divalent and trivalent Eu-ions are ~ -8 to -14 mm/sec and ~ -1 to $+4$ mm/sec respectively, the intermediate position of the same for $Ce_{0.5}Eu_{0.5}Pd_3$ clearly suggest that Eu-ions are in a intermediate valence state in this compound. Taking the IS positions for trivalent (+3.3 mm/sec) and divalent (-8.7 mm/sec) charge states of Eu-ions reported for a binary Eu-Pd compounds as reference [198], the approximate valency of Eu in $Ce_{0.5}Eu_{0.5}Pd_3$ can be estimated as 2.3. It may also be mentioned that Mössbauer spectrum presented here exhibit a single absorption line without any splitting at low temperature [Fig. 4.3], suggesting the absence of any charge-ordering of different valence states of Eu-ions, as observed in the case of $EuPd_3B$ [66].

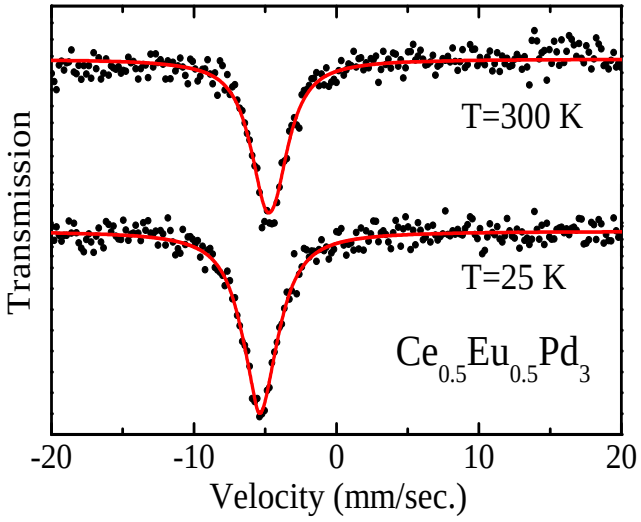

FIGURE 4.3: Eu-Mössbauer spectrum for $Ce_{0.5}Eu_{0.5}Pd_3$ measured at two different temperatures $T = 25$ and 300 K. The spectrum exhibits nearly temperature independent isomer shift of ~ -5 mm/sec.

As the Eu-ions are in mixed-valent state ($+2 < \nu < +3$) in $Ce_{0.5}Eu_{0.5}Pd_3$, their ionic radii are supposed to be more than that of Eu^{+3}. Hence one would expect that the lattice parameter of $Ce_{0.5}Eu_{0.5}Pd_3$ would be noticeably higher than that of $EuPd_3$. The fact that the lattice parameter of $Ce_{0.5}Eu_{0.5}Pd_3$ does not exhibit any enhancement in comparison to that of $EuPd_3$ strongly suggests that this increment is compensated by an equivalent decrease in the ionic radii of Ce-ions having valency greater than +3. In addition, the lower lattice parameter of $Ce_{0.5}Eu_{0.5}Pd_3$ compared with that of $CePd_3$ points to a higher valency of the Ce ions in the former compared with the later. Therefore, it appears that in $Ce_{0.5}Eu_{0.5}Pd_3$ both Ce and Eu-ions exhibit intermediate valence behavior−larger than +3 for Ce and smaller than +3 in the case of Eu.

4.3.2 Study of the magnetic susceptibility of $Ce_{0.5}Eu_{0.5}Pd_3$

The valence fluctuation of RE ions between nonmagnetic and magnetic states is also reflected in the magnetic susceptibility (χ) measurements. Figure 4.4 exhibits temperature variation of zero field cooled χ and χ^{-1} measured at 0.1 T. In contrast to nearly temperature-independent behavior observed in $CePd_3$ and $EuPd_3$ [64, 65], χ(T) of $Ce_{0.5}Eu_{0.5}Pd_3$ exhibits relatively higher magnitude and an upturn below $\sim$ 20 K. The χ(T) also exhibits a broad hump centered at $\sim$ 170 K, which is a signature of the presence of valence fluctuating (VF) ions with temperature dependent valency [157, 199]. At high temperature, χ(T) follows a Curie-Weiss (CW) behavior as evident from linear temperature variation of χ^{-1} for $T > 160$ K [Fig. 4.4]. The value of effective paramagnetic moment (μ_{eff}) and paramagnetic Curie temperature (θ_P) derived from the linear part of χ^{-1}(T) are 4.0 μ_B and -477 K respectively. While the value of μ_{eff} suggests the substantial presence of Eu^{+2} ions (as μ_{eff} for Ce^{+3} is only 2.54 μ_B and Ce^{+4} and Eu^{+3} are nonmagnetic), the large and negative value of θ_P is an indication of the presence of mixed-valent ions in the compound [157, 199].

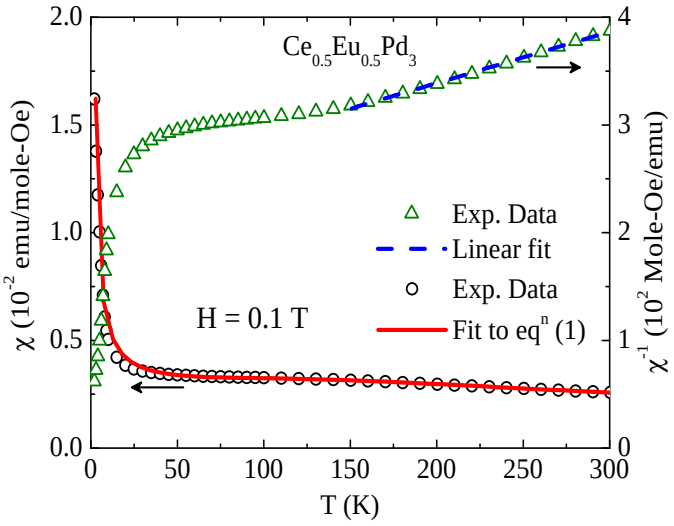

FIGURE 4.4: Molar susceptibility (χ) and inverse molar susceptibility (χ^{-1}) as function of temperature are plotted along left and right axis respectively. The solid line is the fit using the $\chi(T)$ expression given in equation (4.1). Dashed line is linear fit for $T > 160$ K.

Magnetic ions with temperature-independent average valency, which may also be a fractional quantity, exhibit CW behavior as found earlier in the case of $EuPd_3B$ [65, 66]. As the Eu-ions present in $Ce_{0.5}Eu_{0.5}Pd_3$ exhibit temperature independent behavior in Mössbauer measurement, they would essentially exhibit CW behavior with a reduced μ_{eff} value compare to that of free Eu^{+2} ions (7.94 μ_B). The VF Ce-ions are most

likely the source of the broad hump observed in χ(T). There could also be a possibility of existence of very dilute amount of Eu-ions with temperature-dependent valency. However, the Mössbauer measurement does not show any definite evidence for it. Hence, we ignore it in our analysis. The magnetic behavior of Ce-ions with dynamic temperature-dependent valency can be interpreted by the *Interconfigurational Fluctuation (ICF) model* [152, 156, 157], where the valency of unstable valence ions varies with temperature and depends upon two quantities−energy difference between the two valence states (E_{ex}) and spin-fluctuation temperature (T_{sf}) that governs the internal dynamics of fluctuation. Thus χ(T) of $Ce_{0.5}Eu_{0.5}Pd_3$ can be described by equation (4.1), where the first term describes χ(T) of VF Ce-ions (χ_{ICF}) and the second term represents CW behavior originating from temperature independent fractional valency of Eu-ions. The value of C_1, which is the Curie constant for the susceptibility of temperature independent fractional valent Eu-ions, has been taken as 1.386, which produces the relevant value of μ_{eff} (6.64 μ_B) associated with the observed +2.3 valence state of Eu-ions. The value of θ_p is taken as -477 K. The third term of equation (4.1) represents the contribution of small fraction of stable Ce^{+3} as observed in most of the Ce-based VF compounds [157]. C_2 is the Curie constant for the susceptibility of stable Ce^{+3} ions.

$$\chi(T) = \left(\frac{N}{k_B}\right)\left[\frac{\mu_n^2 P_n(T) + \mu_{n-1}^2 P_{n-1}(T)}{\sqrt{T^2 + T_{sf}^2}}\right] + \frac{C_1}{T - \theta_p} + \frac{C_2}{T} + \chi_0 \tag{4.1}$$

In the equation (4.1), μ_n, μ_{n-1} and P_n, P_{n-1} are effective paramagnetic moments and fractional populations of the nonmagnetic ground state and the magnetic excited state, respectively, of VF Ce-ions. The temperature variation of P_n can be described by equation (4.2) where J_n and J_{n-1} are angular momentums of the ground and the excited states respectively.

$$P_n(T) = \frac{(2J_n + 1)}{(2J_n + 1) + (2J_{n-1} + 1)exp(-E_{ex}/\sqrt{T^2 + T_{sf}^2})} \tag{4.2}$$

We have fitted the $\chi(T)$ data using equation (4.1) and (4.2) taking μ_n, μ_{n-1} and J_n, J_{n-1} as 0, 2.54 μ_B and 0, $\frac{5}{2}$, respectively. for nonmagnetic ground and magnetic excited states of Ce. Figure 4.4 exhibits that the resultant fit is good in the entire temperature range of measurement. The values of various fitting parameters are T_{sf} = 62 K, E_{ex} = 358 K, C_2 = 0.03 emu-K/mole-Oe and χ_0 = −0.00021 emu/mole-Oe. Figure 4.5 exhibits the temperature variation of P_{n-1} and χ_{ICF}. As discussed earlier, $\chi_{ICF}(T)$ exhibits a broad hump centered at ∼ 170 K. The P_{n-1}, which represents the fractional population of the magnetic valence state (+3) of Ce-ions, increases with increase in temperature due to

temperature-assisted excitation. The average valency of Ce-ions can be deduced from the values of temperature-dependent fractional populations as ~ 3.95 and 3.35 at $T = 2$ and 300 K, respectively. Various spectroscopic measurements, *viz.* X-ray absorption, X-ray photoemission, energy loss, bremsstrahlung-isochromat spectroscopy etc. yield the valency of Ce present in $CePd_3$ in the range of 3.07-3.15 [200–204]. Thus the Ce valency derived from the $\chi(T)$ of $Ce_{0.5}Eu_{0.5}Pd_3$ supports our conclusion described earlier, that the valency of Ce ions in $Ce_{0.5}Eu_{0.5}Pd_3$ is higher than that in $CePd_3$.

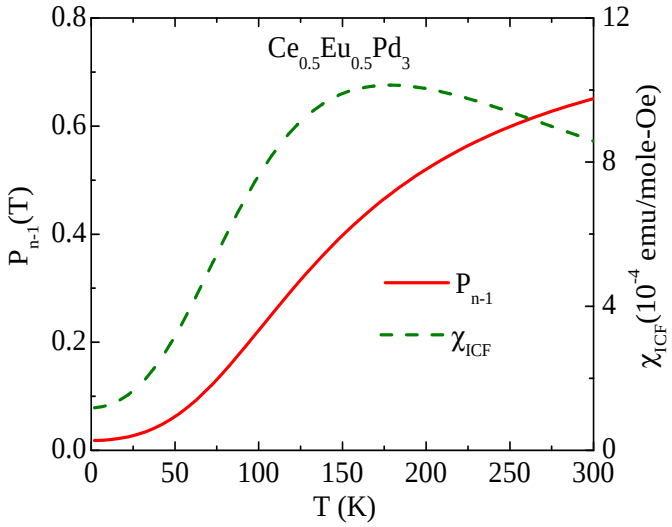

FIGURE 4.5: Temperature dependence of fractional population (P_{n-1}) and susceptibility of the valence fluctuating ions (χ_{ICF}), plotted in left and right axis, respectively.

4.3.3 Origin of the intermediate valence behavior of Ce and Eu ions in $Ce_{0.5}Eu_{0.5}Pd_3$

Since there is no boron in the lattice, which was earlier considered to be responsible for the observed valence instability of Eu in $EuPd_3B$ [65, 66, 68], it is clear that introduction of Ce has stimulated the observed intermediate valency of Eu-ions in $Ce_{0.5}Eu_{0.5}Pd_3$. As the $4f$ levels of both Ce and Eu hybridize with the conduction states due to their proximity to the Fermi-level, one of the possible reasons for the observed intermediate valency of Eu-ions present in $Ce_{0.5}Eu_{0.5}Pd_3$ could be the hybridization-driven charge-transfer between $4f$ states of Ce and Eu ions [$Ce^{+3}+Eu^{+3}+\Delta \rightarrow Ce^{+4}+Eu^{+2}+\Delta^*$, where Δ and Δ^* denote the conduction states before and after the proposed charge-transfer, respectively]. It must be noted that since the proposed charge-transfer between the 4f-states of Ce and Eu is mediated via the conduction states, conservation of the charge *only between* the 4f-states does not hold. However, at low temperatures where the thermal-excitations and manifested modifications in the valencies are minimum, the respective changes in the valencies of Ce and Eu-ions as compared to the parent $CePd_3$ and $EuPd_3$

can be approximately correlated. For example, at 25 K, the approximate change in the valency of Eu-ions present in $Ce_{0.5}Eu_{0.5}Pd_3$ in comparison to the same in $EuPd_3$ is $\Delta\nu(\text{Eu}) \sim -0.7$ $(2.3 - 3.0)$.

On the other hand, at the same temperature (25 K) the change in the valency of Ce-ions present in $Ce_{0.5}Eu_{0.5}Pd_3$ in comparison to the same in $CePd_3$ is $\Delta\nu(\text{Ce}) \sim +0.8$ $(3.9 - 3.1)$. The reasonably close agreement in the values of $\Delta\nu$(Eu) and $\Delta\nu$(Ce) strengthens the possibility of charge-transfer between Ce and Eu-ions as the underlying mechanisms for the observed intermediate valencies of RE ions in $Ce_{0.5}Eu_{0.5}Pd_3$.

4.3.4 Electrical transport behavior of $Ce_{0.5}Eu_{0.5}Pd_3$

We have carried out electrical resistivity measurements for $Ce_{0.5}Eu_{0.5}Pd_3$ to check weather the dense-Kondo behavior and coherence phenomenon observed in the case of $CePd_3$ still persist in present compound or not. The temperature dependence of the resistivity (ρ) is shown in Fig. 4.6. The immediate point to be noticed is that the dense-Kondo lattice behavior observed near room temperature in $CePd_3$ [196] is absent and the high temperature ($T > 50$ K) ρ(T) deviates from linearity and has a negative curvature ($d^2\rho/dT^2 < 0$) [Fig. 4.6]. Many high-resistive compounds and alloys exhibit this kind of non-linear behavior of $\rho(T)$, which occurs when electronic mean-free path becomes short and comparable to a few atomic spacings. This non-linear behavior of $\rho(T)$ can be interpreted using parallel resistor model proposed by Wiesmann *et al.*, [205], given in

$$\frac{1}{\rho(T)} = \frac{1}{\rho_{id}(T)} + \frac{1}{\rho_{max}} \tag{4.3}$$

where

$$\rho_{id}(T) = \rho_{id}(0) + C_1 \left(\frac{T}{\theta_D}\right)^n \int_0^{\theta_D/T} \frac{x^n dx}{(1 - e^{-x})(e^x - 1)} \tag{4.4}$$

Where, $\rho_{id}(0)$ is the residual-resistivity, θ_D is the Debye temperature and C_1 is the numerical constant. ρ_{max} basically plays the role of a shunt resistance. The actual residual resistivity is given by,

$$\rho_0 = \frac{\rho_{id}(0)\rho_{max}}{\rho_{id}(0) + \rho_{max}} \tag{4.5}$$

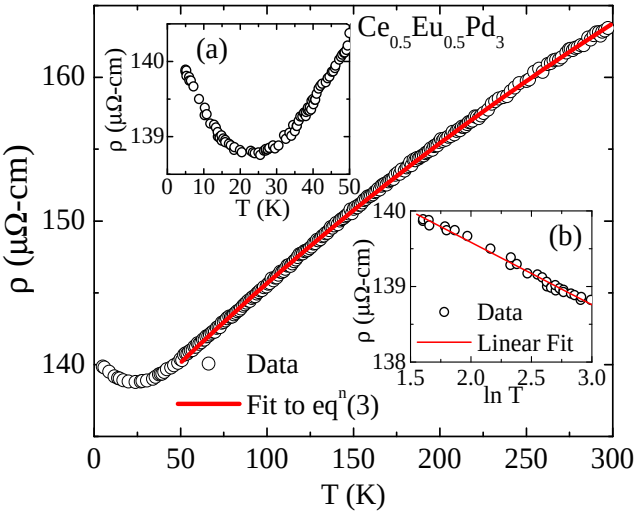

FIGURE 4.6: Resistivity (ρ) as a function of temperature. Solid line is the fit using equation (4.3) for $T > 50$ K. Inset (a) shows $\rho(T)$ in an expanded scale for $T < 50$ K. Inset (b) exhibits the variation of ρ as function of -lnT at low temperatures. The solid line is a linear fit to the data.

ρ_{id}(T) given in equation (4.4) represents the ideal temperature dependence of ρ under *Bloch-Grüeniesen model*, where the dominant scattering mechanism is of electron-phonon in nature. Since ρ_{id}(T) varies linearly with temperature at sufficiently high temperatures, we have approximated the temperature variation of ρ_{id} as, ρ_{id}(T)=ρ_{id}(0)+αT.

Figure 4.6 exhibits that the fit using equation (4.3) is good in the temperature range of 50-300 K. The values of various fitting parameters are $\rho_{id}(0) = 266.2$ $\mu\Omega$-cm, $\alpha = 0.5$ $\mu\Omega$-cmK^{-1} and $\rho_{max} = 270.2$ $\mu\Omega$-cm. The value of ρ_0 calculated from the equation 4.5 is 134.1 $\mu\Omega$-cm, which is close the value obtained by extrapolating ρ values of $T > 25$ K. At low temperatures ρ(T) exhibits a shallow minima at ~ 25 K [inset (a), Fig. 4.6]. Below 25 K, ρ scales with -ln T [inset (b), Fig. 4.6], which is suggestive of Kondo like behavior.

4.4 Intermediate valence behavior in metallic perovskite $Ce_{0.5}Eu_{0.5}Pd_3B_x$ (x =0.5 and 1.0)

To study the effect of lattice parameter enhancement on the valence behavior of RE ions we have investigated the boron-filled compounds $Ce_{0.5}Eu_{0.5}Pd_3B_x$ (x =0.5 and 1.0). As discussed in section 1.2.2 (chapter 1), the incorporated boron atoms occupy the vacant body centre lattice site of the cubic unit cell. The study of $Ce_{0.5}Eu_{0.5}Pd_3B_x$ and comparison of the results with that of $Ce_{0.5}Eu_{0.5}Pd_3$ also helps to understand the

effect of change of chemical environment around RE ions (Ce and Eu) on their valence behavior. As already discussed in section 4.3, in the case of $Ce_{0.5}Eu_{0.5}Pd_3B_x$, while the boron incorporation leads to lattice expansion, the underlying cubic structure remains the same with $Pm\bar{3}m$ space-group symmetry. The cubic lattice parameter of both $Ce_{0.5}Eu_{0.5}Pd_3B_{0.5}$ and $Ce_{0.5}Eu_{0.5}Pd_3B$ are nearly same with the value $a = 4.200$ Å.

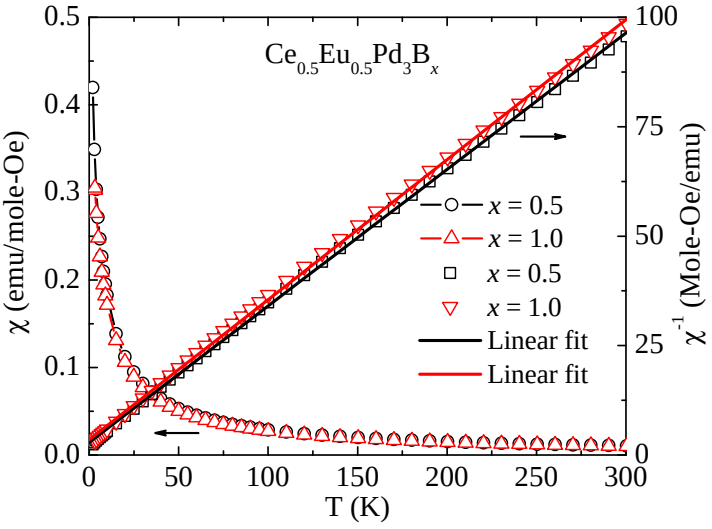

FIGURE 4.7: Temperature variation of zero field cooled magnetization (M) and inverse molar susceptibility (χ^{-1}) of $Ce_{0.5}Eu_{0.5}Pd_3B_x$ (x = 0.5, 1.0) plotted along left and right axis, respectively. The solid lines are the linear fit to $\chi^{-1}(T)$ data.

The temperature variation of molar and inverse molar susceptibilities of $Ce_{0.5}Eu_{0.5}Pd_3B_x$ (x =0.5 and 1.0) is shown in Fig. 4.7. It can be easily noticed from the figure 4.7 that the magnetic behavior of boron-filled $Ce_{0.5}Eu_{0.5}Pd_3B_x$ is significantly different from that of $Ce_{0.5}Eu_{0.5}Pd_3$. In contrast to the relatively complicated variation of $\chi(T)$ in the case of $Ce_{0.5}Eu_{0.5}Pd_3$ (represented by equation 4.1), the $\chi(T)$ of $Ce_{0.5}Eu_{0.5}Pd_3B_x$ exhibits simple CW behavior in the entire temperature range of measurement, as can be seen from the linear variation of $\chi^{-1}(T)$ [Fig. 4.7]. The observed $\chi(T)$ of $Ce_{0.5}Eu_{0.5}Pd_3B_x$ is close to that reported in the case of $EuPd_3B$ [65]. The paramagnetic nature of $\chi(T)$ suggests that the Ce ions, that exhibit dynamic temperature dependent valency in $Ce_{0.5}Eu_{0.5}Pd_3$ (section 4.3.2), are primarily in temperature independent valence state in boron-filled $Ce_{0.5}Eu_{0.5}Pd_3B_x$.

The results of Eu-Mössbauer measurements performed at two different temperatures, T = 25 and 300 K are shown in the Fig. 4.8. The results are quite similar to the Eu-Mössbauer spectra reported for $EuPd_3B$ [66]. In the case of $Ce_{0.5}Eu_{0.5}Pd_3B_{0.5}$ and $Ce_{0.5}Eu_{0.5}Pd_3B$, the low temperature (25 K) spectra consist of primarily two features: a dominant trivalent characteristic (IS $\sim$ +6.4 mm/sec) and an additional mixed-valent feature (IS $\sim$ -4.2 mm/sec). At room temperature two peaks come closer and merge to form a broad peak.

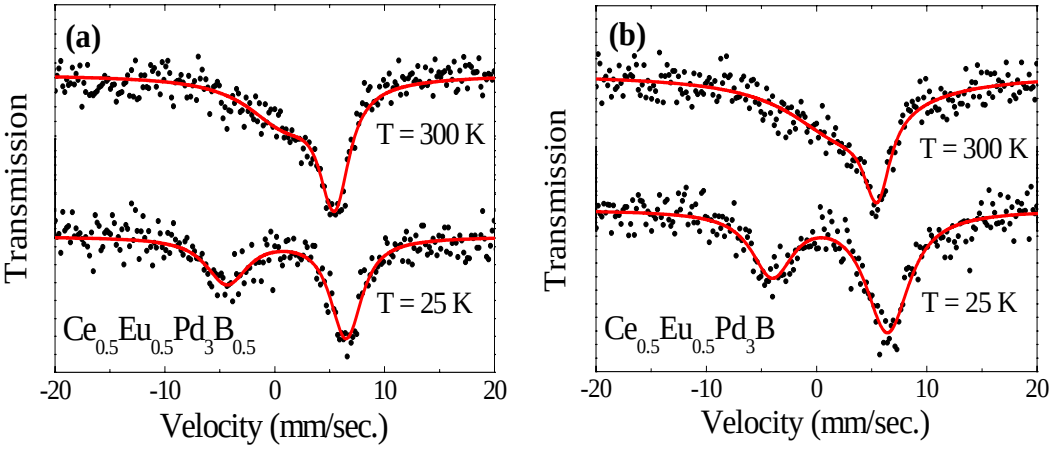

FIGURE 4.8: Eu-Mössbauer spectrum for (a) $Ce_{0.5}Eu_{0.5}Pd_3B_0.5$, and (b) $Ce_{0.5}Eu_{0.5}Pd_3B$, measured at two different temperatures T = 25 and 300 K.

A similar behavior was reported earlier in the case of $EuPd_3B$ [66] and can be attributed to the occurrence of charge ordering of different valence states of Eu ions in $Ce_{0.5}Eu_{0.5}Pd_3B$. In the case of $Ce_{0.5}Eu_{0.5}Pd_3B_{0.5}$, where half of the body centre sites are filled with boron while the remaining half are vacant, there is a possibility of having two different type of Eu sites characterized by the number of nearest neighbor boron atoms. This kind of arrangement may lead to two different environment-dependent excitation energies for the fluctuations of electrons between the localized $4f$ level and conduction band [66]. In such cases, the observation of charge ordering of different valence states of Eu ions can not be ruled out. In addition, physical phase segregation ($Ce_{0.5}Eu_{0.5}Pd_3B_{0.5}$ as a whole can be considered as a combination of two phase − one rich in $Ce_{0.5}Eu_{0.5}Pd_3$ and another rich in $Ce_{0.5}Eu_{0.5}Pd_3B$) can also produce such results. However, the powder XRD data [Fig. 4.2] do not distinguishably suggest any macroscopic phase segregation.

In the case of $Ce_{0.5}Eu_{0.5}Pd_3B$, where all the Eu site are in principle equivalent, the observation of charge ordering is some what surprising. It may be noted that both $Ce_{0.5}Eu_{0.5}Pd_3B_{0.5}$ and $Ce_{0.5}Eu_{0.5}Pd_3B$ crystallize with the same lattice parameter of 4.200 Å and the exhibit nearly similar behavior in magnetic susceptibility [Fig.4.7] and Eu-Mössbauer measurements [Fig.4.8]. Such characteristics hint that the solubility of boron in $Ce_{0.5}Eu_{0.5}Pd_3B_x$ may be limited only up to $x = 0.5$, and the excess amount of boron incorporated in the case of $x = 1.0$ might be going in to interstitial places or forming some boron rich secondary phases. In fact, the powder XRD data of $Ce_{0.5}Eu_{0.5}Pd_3B$ hints for the presence of some additional phases in the compound [Fig. 4.2]. In this scenario, the majority phase of $Ce_{0.5}Eu_{0.5}Pd_3B$ will be effectively equivalent to $Ce_{0.5}Eu_{0.5}Pd_3B_{0.5}$ and one would observe nearly similar physical properties for both of them, which is essentially the situation in the present case.

4.5 Valence instability of Eu ions in $Eu_{0.4}La_{0.6}Pd_3$

As discussed in the section 4.3, the cubic lattice parameters (a) of RPd_3 compounds follow usual lanthanide contraction except in the case of $CePd_3$ [64–66], where the measured value of a is significantly smaller than that expected under normal lanthanide contraction effect. This discrepancy in the value of a has been mainly attributed to the anomalous mixed-valent ($+3 < \nu < +4$) state of Ce-ions in this compound in comparison with the stable +3 valency of RE ions in other RPd_3 compounds [64]. The addition of boron manifests in significant increase in the value of a of resulting RPd_3B in comparison with that of RPd_3 [Fig. 4.1]. Similar to RPd_3, the values of a of boron-doped RPd_3B also follow the normal lanthanide contraction, except $EuPd_3B$ which exhibits a relatively larger value of a [65, 66]. As in the case of $CePd_3$, the anomalous and high value of a in $EuPd_3B$ is a manifestation of valency change of Eu-ions from normal +3 to an intermediate valence state ($+2 < \nu < +3$). Valence transition of Eu-ions from a stable Eu^{+3} in $EuPd_3$ to a predominantly Eu^{+2} state in $EuPd_3B$ brings in substantial modifications in magnetic behavior [65]. $EuPd_3$ exhibits nearly temperature independent susceptibility [65]. In contrast, the divalent state of Eu^{+2} ($^8S_{7/2}$) possesses a fairly large paramagnetic moment of 7.94 μ_B and results in a CW behavior in $EuPd_3B$ [65]. The underlying reason for the valence change of the Eu-ions from +3 in $EuPd_3$ to predominantly +2 in $EuPd_3B$ has been mainly attributed to the change in the crystal environment around Eu-ions and (or) increment in the value of a upon boron addition [65, 68].

In the present work, we demonstrate that the valency of Eu-ions present in $EuPd_3$ can also be altered by exerting negative chemical pressure by doping the non-magnetic RE element La in the compound. The ionic radii of La^{+3} is more than that of Eu^{+3} and hence its introduction in the lattice leads to lattice expansion. To achieve sufficient increase in the unit cell volume as well as to maintain enough stoichiometry of Eu to get adequate magnetic signal, we have selected the composition $Eu_{0.4}La_{0.6}Pd_3$ for the present study. In this work, we report the study of magnetic and electrical-transport properties of this doped compound.

Powder-XRD data suggest the formation of the single phase compound $Eu_{0.4}La_{0.6}Pd_3$ with $Pm\bar{3}m$ space-group symmetry, similar to that of $LaPd_3$ and $EuPd_3$ [178]. As expected, Rietveld analysis of powder-XRD data also suggests that both La and Eu occupy the cube corner site (0, 0, 0) of the cubic unit cell. The value of the cubic lattice parameter obtained from the refinement of powder XRD data of $Eu_{0.4}La_{0.6}Pd_3$ is $a = 4.170$ $\mathring{A}$. The reported value of the lattice parameter of $EuPd_3$ is $a = 4.102$ $\mathring{A}$ and that of B doped $EuPd_3B$ is $a = 4.196$ $\mathring{A}$ [69].

4.5.1 Magnetic susceptibility of $Eu_{0.4}La_{0.6}Pd_3$

Figure 4.9 shows the temperature dependence of the magnetic susceptibility (χ) of $Eu_{0.4}La_{0.6}Pd_3$. The observed χ(T) of $Eu_{0.4}La_{0.6}Pd_3$ clearly deviates from the behavior observed in the case of $EuPd_3$, where the Eu-ions are in trivalent-state [65]. Instead of a nearly temperature independent variation in $EuPd_3$, χ(T) exhibits a relatively higher value and exhibits an upturn below T$\sim$ 25 K. The observed χ(T) also deviates from a CW behavior observed in the case of $EuPd_3B$ [65], where the Eu-ions are in divalent state. Hence, the observed χ(T) behavior of $Eu_{0.4}La_{0.6}Pd_3$ suggests that Eu-ions are neither in purely trivalent and nor in divalent-state in this compound. The χ(T) data also exhibits a broad hump near T$\sim$ 125 K, which is often considered as the signature of the presence of ions having temperature dependent valency [157, 199].

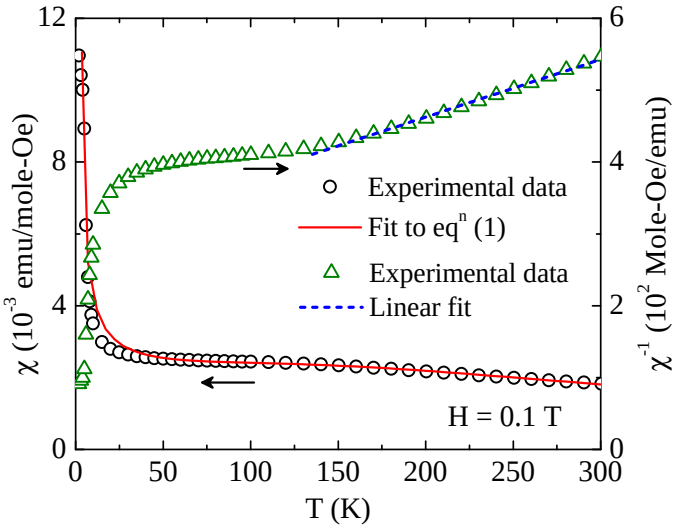

FIGURE 4.9: Temperature variation of the molar susceptibility (χ) and inverse molar susceptibility (χ^{-1}) of $Eu_{0.4}La_{0.6}Pd_3$. The continuous line is the fit to χ(T) data using the $\chi(T)$ expression given by the equation (4.6) in the text. Dashed line is the linear-fit of $\chi^{-1}(T)$ data in the range of 150-300 K.

As discussed in section 4.3.2, this broad hump in χ(T) occurs due to the competition between two effects; an increase in the χ with decrease in temperature and decrease in the population of exited magnetic state of unstable valence ion with decrease in temperature. The χ(T) of $Eu_{0.4}La_{0.6}Pd_3$ follows CW behavior above 150 K as evident from the linear variation of inverse-susceptibility (χ^{-1}) in the temperature range 150-300 K [Fig. 4.9]. The values of effective paramagnetic moment (μ_{eff}) and paramagnetic Curie temperature (θ_P) derived from the linear part of the $\chi^{-1}(T)$ plot are 3.15 μ_B/formula unit and -378 K, respectively. Although, the value of μ_{eff} suggests that large fraction of Eu-ions present in the lattice are in magnetic Eu^{+2} state near the room temperature,

the large and negative value of θ_P suggests of presence of valence fluctuating ions in the compound [157, 199].

We have analyzed the χ(T) data of $Eu_{0.4}La_{0.6}Pd_3$ under ICF model [152, 156] discussed in section 4.3.2. As mentioned there, in the ICF model, the valency of the unstable valence ions is a function of temperature and depends on basically two parameters; energy difference (E_{ex}) between ground state (Eu^{+3}, non-magnetic in the present case) and the exited state (Eu^{+2}, magnetic in the present case) and characteristic spin-fluctuation temperature (T_{sf}) that describes the internal dynamics of the fluctuations. It is worth mentioning that in the ICF model we consider that E_{ex} is relatively small compared to all the multiplet-splittings. Hence, thermal-excitation of only Hund's-ground states of each configuration is needed to be taken in to the account [152]. However, in the case of Eu^{+3}, due to the similar values of orbital and spin-angular-momentums, the multiplet-splittings of the ground level are small in energy and comparable to thermal excitations. Hence consideration of only nonmagnetic ground state ($^7F_0$, Eu^{+3}) and magnetic excited state ($^8S_{7/2}$, Eu^{+2}) will not present the complete picture. However, as a first approximation one can neglect the effect of multiplets as it will only marginally modify the relative populations of Eu^{+3} and Eu^{+2} ions, particularly in the low temperatures. It may also be mentioned here that normally average fractional valency of valence-fluctuating ions (*e.g.* Eu in this case) is a temperature dependent quantity. However, in contrast to this Dhar *et al.* [66] have shown that the average valency of Eu-ions is temperature independent for $T > 160$ K in $EuPd_3B$. The Eu-ions with such kind of temperature independent population would effectively exhibit a CW behavior with a lower value of μ_{eff} ($< 7.94\ \mu_B$) originating from the fraction of Eu-ions in Eu^{+2} valence state. To include the effect of such Eu-ions with temperature independent valency, an additional CW term is needed in the χ(T) expression. Hence, the χ(T) of the present compound can be described by the equation (4.6), where the temperature dependence of magnetic-susceptibility of valence fluctuating ions (χ_{ICF}) is described by first term of the equation (4.6), while the second term represents CW susceptibility.

$$\chi(T) = (1-f)\left(\frac{N}{3k_B}\right)\left[\frac{\mu_n^2 P_n(T) + \mu_{n-1}^2 P_{n-1}(T)}{\sqrt{T^2+T_{sf}^2}}\right] + \frac{fC}{T} + \chi_0 \tag{4.6}$$

Here, μ_n, μ_{n-1} and P_n, P_{n-1} are the effective paramagnetic moments and fractional populations of nonmagnetic ground state and magnetic excited state, respectively, f is the fraction of Eu-ions with temperature independent valence state that exhibit CW behavior, C is the Curie constant and χ_0 is temperature independent susceptibility. Fractional population of ground state can be described by the equation (4.6) given in section 4.3.2.

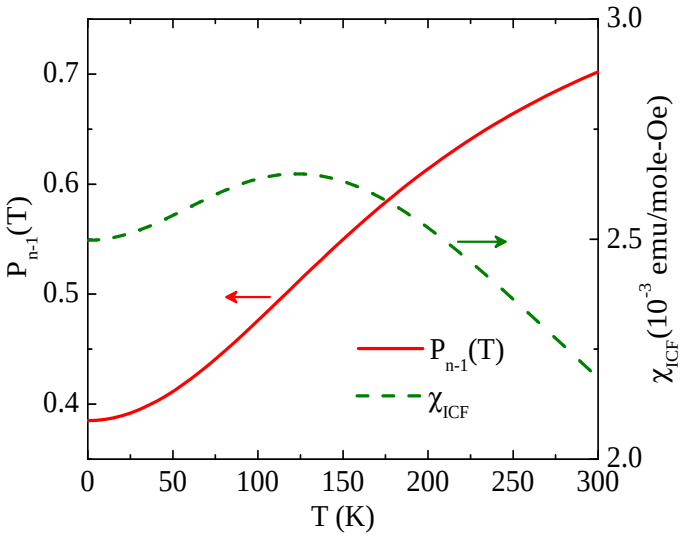

FIGURE 4.10: Temperature dependence of the fractional occupation, $P_{n-1}(T)$, of the Eu exited state (Eu^{+2}) and molar susceptibility resulting from interconfigurational fluctuations of Eu-ions (χ_{ICF}), plotted along the left and right vertical axis, respectively.

As mentioned above, we have considered non-magnetic Eu^{+3} as the ground state (E_n) and magnetic Eu^{+2} state as the excited state (E_{n-1}). Hence, we have taken the effective paramagnetic moments of ground state (μ_n) and excited state (μ_{n-1}) as 0 and 7.94 μ_B, respectively. The angular momentum values J_n and J_{n-1} have been taken as 0 and $\frac{7}{2}$, respectively. We have fitted the χ(T) data to equation (4.6) and the result is shown by the continuous solid line in Fig. 4.9. The resulting fit satisfactorily describes the temperature dependence of χ(T) of $Eu_{0.4}La_{0.6}Pd_3$ over the whole temperature range of measurement. The values of various fitting parameters are as follows; $f = 0.66$, $T_{sf} = 164$ K, $E_{ex} = 418$ K and $\chi_0 = -0.00045$ emu/mole-oe. The high value of f suggests that a large fraction of Eu-ions are in magnetic state Eu^{+2}. The value of μ_{eff} for $EuPd_3B$ calculated by Dhar *et al.* is 6.77 μ_B [65]. Considering the moment value of Eu^{+2} ions (7.94 μ_B), the time-averaged fraction of Eu^{+2} ions present in $EuPd_3B$ can be estimated as 0.85. The value of $f = 0.66$ obtained in the present work for $Eu_{0.4}La_{0.6}Pd_3$ is smaller than that in $EuPd_3B$. Figure 4.10 represents the variation of χ_{ICF} and P_{n-1} with temperature. One can see from this figure that the value of P_{n-1} that represents the fractional population of magnetic Eu^{+2} state increases with increase in temperature due to thermal excitations. As mentioned earlier, the value of χ_{ICF} exhibits a broad maxima centered around T=125 K. We would like to mention it here that, although the magnetic susceptibility of $Eu_{0.4}La_{0.6}Pd_3$ suggests for the presence of valence valence fluctuating Eu ions, Mössbauer measurements are needed to firmly conclude the same.

4.5.2 Resistivity behavior of $Eu_{0.4}La_{0.6}Pd_3$

We have also investigated the electrical resistivity (ρ) behavior of the compound [Fig. 4.11]. The $\rho(T)$ exhibits a normal tendency of saturation at low temperatures, however it exhibits a non-linear temperature dependence for T> 25 K. This kind of behavior has been observed in many high-resistivity materials whose resistivity approaches $\rho \sim 150$ $\mu\Omega$-cm [206–208]. A similar high temperature $\rho(T)$ behavior was observed in the case of $Ce_{0.5}Eu_{0.5}Pd_3$ (section 4.3.4). As discussed in section 4.3.4, such $\rho(T)$ behavior occurs when the electronic mean-free path becomes very short (of the order of a few atomic spacings). Such non-linear temperature variation of ρ exhibits a negative curvature ($d^2\rho/d\mathrm{T}^2$) and can be interpreted using parallel-resistance model [205] given in equation 4.3.

Similar to the case of $Ce_{0.5}Eu_{0.5}Pd_3$ described in section 4.3.4, we can approximate the temperature variation of ρ_{id} as, $\rho_{id}(\mathrm{T})=\rho_{id}(0)+\alpha\mathrm{T}$. Figure 4.11 shows that the fit is quite good in temperature range 25<T<300 K. The values of fitting parameters are; $\rho_{id}(0) = 354.4$ $\mu\Omega$-cm, $\alpha = 1.05$ $\mu\Omega$-cmK^{-1} and $\rho_{max} = 243.1$ $\mu\Omega$-cm. The value of actual residual-resistivity obtained using expression given in equation (4.5) is $\rho_0 = 144.2$ $\mu\Omega$-cm, which is very close to the value obtained by extrapolating the ρ(T) data to $T = 0$ K.

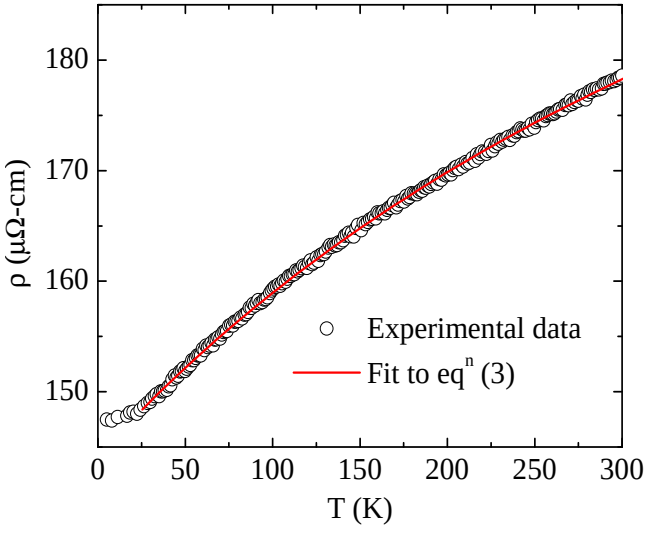

FIGURE 4.11: Electrical resistivity (ρ) as a function of temperature. Solid line is the fit using the parallel-resistor model given by the equation (4.3) in the text.

4.6 Conclusion

In this chapter, we have studied the valence, magnetic and electrical transport behavior of cubic $Ce_{0.5}Eu_{0.5}Pd_3B_x$ (x =0.0, 0.50, 1.0) and $Eu_{0.4}La_{0.6}Pd_3$. The boron incorporated $Ce_{0.5}Eu_{0.5}Pd_3B_x$ compounds have perovskite like atomic arrangements in the cubic unit cell while $Ce_{0.5}Eu_{0.5}Pd_3$ and $Eu_{0.4}La_{0.6}Pd_3$ crystallize with vacant body centre site. The Ce and Eu ions, both capable of exhibiting valence fluctuation, occupy the same cube corner lattice site in $Ce_{0.5}Eu_{0.5}Pd_3B_x$ (x =0.0, 0.50 and 1.0). Similarly, in $Eu_{0.4}La_{0.6}Pd_3$, non-magnetic La ions and unstable valence Eu ions occupy the cube corner lattice site.

Our experimental data suggest that the valency of Eu-ions in $Ce_{0.5}Eu_{0.5}Pd_3$ differs from the stable +3 observed in parent $EuPd_3$. The presence of intermediate-valence Ce ions is believed to be the stimulating factor for the observed change in the Eu valency. This kind of interdependence of the valency of RE ions is a unique phenomenon. The observed valence transition of Eu ions without any associated modification of the unit cell volume is also of rare occurrence. The temperature variation of electrical resistivity of $Ce_{0.5}Eu_{0.5}Pd_3$ has been interpreted using parallel-resistance model at high temperatures ($T > 50$ K) and Kondo-like behavior at low temperatures ($T < 50$ K).

The valence and magnetic behavior of RE ions in boron-filled $Ce_{0.5}Eu_{0.5}Pd_3B_x$ (x = 0.50 and 1.0) is substantially different from that of $Ce_{0.5}Eu_{0.5}Pd_3$. The magnetic susceptibility of boron-filled compounds exhibit paramagnetic CW behavior in the entire temperature range of measurement, while the same in $Ce_{0.5}Eu_{0.5}Pd_3$ shows the significant contribution coming from the temperature dependent valence change of RE ions. In contrast to $Ce_{0.5}Eu_{0.5}Pd_3$, the $Ce_{0.5}Eu_{0.5}Pd_3B_x$ compounds also exhibit the presence of charge ordering of different valence states of Eu ions.

We have also shown that the valency of Eu-ions, which is trivalent in binary $EuPd_3$, can be altered by doping nonmagnetic RE ion La in the lattice. Although, the resulting compound $Eu_{0.4}La_{0.6}Pd_3$ preserves the cubic symmetry, a larger than expected increase in unit cell volume has been noticed. Result of χ(T) has been interpreted in terms of ICF model and an additional C-W term originated from the fraction of Eu-ions in temperature independent valence state. The analysis suggest that at high temperature there is a substantial presence of magnetic Eu^{+2} state in $Eu_{0.4}La_{0.6}Pd_3$. Similar to $Ce_{0.5}Eu_{0.5}Pd_3$, the temperature variation of electrical resistivity of $Eu_{0.4}La_{0.6}Pd_3$ has been interpreted using parallel-resistance model. Our work suggests that the observed valence transition in this compound is due to negative-pressure-driven lattice parameter enhancement. This work also demonstrate that the valency of Eu-ions present in the cubic lattice of $EuPd_3$ can be altered without filling the body center site of the cubic unit cell.

Chapter 5

Structural, magnetic and transport properties of binary intermetallic compound YPd_3

5.1 Introduction

As mentioned in chapter 1 (section 1.2.2), the rare-earth (RE) and transition metal based series of binary and ternary compounds have been extensively investigated during last few decades due to their various interesting physical properties, *viz.* superconductivity [209, 210], Kondo phenomenon [211], magneto-caloric effects [212] etc. One of the such series is palladium based RPd_3, and related RPd_3B (R: rare-earth) compounds [213–220]. Significant amount of work has been done on this series and in particular magnetic [178, 221], transport [216] and valence fluctuating properties [64, 66] of these compounds have been investigated.

It has been earlier mentioned in chapter 1 (section 1.2.2) and later discussed for $GdPd_3$ in chapter 3 (section 1.3) that RPd_3 (R: Sc, Y and La to Lu) compounds crystallize in a cubic $AuCu_3$ structure with $Pm\bar{3}m$ space group symmetry. Magnetism in this series of compounds arises from the localized 4f moments of RE ions [178] (see the section 1.3 of chapter 1 for details). The compounds containing magnetic RE ions (*e.g.* Gd, Tb, Dy, Ho etc.) exhibit magnetic ordering (in general of predominant antiferromagnetic (AFM) nature) or a paramagnetic behavior down to the lowest measurable temperature [178]. In contrast, the compound containing non-magnetic RE ions (*e.g.* Y and La) show diamagnetic character [222]. One of such diamagnetic compound, YPd_3, is a known

Some of the contents of this chapter are published in the following article;
1. Abhishek Pandey *et al. J. Alloys Compd.* **476**, 14 (2009).

hydrogen storage material [223, 224], thus relate to one the most demanding area of present day energy-based research. YPd_3 has also extensively been used as a matrix material for studying various physical properties of dilute mixture of magnetic rare-earths to host YPd_3 [225–227]. The advantage of such dilute mixture of magnetic RPd_3 to non-magnetic YPd_3 is; the structure and symmetries of the mixed phase does not alter. However, the lattice parameter of the mixed phase is sensitive to the amount of RPd_3 present in the mixed phase and to the ionic radii of RE ion of RPd_3 dopant [225]. In addition, the heat capacity data of YPd_3 have been used to subtract from that of RPd_3 or $R_xY_{1-x}Pd_3$ to find out the magnetic contribution to the heat capacity in the latter [228]. The same is done in the case of electrical resistivity [229], to calculate the spin disorder (magnetic) contribution in the resistivity of RPd_3 or $R_xY_{1-x}Pd_3$ compounds.

Gardner *et al.* [178] have made some attempts to investigate the magnetic behavior of YPd_3. However, the magnetic and magneto-transport properties of this compound is yet to be studied in detail. In view of this, we feel that it is worth performing the detailed studies of magnetic properties of YPd_3 by using a sensitive magnetometer suitable for detecting very small strength of magnetic signal originated from this compound. In the present work, we investigate the magnetic properties of YPd_3 and find the significant effect of trace magnetic element (possibly magnetic RE ions) on the magnetic properties of the compound at lower applied magnetic fields [230]. In addition, we have also observed an anomaly in low temperature resistivity behavior, in that the resistivity values exhibits a shallow minima at $T = 14$ K and suggest for Kondo like behavior. In contrast, our high resolution powder X-ray diffraction (XRD) measurement and structural analysis suggest for a well ordered crystal lattice free from any detectable additional phase present in the compound.

5.2 Experimental details

The polycrystalline sample of YPd_3 was prepared by arc-melting technique described in chapter 2. The stoichiometric amount of yttrium (99.9% pure) and palladium (>99.95% pure) were melted under flowing argon atmosphere. By careful weighing, the stoichiometry of YPd_3 could be controlled up to 99.992% (stoichiometrically). The constituent elements were cleaned thoroughly to minimize any external impurity. At first, surface of yttrium was removed by a fine cleaning bit using DREMEL kit (DREMEL, The Netherlands) to minimize the surface impurities. Before use, the bit was cleaned in an ultrasonic bath. After removing the suface of yttrium, both Y and Pd were cleaned in the ultrasonic bath.

The sample chamber was first vacuumed and then a steady flow of argon coming from guttering furnace was maintained for several minutes before the start of melting process. We first thoroughly melted a titanium ball to insure that the argon coming from guttering furnace does not contain any oxygen. The shining surface of melted titanium ball insured for oxygen free argon. The sample was then melted quite a few times after flipping each time to insure proper homogeneity and then casted in the form of a rod of 1.9 mm diameter. The weight loss during the melting was less than 0.1%. Sample was then wrapped in a molybdenum foil and sealed in a quartz tube and then annealed for 240 hours at 1000 ^{0}C to increase the homogeneity. Structural characterization was performed by powder XRD technique using CuKα radiation in a Rigaku-D/max-2500/PC high resolution powder diffractometer having a rotating anode X-ray source. This diffractometer is fitted with a curved crystal monochromator in the diffraction beam, that enables the detection of even very weak reflections. The DC-magnetic measurements on cylindrical piece of the sample were performed using a SQUID (MPMS-7, Quantum design Inc., USA) magnetometer. The zero field cooled (ZFC) and field cooled (FC) magnetization measurements were carried out in the temperature range 2 - 300 K at two different applied DC fields, $H = 0.1$ and 7.0 T. Isothermal magnetization (hysteresis) measurements were carried out at three different temperatures, $T = 5$, 50 and 300 K, by varying the field from -7.0 to +7.0 T in all quadrants. The electrical resistivity measurement were performed by four probe method both in zero field as well as in the presence of applied magnetic field of 7.0 T. We have also performed inductively coupled plasma-atomic emission spectroscopic (ICP-AES) measurement for the trace impurity detection.

5.3 Structural characterization

Experimental powder XRD data along with Rietveld fit, difference profile and Bragg positions have been presented in Fig. 5.1. Full Rietveld refinement of powder XRD data performed using *FullPROF* package [159] clearly exhibits ordered and single phase nature of the compound. Our XRD data refinement concludes that the compound forms in a cubic structure and as reported earlier crystallize with $Pm\bar{3}m$ space group symmetry [223]. The value of lattice parameter and other refinement parameters have been listed in Table 5.1. The presence of very low intensity ($< 1\%$) Bragg peaks [inset, Fig. 5.1] can be taken as an evidence for the absece of any Y/Pd antisite disorder in the compound. In powder XRD patterns for a cubic compound, the cube corner positions $(0, 0, 0)$ interfere destructively with the face-centre positions $(1/2, 1/2, 0)$ for mixed indices Bragg peaks. Therefore, in the presence of uniform Y/Pd disorder, the crystal lattice will become a face centred cubic lattice and as a result, one would not observe any Bragg peak with mixed indices (both even and odd). Hence (100) and (110) reflections will remain absent.

In contrast, in an ordered cubic lattice, where Y occupies cube corner site (0, 0, 0) and Pd occupies three face-centred sites $(1/2, 1/2, 0)$, one would observe these low intensity mixed-indices Bragg peaks. However, due to close atomic numbers of Y and Pd, the intensity of (100) and (110) reflections becomes very low ($< 1\%$) in YPd_3. The inset in figure 5.1 exhibits the observed data and calculated profile in the low angle reagion for (100) and (110) Bragg reflections. The sufficeintly good fit for these very low intensity peaks suggests the formation of a crytal lattice with an ordered arragnment of Y and Pd at cube corner and face-centre positions respectively. In addition, we do not observe presence of any impurity peak due to any additional phase present in the compound. Thus XRD data confirms a single phase compound with an ordered arrangement of atoms free from any detectable impurity present in the material.

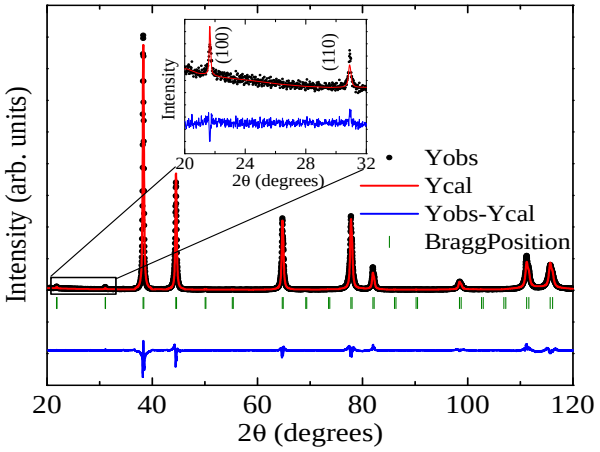

FIGURE 5.1: Experimentally observed powder XRD pattern, Rietveld fit, Bragg peak positions and difference pattern for YPd_3. Inset depicts low angle region exhibiting (100) and (110) Bragg peaks in an expanded scale.

Parameters	Values/Symbols
Space group	$Pm\bar{3}m$ (No. 221)
Lattice parameter	4.0694 ± 0.0003 Å
Maximum intensity	16105 [(111) Bragg peak]
Atomic positions	Y (0, 0, 0) & Pd $(\frac{1}{2}, \frac{1}{2}, 0)$
Atomic displacement factor	Y (0.09) & Pd (0.12)
R-factors	$R_p = 11.7$, $R_{wp} = 15.3$, $R_{exp} = 8.95$

TABLE 5.1: Structural refinement results: Space group symbol, cubic lattice parameter, maximum intensity of the highest intensity Bragg peak, atomic positions, atomic displacement factors and R-factor for YPd_3 as obtained from full Rietveld refinement. The refinement has been performed keeping full occupation of Y and Pd sites.

5.4 Magnetic behavior of YPd_3

Figure 5.2 shows the temperature dependence of zero field cooled (ZFC) and field cooled (FC) susceptibility (M/H) of YPd_3 taken at $H = 0.1$ T. The susceptibility values are very small and positive throughout the temperature range of measurement. This data thus does not suggest for the diamagnetic character of YPd_3 as suggested earlier [178], which indeed would have lead to negative values of susceptibility. The susceptibility takes a sharp upturn below $T = 25$ K, below which FC susceptibility values slightly differ from that of ZFC values. We repeated the ZFC and FC magnetization measurements at higher applied magnetic field of $H = 7.0$ T, and the results are shown in the inset of Fig. 5.2. At higher applied field, the susceptibility (both ZFC and FC) turn to negative. At $H = 7.0$ T, the ZFC and FC data overlap each other in the entire temperature range of measurement. The negative values of susceptibility suggest for a predominant diamagnetic character of the material at higher fields.

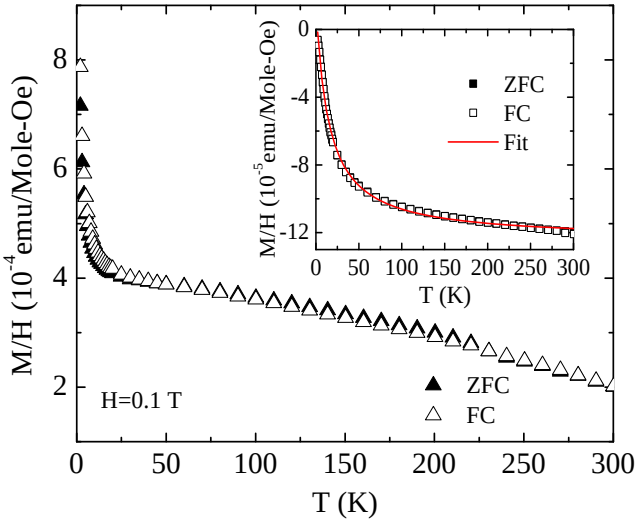

FIGURE 5.2: Zero field cooled and field cooled DC-magnetization as a function of temperature, performed at $H = 0.1$ T. Inset shows the same at $H = 7.0$ T. Continuous red line in inset is the plot of fitting function $\chi = \frac{C}{T-\theta} - \chi_0$.

We have fitted the susceptibility data at $H = 7.0$ T with the function $\chi(T) = [C/(T - \theta_c) - \chi_0]$ [Fig. 5.2]. The values of fitting parameters are as follows: Curie constant (C)=0.00208 emu-K/Mole-Oe, paramagnetic Curie temperature $(\theta_c) = -14.9$ K and temperature independent diamagnetic susceptibility $(\chi_0) = 0.00012$ emu/Mole-Oe. The calculated value of the Curie constant leads to a value of effective paramagnetic moment, $\mu_{eff} = 0.129\ \mu_B$. These anomalous magnetization results suggest the presence of some additional magnetic phase in the compound, which could not be detected through our high resolution powder XRD measurement (resolution limit $\sim 0.2\%$). Gardner *et al.* performed the magnetization measurements at intermediate fields (0.5 - 1.3 T) and

observed the effect of some magnetic impurity present in the compound [178]. Due to the presence of such additional magnetic phase, the diamagnetic character of the pure YPd_3 is seems to be suppressed at lower applied fields. However, at higher applied magnetic field, the diamagnetic susceptibility dominates over the small positive signal generated due to the the additional magnetic phase. The variation of inverse susceptibility with temperature in zero field cooled condition has been plotted in Fig. 5.3. The data at $H = 0.1$ T does not suggest for any paramagnetic character at low temperature as obtained by Gardner *et al.* [178] for weakly diamagnetic $LaPd_3$ and $LuPd_3$.

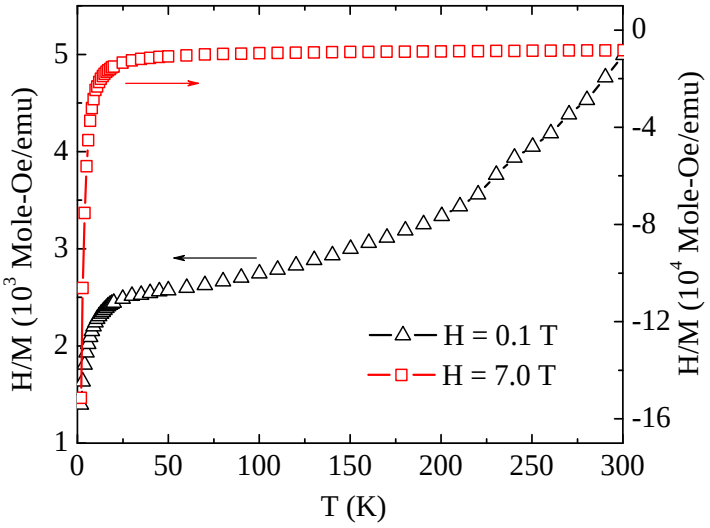

FIGURE 5.3: Inverse molar susceptibility as a function of temperature at two different applied magnetic fields, $H = 0.1$ and 7.0 T.

The result of isothermal magnetization (hysteresis) measurement performed at $T = 5$ K has been shown in Fig. 5.4. The data exhibit anomalous, tilted 'S' shaped variation of magnetization with applied magnetic field [231]. This data also strengthen the scenario predicted on the basis of ZFC/FC magnetization measurements. The nature of hysteresis behavior suggests for the presence of two competing contributing factors to the magnetization−one with positive and another with negative magnetization values. The data suggest that as we increase the applied magnetic field the contribution of positive magnetization keeps increasing up to H $\sim$ 2.0 T. Above this field, the contribution of negative magnetization starts dominating and finally the magnetization values turn to negative at H $\sim$ 5.8 T. The diamagnetic contribution in general varies linearly with the applied magnetic field and posses a negative value of slope. Thus one would expect the variation of positive contribution to be of non linear in nature, as two linear contribution would have resulted in a linear variation of resulting magnetization with applied field. Therefore, the hysteresis behavior presented in figure 5.4 indicate the presence of following two contributions: (i) negative diamagnetic contribution, which possibly varies linearly with the applied magnetic field and (ii) positive contribution which first

increases with increase in the field and then tends to saturated above H $\sim$ 2.0 T. This suggests that the observed trace effect of magnetism could be of ferromagnetic type.

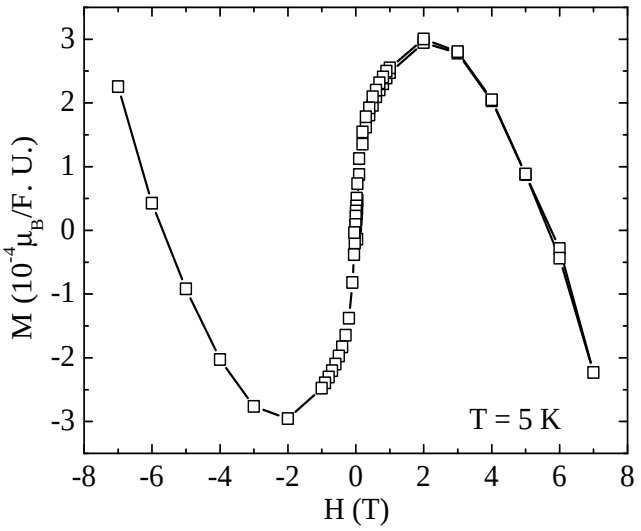

FIGURE 5.4: Isothermal magnetization as a function of applied DC-magnetic field performed at $T = 5$ K.

In RPd_3 series, $GdPd_3$ crystallizes with the same structure with a cubic lattice parameter value, a = 4.081 Å [178] nearest to that of YPd_3 (a = 4.069 Å), in comparison with other RE ions. Thus the presence of very small amount of $GdPd_3$ in YPd_3 will be difficult to detect by powder XRD technique. The isothermal magnetization value of $GdPd_3$ tends to saturate at H $\sim$ 2.0 T (section 1.6, Chapter 3). Since the positive contribution coming from impurity phase also tends to saturate at $\sim$ 2.0 T, $GdPd_3$ could be a possible candidate for the impurity phase present in the material. Assuming the above mentioned magnetic impurity phase is the minor presence of $GdPd_3$ in YPd_3, the following estimate can be made about the amount of the impurity phase: Isothermal magnetization of $GdPd_3$ at $T = 2$ K possess a value ~ 6 μ_B/F.U. at H $\sim$ 2 T (section 1.6, Chapter 3). The same in the case of YPd_3 is $\sim 3 \times 10^{-4}$ μ_B/F.U. at $T = 5$ K. Assuming the whole positive contribution to the magnetization is coming from the magnetic impurity phase of $GdPd_3$ in YPd_3, the amount of impurity phase would be close to 0.005% or 50 ppm of Gd in Y. Hence the atomic percentage of Gd impurity would be $\sim$ 12.5 ppm. Since the purity of yttrium metal used by us was 99.9%, the amount of impurity estimated can easly be present in the sample.

This small amount of impurity can definitely not be avoided by any sample preparation technique, as to avoid such an impurity one needs starting materials (in particular RE metal) of purity 99.995%, which is not used in general. In addition, such a small amount of impurity (0.005%) can not be detected using any high resolution X-ray diffractometer, as most of the high resolution X-ray diffractometers have sensitivity below 0.1%. We have

also calculated the amount of additional magnetic phase using the effective paramagnetic moment value obtained in ZFC magnetization measurement performed at $H = 7.0$ T. As mentioned earlier, the value of effective paramagnetic moment at $H = 7.0$ T is 0.129 μ_B. The free ion paramagnetic moment value of Gd^{+3} ion is 7.94 μ_B. This leads to the 1.63% presence of $GdPd_3$ in YPd_3, which is much higher compare to that obtained in the isothermal magnetization measurements. This discrepancy may have arisen due to the contribution of polarized conduction electrons to the effective paramagnetic moment at high applied field of 7.0 T.

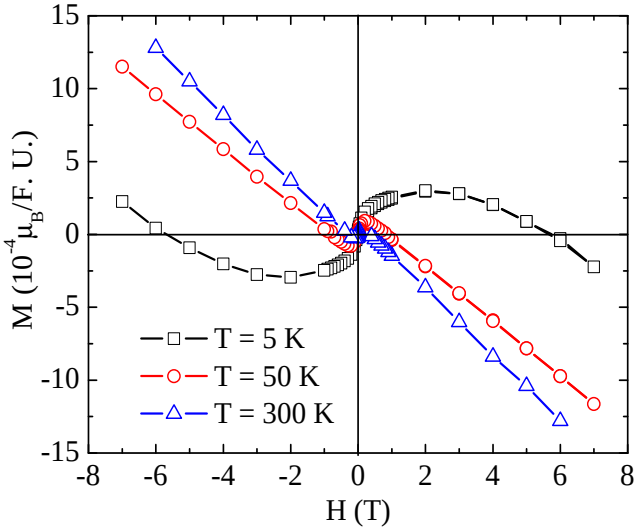

FIGURE 5.5: Isothermal magnetization as a function of applied DC-magnetic field performed at three different temperatures $T = 5$, 50 and 300 K. The data for $T = 5$ K is same as that presented in Fig. 5.4.

To quantitatively detect the exact amount and nature of RE impurities present in our compound, we performed ICP-AES measurement. The results suggest that the sample of YPd_3 investigated in this study contain 9 ppm of Gd and 8 ppm of Tb impurities. These values are very close to the values estimated through macroscopic magnetic measurements ($\sim$ 12.5 ppm). We did not observe the presence of any other magnetic RE elements, *viz.* Dy, Ho, Pr etc. It may be mentioned here that Borchardt *et al.* have reported the results of isothermal magnetization measurements performed at $T = 15$ mK on YPd_3 sample containing 0.01% Gd impurity [227]. Their data show saturation of moments and do not exhibit negative magnetization values as observed by us at $T = 5$ K [Fig. 5.4]. The first reson for this discrepancy could be the differance in the temperature of measurement; as at the lower temperature the positive contribution from impurity phase is expected to increase. The second reason could be the lower value of impurity present in our sample compare to the 0.01% Gd impurity present in the sample of Borchardt *et al.*

We also performed the isothermal magnetization measurements at $T = 50$ and 300 K [Fig. 5.5]. The data show that, as we increase the temperature, the negative contribution originating from diamagnetism takes a lead and in that the slope of the M-H plot becomes more negative for the positive applied magnetic fields. However, the positive contribution exhibit its weak presence at lower fields even at $T = 300$ K.

5.5 Electrical transport properties of YPd_3

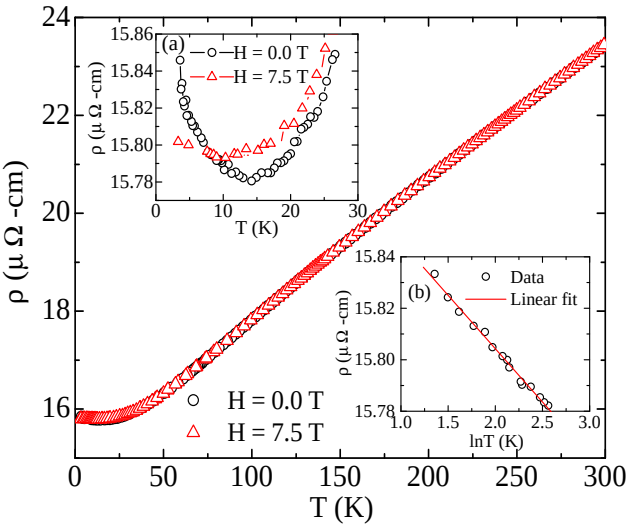

FIGURE 5.6: Electrical resistivity as a function of temperature at two different applied field conditions, H = 0 and 7.5 T. Inset (a) shows the low temperature resistivity data at $H = 0$ and 7.5 T in a magnified scale. Inset (b) exhibits the plot of resistivity at zero field as a function of lnT. The continuous line is a linear fit.

To check the effect of this small additional magnetic phases on electrical and magneto transport behavior of YPd_3, we carried out field dependent electrical resistivity measurements. The results suggest that this additional phase does not cast any signature on high temperature electrical transport properties of the compound, and resistivity exhibits a normal metallic behavior for T > 14 K with a room temperature value, ρ(300 K) $\sim$ 24 $\mu\Omega-$cm [Fig. 5.6]. However, at low temperature we observe an anomaly in the resistivity behavior. The resistivity values produce a shallow minima at $T = 14$ K, below which resistivity increases with a decrease in temperature [inset (a), Fig. 6]. Below $T = 14$ K, resistivity values scale with -lnT [inset (b), Fig. 5.6]. This suggest for a Kondo like behavior and also strengthen the conception of the presence of small amount of additional magnetic phase in non-magnetic YPd_3. This minima in resistivity disappears on the application of external magnetic field of 7.5 T. The resistivity values indicate a weak negative magnetoresistance below $T = 10$ K, and suggest for reduction

in spin disorder scattering originated from additional magnetic phase present in the material by the application of external magnetic field. At higher temperature, the values of electrical resistivity retrace themselves at $H = 7.5$ T, thus exhibiting field independent electrical transport behavior [Fig. 5.6]. We would like to point out here that the electrical transport in YPd_3 is very sensitive to the doping of external ions. One of such doped compound $Y_{0.98}U_{0.02}Pd_3$ exhibits non-Fermi liquid behavior and multichannel Kondo phenomena [226], in that its electrical resistivity exhibit a negative temperature coefficient of resistance near room temperature.

5.6 Conclusion

We have studied the structural, magnetic and electrical transport properties of one of the possible hydrogen storage materials, YPd_3, through high resolution powder XRD measurement, DC-magnetic measurements and field dependent electrical resistivity measurements. The material exhibit predominant diamagnetic character at high magnetic fields. On the other hand at lower applied fields, the magnetic behavior of the compound is seriously affected by the presence of very dilute amount (9 ppm of Gd and 8 ppm of Tb) additional magnetic elements. Similarly, we obtained a weak effect of these additional magnetic elements on electrical conduction of this material at low temperatures, in that resistivity values produce a shallow minima at $T = 14$ K. The resistivity values scale with -lnT below 14 K and thus suggest for Kondo like behavior. On the other hand, the XRD data do not show any signature of such a phase and suggest for a well ordered cubic phase, free from any antisite disorder. To the best of our knowledge, no attempt has been made to prepare a ultra pure YPd_3 that exhibits expected pure diamagnetic character even at lower applied magnetic fields. The data and their analysis presented here can be used in physical measurements when YPd_3 is being treated as a non-magnetic analogy phase in the study of RPd_3 or $R_xY_{1-x}Pd_3$ compounds.

Chapter 6

Magnetic and magneto-transport properties of $TbPd_3B_x$ $(x = 0, 1)$

6.1 Introduction

Some of the underlying features of metallic perovskite compounds have been discussed in chapter 1 (section 1.2.2). As mentioned there, the observation of many intriguing and application-oriented properties has made study of metallic perovskite compounds a topic of current interest [20, 22, 30, 47, 55, 195]. Though metallic perovskite compounds are structurally related to their oxygen-based variants, the basic electronic-structure and physical properties are often quite different (section 1.2.2, chapter 1). One such series of metallic perovskite compounds, $RPd_3B_xC_{1-x}$ (R: rare-earth ion), has been reported to exhibit many interesting phenomena *e.g.* negative temperature coefficient of resistance (chapter 3), negative thermal expansion, intermediate valence behavior (chapter 3), etc. (chapter 4).

As discussed in section 1.2.2, one of the advantages in the study of $RPd_3B_xC_{1-x}$ series is that one can also prepare a stable phase of undoped RPd_3 compounds [178] and perform a comparative study with respect to the effect of negative chemical pressure, change in the electronic-structure near the Fermi level etc. induced by boron and carbon doping. These effects lead to quite contrasting physical properties of undoped and doped compounds (chapter 3). Undoped RPd_3 compounds form with the same crystal structure and space group symmetry (space group: $Pm\bar{3}m$) as that of boron-doped RPd_3B compounds, except that the body center position of the cubic unit cell remains vacant in the former. We present in this work, the study of magnetic, transport and

Some of the contents of this chapter are published in the following article;
1. Abhishek Pandey *et al. Appl. Phys. Lett.* **94**, 172509 (2009).

magnetotransport properties of Tb-based members of RPd_3 and RPd_3B series [232]. Our results show that $TbPd_3$ exhibits *negative giant magnetoresistance (GMR)* at low temperatures. Introduction of boron at body centre site leads to substantial modification in magnetic and transport properties of the resultant $TbPd_3B$ that exhibits *positive GMR*. Electrical transport behaviors of the two compounds also exhibit quite contrasting features.

6.2 Experimental details

Compounds were synthesized by standard argon arc-melting procedure described in chapter 2 (section 1.2). The samples were cast in the form of a cylindrical rod of diameter 1.9 mm. Cylindrical shape of the samples minimizes the effect of demagnetization factor in magnetization data and also reduces the errors in resistivity values. As-cast samples were sealed in separate quartz tubes under vacuum and then annealed at 1000 ^{0}C for 240 hours to homogenize the phase. Magnetic measurements were carried out using superconducting quantum interference device magnetometer (MPMS-7, Quantum design-Inc., USA) in the temperature range 2-300 K. Resistivity and magnetoresistance (MR) measurements were performed using conventional four-probe technique in a home-build set up in the temperature range 1.8-300 K by varying DC-magnetic fields in the range 0-7 T.

6.3 Magnetic properties of $TbPd_3$ and $TbPd_3B$

Figure 6.1 shows the temperature dependence of DC-magnetization (M) that exhibits a peak at temperatures 4 and 3 K, respectively, for $TbPd_3$ and $TbPd_3B$, suggesting antiferromagnetic (AFM) like ordering in these compounds. The values of effective paramagnetic moment (μ_{eff}), paramagnetic Curie-temperature (θ_p) and magnetic transition temperature (T_N) are summarized in table 6.1. The μ_{eff} and θ_p have been calculated from high temperature ($T > 50$ K) data of inverse molar susceptibility (χ^{-1}) [Fig. 6.2]. The observed values of μ_{eff} are close to that expected for a free Tb^{+3} ion (9.72 μ_B) [1] and suggest that only rare-earth (RE) Tb^{+3} ions are responsible for magnetism in these compounds.

In the case of $TbPd_3$, though we observe a peak in $M(T)$ resembling AFM like ordering, the positive θ_p suggests that in addition to AFM interaction, ferromagnetic (FM) interaction also has a prominent contribution. In addition, the isothermal magnetization of

[1] See the section 1.3 of chapter 1 for the table that summarizes the various ground state properties of R^{+3} ions.

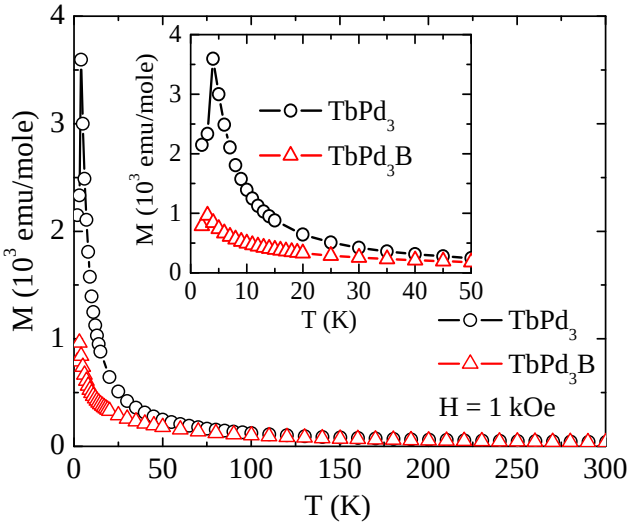

FIGURE 6.1: Magnetization as a function of temperature for $TbPd_3$ and $TbPd_3B$. Inset exhibits the same in an expanded scale close to magnetic ordering temperatures.

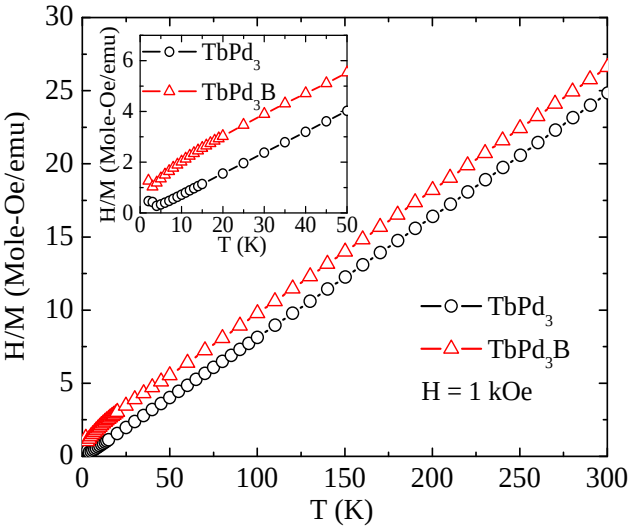

FIGURE 6.2: Variation of inverse molar susceptibility with temperature. Inset exhibits the same in an expanded scale close to magnetic ordering temperatures.

$TbPd_3$ exhibits the tendency of saturation [Fig. 6.3], which also refutes the existence of pure AFM ordering in this compound and suggests for the significant contribution coming from FM interactions. A similar behavior was earlier observed in the case of $GdPd_3$ (section 3.6, chapter 3). Such magnetic behavior indicates the presence of competing interactions in this compound. On the introduction of boron at the body center site, the lattice parameter of the resultant $TbPd_3B$ increases up to a value $a = 4.129$ Å in comparison to 4.081 Å for $TbPd_3$. The boron addition and manifested lattice parameter increment leads to significant modification in the magnetic properties of $TbPd_3B$ in comparison to that of $TbPd_3$. For example, (i) in the low temperature region the value of M for $TbPd_3B$ is considerably smaller than that of $TbPd_3$ [Fig. 6.1] (ii) the

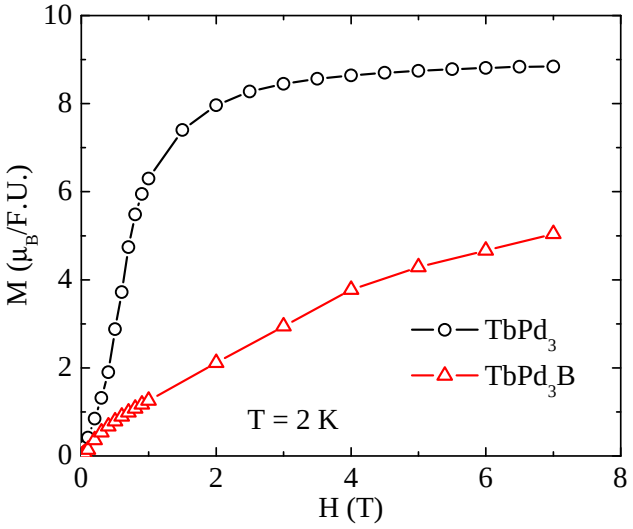

FIGURE 6.3: Isothermal magnetization of $TbPd_3$ and $TbPd_3B$ as function of applied DC-magnetic field. The measurements have been taken at $T = 2$ K.

value of θ_p for $TbPd_3B$ is larger in magnitude and negative in sign in comparison to small positive value for $TbPd_3$, (iii) χ^{-1}(T) differs from linearity below $\sim$ 25 K in the case of $TbPd_3B$ [Fig. 6.2], and (iv) in contrast to $TbPd_3$, the isothermal magnetization of $TbPd_3B$ does not show any tendency for saturation [Fig. 6.3]. The above mentioned observations suggest that the change in the distance between magnetic Tb^{+3} ions leads to modification in the nature of magnetic exchange interactions. This results in a dominant AFM interaction in $TbPd_3B$ instead of a competing one observed in the case of $TbPd_3$.

Compounds	a**(Å)**	T_N**(K)**	θ_p**(K)**	$\mu_{\mathbf{eff}}(\mu_{\mathbf{B}})$
$TbPd_3$	4.081	4	2.1	9.79
$TbPd_3B$	4.129	3	-15.8	9.71

TABLE 6.1: The lattice parameter (a), Néel temperature (T_N), paramagnetic Curie temperature (θ_P) and effective paramagnetic moment (μ_{eff}) of $TbPd_3$ and $TbPd_3B$.

6.4 Electrical and magneto-transport behavior of $TbPd_3$ and $TbPd_3B$

Figure 6.4 and 6.5 exhibit temperature variation of resistivity (ρ) for $TbPd_3$ and $TbPd_3B$, respectively. At high temperatures, ρ(T) of $TbPd_3$ exhibits a typical metallic character, while at low temperatures it undergoes an upturn below $\sim$ 4.5 K [Fig. 6.4].

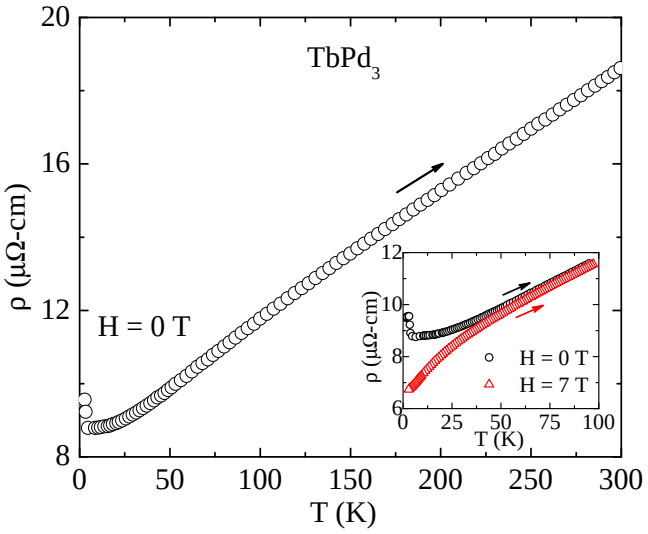

FIGURE 6.4: Resistivity as a function of temperature for $TbPd_3$ at $H = 0$ T. Inset depicts the same at two different applied magnetic fields, $H = 0$ and $H = 7$ T, in the low temperature region.

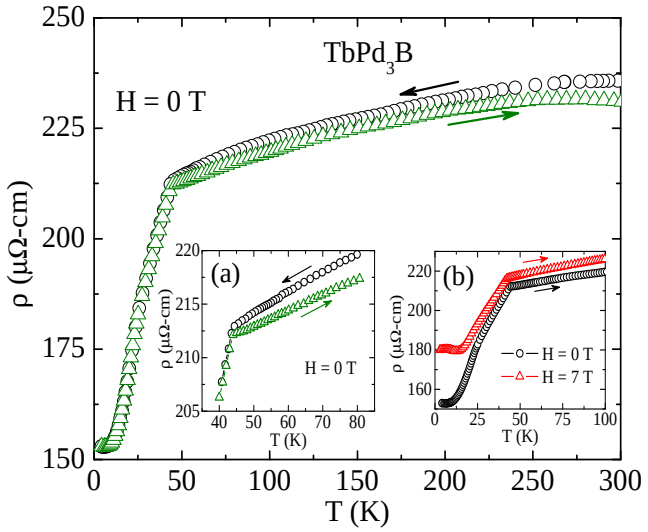

FIGURE 6.5: Variation of resistivity (ρ) as a function of temperature for $TbPd_3B$ in both cooling and heating directions. At first the data were taken when sample was being cooled followed by the heating direction. Inset (a) depicts the same in an expanded temperature scale near the transition point. Inset (b) exhibits the variation of ρ with temperature for $H = 0$ and $H = 7$ T.

This temperature coincides with $T = 4.0$ K (Table 6.1), where M(T) exhibits a peak. Such behavior has been observed in many systems possessing AFM-like ordering and can be attributed to superzone gap effect which arise when magnetic lattice, which is incommensurate with the periodicity of crystal lattice, distorts the Fermi surface leading to formation of an energy gap in the conduction band [190, 191]. In most of the cases, application of external DC-magnetic field suppresses the effect of superzone

gap [190, 191] (section 1.6, chapter 3). We have observed a similar behavior in the case of $TbPd_3$, where the application of magnetic field of $H = 7$ T significantly reduces the ρ(T) values at low temperatures leading to negative MR.

On the other hand, in the case of $TbPd_3B$, ρ(T) values exhibit a sharp transition at $T \sim 44$ K [Fig. 6.5]. Similar ρ(T) behavior was earlier observed in the case of B (and/or C) doped $GdPd_3$ and was attributed to structural anomalies occurring at this temperature (section 1.5, chapter 3). In addition, cooling and heating cycles of ρ(T) data for $TbPd_3B$ clearly show a bifurcation at $T \sim 44$ K [inset (a), Fig. 6.5] and thus suggest that the proposed structural transition is of the first-order in nature. In contrast to $TbPd_3$, the ρ(T) behavior of this compound does not show any upturn at low temperatures. Instead ρ(T) of $TbPd_3B$ shows a tendency towards saturation as temperature decreases below ~ 10 K [inset (b), Fig. 6.5]. At low temperatures ρ(T) values in the presence of $H = 7$ T are higher than that in the case of $H = 0$ [inset (b), Fig. 6.5], and thus lead to a positive MR in $TbPd_3B$ in contrast to the negative one observed for $TbPd_3$.

Temperature dependence of MR is shown in Fig. 6.6. $TbPd_3$ exhibits a negative MR with a monotonic increase in the magnitude with decreasing temperature. The value of MR is $\sim -30\%$ at the lowest temperature of measurement ($T = 1.6$ K), which is fairly large as comparison to most intermetallic compounds. The value of MR observed in the case of $TbPd_3$ is largest among the RPd_3 compounds [Fig. 6.7]. The negative value of MR suggests that the dominating interaction in $TbPd_3$ is of FM nature, as was also inferred by the positive value of θ_p (Table 6.1).

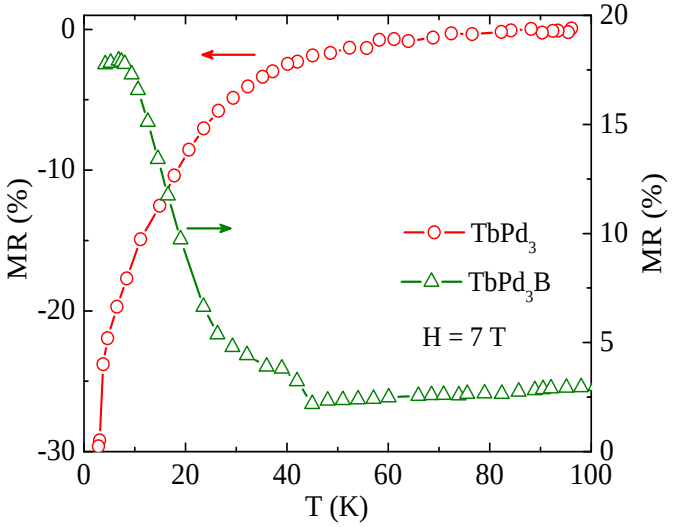

FIGURE 6.6: Magnetoresistance (MR), $R_H = \frac{\rho(H)-\rho(H=0)}{\rho(H=0)}$(%), as function of temperature for $TbPd_3$ and $TbPd_3B$, in the presence of $H = 7$ T applied field.

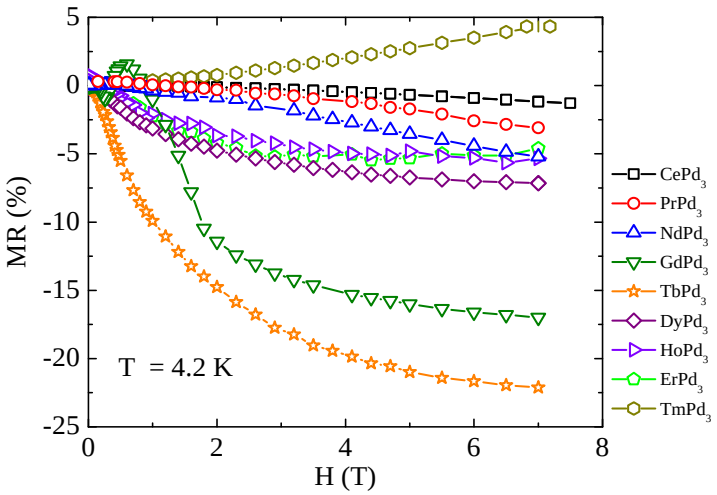

FIGURE 6.7: Magnetoresistance (MR), $R_H = \frac{\rho(H)-\rho(H=0)}{\rho(H=0)}$(%), of RPd_3 compounds (R: Ce, Pr, Nd, Gd, Tb, Dy, Ho, Er and Tm) as function of applied DC-magnetic field measured at $T = 4.2$ K.

The field variation of MR of $TbPd_3$ is shown in the Fig. 6.8. The magnitude of the observed MR decrease with the increase in temperature. At $T = 50$ K, which is sufficiently higher than the ordering temperature of $TbPd_3$, MR exhibits a typical H^2 dependence. This behavior is expected in the paramagnetic region due to the suppression of paramagnetic spin-fluctuations on the application of external magnetic field [192, 193].

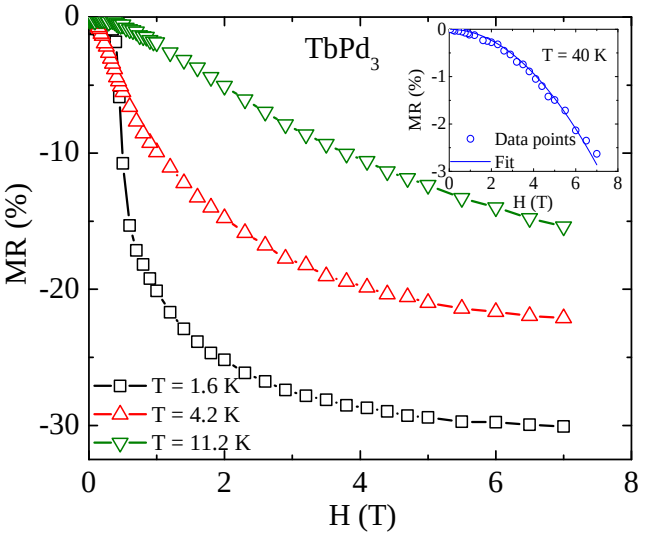

FIGURE 6.8: Magnetoresistance (MR), $R_H = \frac{\rho(H)-\rho(H=0)}{\rho(H=0)}$(%), of $TbPd_3$ as function of applied DC-magnetic field, measured at three different temperatures, 1.6, 4.2 and 10.0 K. The inset exhibits field variation of MR at 50 K. The solid line in inset is the H^2 fit of the data.

As mentioned earlier, in contrast to $TbPd_3$, the B-doped compound $TbPd_3B$ exhibits a positive MR with a value of $\sim +18\%$ at 1.6 K [Fig. 6.6]. The positive MR observed

for $TbPd_3B$ suggests an increase in spin-disorder scattering upon application of external magnetic field. Nearly linear variation of MR with H [Fig. 6.9] suggests a proportional increment of spin-dependent scattering with the applied magnetic field. Similar to $TbPd_3$, MR of $TbPd_3B$ at 50 K also exhibits H^2 field dependence in paramagnetic region [inset, Fig. 6.9]. The MR values of $TbPd_3B$ exhibit a sharp change of slope at $\sim$ 44 K [Fig. 6.6] due to occurance of structural anomalies at this temperature. As both $TbPd_3$ and $TbPd_3B$ contain the same magnetic RE ion and possess similar values of μ_{eff}, it is inferred that there is no correlation between the sign of the observed MR and the moment values of the magnetic ions. However, the correspondence between respective values of θ_p and sign of observed MR clearly suggest that there is a distinct correlation between the origin of MR and the type of magnetic exchange interaction present in the compounds. Although there exists a posibility of positive MR in AFM compounds due to enhancement of spin-fluctuations in magnetic sublattices, the values observed in such cases are usually small [233]. Since in the present case, the observed positive values of MR for $TbPd_3B$ are relatively high, it may not be attributed to the above mentioned effect. Simple cubic structure of $TbPd_3B$ also rules out the possibility of interfacial-reflectivity-driven positive GMR that occurs in some layered structures and superlattices [233, 234].

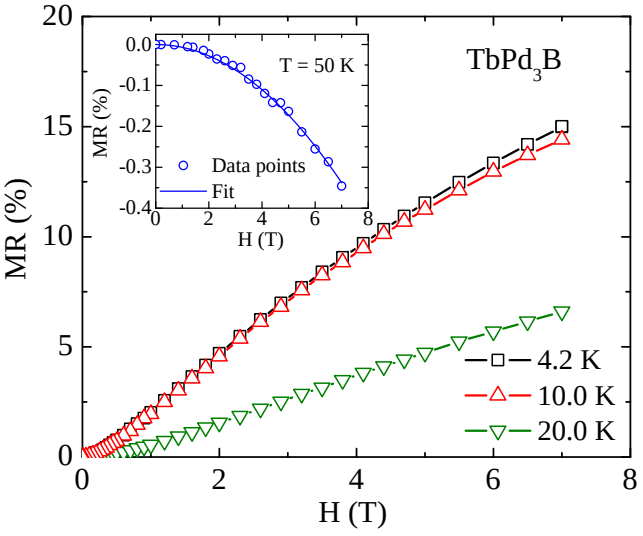

FIGURE 6.9: Magnetoresistance (MR), $R_H = \frac{\rho(H)-\rho(H=0)}{\rho(H=0)}$(%), of $TbPd_3B$ as function of applied DC-magnetic field, measured at three different temperatures, 4.2, 10.0 and 20.0 K. The inset exhibits field variation of MR at 50 K. The solid line in inset is the H^2 fit of the data.

The significant difference between the ρ(T) values of $TbPd_3B$ measured at H=0 and 7 T occurs only below $T \sim 25$ K [inset (b), Fig. 6.5]. This temperature coincides with the temperature below which χ^{-1}(T) for $TbPd_3B$ starts exhibiting non-linear temperature dependence [inset, Fig. 6.5]. The observed non linearity in χ^{-1}(T) above the magnetic

ordering temperature (3 K) is a signature of the presence of short-ranged magnetic correlations in $TbPd_3B$ which persists up to ~ 25 K. The occurrence of both the anomalies, in MR as well as in χ^{-1}(T), around the same temperature (25 K) suggests that the observed positive MR in $TbPd_3B$ could be due to strong magnetic scattering occurring in the vicinity of these short-ranged, uncorrelated magnetic domains. However more detailed investigations are needed to unravel the exact mechanism behind the observed positive GMR in $TbPd_3B$ and is beyond the scope of this work.

6.5 Conclusion

In summary, we have studied magnetic and transport properties of cubic $TbPd_3$ and boron-incorporated metallic perovskite compound $TbPd_3B$. While the former exhibits the largest negative GMR ($\sim -30\%$) in RPd_3 series, the latter exhibits a positive GMR ($\sim +18\%$). Both $TbPd_3$ and $TbPd_3B$ also exhibit quite distinct ρ(T) behavior. $TbPd_3B$ exhibits a structural anomaly at 44 K, which also reflects its signature in magneto-transport properties. The magnetotransport behavior seems to be correlated with the magnetic interactions such that the small perturbation introduced via doping of a light nonmagnetic element B, without altering the crystal symmetries, leads to the sign reversal of MR.

Chapter 7

Summary and scope for further work

7.1 Summary

This thesis is based on the experimental investigations performed on metallic perovskite compounds of $RT_3B_xC_{1-x}$ (R: rare-earth and T: transition metal) series and the parent binary RT_3 compositions. As mentioned in the chapter 1, the cubic structure of these compounds makes theoretical modeling easy as well as experimental manipulations possible. In our investigations, we have observed that the various physical properties (such as magnetic, electrical-transport, valence, thermal expansion etc.) of $RT_3B_xC_{1-x}$ compounds change significantly upon boron (and/or carbon) incorporation as well as with the relative variation of the boron and carbon stoichiometries.

Some of the main findings of the investigations reported in the thesis are; (i) the observation of negative thermal expansion in $GdPd_3B_{0.25}C_{0.75}$, (ii) occurrence of negative temperature coefficient of resistance in ordered metallic compound $GdPd_3B$, (iii) variation of strength and nature of the magnetic interactions with the rare-earth ion distance, (iv) correlation between magnetic and magneto-transport properties of $GdPd_3B_{0.25}C_{0.75}$ compounds, (v) interdependence of the valencies of Ce and Eu ions in $Ce_{0.5}Eu_{0.5}Pd_3B_x$ compounds, and (vi) the sign reversal of the magnetoresistance upon boron incorporation in $TbPd_3$.

The results of temperature dependent structural analysis presented in the chapter 3 conclusively prove that the $GdPd_3B_xC_{1-x}$ compounds are formed essentially in single phase and crystallize in the cubic perovskite like structure with $Pm\bar{3}m$ space group symmetry. The parent $GdPd_3$ also crystallizes with the same space group symmetry

but with vacant body centre lattice site. The off-stoichiometric compositions crystallize with $Pm\bar{3}m$ space group symmetry as well. The structural analysis presented in this chapter is quite relevant to the compounds discussed in subsequent chapters as well.

We have observed negative thermal expansion (NTE) in $GdPd_3B_{0.25}C_{0.75}$ that have an asymmetric distribution of boron and carbon. The observed NTE has been attributed to the low energy transverse vibrations of relatively loosely packed Pd-atoms. As $GdPd_3B_{0.25}C_{0.75}$ is a crystalline metallic compound having e-ph interactions as the dominant mechanism of scattering, the phonon modes that lead to NTE are expected to show their signature in the electrical transport behaviour as well. We have indeed observed such correlation in the observed NTE and electrical transport properties of the compound.

We have observed novel result of negative temperature coefficient of resistivity (NTCR) in ordered metallic perovskite compound $GdPd_3B$. The occurrence of NTCR in this compound has been attributed to the reduction in the strain modulated electron effective mass with increase in temperature. Substitution of boron with carbon leads to change in the sign of the TCR of $GdPd_3B_xC_{1-x}$ compounds, and we observe a positive TCR for the composition with carbon stoichiometry ≥ 0.5.

The analysis of the results of temperature dependent AC and DC magnetic measurements suggest that the nature and strength of magnetic interactions present in $GdPd_3B_xC_{1-x}$ compounds can be modified by changing the rare-earth ion distances. The variation of paramagnetic Curie temperatures with the distance of rare-earth ions suggests for the occurrence of RKKY like oscillations in these bulk compositions. Magneto-transport studies suggest a close correlation between the magnetic interactions present in the compound and the field-dependent low temperature electrical transport properties.

Interdependence of the valence behavior of Ce and Eu ions (that occupy the same crystallographic site (0, 0, 0) of the cubic unit cell) present in $Ce_{0.50}Eu_{0.50}Pd_3B_x$ is investigated in chapter 4. The analysis of the results of Eu-Mössbauer and magnetic measurements performed on $Ce_{0.50}Eu_{0.50}Pd_3$ suggests that both Ce as well as Eu are in intermediate valence state in this compound. The analysis suggest that valency of Ce ions in this compound is relatively higher than the valency of Ce ions present in $CePd_3$. Hybridization-induced charge transfer between the $4f$ states of Ce and Eu ions is believed to be the underlying reason for the intermediate valency of Ce and Eu ions in this compound. The valence and magnetic behavior of rare-earth ions in boron-filled $Ce_{0.5}Eu_{0.5}Pd_3B_x$ ($x = 0.50$ and 1.0) is substantially different from that of $Ce_{0.5}Eu_{0.5}Pd_3$. In contrast to $Ce_{0.5}Eu_{0.5}Pd_3$, the $Ce_{0.5}Eu_{0.5}Pd_3B_x$ compounds also exhibit the presence of charge ordering of different valence states of Eu ions.

We have also investigated the effect of doping a non-magnetic rare-earth ion on the valency of Eu ions present in binary $EuPd_3$. The results of DC magnetic measurements suggest that the valency of Eu ions present in doped composition $Eu_{0.4}La_{0.6}Pd_3$ differs from the normal +3 observed in the case of $EuPd_3$. The change in the valency of Eu ions present in $Eu_{0.4}La_{0.6}Pd_3$ in comparison with that in $EuPd_3$ has been attributed to the negative chemical pressure driven lattice parameter enhancement. More detailed experiments and analysis is indeed required to conclusively prove the presence of valence fluctuating Eu ions in this compound.

The magnetic behavior of binary YPd_3 is discussed in chapter 5. YPd_3 is one of the possible candidates for the hydrogen storage materials and hence relate to one of the most demanding area of energy based research. Our results suggest that although YPd_3 is diamagnetic, the presence of very dilute amount (only a few ppm) of magnetic ions can significantly alter the magnetic behavior of this compound. Such additional magnetic impurity elements also modify the low temperature electrical transport behavior of the compound.

Experimental investigations on binary $TbPd_3$ and boron incorporation metallic perovskite $TbPd_3B$ suggest that magneto-transport behavior of these compounds delicately correlates with the type of magnetic interactions present in the materials. Results of magnetic measurements suggest that dominating magnetic interaction in $TbPd_3$ is of ferromagnetic in nature, while the same for boron-incorporated $TbPd_3B$ is of antiferromagnetic. Boron-incorporation not only changes the nature of magnetic interactions present in the compounds under considerations but also significantly alters their magneto-transport behaviour. On one hand $TbPd_3$ exhibits the negative GMR of $\sim 30\%$, and on the other hand boron-incorporated $TbPd_3B$ exhibits the positive MR of $\sim 18\%$. The observed negative GMR in $TbPd_3$ can be attributed to the presence of prominent ferromagnetic interaction in the compound. Strong scattering occurring in the vicinity of short-range magnetic correlations present in $TbPd_3B$ is believed to be the underlying reason for the observed positive MR in this compound.

As mentioned in the preface as well as in chapter 1, there are indeed very less investigation on metallic perovskite materials compared to their oxygen-based counterparts. Hence there is a large scope for further work (both experimental as well as theoretical) related to such materials. Some of the possible future works are briefly discussed below.

7.2 Future prospects

In the present thesis, we have only concentrated on the measurement of a few physical properties of the bulk polycrystalline phase of the materials. Extension of the work on the same materials in single crystal form will be very helpful in conclusively answering some of the questions, such as what is the effect of grain boundaries and microscopic disorder on the electrical transport properties of these materials, etc. Calculation and measurement of phonon dispersion could be helpful to understand the effect of proposed transverse vibrations of Pd atoms on thermal expansion and electrical transport properties. Study of the electrical transport behaviour in the thin film samples of $GdPd_3B$ would be helpful to probe the mechanisms that govern electrical transport in this material. It may be mentioned that reducing the dimension of the material also modifies its electronic structure. Study of related materials, such as $RRh_3B_xC_{1-x}$ etc., where some other transition metal (Rh in this case) is used in place of Pd will be helpful to make comparative study and to find out the role played by the transition metal atoms in defining various physical properties of these materials.

Bibliography

[1] C. N. R. Rao and B. Raveau (Editors). Colossal magnetoresistance, charge ordering and related properties of manganese oxide. *World Scientific*, (1998).

[2] M. A. Peña and J. L. G. Fierro. *Chem. Rev.*, **101**:1981, (2001). URL http://pubs.acs.org/doi/abs/10.1021/cr980129f.

[3] N. W. Ashcroft and N. D. Mermin. Solid state physics, chapter 27. *Thomson Learning Press*, (2004).

[4] H. D. Megaw. *Proc. Phys. Soc.*, **58**:133, (1946). URL http://www.iop.org/EJ/abstract/0959-5309/58/2/301.

[5] W. E. Pickett and D. J. Singh. *Phys. Rev. B*, **53**:1146, (1996). URL http://prola.aps.org/abstract/PRB/v53/i3/p1146_1.

[6] H. Röder, J. Zang, and A. R. Bishop. *Phys. Rev. Lett.*, **76**:1356, (1996). URL http://prola.aps.org/abstract/PRL/v76/i8/p1356_1.

[7] Y. Uozu, Y. Wakabayashi, Y. Ogimoto, N. Takubo, H. Tamaru, N. Nagaosa, and K. Miyano. *Phys. Rev. Lett.*, **97**:037202, (2006). URL http://link.aps.org/doi/10.1103/PhysRevLett.97.037202.

[8] A. P. Ramirez. *J. Phys. Condens. Matter*, **9**:8171, (1997). URL http://www.iop.org/EJ/abstract/0953-8984/9/39/005.

[9] W. Bao, J. D. Axe, C. H. Chen, and S-W. Cheong. *Phys. Rev. Lett.*, **78**:543, (1997). URL http://link.aps.org/doi/10.1103/PhysRevLett.78.543.

[10] O. Tegus, E. Brück, K. H. J. Buschow, and F. R. de Boer. *Nature (London)*, **415**: 150, (2002). URL http://www.nature.com/nature/journal/v415/n6868/abs/415150a.html.

[11] M. H. Phan and S. C. Yu. *J. Magn. Magn. Mater.*, **308**:325, (2007).

[12] D. C. Arnold, K. S. Knight, F. D. Morrison, and P. Lightfoot. *Phys. Rev. Lett.*, **102**:027602, (2009). URL http://link.aps.org/doi/10.1103/PhysRevLett.102.027602.

[13] Y. Yao and H. Fu. *Phys. Rev. B*, **79**:014103, (2009). URL http://link.aps.org/doi/10.1103/PhysRevB.79.014103.

[14] W. Eerenstein, N. D. Mathur, and J. F. Scott. *Nature (London)*, **442**: 759, (2006). URL http://www.nature.com/nature/journal/v442/n7104/abs/nature05023.html.

[15] S. W. Cheong and M. Mostovoy. *Nature Materials*, **6**:13, (2007). URL http://www.nature.com/nmat/journal/v6/n1/abs/nmat1804.html.

[16] C. W. Nan, M. I. Bichurin, S. Dong, D. Viehl, and G. Srinivasan. *J. Appl. Phys.*, **103**:031101, (2008). URL http://link.aip.org/link/?JAPIAU/103/031101/1.

[17] T. Shishido, J. Ye, S. Okada, K. Kudou, K. Iizumi, M. Oku, Y. Ishizawa, T. Amano, S. Kohiki, Y. Kawazoe, and K. Nakajima. *J. Alloys Compd.*, **354**: 198, (2003).

[18] R. Sahara, T. Shishido, A. Nomura, K. Kudou, S. Okada, and V. Kumar. *Phys. Rev. B*, **73**:184102, (2006). URL http://link.aps.org/doi/10.1103/PhysRevB.73.184102.

[19] R. Sahara, T. Shishido, A. Nomura, K. Kudou, S. Okada, and V. Kumar. *Phys. Rev. B*, **76**:024105, (2007). URL http://link.aps.org/doi/10.1103/PhysRevB.76.024105.

[20] H. Kojima, R. Sahara, T. Shishido, A. Nomura, K. Kudou, S. Okada, and V. Kumar. *Appl. Phys. Lett.*, **91**:081901, (2007). URL http://link.aip.org/link/?APPLAB/91/081901/1.

[21] D. Music, Z. Sun, and J. M. Schneider. *Phys. Rev. B*, **71**:052104, (2005). URL http://link.aps.org/doi/10.1103/PhysRevB.71.052104.

[22] D. Music and J. M. Schneider. *Appl. Phys. Lett.*, **89**:121914, (2006). URL http://link.aip.org/link/?APPLAB/89/121914/1.

[23] D. Music, R. Ahuja, and J. M. Schneider. *Phys. Lett. A*, **356**:251, (2006).

[24] P. Ravindran, S. Sankaralingam, and A. Ashokamani. *Phys. Rev. B*, **52**:12921, (1995). URL http://link.aps.org/doi/10.1103/PhysRevB.52.12921.

[25] C. Loison, A. Leithe-Jasper, and H. Rosner. *Phys. Rev. B*, **75**:205135, (2007). URL http://link.aps.org/doi/10.1103/PhysRevB.75.205135.

[26] A. S. Mikhaylushkin, C. Höglund, J. Birch, Zs. Czigány, L. Hultman, S. I. Simak, B. Alling, F. Tasnádi, and I. A. Abrikosov. *Phys. Rev. B*, **79**:134107, (2009). URL http://link.aps.org/doi/10.1103/PhysRevB.79.134107.

[27] B. Wiendlocha, J. Tobola, and S. Kaprzyk. *Phys. Rev. B*, **73**:134522, (2006). URL http://link.aps.org/doi/10.1103/PhysRevB.73.134522.

[28] M. Mattesini. *Phys. Rev. B*, **79**:125122, (2009). URL http://link.aps.org/doi/10.1103/PhysRevB.79.125122.

[29] M. Magnuson, M. Mattesini, C. Höglund, I. A. Abrikosov, J. Birch, and L. Hultman. *Phys. Rev. B*, **78**:235102, (2008). URL http://link.aps.org/doi/10.1103/PhysRevB.78.235102.

[30] T. He, Q. Huang, A. P. Ramirez, Y. Wang, K. A. Regan, N. Rogado, M. A. Hayward, M. K. Haas, J. S. Slusky, K. Inumara, H. W. Zandbergan, N. P. Ong, and R. J. Cava. *Nature (London)*, **411**:54, (2001). URL http://www.nature.com/nature/journal/v411/n6833/abs/411054a0.html.

[31] H. Rosner, R. Weht, M. D. Johannes, W. E. Pickett, and E. Tosatti. *Phys. Rev. Lett.*, **88**:027001, (2001). URL http://link.aps.org/doi/10.1103/PhysRevLett.88.027001.

[32] Z. Q. Mao, M. M. Rosario, K. D. Nelson, K. Wu, I. G. Deac, P. Schiffer, Y. Liu, T. He, K. A. Regan, and R. J. Cava. *Phys. Rev. B*, **67**:094502, (2003). URL http://link.aps.org/doi/10.1103/PhysRevB.67.094502.

[33] A. Y. Ignatov, S. Y. Savrasov, and T. A. Tyson. *Phys. Rev. B*, **68**:220504(R), (2003). URL http://link.aps.org/doi/10.1103/PhysRevB.68.220504.

[34] C. Sulkowski, T. Klimczuk, R. J. Cava, and K. Rogacki. *Phys. Rev. B*, **76**:060501, (2007). URL http://link.aps.org/doi/10.1103/PhysRevB.76.060501.

[35] G. Zhong, J. Wang, Z. Zeng, X. Zheng, and H. Lin. *J. Appl. Phys.*, **101**:09G520, (2007). URL http://link.aip.org/link/?JAPIAU/101/09G520/1.

[36] P. K. Jha. *Phys. Rev. B*, **72**:214502, (2007). URL http://link.aps.org/doi/10.1103/PhysRevB.72.214502.

[37] P. Zheng, J. L. Luo, G. T. Liu, Y. L. Zhang, R. C. Yu, C. Q. Jin, N. L. Wang, and M. Q. Tan. *Phys. Rev. B*, **72**:092509, (2005). URL http://link.aps.org/doi/10.1103/PhysRevB.72.092509.

[38] T. Klimczuk, M. Avdeev, J. D. Jorgensen, and R. J. Cava. *Phys. Rev. B*, **71**:184512, (2005). URL http://link.aps.org/doi/10.1103/PhysRevB.71.184512.

[39] D. P. Young, M. Moldovan, and P. W. Adams. *Phys. Rev. B*, **70**:064508, (2004). URL http://link.aps.org/doi/10.1103/PhysRevB.70.064508.

[40] S. Bağci, S. Duman, H. M. Tütüncü, and G. P. Srivastava. *Phys. Rev. B*, **78**:174504, (2008). URL http://link.aps.org/doi/10.1103/PhysRevB.78.174504.

[41] I. R. Shein and A. L. Ivanovskii. *Phys. Rev. B*, **77**:104101, (2008). URL http://link.aps.org/doi/10.1103/PhysRevB.77.104101.

[42] R.E. Schaak, M. Avdeev, W.-L. Lee, G. Lawes, H.W. Zandbergen, J.D. Jorgensen, N.P. Ong, A.P. Ramirez, and R.J. Cava. *J. Solid State Chem.*, **177**:1244, (2004).

[43] P. Tong, Y. P. Sun, X. B. Zhu, and W. H. Song. *Phys. Rev. B*, **74**:224416, (2006). URL http://link.aps.org/doi/10.1103/PhysRevB.74.224416.

[44] M. D. Johannes and W. E. Pickett. *Phys. Rev. B*, **70**:060507, (2004). URL http://link.aps.org/doi/10.1103/PhysRevB.70.060507.

[45] P. Tong, Y. P. Sun, X. B. Zhu, and W. H. Song. *Phys. Rev. B*, **73**:245106, (2006). URL http://link.aps.org/doi/10.1103/PhysRevB.73.245106.

[46] J. V. Appen, H. Lueken, and R. Dronskowski. *Angew. Chem. Int. Ed.*, **44**:1205, (2005). URL http://www3.interscience.wiley.com/journal/109862170/abstract.

[47] A. Houben, P. Müller, J. V. Appen, H. Lueken, R. Niewa, and R. Dronskowski. *Angew. Chem. Int. Ed.*, **44**:7212, (2005). URL http://www3.interscience.wiley.com/journal/112125770/abstract.

[48] C. Paduani. *J. Magn. Magn. Mater.*, **278**:231, (2004).

[49] Z. Wu and J. Meng. *Appl. Phys. Lett.*, **90**:241901, (2007). URL http://link.aip.org/link/?APPLAB/90/241901/1.

[50] D. Music and J. M. Schneider. *Appl. Phys. Lett.*, **88**:031914, (2006). URL http://link.aip.org/link/?APPLAB/88/031914/1.

[51] E. Zhao, H. Xiang, J. Meng, and Z. Wu. *Chem. Phys. Lett.*, **449**:96, (2007).

[52] S. K. Chen, S. Jin, T. H. Tiefel, Y. F. Hsieh, E. M. Gyorgy, and D. W. Johnson Jr. *J. Appl. Phys.*, **70**:6247, (1991). URL http://link.aip.org/link/?JAPIAU/70/6247/1.

[53] C. M. Deng, C. F. Huo, L. L. Bao, X. R. Shi, Y. W. Li, J. Wang, and H. Jiao. *Chem. Phys. Lett.*, **448**:83, (2007).

[54] S. Iikubo, K. Kodama, K. Takenaka, H. Takagi, M. Takigawa, and S. Shamoto. *Phys. Rev. Lett.*, **101**:205901, (2008). URL http://link.aps.org/doi/10.1103/PhysRevLett.101.205901.

[55] K. Takenaka and H. Takagi. *Appl. Phys. Lett.*, **87**:261902, (2005). URL http://link.aip.org/link/?APPLAB/87/261902/1.

[56] R. Huang, L. Li, F. Cai, X. Xu, and L. Qian. *Appl. Phys. Lett.*, **93**:081902, (2008). URL http://link.aip.org/link/?APPLAB/93/081902/1.

[57] Y. Sun, C. Wang, Y. Wen, and K. Zhu. *Appl. Phys. Lett.*, **91**:231913, (2007). URL http://link.aip.org/link/?APPLAB/91/231913/1.

[58] Y. B. Li, W. F. Li, W. J. Feng, Y. Q. Zhang, and Z. D. Zhang. *Phys. Rev. B*, **72**:024411, (2005). URL http://link.aps.org/doi/10.1103/PhysRevB.72.024411.

[59] W. S. Kim, E. O. Chi, J. C. Kim, N. H. Hur, K. W. Lee, and Y. N. Choi. *Phys. Rev. B*, **68**:172402, (2003). URL http://link.aps.org/doi/10.1103/PhysRevB.68.172402.

[60] M. H. Yu, L. H. Lewis, and A. R. Moodenbaugh. *J. Appl. Phys.*, **93**:10128, (2003). URL http://link.aip.org/link/?JAPIAU/93/10128/1.

[61] J. H. Shim, S. K. Kwon, and B. I. Min. *Phys. Rev. B*, **66**:020406(R), (2002). URL http://link.aps.org/doi/10.1103/PhysRevB.66.020406.

[62] K. Kamishima, T. Goto, H. Nakagawa, N. Miura, M. Ohashi, and N. Mori. *Phys. Rev. B*, **63**:024426, (2000). URL http://link.aps.org/doi/10.1103/PhysRevB.63.024426.

[63] E. O. Chi, W. S. Kim, and N. H. Hur. *Solid State Comm.*, **120**:307, (2001).

[64] S. K. Dhar, S. K. Malik, and R. Vijayaraghavan. *Phys. Rev. B*, **24**:6182, (1981). URL http://link.aps.org/doi/10.1103/PhysRevB.24.6182.

[65] S. K. Dhar, S. K. Malik, D. Rambabu, and R. Vijayaraghavan. *J. Appl. Phys.*, **53**:8077, (1982). URL http://link.aip.org/link/?JAPIAU/53/8077/1.

[66] S. K. Dhar, S. K. Malik, R. Vijayaraghavan, M. M. Abd-Elmeguid, and H. Micklitz. *Phys. Rev. B*, **29**:5953, (1984). URL http://link.aps.org/doi/10.1103/PhysRevB.29.5953.

[67] B. Darshan, B. D. Padalia, R. Nagarajan, S. K. Dhar, S. K. Malik, and R. Vijayaraghavan. *Phys. Rev. B*, **30**:4031, (1984). URL http://link.aps.org/doi/10.1103/PhysRevB.30.4031.

[68] C. L. Cianchi, S. De Gennaro, F. Gulisano, M. Mancini, and G. Spina. *J. Phys. Condens. Matter*, **3**:781, (1991). URL http://www.iop.org/EJ/abstract/0953-8984/3/7/002.

[69] S. K. Dhar, S. K. Malik, and R. Vijayaraghavan. *Mat. Res. Bull.*, **16**:1557, (1981).

[70] T. Shishido, H. Yamauchi, K. Kudou, S. Okada, J. Ye, A. Yoshikawa, H. Horiuchi, and T. Fukuda. *Jpn. J. Appl. Phys.*, **36**:L1436, (1997). URL http://jjap.ipap.jp/link?JJAP/36/L1436/.

[71] T. Shishido, J. Ye, K. Kudou, S. Okada, K. Obara, T. Sugawara, M. Oku, K. Wagatsuma, H. Horiuchi, and T. Fukuda. *J. Alloys Compd.*, **291**:52, (1999).

[72] T. Shishido, J. Ye, S. Okada, K. Kudou, K. Iizumi, M. Oku, Y. Ishizawa, R. Sahara, V. Kumar, A. Yoshikawa, M. Tanaka, H. Horiuchi, A. Nomura, T. Sugawara, K. Obara, T. Amano, S. Kohiki, Y. Kawazoe, and K. Nakajima. *J. Alloys Compd.*, **408**:379, (2006).

[73] H. Takei, N. Kobayashi, H. Yamauchi, T. Shishido, and T. Fukase. *J. Less Common Met.*, **125**:233, (1986).

[74] J. T. Zhao, Z. C. Dong, J. T. Vaughey, J. E. Ostenson, and J. D. Corbett. *Solid State Comm.*, **230**:1, (1995).

[75] M. Y. Chern, D. A. Vennos, and F. J. Disalvo. *J. Solid State Chem.*, **96**:415, (1992).

[76] F. Bondino, M. Malvestuto, E. Magnano, M. Zangrando, M. Zacchigna, P. Ghigna, and F. Parmigiani. *Phys. Rev. B*, **79**:115120, (2009). URL http://link.aps.org/doi/10.1103/PhysRevB.79.115120.

[77] J. Deisenhofer, I. Leonov, M. V. Eremin, Ch. Kant, P. Ghigna, F. Mayr, V. V. Iglamov, V. I. Anisimov, and D. van der Marel. *Phys. Rev. Lett.*, **101**:157406, (2008). URL http://link.aps.org/doi/10.1103/PhysRevLett.101.157406.

[78] M. V. Eremin, D. V. Zakharov, H.-A. Krug von Nidda, R. M. Eremina, A. Shuvaev, A. Pimenov, P. Ghigna, J. Deisenhofer, and A. Loidl. *Phys. Rev. Lett.*, **101**:147601, (2008). URL http://link.aps.org/doi/10.1103/PhysRevLett.101.147601.

[79] A. Salazar, M. Massot, A. Olega, A. Pawlak, and W. Schranz. *Phys. Rev. B*, **75**:224428, (2007). URL http://link.aps.org/doi/10.1103/PhysRevB.75.224428.

[80] J. J. Pearson. *Phys. Rev.*, **121**:695, (1961). URL http://link.aps.org/doi/10.1103/PhysRev.121.695.

[81] V. Minkiewicz and A. Nakamura. *Phys. Rev.*, **143**:356, (1966). URL http://link.aps.org/doi/10.1103/PhysRev.143.356.

[82] I. Maartense and C. W. Searle. *Phys. Rev. B*, **6**:894, (1972). URL http://link.aps.org/doi/10.1103/PhysRevB.6.894.

[83] J. R. Seretlo, J. J. Martin, and E. sonder. *Phys. Rev. B*, **14**:5404, (1976). URL http://link.aps.org/doi/10.1103/PhysRevB.14.5404.

[84] C. Dotzler, G. V. M. Williams, U. Rieser, and A. Edgar. *Appl. Phys. Lett.*, **91**:121910, (2007). URL http://link.aip.org/link/?APPLAB/91/121910/1.

[85] D. T. Teaney and M. J. Freiser. *Phys. Rev. Lett.*, **9**:212, (1962). URL http://link.aps.org/doi/10.1103/PhysRevLett.9.212.

[86] E. R. Naimon. *Phys. Rev. B*, **9**:737, (1974). URL http://link.aps.org/doi/10.1103/PhysRevB.9.737.

[87] H. Ikeda, J. A. Fernandez-Baca, R. M. Nicklow, M. Takahashi, and K. Iwasa. *J. Phys. Condens. Matter*, **6**:10543, (1994). URL http://www.iop.org/EJ/abstract/0953-8984/6/48/015.

[88] D. A. Tennant, D. F. McMorrow, S. E. Nagler, R. A. Cowley, and B. Fak. *J. Phys. Condens. Matter*, **6**:10341, (1994). URL http://www.iop.org/EJ/abstract/0953-8984/6/47/017.

[89] S. H. Tsai, A. Bunker, and D. P. Landau. *Phys. Rev. B*, **61**:333, (2000). URL http://link.aps.org/doi/10.1103/PhysRevB.61.333.

[90] R. Coldea, R. A. Cowley, D. F. McMorrow, and B. Roessli. *Phys. Rev. B*, **57**:5281, (1998). URL http://link.aps.org/doi/10.1103/PhysRevB.57.5281.

[91] M. Marinelli, F. Mercuri, S. Foglietta, and D. P. Belanger. *Phys. Rev. B*, **54**:4087, (1996). URL http://link.aps.org/doi/10.1103/PhysRevB.54.4087.

[92] A. Stunault, F. de Bergevin, D. Wermeille, C. Vettier, Th. Brückel, N. Bernhoeft, G. J. McIntyre, and J. Y. Henry. *Phys. Rev. B*, **60**:10170, (1999). URL http://link.aps.org/doi/10.1103/PhysRevB.60.10170.

[93] M. Fornari, A. Subedi, and D. J. Singh. *Phys. Rev. B*, **76**:214118, (2007). URL http://link.aps.org/doi/10.1103/PhysRevB.76.214118.

[94] E. Orgaz, V. Mazel, and M. Gupta. *Phys. Rev. B*, **54**:16124, (1996). URL http://link.aps.org/doi/10.1103/PhysRevB.54.16124.

[95] A. W. Overhauser. *Phys. Rev. B*, **35**:411, (1987). URL http://link.aps.org/doi/10.1103/PhysRevB.35.411.

[96] N. A. Spaldin. Magnetic materials: Fundamentals and device applications, chapter 3. *Cambridge University Press*, (2003).

[97] J. H. van Vleck. Theory of electric and magnetic susceptibility. *Oxford University Press*, (1931).

[98] M. A. Ruderman and C. Kittel. *Phys. Rev.*, **96**:99, (1954). URL http://link.aps.org/doi/10.1103/PhysRev.96.99.

[99] T. Kasuya. *Proc. Theor. Phys. (Kyoto)*, **16**:45, (1956).

[100] K. Yosida. *Phys. Rev.*, **106**:893, (1957). URL http://link.aps.org/doi/10.1103/PhysRev.106.893.

[101] P. G. deGennes. *J. Phys. Radium*, **23**:510, (1962).

[102] E. T. Lacheisserie, D. Gignoux, and M. Schlenker. Magnetism: I-fundamentals, chapter 3. *Kluwer Academic Publishers*, (2002).

[103] P. G. deGennes. *J. Phys. Radium*, **23**:630, (1962).

[104] T. A. Kaplan and D. H. Lyons. *Phys. Rev.*, **129**:2072, (1963). URL http://link.aps.org/doi/10.1103/PhysRev.129.2072.

[105] P. M. Levy. *Solid State Commun.*, **7**:1813, (1969).

[106] C. Mazumdar. Superconducting, valence fluctuating and magnetic properties of some rare-earth intermetallic compounds: Ph.d thesis, chapter 1. *Indian Institute of Technology, Bombay*, (1995).

[107] J. Z. Tao and A. W. Sleight. *J. Solid State Chem.*, **173**:442, (2003).

[108] N. Khosrovani and A. W. Sleight. *J. Solid State Chem.*, **121**:2, (1996).

[109] R. W. Cahn. *Nature (London)*, **386**:22, (1997).

[110] M. Shiga. *Curr. Opin. Solid State Mater. Sci.*, **1**:340, (1996).

[111] T. A. Marry, J. S. O. Evans, T. Vogt, and A. W. Sleight. *Science*, **272**:90, (1996).

[112] G. D. Barrera, J. A. O. Bruno, T. H. K. Barron, and N. L. Allan. *J. Phys. Condens. Matter*, **17**:R217, (2005). URL http://www.iop.org/EJ/abstract/0953-8984/17/4/R03.

[113] A. Sleight. *Nature (London)*, **425**:674, (2003). URL http://www.nature.com/nature/journal/v425/n6959/full/425674a.html.

[114] J. S. O. Evans, Z. Hu, J. D. Jorgensen, D. N. Argyiou, S. Short, and A. W. Sleight. *Science*, **275**:61, (1997).

[115] G. Ernst, C. Broholm, G. R. Kowach, and A. P. Ramirez. *Nature (London)*, **396**: 147, (1998). URL http://www.nature.com/nature/journal/v396/n6707/abs/396147a0.html.

[116] J. N. Hancock, C. Turpen, Z. Schlesinger, G. R. Kowach, and A. P. Ramirez. *Phys. Rev. Lett.*, **93**:225501, (2004). URL http://link.aps.org/doi/10.1103/PhysRevLett.93.225501.

[117] W. I. F. David, J. S. O. Evans, and A. W. Sleight. *Europhys. Lett.*, **46**:661, (1999). URL http://www.iop.org/EJ/abstract/0295-5075/46/5/661.

[118] J. R. Salvador, F. Guo, T. Hogan, and M. G. Kanatzidis. *Nature (London)*, **425**: 702, (2003). URL http://www.nature.com/nature/journal/v425/n6959/abs/nature02011.html.

[119] J. Arvanitidis, K. Papagelis, S. Margadonna, K. Prassides, and A. N. Fitch. *Nature (London)*, **425**:599, (2003). URL http://www.nature.com/nature/journal/v425/n6958/abs/nature01994.html.

[120] X. G. Zheng, H. Kubozono, H. Yamada, K. Kato, Y. Ishiwata, and C. N. Xu. *Nature Nanotech.*, **3**:724, (2008). URL http://www.nature.com/nnano/journal/v3/n12/abs/nnano.2008.309.html.

[121] A. W. Sleight. *Endeavour*, **19**:764, (1995).

[122] W. C. M. Mattens, H. Holscher, G. J. M. Tuin, A. C. Moleman, and F. R. de Boer. *J. Magn. Magn. Mater.*, **15-18**:982, (1980).

[123] N. W. Ashcroft and N. D. Mermin. Solid state physics, chapter 26. *Thomson Learning Press*, (2004).

[124] H. Y. Bai, C. Z. Tong, and P. Zheng. *J. Appl. Phys.*, **95**:1269, (2004). URL http://link.aip.org/link/?JAPIAU/95/1269/1.

[125] R. Tamura, T. Araki, and S. Takeuchi. *Phys. Rev. Lett.*, **90**:226401, (2003). URL http://link.aps.org/doi/10.1103/PhysRevLett.90.226401.

[126] S. R. Nagel. *Phys. Rev. B*, **16**:1694, (1977). URL http://link.aps.org/doi/10.1103/PhysRevB.16.1694.

[127] J. Hasegawa, R. Tamura, and S. Takeuchi. *Phys. Rev. B*, **66**:132201, (2002). URL http://link.aps.org/doi/10.1103/PhysRevB.66.132201.

[128] J. H. Mooij. *Phys. Status. Solidi*, **17**:521, (1973). URL http://www3.interscience.wiley.com/journal/112438122/abstract.

[129] C. C. Tsuei. *Phys. Rev. Lett.*, **57**:1943, (1986). URL http://link.aps.org/doi/10.1103/PhysRevLett.57.1943.

[130] U. Mizutani. Introduction to the electron theory of metals, chapter 15. *Cambridge University Press*, (2001).

[131] J. M. Ziman. *Philos. Mag.*, **6**:1013, (1961).

[132] G. Baym. *Phys. Rev.*, **135**:A1691, (1964). URL http://link.aps.org/doi/10.1103/PhysRev.135.A1691.

[133] P. J. Cote and L. V. Meisel. *Phys. Rev. Lett.*, **39**:102, (1977). URL http://link.aps.org/doi/10.1103/PhysRevLett.39.102.

[134] L. V. Meisel and P. J. Cote. *Phys. Rev. B*, **16**:2978, (1977). URL http://link.aps.org/doi/10.1103/PhysRevB.16.2978.

[135] L. V. Meisel and P. J. Cote. *Phys. Rev. B*, **17**:4652, (1978). URL http://link.aps.org/doi/10.1103/PhysRevB.17.4652.

[136] P. W. Anderson. *Phys. Rev.*, **109**:1492, (1958). URL http://link.aps.org/doi/10.1103/PhysRev.109.1492.

[137] B. L. Altshuler and A. G. Aronove. Electron-electron interaction in disordered systems, edited by a. j. efros and m. pollak. *Elsevier Science Publications*, pages 1–153, (1985).

[138] N. W. Ashcroft and N. D. Mermin. Solid state physics, chapter 28. *Thomson Learning Press*, (2004).

[139] K. Gofryk, D. Kaczorowski, T. Plackowski, J. Mucha, A. Leithe-Jasper, W. Schnelle, and Yu. Grin. *Phys. Rev. B*, **75**:224426, (2007). URL http://link.aps.org/doi/10.1103/PhysRevB.75.224426.

[140] J. M. Lawrence, P. S. Riseborough, and R. D. Parks. *Rep. Prog. Phys.*, **44**:1, (1981). URL http://www.iop.org/EJ/abstract/0034-4885/44/1/001.

[141] G. R. Stewart. *Rev. Mod. Phys.*, **56**:755, (1984). URL http://link.aps.org/doi/10.1103/RevModPhys.56.755.

[142] C. M. Verma. *Rev. Mod. Phys.*, **48**:219, (1976). URL http://link.aps.org/doi/10.1103/RevModPhys.48.219.

[143] A. C. Hewson. *J. Magn. Magn. Mater.*, **12**:83, (1979).

[144] T. Kasuya and T. Saso (Editors). Theory of heavy fermions and valence fluctuations. *Springer-Varlac, Berlin*, page 23, (1985).

[145] Z. Fisk, H. R. Ott, T. M. Rice, and J. L. Smith. *Nature (London)*, **320**: 124, (1986). URL http://www.nature.com/nature/journal/v320/n6058/pdf/320124a0.pdf.

[146] K. A. Gschneidner (Jr.) and L. R. Eyring (Editors). Handbook on the physics and chemistry of rare earths. *North-Holland Publishing Company*, (1978).

[147] H. R. Ott. *Prog. Low. Temp. Phys.*, **11**:215, (1987).

[148] L. L. Hirst. *Kondens. Matter.*, **11**:255, (1970).

[149] L. L. Hirst. *J. Phys. Chem. Solids*, **35**:1285, (1974).

[150] L. L. Hirst. *AIP Conf. Proc.*, **24**:11, (1975). URL http://link.aip.org/link/?APCPCS/24/11/1.

[151] L. L. Hirst. *Phys. Rev. B*, **15**:1, (1977). URL http://link.aps.org/doi/10.1103/PhysRevB.15.1.

[152] B. C. Sales and D. K. Wohlleben. *Phys. Rev. Lett.*, **35**:1240, (1975). URL http://link.aps.org/doi/10.1103/PhysRevLett.35.1240.

[153] J. Friedel. *Nuovo Cimento Suppl.*, **7**:287, (1958).

[154] P. W. Anderson. *Phys. Rev.*, **124**:41, (1961). URL http://link.aps.org/doi/10.1103/PhysRev.124.41.

[155] J. C. P. Klaasse, W. C. M. Mattens, F. R. de Boer, and P. F. de Châtel. *Physica B+C*, **86-88**:234, (1977).

[156] W. Franz, F. Steglich, W. Zell, D. Wohlleben, and F. Pobell. *Phys. Rev. Lett.*, **45**: 64, (1980). URL http://link.aps.org/doi/10.1103/PhysRevLett.45.64.

[157] C. Mazumdar, R. Nagarajan, S. K. Dhar, L. C. Gupta, R. Vijayaraghavan, and B. D. Padalia. *Phys. Rev. B*, **46**:9009, (1992). URL http://link.aps.org/doi/10.1103/PhysRevB.46.9009.

[158] A. Pandey and C. Mazumdar. *Unpublished*.

[159] J. R. Carvajal. *Abstract of the Satellite Meeting on Powder Diffraction of the XV Congress of the IUCr, Toulouse, France*, page 127, (1990).

[160] B. D. Cullity. Elements of x-ray diffraction (second edition). *Addison Wesley Publishing Company, Inc.*, (1978).

[161] Anis Biswas. Charge ordering and related phenomenon in nanocrystalline manganites, ph. d thesis. *Jadavpur University*, (2008).

[162] B. D. Josephson. *Phys. Lett.*, **1**:251, (1962).

[163] U. Mizutani. Introduction to electron thery of metals. *Camrbridge University Press*, (2003).

[164] J. C. Jaklevic, J. Lambe, A. H. Silver, and J. E. Mercereau. *Phys. Rev. Lett.*, **12**: 159, (1964). URL http://link.aps.org/doi/10.1103/PhysRevLett.12.159.

[165] R. L. Mössbauer. *Z. Physik*, **151**:124, (1958). URL http://www.springerlink.com/content/p4335870w53k7834/?p=784e8c80fa814412af49977976fda1b0&pi=3.

[166] J. Freeman and R. B. Frankel. Hyperfine interactions. *Academic Press, New York*, (1967).

[167] R. M. Steffen, E. Matthias, and W. Schneider. Table of eigenvalues and eigenvectors of hamiltonian describing the combined static, magnetic dipole and electrical quadrupole interaction of nuclear levels. *Office of Technical Services, Department of Commerce, Washington 25 D.C., USA*, (1962).

[168] J. G. Stevans and R. S. Preston. Mössbauer effect data journal. *Mössbauer Effect Data Journal, IFI/Plenum Press*, page Appendix G p. 16, (1970).

[169] A. Pandey, C. Mazumdar, R. Ranganathan, S. Tripathi, D. Pandey, and S. Dattagupta. *Appl. Phys. Lett.*, **92**:261913, (2008). URL http://link.aip.org/link/?APPLAB/92/261913/1.

[170] A. Pandey, C. Mazumdar, R. Ranganathan, M. De Raychaudhury, T. Saha-Dasgupta, S. Tripathi, D. Pandey, and S. Dattagupta. *Europhys. Lett.*, **84**:47007, (2008). URL http://www.iop.org/EJ/abstract/0295-5075/84/4/47007.

[171] A. Pandey, C. Mazumdar, R. Ranganathan, and S. Dattagupta. *J. Magn. Magn. Mater.*, **321**:2311, (2009).

[172] D. Vaderbilt. *Phys. Rev. B*, **41**:7892, (1990). URL http://link.aps.org/doi/10.1103/PhysRevB.41.7892.

[173] G. Kresse and J. Hafner. *Phys. Rev. B*, **47**:558, (1993). URL http://link.aps.org/doi/10.1103/PhysRevB.47.558.

[174] G. Kresse and J. Furthmüller. *Comput. Mater. Sci.*, **6**:15, (1996).

[175] G. Kresse and J. Furthmüller. *Phys. Rev. B*, **54**:11169, (1996). URL http://link.aps.org/doi/10.1103/PhysRevB.54.11169.

[176] L. Ouyang, Y. N. Xu, and W. Y. Ching. *Phys. Rev. B*, **65**:113110, (2002). URL http://link.aps.org/doi/10.1103/PhysRevB.65.113110.

[177] Y. K. Kuo, K. M. Sivakumar, C. A. Su, C. N. Ku, S. T. Lin, A. B. Kaiser, J. B. Qiang, Q. Wang, and C. Dong. *Phys. Rev. B*, **74**:014208, (2006). URL http://link.aps.org/doi/10.1103/PhysRevB.74.014208.

[178] W. E. Gardner, J. Penfold, T. F. Smith, and I. R. Harris. *J. Phys. F: Metal Phys.*, **2**:133, (1972). URL http://www.iop.org/EJ/abstract/0305-4608/2/1/019.

[179] O. K. Anderson. *Phys. Rev. B*, **12**:3060, (1975). URL http://link.aps.org/doi/10.1103/PhysRevB.12.3060.

[180] P. Blaha et al. *WIEN2k.*

[181] E. Abrahams, P. W. Anderson, D. C. Licciardello, and T. V. Ramakrishnan. *Phys. Rev. Lett.*, **42**:673, (1979). URL http://link.aps.org/doi/10.1103/PhysRevLett.42.673.

[182] J. Dolinšek, S. Vrtnik, M. Klanjšek, Z. Jaglicic, A. Smontara, I. Smiljanic, A. Bilušic, Y. Yokoyama, A. Inoue, and C. V. Landauro. *Phys. Rev. B*, **76**:054201, (2007). URL http://link.aps.org/doi/10.1103/PhysRevB.76.054201.

[183] R. J. Elliot and A. F. Gibson. An introduction to solid state physics and its applications. *MacMillan-London.*

[184] N. A. Spaldin. Magnetic materials: Fundamentals and device applications, chapter 8. *Cambridge University Press.*

[185] R. Feyerherm, A. Loose, T. Ishida, T. Nogami, J. Kreitlow, D. Baabe, F. J. Litterst, S. Süllow, H.-H. Klauss, and K. Doll. *Phys. Rev. B*, **69**:134427, (2004). URL http://link.aps.org/doi/10.1103/PhysRevB.69.134427.

[186] D. N. Argyriou, J. F. Mitchell, C. D. Potter, D. G. Hinks, J. D. Jorgensen, and S. D. Bader. *Phys. Rev. Lett.*, **76**:3826, (1996). URL http://link.aps.org/doi/10.1103/PhysRevLett.76.3826.

[187] N. A. Chernova, Y. Song, P. Y. Zavalij, and M. S. Whittingham. *Phys. Rev. B*, **70**:144405, (2004). URL http://link.aps.org/doi/10.1103/PhysRevB.70.144405.

[188] V. Hardy, B. Raveau, R. Retoux, N. Barrier, and A. Maignan. *Phys. Rev. B*, **73**:094418, (2006). URL http://link.aps.org/doi/10.1103/PhysRevB.73.094418.

[189] Z. Y. Liu and S. Adenwalla. *Phys. Rev. Lett.*, **91**:037207, (2003). URL http://link.aps.org/doi/10.1103/PhysRevLett.91.037207.

[190] T. Park, V. A. Sidorov, H. Lee, Z. Fisk, and J. D. Thompson. *Phys. Rev. B*, **72**:060410, (2005). URL http://link.aps.org/doi/10.1103/PhysRevB.72.060410.

[191] M. Ellerby, K. A. McEwen, and J. Jensen. *Phys. Rev. B*, **57**:8416, (1998). URL http://link.aps.org/doi/10.1103/PhysRevB.57.8416.

[192] H. Yamada and S. Takada. *J. Physical Soc. Japan*, **34**:51, (1973). URL http://jpsj.ipap.jp/link?JPSJ/34/51/.

[193] K. Sengupta, S. Rayaprol, and E. V. Sampathkumaran. *J. Phys. Condens. Matter*, **16**:L495, (2004). URL http://www.iop.org/EJ/abstract/0953-8984/16/45/L02.

[194] C. Mazumdar, A. K. Nigam, R. Nagarajan, L. C. Gupta, C. Godart, B. D. Padalia, G. Chandra, and R. Vijayaraghavan. *Phys. Rev. B*, **54**:6069, (1996). URL http://link.aps.org/doi/10.1103/PhysRevB.54.6069.

[195] K. Takenaka, K. Asano, M. Misawa, and H. Takagi. *Appl. Phys. Lett.*, **92**:011927, (2008). URL http://link.aip.org/link/?APPLAB/92/011927/1.

[196] J. R. Thompson, S. T. Sekula, C.-K. Loong, and C. Stassis. *J. Appl. Phys.*, **53**:7893, (1982). URL http://link.aip.org/link/?JAPIAU/53/7893/1.

[197] A. Pandey, C. Mazumdar, R. Ranganathan, V. R. Reddy, and A. Gupta. *Appl. Phys. Lett.*, **94**:182503, (2009). URL http://link.aip.org/link/?APPLAB/94/182503/1.

[198] J. A. Hodges and J. B. Marimon da Cunha. *Solid State Comm.*, **64**:847, (1987).

[199] A. M. Strydom and R. Troc. *Solid State Comm.*, **126**:207, (2003).

[200] D. Malteree, G. Krill, J. Durand, and G. Marchal. *Phys. Rev. B*, **38**:3766, (1988). URL http://link.aps.org/doi/10.1103/PhysRevB.38.3766.

[201] E. Wuilloud, W. D. Schneider, B. Delley, Y. Baer, and F. Hulliger. *J. Phys. C: Solid State Phys.*, **17**:4799, (1984). URL http://www.iop.org/EJ/abstract/0022-3719/17/27/010.

[202] D. Malterre, M. Grioni, B. Daradel P. Weibel, and Y. Baer. *Phys. Rev. Lett.*, **68**: 2656, (1992). URL http://link.aps.org/doi/10.1103/PhysRevLett.68.2656.

[203] D. Jaccard, M. J. Besnus, and J. P. Kappler. *J. Magn. Magn. Mater.*, **63**:572, (1987).

[204] J. M. Lawrence, T. Graf, M. F. Hundley, D. Mandrus, J. D. Thompson, A. Lacerda, M. S. Torikachvili, J. L. Sarrao, and Z. Fisk. *Phys. Rev. B*, **53**:12559, (1996). URL http://link.aps.org/doi/10.1103/PhysRevB.53.12559.

[205] H. Wiesmann, M. Gurvitch, H. Lutz, A. Ghosh, B. Schwarz, M. Strongin, P. B. Allen, and J. W. Halley. *Phys. Rev. Lett.*, **38**:782, (1977). URL http://link.aps.org/doi/10.1103/PhysRevLett.38.782.

[206] F. P. Mena, D. van der Mare, A. Damascelli, M. Fth, A. A. Menovsky, and J. A. Mydosh. *Phys. Rev. B*, **67**:241101(R), (2003). URL http://link.aps.org/doi/10.1103/PhysRevB.67.241101.

[207] U. Bohnenkamp, R. Sandström, and G. Grimvall. *J. Appl. Phys.*, **92**:4402, (2002). URL http://link.aip.org/link/?JAPIAU/92/4402/1.

[208] S. Ramakrishnan, N. G. Patil, A. D. Chinchure, and V. R. Marathe. *Phys. Rev. B*, **64**:064514, (2001). URL http://link.aps.org/doi/10.1103/PhysRevB.64.064514.

[209] E. Bauer, G. Hilscher, H. Michor, Ch. Paul, E. W. Scheidt, A. Gribanov, Yu. Seropegin, H. Noël, M. Sigrist, and P. Rogl. *Phys. Rev. Lett.*, **92**:027003, (2004). URL http://link.aps.org/doi/10.1103/PhysRevLett.92.027003.

[210] R. Nagarajan, C. Mazumdar, Z. Hossain, S. K. Dhar, K. V. Gopalakrishnan, L. C. Gupta, C. Godart, B. D. Padalia, and R. Vijayaraghavan. *Phys. Rev. Lett.*, **72**: 274, (1994). URL http://link.aps.org/doi/10.1103/PhysRevLett.72.274.

[211] J. M. Lawrence, J. D. Thompson, and Y. Y. Chen. *Phys. Rev. Lett.*, **54**:2537, (1985). URL http://link.aps.org/doi/10.1103/PhysRevLett.54.2537.

[212] A. O. Pecharsky, Yu. Mozharivskyj, K. W. Dennis, K. A. Gschneidner, R. W. McCallum, G. J. Miller, and V. K. Pecharsky. *Phys. Rev. B*, **68**:134452, (2003). URL http://link.aps.org/doi/10.1103/PhysRevB.68.134452.

[213] T. Nautiyal, A. Kashyap, S. Auluck, and M. S. S. Brooks. *J. Appl. Phys.*, **75**: 6298, (1994). URL http://link.aip.org/link/?JAPIAU/75/6298/1.

[214] J. M. Machado da Silva. *Solid State Commu.*, **28**:857, (1978).

[215] S. Danzenbächer, Yu. Kucherenko, M. Heber, D. V. Vyalikh, S. L. Molodtsov, V. D. P. Servedio, and C. Laubschat. *Phys. Rev. B*, **72**:033104, (2005). URL http://link.aps.org/doi/10.1103/PhysRevB.72.033104.

[216] Y. Ijiri and F. J. DiSalvo. *Phys. Rev. B*, **55**:1283, (1997). URL http://link.aps.org/doi/10.1103/PhysRevB.55.1283.

[217] A. P. Murani, R. Raphel, Z. A. Bowden, and R. S. Eccleston. *Phys. Rev. B*, **53**: 8188.

[218] S. Wieling, S. L. Molodtsov, T. Gantz, J. J. Hinarejos, C. Laubschat, and M. Richter. *Phys. Rev. B*, **58**:13219, (1998). URL http://link.aps.org/doi/10.1103/PhysRevB.58.13219.

[219] J.M. Lawrence, V.R. Fanelli, E.A. Goremychkin, R. Osborn, E.D. Bauer, K.J. McClellan, and A.D. Christianson. *Physica B*, **403**:783, (2008).

[220] K. Petukhov, P. Weber, and M. Dressel. *J. Magn. and Magn. Mater.*, **272-276**: E105, (2004).

[221] N. B. Kolchugina, O. D. Chistyakov, G. S. Burkhanov, I. S. Tereshina, T. Palewski, and W. Suski. *J. Magn.Magn. Mater.*, **300**:E425, (2006).

[222] M. J. Besnus, J. P. Kappler, and A. Meyer. *J. Phys. F: Met. Phys.*, **13**:597, (1983). URL http://www.iop.org/EJ/abstract/0305-4608/13/3/010.

[223] S. Yamaguchi, Z. Q. Li, R. T. Fu, and Y. Kawazoe. *Phys. Rev. B*, **55**:14051, (1997). URL http://link.aps.org/doi/10.1103/PhysRevB.55.14051.

[224] S. Yamaguchi, M. Ohashi, T. Kajitani, K. Aoki, and S. Ikeda. *J. Alloys Compd.*, **253-254**:308, (1997).

[225] T. Gambke, B. Elschner, and L. L. Hirst. *Phys. Rev. Lett.*, **40**:1290, (1978). URL http://link.aps.org/doi/10.1103/PhysRevLett.40.1290.

[226] C. L. Seaman and M. B. Maple. *Physica B*, **199**:396, (1994).

[227] H. Borchardt, R. F. Hoyt, A. C. Mota, and D. Wohlleben. *Physica*, **108B**:1353, (1981).

[228] S. K. Dhar, S. Ramakrishnan, K. Ghosh, G. Chandra, and R. Vijayaraghavan. *Physica B*, **205**:249, (1995).

[229] H. Schneider and D. Wohlleben. *Z. Phys. B-Cond. Matter.*, **44**:193, (1981). URL http://www.springerlink.com/content/u87461t7k1ult346/?p=fcd7af08ed37456e8b231dab64314f08&pi=6.

[230] A. Pandey, C. Mazumdar, and R. Ranganathan. *J. Alloys Compd.*, **476**:14, (2009).

[231] M. H. Kane, K. Shalini, C. J. Summers, R. Varatharajan, J. Nause, C. R. Vestal, Z. J. Zhang, and I. T. Ferguson. *J. Appl. Phys.*, **97**:23906, (2005). URL http://link.aip.org/link/?JAPIAU/97/023906/1.

[232] A. Pandey, C. Mazumdar, and R. Ranganathan. *Appl. Phys. Lett.*, **94**:172509, (2009). URL http://link.aip.org/link/?APPLAB/94/172509/1.

[233] C. Mazumdar, A. K. Nigam, R. Nagarajan, C. Godart, L. C. Gupta, B. D. Padalia, G. Chandra, and R. Vijayaraghavan. *Appl. Phys. Lett.*, **68**:3647, (1996). URL http://link.aip.org/link/?APPLAB/68/3647/1.

[234] F. Tsui, C. Uher, and C. P. Flynn. *Phys. Rev. Lett.*, **72**:3084, (1994). URL http://link.aps.org/doi/10.1103/PhysRevLett.72.3084.